Northumbria University
NEWCASTLE

EVAPORATION OF SESSILE DROPLETS ON PINNING-FREE SURFACES

STEVEN ARMSTRONG

PhD

2021

EVAPORATION OF SESSILE DROPLETS ON PINNING-FREE SURFACES

STEVEN ARMSTRONG

A thesis submitted in partial fulfilment of the requirements of the University of Northumbria at Newcastle for the degree of Doctor of Philosophy

Faculty of Engineering & Environment

January 2021

Abstract

Contact-line pinning is a fundamental limitation of diffusion-limited evaporation of sessile droplets. Sessile droplet evaporation is pervasive in a wide range of situations from ink-jet printing, to pesticide sprays and spotted microarrays. Contact-line pinning drives, for example, stick-slip motion and non-uniform deposition of solute within the droplet. Moreover, contact-line pinning is problematic in a wide range of situations, such as droplet microfluidics where capillary forces dominate the motion of liquid fronts.

Recently, Slippery Liquid-Infused Porous Surfaces (SLIPS) have shown excellent droplet shedding abilities by use of a lubricating liquid, imbibed into a porous structure, immiscible to droplets on the surface. However, the lubricating liquid removes the droplet-solid-interaction, can cloak the droplet, can be several microns in thickness and the porous structure can be fragile to external mechanical forces. Slippery Omniphobic Covalently Attached Liquid-Like (SOCAL) is a new type of liquid-like surface, which is an attached coating rather than a retained liquid. SOCAL promises pinning-free properties while being nanometres thick and demonstrating mechanical robustness. Few research groups have reported successful creation of SOCAL surfaces.

This thesis shows an optimised methodology to make reliably, pinning-free low-hysteresis SOCAL surfaces. This is done by modifying the parameters to create SOCAL and measuring the contact-angle hysteresis. A low contact-angle hysteresis of $< 1^\circ$ is achieved. These surfaces then show, for the first time, constant contact angle mode evaporation of sessile water droplets from a solid surface. This allows for the accurate measurement of the diffusion coefficient of water. An unexpected feature of the evaporation sequences is a step change increase in contact angle reminiscent of a type V adsorption isotherm. Attempts are made to characterise this using Dynamic Vapour Sorption (DVS) and Quartz Crystal Microbalance (QCM) techniques.

This thesis also shows voltage-programmable control of water droplets on SOCAL using electrowetting. The unexpected behaviour of droplets on SOCAL is investigated and the electrowetting device is optimised. This allows control of the constant contact angle evaporation on both SLIPS and SOCAL. This is used to study the effect on the contact angle during the evaporation of sessile water droplets. The results of this thesis will benefit the aforementioned applications overcoming contact-line pinning and introducing new methods of controlling sessile droplet evap-

oration.

Contents

List of Figures

List of Tables

Acronyms

AC	Alternating Current 3, 20, 29, 30, 53, 82, 83, 92, 97, 106
AFM	Atomic Force Microscopy 44, 67, 106
CCA	Constant Contact Angle 22, 23, 55, 57, 59–61, 68, 69, 71, 95, 105, 107
CCR	Constant Contact Radius 22, 23
DI	De-ionised 38, 39, 41, 47, 48
DMS	Dichlorodimethylsilane 47
DSA	Drop Shape Analysis 51
DVS	Dynamic Vapour Sorption 3, 55, 64, 106
EDL	Electric Double Layer 28
EWOD	Electrowetting-on-Dielectric 27–29, 33, 53, 77, 93
IPA	Isopropyl Alcohol 39–41, 45
LIS	Liquid Infused Surfaces 16, 17, 23, 49
LLD	Landau–Levich–Derjaguin 46
MKT	Molecular Kinetic Theory 13, 14
OH	Oxygen-Hydrogen 39, 40
OpenCV	Open Source Computer Vision Library 52

OTS Octadecyltrichlorosilane 45

PDMS Polydimethylsiloxane 18, 40, 94, 99

PID Proportional Integral Differential 50

PTFE Polytetrafluoroethylene 3, 10, 14, 73, 74, 88, 106

QCM Quartz Crystal Microbalance vi, 3, 31, 32, 35, 55, 66, 106

RH Relative Humidity 40, 50, 55–57, 59–63, 69–71, 81

SAW Surface Acoustic Wave 108

SLIPS Slippery Liquid Infused Porous Surfaces 3, 4, 13, 15–17, 23, 32, 38, 44–49, 53, 54, 68, 75, 76, 88, 91–95, 97, 98, 100, 103–107

SOCAL Slippery Omni-phobic Covalently Attached Liquid xiii, 3, 4, 18, 19, 32, 35, 38–42, 44, 50, 53–57, 64, 66, 67, 69–71, 73, 76, 79, 80, 82, 83, 85, 88, 91–95, 97–100, 103–108

Nomenclature

α	Droplet sliding angle
Δc	Chance in vapour concentration
Δf	Change in frequency
Δm	Change in mass
ΔP	Pressure difference between two phases.
δ	penetration depth of the non-uniform electric field
$\Delta\theta_{CAH}$	Contact-angle hysteresis
ϵ_0	Permittivity of free space
ϵ_d	Dielectric constant of insulator
ϵ_l	dielectric constant of liquid
η	Viscosity
γ_{lv}	Liquid-Vapour surface tension. Commonly shortened to γ.
γ_{sl}	Solid-Liquid surface tension.
γ_{sv}	Solid-Vapour surface tension.
κ^{-1}	Capillary length.
Ω	Volume.
g	Gravitational acceleration

μ_q	Sheer modulus of quartz
ϕ_s	solid-vapour fraction of a surface
ρ	Density
ρ_q	Density of quartz
Ca	Capillary number
θ_e^{CB}	Cassie-Baxter contact-angle
θ_e^W	Wenzel contact-angle
θ_S	Static contact-angle
θ_A	Advancing angle
θ_e	Young's equilibrium contact angle
θ_R	Receding angle
ζ	Average distance between molecules
c_0	Vapour concentration at surface of droplet
c_∞	Vapour concentration far from droplet
C_d	Capacitance per unit area
D	Diffusion Coefficient
d	Dielectric thickness
E_{ds}	Dielectric strength
h	Droplet height
h_d	Film thickness
K_0	Adsorption-desorption frequency at the contact-line
k_B	Boltzmann constant
L	Typical macroscopic length scale
l_m	Microscopic cut-off length scale

R	Spherical Radius
r	Contact-radius
r_w	Roughness factor
S	Spreading coefficient, for a liquid on a solid in the presence of air.
T	Absolute temperature
U	Withdrawal speed
V	Voltage
v	Contact-line velocity
V_{bd}	Breakdown Voltage

Acknowledgements

Firstly, I would like thank my primary supervisor Professor Glen McHale and co-supervisors Dr Gary G. Wells and Dr Rodrigo Ledesma-Aguilar for their guidance and support throughout this project. Their extensive experimental and theoretical knowledge has been invaluable not only through this project, but in my development as a researcher.

I owe the technical staff at Northumbria University, Dr Pietro Maiello, Rebecca Payne and Gavin Warburton, my thanks for their assistance and valuable experience. I would like to thank the staff, academics and fellow Ph.D students I have had the pleasure of working with at Northumbria University. In particular I would like to thank; Dr Prashant Agrawal, Dr Élfego Ruiz-Gutiérrez, Dr Gaby Launay, Dr Nicasio Geraldi, Dr Bethany Orme, Bethan Ford, Becky McCerery and Hernán Barrio-Zhang. I would also like to thank my family and friends for their continuing support and understanding throughout this project. I would like to thank Northumbria University for the opportunity and funding of this Ph.D studentship.

Finally, I would like to express my deepest gratitude to my fiancée Rebecca Julie Wood for her continuous support throughout the three year project and in particular during the writing of the thesis. It is a cliché, but I could not have done it without her and for that reason, I dedicate this work to Rebecca.

Declaration

I declare that the work contained in this thesis has not been submitted for any other award and that it is all my own work. I also confirm that this work fully acknowledges opinions, ideas and contributions from the work of others. The work was done in collaboration with *Professor Glen McHale, Dr Gary G. Wells* and *Dr Rodrigo Ledesma-Aguilar*.

Any ethical clearance for the research presented in this thesis has been approved. Approval has been sought and granted by the *Faculty Ethics Committee* on *16/11/2017*.

I declare that the Word Count of this thesis is 35848 words.

Name: Steven Armstrong

Signature:

Date: 31/08/2020

Chapter 1

Overview

Consider a droplet of morning dew suspended on a thread of a spiders web. As the thread is so small and thin in comparison to the droplet, the droplet can be considered to be completely surrounded by air. The water droplet acts to minimise the surface area exposed to the surrounding air - providing the droplet is small enough such that surface tension dominates over gravity - it will form a spherical shape. When a droplet of water is surrounded by air which is not saturated by water vapour it will begin to evaporate. As the droplet is a spherical shape, the evaporation will occur radially in all directions. The evaporation rate and total drying time can be described by the properties of the system, such as density and volume of the liquid, surrounding temperature and relative humidity.

Now consider a droplet resting on a leaf. The shape is no longer spherical, again providing the droplet is small enough such that surface tension dominates over gravity, it will form the shape of a spherical cap. The droplet surrounded by air which is not saturated with water vapour can no longer evaporate radially outward in all directions, but is perturbed by the solid surface of the leaf. The surface has many implications to the description of the evaporation.

In the ideal case, a droplet in equilibrium on a surface forms a spherical cap based on the surface tensions of the three phases (solid, liquid and gas). This shape can be described by the contact angle the droplet makes with the surface. The ideal interactions between liquids and solids where first explored in the early 19^{th} century by Young and Laplace [1, 2]. However, experimentally observed droplets on surfaces often diverge from ideal. The contact angle a droplet makes with a

surface is also effected by chemical heterogeneity and surface roughness. In experiments, rather than a droplet adopting a single equilibrium contact angle, it can remain in equilibrium on a surface at a range of angles, known as the contact angle hysteresis. When a droplet makes a contact angle with a surface outside of the range defined by the contact angle hysteresis, it will move the contact line until a contact angle is reached within the contact angle hysteresis. Contact angle hysteresis also poses problems for droplet evaporation. A droplet on a non-ideal surface will evaporate in an uncontrolled stick-slip manner where the contact angle and contact line change as chemical heterogeneities and surface roughness, which cause contact-line pinning, are overcome. It is possible to engineer surfaces which reduce contact angle hysteresis and introducing more control to droplets on surfaces.

The ability to modify a surface to enable control of droplets and their evaporation is of great importance in both the nature and engineering and there are several strategies in both to enable this. In nature, the lotus leaf has a surface coated in waxy bumps that water struggles to penetrate, this causes water to ball up and simply roll-off the surface. The Nepenthes pitcher plant adopts a different strategy, allowing water to wick into a surface and hold it, this water is immiscible to the oils on the feet of flying insects which land on the plant, causing them to slip into a chamber to be eaten and digested. In Engineering, taking inspiration from the lotus leaf, a textured hydrophobic surface can be made superhydrophobic with contact angles $> 150°$. Another approach is to retain a liquid in a structured surface which is immiscible to water to remove any contact water has with the solid, thus removing contact line pinning. Both these methods require a surface structure which can often be fragile, and the surface is no longer smooth and flat. Recently a new type of liquid-like surface has been developed which allows the almost complete removal of contact angle hysteresis, whilst retaining a smooth flat surface which is mechanically robust.

Removing contact-angle hysteresis and reducing contact-line pinning has many applications. It can aid in heat transfer from evaporating liquids, allow more uniform deposition from particle-laden evaporating droplets and allows for more precise predictions on overall droplet evaporation times.

This thesis explores pinning-free surfaces and combines them with studies of evaporating droplets, and introduces fine control over the evaporation using electrowetting. The theory and relevant literature is detailed, covering, wetting, contact-line pinning, droplet evaporation and electrowet-

ting. Materials and experimental techniques used in this thesis include surface characterisation, preparation of pinning-free surfaces, experimental control of humidity, image analysis and electrowetting.

SOCAL surfaces are created and the procedure of manufacture is optimised for the equipment available. This results in reliably low contact-angle hysteresis surfaces $\Delta\theta_{CAH} < 1^\circ$ [3]. They are then observed to evaporate in an ideal constant contact angle mode of evaporation for the majority of the droplet lifetime for a broad range of relative humidities. This is the first report of constant contact angle evaporation of sessile water droplets from a smooth flat solid surface. This ideal evaporation allows accurate calculation of the diffusion coefficients of water. As SOCAL is omniphobic, opportunity exists to use sessile droplet evaporation as a method of calculating diffusion coefficients for a broad range of volatile liquids. An unexpected effect of the relative humidity is an apparent increase in the evaporation contact angle above a threshold humidity. While attempts are made to characterise why this step-change in contact angle occurs, using Dynamic Vapour Sorption (DVS) and QCM, results proved inconclusive, however, the most probable explanation for this change remains a type V adsorption isotherm.

At near-zero hysteresis, a droplet can only obtain a single contact-angle on a surface, to introduce control of the contact-angle electrowetting is used. Electrowetting is a vast subject with a lot of research interest. In this thesis, the performance of electrowetting equipment used is evaluated using Polytetrafluoroethylene (PTFE) surfaces, which prevent reversible changes to the contact-angle due to hysteresis. Then, in following the work of Brabcova *et al.*, electrowetting on Slippery Liquid Infused Porous Surfaces (SLIPS) shows a hysteresis-free reversible modification of the contact angle by application of a voltage. The electrowetting of SLIPS on a glass dielectric allows the use of experiments and theory to help inform an appropriate dielectric thickness to prevent device failure through voltage breakdown, while allowing the droplet to spread to the electrowetting contact angle saturation limit within the maximum voltage limits of the used equipment. Electrowetting on SOCAL does not provide the expected contact angle voltage relationship described by theory. To investigate, the salt type and concentration used in the water droplets for electrowetting is investigated, along with Alternating Current (AC) frequency and the rate of change in the voltage. It is concluded that although low hysteresis, the contact-line velocity is too great in these experiments to observe a quasi-static equilibrium angle.

Previously, water has only been shown to evaporate at a fixed contact angle on pinning free surfaces close to the expected equilibrium angle. In this thesis droplets are observed to evaporate at constant contact angle mode evaporation on both SOCAL and SLIPS at a voltage programmable contact angle for a broad range of contact angles using electrowetting. The constant contact angle obtained during evaporation corresponds to the expected value for a given voltage in the theory. This allows for the first time, constant contact angle evaporation at hydrophilic angles $\theta < 90°$. The constant contact angle evaporation also allows estimation of the diffusion coefficient, showing negligible effect from the oil layer in SLIPS to effect the evaporation. The electric field also doesn't appear to have an effect on the evaporation. This allows the theoretical calculation of the evaporation time dependence on contact angle to be compared to experiments, Providing a method of controlling the evaporation time using pinning free evaporation, useful for applications where pinning free evaporation and control of drying times is important, such as inkjet printing, and uniform florescence in DNA spotted micro arrays.

The results of this thesis contribute to the emerging and expanding field of liquid-like water repellent surfaces such as SOCAL. SOCAL provides pinning-free properties while being a smooth flat mechanically robust surface. This could rival other water repellent surfaces such as widely researched SLIPS surfaces, which require a retained liquid and a potentially fragile, retaining structure. This thesis shows pinning free evaporation of water from a smooth solid, flat surface for the first time. It also shows the pinning-free evaporation of droplets can be controlled using electrowetting, allowing precise control and prediction of the effect of contact angle on the drying time. This allows opportunities for further study of droplet evaporation on pinning-free surfaces in areas such as heat transfer, particle deposition and even and virus-resistant anti-bio-fouling surfaces.

Chapter 2

Introduction

This chapter looks at the background and theory of wetting, contact-line pinning, sessile droplet evaporation and manipulation of droplets using electrowetting. The section also provides a literature review on the topics covered in this thesis, to give an overview of recent and relevant research in the field. The topic of wetting is first covered, how droplets interact with solid surfaces and the forces that govern these interactions. Droplet mobility on surfaces is often inhibited by contact-line pinning. The source of contact-line pinning is discussed, along with its implications for various applications and strategies to over come it.

Evaporation occurs anywhere a volatile liquid is in the presence of a gas which is not saturated with a vapour of the liquid. Diffusion-limited evaporation is the effect of the vapour of the evaporating liquid on the evaporation of more liquid. A simple case of an aerosol droplet in free space is considered, then advancing to the case of sessile droplet evaporation, where the droplet is perturbed by the presence of a solid surface. There are two ideal modes of sessile droplet evaporation which are detailed. A gap in the literature is highlighted in the study of pinning-free droplets on solid surfaces. By removing pinning, evaporating droplet lifetime for a constant contact angle can be studied. Finally, this chapter discusses the fundamentals of electrowetting, a tool which can be used to spread a droplet on a surface.

2.1 Wetting

When a liquid comes into contact with a solid, it will either spread into a film or partially spread into a puddle or droplet, maintaining contact with the solid due to intermolecular interactions. These interactions and the degree to which a liquid will spread on a solid are known as wetting. It provides an explanation as to why a rain droplet will roll off a leaf but will penetrate into soil [2]. The behaviour of droplets on surfaces has many industrial applications, which makes it a field of significance and importance [4]. Wetting plays an important role in oil recovery [5], the distribution of active matter in pesticides [6] and even road water drainage. Wetting of droplets has applications such as inkjet printing [7], and heat transfer [8]. By understanding the behaviour of liquids interacting with solids, surfaces can be exploited to either attract liquids, repel liquids and even sort droplets of different surface tensions [9].

2.1.1 Surface Tension

A liquid is a state of matter that has a fixed volume (in equilibrium when evaporation is equal to condensation), but no fixed shape. Molecules in a liquid are held together by cohesive weak Van der Waals forces. Consider a droplet of liquid surrounded only by air. Cohesive forces of the molecules inside the bulk of the liquid will be pulled equally in all directions by surrounding molecules of the same element or compound (Figure. 2.1 (a)). Molecules at the edge of the liquid will not have the same molecules on all sides, they will therefore try to minimise their surface energy to satisfy their bonds by pulling inwards (Figure. 2.1 (b)). The forces will pull inwards creating an internal pressure forcing the liquid surface to reduce to a minimum. The result, is the liquid will make a perfect sphere as this is the shape where the least number of molecules are exposed to the surrounding air, in other words, the shape with the lowest surface area for a given volume. The force at which one phase opposes another is known as the surface tension, γ_{lv}. The surface tension of water in air at $25\,^{\circ}\mathrm{C}$ is typically $72.8\,\mathrm{mNm}^{-1}$ [10].

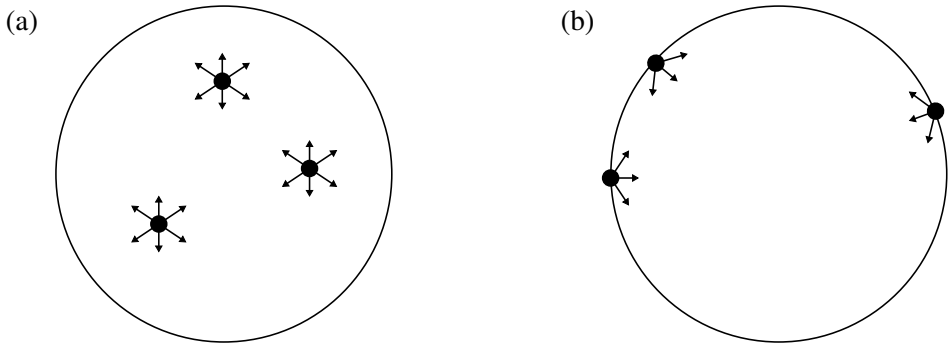

Figure 2.1: A spherical droplet of liquid surrounded by vapour where (a) shows molecules in the bulk of the liquid with cohesive forces pulling equally in all directions and (b) shows molecules at the liquid-vapour interface with uneven cohesive bonds pulling inwards to reduce the surface area.

2.1.2 Laplace Pressure

Considering again the sphere of liquid surrounded by air or a vapour phase. The pressure inside the drop will be driven by the liquid-vapour surface tension, γ_{lv}. The difference in pressure between the inside of the liquid and outside the liquid is known as the Laplace excess pressure.

$$\Delta P = P_{in} - P_{out} = \gamma_{lv} \left(\frac{1}{R_1} + \frac{1}{R_2} \right), \tag{2.1}$$

where ΔP is the pressure difference between the two phases and R is the radii of curvature of the droplet. This difference in pressure causes smaller droplets to empty into larger ones in an emulsion (figure 2.2). It also explains why smaller droplets will evaporate at a faster rate than larger droplets. It also explains why capillary bridges form and can create strong adhesion between fibres or wet sand.

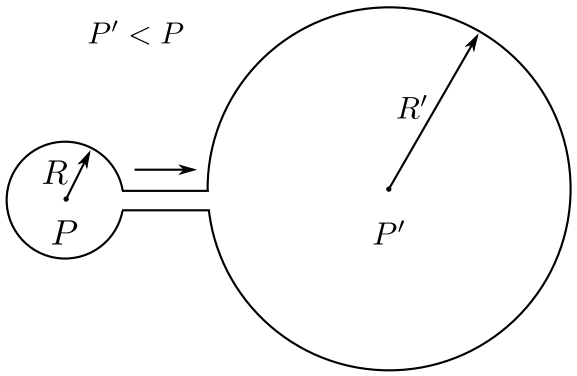

Figure 2.2: A smaller droplet with a smaller spherical radius R has a larger pressure P than a larger droplet with spherical radius R' and pressure P'

2.1.3 Capillary Length

Two competing forces which act upon on sessile droplets are surface tension and gravity. A simple dimensional argument can be made to compare the two forces. Surface tension, γ_{lv}, scales as a function of length, whereas gravitational forces, g, scale as a function of the mass of the drop (density multiplied by the volume) [11]. The ratio of the forces as the drop size scales as

$$\frac{\rho \mathrm{g} R^3}{\gamma_{lv} R} \propto R^2. \tag{2.2}$$

When the gravitational forces and surface tension forces are equal, $\sqrt{\gamma_{lv}/\rho \mathrm{g}} = 1$, with has units of length. This length is refereed to as the capillary length, κ^{-1} and is defined as

$$\kappa^{-1} = \sqrt{\frac{\gamma_{lv}}{\rho \mathrm{g}}} \tag{2.3}$$

where γ_{lv}, is the liquid-vapour surface tension, ρ, is the density of the liquid and, g, is gravitational acceleration $\mathrm{g} = 9.8\,\mathrm{m\,s^{-1}}$. Inputting the properties of water into equation (2.3), $\gamma_{lv} = 72.8\,\mathrm{mN\,m^{-1}}$, $\rho = 997\,\mathrm{kg\,m^{-3}}$ [12], the capillary length of water is $\kappa^{-1} = 2.7\,\mathrm{mm}$.

The capillary length can be used as a guide in experiments as to the typical length scale when surface tension dominates and the effects of gravity can be ignored, typically when the droplet is an order of magnitude less than the capillary length. This is particularly useful to the study of sessile droplets, when they are small enough, so that surface tension dominates gravity, the shape can be approximated to that of a spherical cap. A simple experiment to demonstrate this is to increase a droplets volume, Ω, and measure the height. If the droplet was unaffected by gravity, it would retain a spherical cap geometry as the volume increased, therefore the height would increase linearly with the volume. Figure 2.3 shows the droplet height increases linearly with volume up until $\Omega \approx 14\,\mu\mathrm{L}$. As the volume continues to increase the rate of change in the height begins to slow, this is visible on the inset droplet images in figure 2.3 where the $4\,\mu\mathrm{L}$ droplet is almost spherical, whereas the $150\,\mu\mathrm{L}$ droplet is visibly flattened by gravity. Experimentally, the effects of gravity can be neglected when looking at small droplets whose contact radius is below the capillary length.

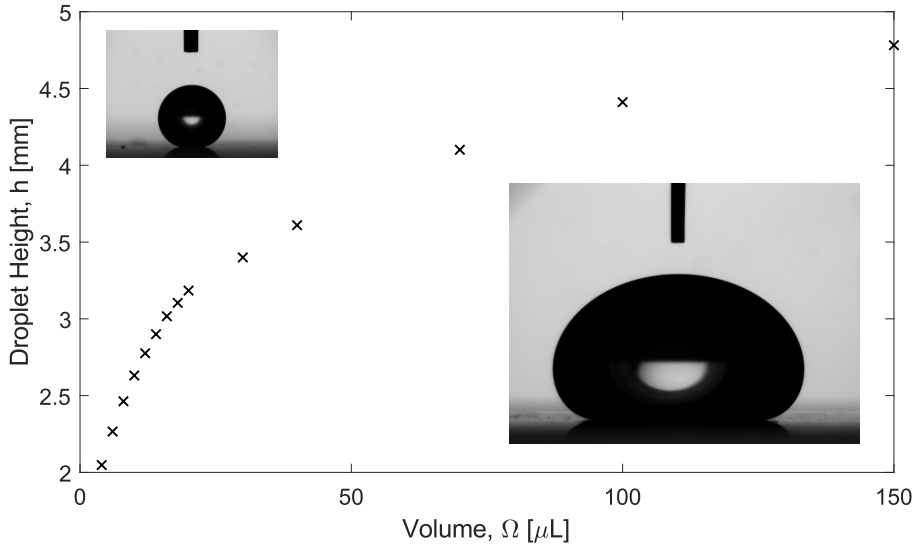

Figure 2.3: Droplet height, h as a function of volume, Ω of a DI water droplet on a superhydrophobic GLACO™ coated surface. The top left inset image shows a $4\,\mu$L droplet and the bottom right inset image shows a $150\,\mu$L droplet. The $0.4737\,\mathrm{mm}$ diameter needle is kept in both images for scale.

2.1.4 Spreading Coefficient

The interfacial energy of a dry smooth flat solid surface in air is γ_{sv}. If the same surface is coated in a thin layer of liquid there are now two interfaces, the solid-liquid interface (γ_{sl}) and the liquid-vapour interface (γ_{lv}), giving a combined interfacial energy of $\gamma_{sl} + \gamma_{lv}$. The combined interfacial energy of $\gamma_{sl} + \gamma_{lv}$ must be lower than that of γ_{sv} for a liquid film to form.

$$\gamma_{sl} + \gamma_{lv} < \gamma_{sv} \tag{2.4}$$

The comparison of these energy states is the spreading coefficient, S, for a liquid on a solid in the presence of air, i.e.

$$S = \gamma_{sv} - (\gamma_{sl} + \gamma_{lv}) \tag{2.5}$$

when $S \geq 0$, a film of liquid will form, the droplet will completely spread in order to reduce its surface energy. This will reduce the solid-vapour interface as it is a higher energy state than the combination of solid-liquid and liquid-vapour interfaces ($\gamma_{sv} > \gamma_{sl} + \gamma_{lv}$). When $S < 0$, a partial wetting scenario is seen.

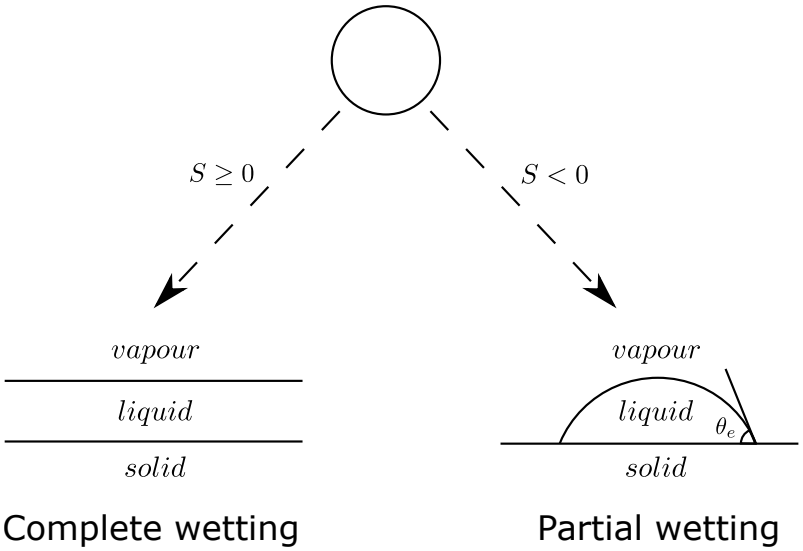

Figure 2.4: A liquid spreading into a complete film over a solid when $S \geq 0$ and a liquid forming a spherical cap shape in a partial wetting state when $S < 0$.

2.1.5 Young's Law

The shape of a droplet below the capillary length in equilibrium on a smooth flat surface is determined by the interfacial tensions between the solid-liquid, solid-vapour and liquid-vapour (Figure 2.5). This balance is defined by Young's equation (2.6) [1]

$$\gamma_{sv} - \gamma_{sl} - \gamma_{lv} cos\theta_e = 0 \tag{2.6}$$

where θ_e is Young's angle, γ_{sv} is the solid-vapour surface tension, γ_{sl} is the solid-liquid surface tension and γ_{lv} is the liquid-vapour surface tension γ_{lv} (commonly shortened to γ.) For water on a solid surface, a contact angle $\theta_e < 90°$ is considered hydrophillic and a contact angle $\theta_e \geq 90°$ is considered hydrophobic. One of the largest contact angle achievable on a solid flat surface is on PTFE (more commonly known as Teflon™) where $\theta \approx 120°$ [13]. It is possible to achieve larger contact angles by modifying the surface structure to make a surface superhydrophobic. Superhydrophobic surfaces are characterised by $\theta \geq 150°$ and contact angle hysteresis $< 10°$ [11].

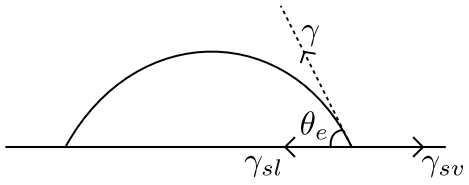

Figure 2.5: A Droplet on a smooth flat surface, the three interfacial tensions are shown as liquid-vapour (γ_{lv}), solid-liquid (γ_{sl}) and solid-vapour (γ_{sv}). θ_e is the equilibrium contact angle.

2.1.6 Cassie-Baxter & Wenzel States

Typically surfaces are not smooth and flat but rough and textured. The texture of a surface can alter how a droplet interacts with it. This can be in the form of roughness, dimples and protrusions [4, 11, 14–16]. When a droplet is in contact with a roughened surface it can adopt, a Cassie-Baxter state [17], Wenzel state [18] or a mix state between the two. A Cassie-Baxter state is where the droplet sits on top of the protrusions on the surface (figure 2.7 (a)). This reduces the contact the liquid has with the surface, causing the droplet to almost completely ball up allowing a droplet to move more freely [19]. The effect of the roughness on the equilibrium in a Cassie-Baxter state contact angle can be given in a simplified equation where liquid is bridging horizontally across flat topped pillars is given by

$$\cos\theta_e^{CB} = \phi_s \cos\theta_e^s - (1 - \phi_s) \tag{2.7}$$

where θ_e^{CB} is the Cassie-Baxter contact angle, θ_e^s is the equilibrium angle on a solid flat surface of the same chemical composition and ϕ_S is the solid-vapour fraction of the surface. The more complete Cassie-Baxter equation looked at a droplet wetting horizontal round wires (figure 2.6). This allows for a roughness factor that accounts for the surface area from the fraction of the surface of each round wire that was wetted. Essentially he used $f_1 \cos\theta - f_2$ where f_1 and f_2 where defined as total areas (and so allow for a non-planar meniscus shape and the curvature of the wire). This also means these factors depend on the Young contact angle.

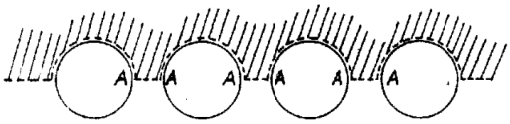

Figure 2.6: Water on cylinders. Figure from (Cassie & Baxter, 1944).

A Wenzel state is where the droplet penetrates between the surface protrusions. This increases the area in which the droplet is in contact with the surface, this can reduce droplet mobility, increasing pinning. [20] The effect of the roughness on the equilibrium contact angle in a Wenzel state is given by

$$\cos\theta_e^W = r_w \cos\theta_e^s \tag{2.8}$$

where θ_e^W is the Wenzel contact angle and r_W is the roughness factor, which acts as an amplification effect on the surface chemistry.

(a) Cassie-Baxter state (b) Wenzel state

Figure 2.7: (a) A droplet in a Cassie-Baxter state sits on top of any protrusions on the surface. (b) A droplet in a Wenzel state fills any protrusions in a surface.

2.2 Contact-line Pinning

Young's law is often used in many studies on wetting, however, it is rarely observed in practice. Contact-line pinning is a fundamental limitation that prevents droplets from reaching equilibrium. This section looks at the source of contact line pinning, how it is characterised and importantly, how it is overcome. Overcoming contact line pinning has great implications for many applications such as ink jet printing [21], precise deposition of particles [22,23] control of microfluidic droplets [24], prevention of biofouling in medical devices [25], cell analysis [26], and self cleaning surfaces [14].

There are two sources of pinning on surfaces; chemical and topographical. Chemical heterogeneity

can cause pinning on surfaces where liquids preferentially wet a solid rather than repel. Surface topography can cause pinning by way of defects on a surface that a contact line must overcome to advance.

2.2.1 Contact-Angle Hysteresis

Contact-line pinning can prevent a droplet from reaching Young's equilibrium angle, for most surfaces there are a range of angles a droplet can remain stationary on a surface. This can be a useful tool in the measurement of the adhesion of a surface [27]. Consider a droplet on a surface with a thin syringe filled with the same liquid and needle placed into the centre of the droplet. When inflating the droplet, the contact-angle the droplet makes with the surface directly before contact line motion is defined as the advancing angle, θ_A. During deflation the contact-angle the droplet makes with the surface directly before contact-line motion is defined as the receding angle, θ_R. The difference between the advancing and receding angles is known as the contact-angle hysteresis,$\Delta\theta_{CAH}$, again this is an inherent property of the droplet and the surface [28, 29]. Contact-angle hysteresis measurements are discussed in detail in Chapter 3.1.1. Another method to help quantify droplet adhesion to a surface when it is not possible to directly measure a contact angle, such as on some SLIPS, is through the sliding angle. Consider a droplet on a surface, if the surface begins to tilt the droplet will initially remain stationary, as the angle is increased the droplet will form a tear drop shape until such an angle is achieved where the droplet can move. The angle at which the droplet begins to move is known as the sliding angle (α); which is a property characteristic to the droplet and the surface. As the effect of gravity on the droplet scales with droplet volume rather than a linear size, it is easier to shed larger droplets than smaller ones, therefore care must be taken to state the size of droplets used in sliding angle measurements. Recently, efforts have been made to measure droplets adhesion to a surface using a capillary attached to the droplet and moving the surface underneath. The adhesion force is then calculated through the defection of the capillary [30, 31].

2.2.2 Contact-Line Dynamics

Contact line dynamics looks at the effect of the velocity of a moving contact line v, on the contact angle of the droplet. Two well known models that try to elucidate the motion of contact lines are the Cox-Voinov hydrodynamic model [32, 33] and the Molecular Kinetic Theory (MKT) model

[34]. Cox-Voinov theory states that viscous stresses from the surface and the surface tension of the liquid govern the deformation of the interface when a droplet is in motion, this deformation can be characterised as the contact angle as a function of the contact line velocity

$$\theta^3 = \theta_e^3 + 9\mathrm{Ca}\ln\left(\frac{L}{l_m}\right), \tag{2.9}$$

where $\mathrm{Ca} = \eta v/\gamma$ is the capillary number, η is the viscosity, L is the typical macroscopic length scale where the apparent contact angle is measured, and θ_e is the equilibrium contact angle and l_m is the microscopic cut-off length scale.

MKT states the contact line velocity is driven by the imbalance between the static and dynamic contact angles [34]. Adsorption of liquid molecules at the interface between the solid and liquid occurs when the contact line is advancing and desorption occurs when the contact line is receding. The balance between both processes gives the contact-line velocity [31],

$$v = 2K_0\zeta\sinh\left(\frac{\gamma\zeta^2(\cos\theta_e - \cos\theta)}{2k_BT}\right), \tag{2.10}$$

where K_0 is the frequency of adsorption-desorption of molecules at the contact line, ζ is the average distance between molecules, k_B is the Boltzmann constant and T is the absolute temperature.

2.2.3 Overcoming Pinning

Modifying a surface can be an effective way of reducing contact-line pinning with many different approaches available. One such well-known approach is the use of PTFE, also known as Teflon [35]. This approach modifies the surface chemistry to be hydrophobic to water. Recently there have been many advances in surface modification to increase water repellance.

Superhydrophobic Surfaces

Water repellance is often observed in nature. Many species of plants have hydrophobic leaves to allow water to either slide or roll-off, cleaning any dust and debris from the leaf and allowing the water to reach the ground where it can then be absorbed by the plant. The Lotus leaf uses surface roughness in the form of waxy bumps to cause water droplets to roll off [11, 36]. The bumps

are small enough so that a droplet sits on top of them in a Cassie-Baxter state, this increases the contact angle the droplet makes with the surface. This principle has been utilized to manufacture superhydrophobic surfaces using a range of different techniques. Barthlott & Neinhuis were the first to coin the terms *Lotus effect* and *superhydrophobicity* when characterising the water repellance of plant surfaces [36, 37]. T. Onda *et al.* show droplets ball up on fractal wax surfaces with contact angles $\theta = 174°$ [38]. Super hydrophobic surfaces have also been manufactured using lithography [39, 40] and sol-gel surfaces [41, 42]. Recently superhydrophobic surfaces have been made using soot from rapeseed oil [43] and using commercial nanoparticle sprays [44]. All of these approaches use a a rough patterned or porous surface which is either intrinsically hydrophobic or a hydrophobic coating is later added. While these surfaces offer excellent water shedding ability they have an inherent weakness that should a sufficient pressure be applied to the droplet, it will become impaled by the structure and no longer be able to move as the droplet is then in a Wenzel state. Because of the complex nano-scale structure of superhydrophobic surfaces, they are also not mechanically robust, limiting their potential applications. However, recently Wang *et al.* have shown that robust superhydrophobicity can be realized by structuring surfaces at two different length scales, with a nanostructure design to provide water repellency and a microstructure design to provide durability [45].

Slippery Liquid Infused Porous Surfaces (SLIPS)

The Nepethes pitcher plant also utilises surface topography to repel liquids [46, 47], however this complex topography is highly wetting to water. Condensing vapour from the atmosphere produces a thin water film on the surface, this repels the oils on the surface of insects feet, as they step onto the plant the insect slips and falls into the plant to be digested. The lubricating layer acts to reduce contact-line pinning.

In recent years, lubricant infused surfaces have been created to mimic these effects found in nature. One such surface is SLIPS [47]. These surfaces uses a complex topography to infuse an oil. The oil then acts as a lubricating layer between the surface and water droplets in contact with it as in figure 2.8.

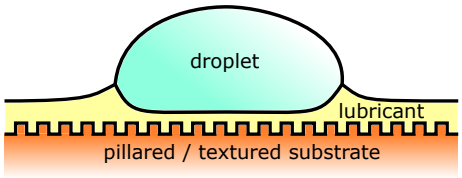

Figure 2.8: Illustration of a sessile droplet on a pillared SLIPS

To produce a SLIPS three critera must be met:

1. the lubricating liquid must wick into, wet and stably adhere within the substrate.
2. The solid must be preferentially wetted by the lubricating liquid rather than by the liquid one wants to repel.
3. The lubricating and impinging test liquids must be immiscible.

There also exists Liquid Infused Surfaces (LIS), which are again lubricant filled surfaces. However, in these surfaces, often the tops of the structures are in direct contact with the droplet which violates the first criteria of SLIPS. The second criteria of SLIPS is not always completely fulfilled, which can cause depletion of the lubricating layer over time exposing the solid surface to the liquid droplet [48]. LIS surfaces can be categorised depending on the wetting configurations underneath the drop and outside the drop (Figure 2.10). These states can be further expanded upon depending on whether the oil cloaks the droplet (Figure 2.10), with SLIPS occupying the A3-W3 state.The individual interfacial energies that define the spreading coefficients can be estimated using various methods [49–52].

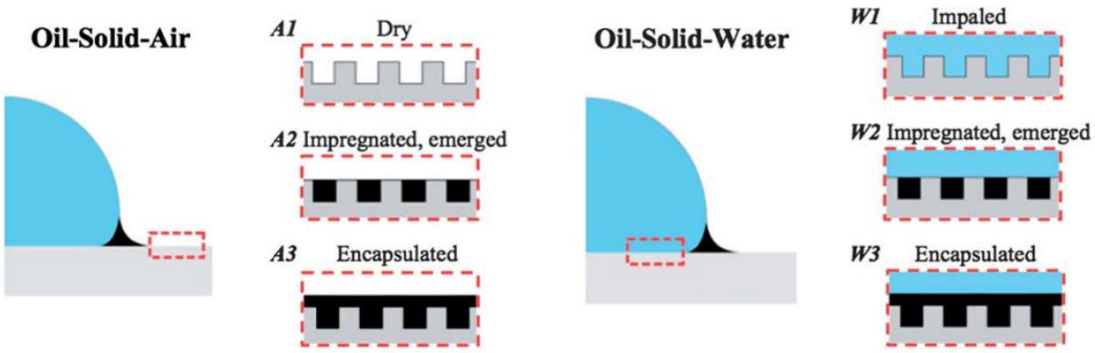

Figure 2.9: Schematics of wetting configurations outside and underneath the drop. Diagram from Smith *et al.* (2013).

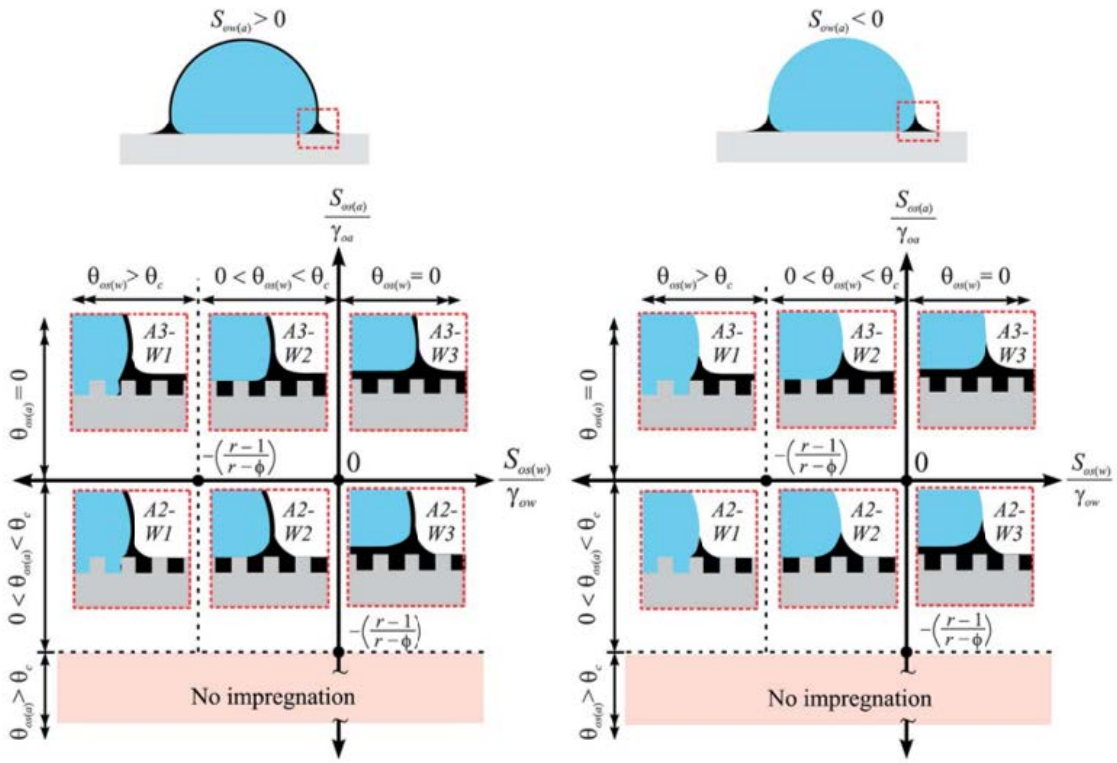

Figure 2.10: Possible thermodynamic states of a water droplet placed on a lubricant-impregnated surface. The top two schematics show whether or not the droplet gets cloaked by the lubricant. For each case, there are six possible states depending on how the lubricant wets the texture in the presence of air (the vertical axis) and water (horizontal axis). Diagram from Smith *et al.* (2013).

A key difference between SLIPS/ LIS and other water shedding surfaces is the formation of what is known as a wetting ridge [53]. This is the apparent movement of the oil up the side of the droplet. To better understand the interactions between a droplet and a liquid infused porous surface, one can consider a droplet on an immiscible liquid. The droplet deforms the liquid it is sitting on to create a lens shape [54] as in figure 2.11a, the three contact angles form what is known as a Neumann triangle [55] shown in figure 2.11b. This triangle is constructed from the three surface tensions and each of the contact angles. These three angles remain constant even in a SLIPS configuration, where the base liquid becomes very thin, giving rise to the appearance of a wetting ridge [53] shown in figure 2.11c. This ridge can make it difficult to observe the contact line dynamics of the droplet on a SLIP surface.

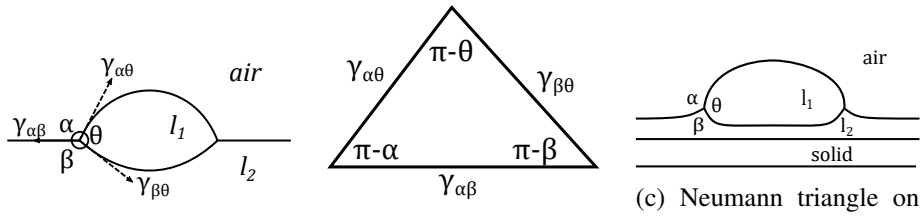

(a) Liquid lens (b) Neumann triangle (c) Neumann triangle on SLIPS

Figure 2.11: (a) A droplet (l_1) on a liquid surface (l_2) forming a liquid lens. ($\gamma_{\alpha\beta}$) is the surface tension between l_2 and air, ($\gamma_{\beta\theta}$) is the surface tension between l_1 and l_2, ($\gamma_{\alpha\theta}$) is the surface tension between l_1 and air. α, β and θ are the angles made between each phase (b) A Neumann triangle showing how each of the contact angles and surface tensions effect one and other. (c) A SLIP surface, where the Neumann triangle is still present.

Slippery Omniphobic Covalently Attached Liquid (SOCAL) Surfaces

Recently, Wang and McCarthy report the creation of a new hydrophobic surface that is an alternative to others such as SLIPS [3]. SOCAL surfaces are created through acid-catalysed graft polycondensation of dimethyldimethoxysilane onto a smooth flat surface, such as glass, or silicon. The result is a homogeneous layer of Polydimethylsiloxane (PDMS) grafted to the surface. This layer of PDMS acts as a liquid-like coating that the water droplet moves freely across, removing pinning and in turn, reducing contact-angle hysteresis ($\Delta\theta_{CAH} < 1°$). This low contact-angle hysteresis is reportedly the lowest achieved for a solid smooth flat surface.

When the contact-angle hysteresis of a surface is reduced to near zero, there can only be a single angle - within experimental uncertainty - that the droplet can make with the surface in equilibrium, the true Young's equilibrium contact angle (equation (2.6)). Currently, the suitability for SOCAL as a material to be used for fog harvesting is being researched [56]. It is also a potential candidate to be used in control of the wet-ability of soil, something that will make rare mineral extraction easier, a field with ever increasing demand as resources are used in technology and renewable sectors [57].

At present the successful creation of SOCAL has been limited, with the water shedding abilities reported vary in their level of success and detail in the literature. Wang and McCarthy report contact angles of $\theta_A = 104.6 \pm 0.6°$ and $\theta_R = 103.6 \pm 0.9°$, with tilt angles for motion of $4.7°$ and $1.3°$ for droplet volumes of 3 and 20 µL respectively [3]. The error bars in these measurements are the standard deviation from five independent measurements for contact angle hysteresis and three independent measurements for sliding angle. Jin *et al.* reported contact angles of $\theta_A =$

$103.0 \pm 0.3°$ and $\theta_R = 98.2 \pm 0.4°$ on silicon substrates [56]. They characterise the hysteresis by inflating and deflating a $4\,\mu L$ droplet at a speed of $0.5\,\mu L\,s^{-1}$, with each reported measurement compromising the average of four individual measurements on the same surface. Mizutani *et al.* report static contact as $\theta_S = 94.1°$ and a sliding angle of $40°$ on a nickel substrate for surgical bone drilling, no contact-angle hysteresis values are reported [58]. Dissipative forces acting on a droplet moving on several types of low-hysteresis surfaces has been reported by Daniel *et al.* This includes a SOCAL surfaces with a minimum critical tilt angle between $5°$ and $15°$ to move a $10\,\mu L$ water droplet but with no values reported for their advancing or receding contact angles [31]. Wang *et al.* graft SOCAL to a grooved silicon surface for directional droplet control. They measure $\theta_A = 106.7°$, $\theta_R = 104.2°$ and sliding angle $\theta_\alpha = 15.1 \pm 3.5°$ for $5\,\mu L$ water droplets [59]. Zhao *et al.* take a different approach than the volumetric method to characterization of advancing an receding contact angle [60]. SOCAL coated glass and silicon samples are placed on a temperature controlled stage. A piezoelectric dispenser is set 5-$10\,mm$ above the substrate, micro-scale droplets are dispensed allowing droplets to accumulate into larger droplets at $20\,°C$ at a rate of $150\,Hz$. This was recorded as the advancing angle. The receding angle was taken by allowing the same droplet to evaporate and measuring the angle. $\theta_A = 104.7 \pm 0.5°$, $\theta_R = m103.5 \pm 0.4°$ and $\Delta\theta_{CAH} = 1.1 \pm 0.6°$ on silicon. $\theta_A = 108.3 \pm 0.6°$, $\theta_R = 103.9 \pm 0.5°$ and $\Delta\theta_{CAH} = 4.4 \pm 0.8°$ on glass taken from the average of 5 independent measurements on a substrate.

2.3 Droplet Evaporation

Far away from any surface - providing the surrounding atmosphere is not saturated with the vapour of the liquid and there are no currents of air - an aerosol droplet of liquid will evaporate outward in all directions [6]. The spherical shape of small airborne droplets is deformed when in contact with a solid surface. Providing there is no contact line pinning, the small droplet forms an axially-symmetric spherical cap shape and can no longer evaporate equally in all directions because the diffusion is limited by the surface. The shape of the droplet on the surface can be defined by the contact angle, therefore, the contact angle will effect how the liquid vapour diffuses around the droplet ultimately effecting the evaporation rate. In practice, most surfaces exhibit contact-line pinning to some extent which can have practical consequences for applications that utilise droplet

evaporation. A famous example of contact-line pinning is non-uniform particle deposition known as the coffee-ring stain effect [22]. Contact-line pinning can cause problems from, preventing uniform delivery of the active compounds in pesticides to non-uniform fluorescence in spotted microarrays [61–63]. Contact line pinning during evaporation can be removed via active means, such as surface acoustic waves [64], or by high frequency AC electrowetting [62]. Due to the importance of evaporation of sessile droplets to a wide range of physical processes, the literature is extensive (see the reviews by, e.g., Erbil [6], Cazabat & Guéna [65], and Larson [66]). In general, the evaporation rate due to diffusion through the liquid-vapour interface is given as [65]

$$\frac{d\Omega}{dt} = -\frac{D}{\rho}\int \nabla C \cdot dS \tag{2.11}$$

where D is the diffusion coefficient of the vapour and ρ is the density of the liquid and $\bigtriangledown C$ is the vapour density integrated over the surface of the droplet.

2.3.1 Aerosol Droplet

A droplet in free space will adopt a spherical shape as this will minimise the surface free energy. The volume, Ω, of the liquid can therefore be defined as.

$$\Omega = \frac{4}{3}\pi R^3 \tag{2.12}$$

where R is the spherical radius. As there is no obstructions to the vapour, the droplet will evaporate radially outward in all directions (figure 4.16 (a)) [6]. The diffusion through the surface of the sphere of liquid will be defined as

$$\frac{d\Omega}{dt} = -\frac{4\pi R D \Delta c}{\rho} \tag{2.13}$$

where R is the spherical radius of the droplet and $\Delta c = c_\infty - c_0$ is the change in concentration is assumed to be radially outward and equal to $(c_\infty - c_0)/R$ where c_∞ and c_0 are the vapour concentrations of the vapour far removed from the droplet and close to the droplet.

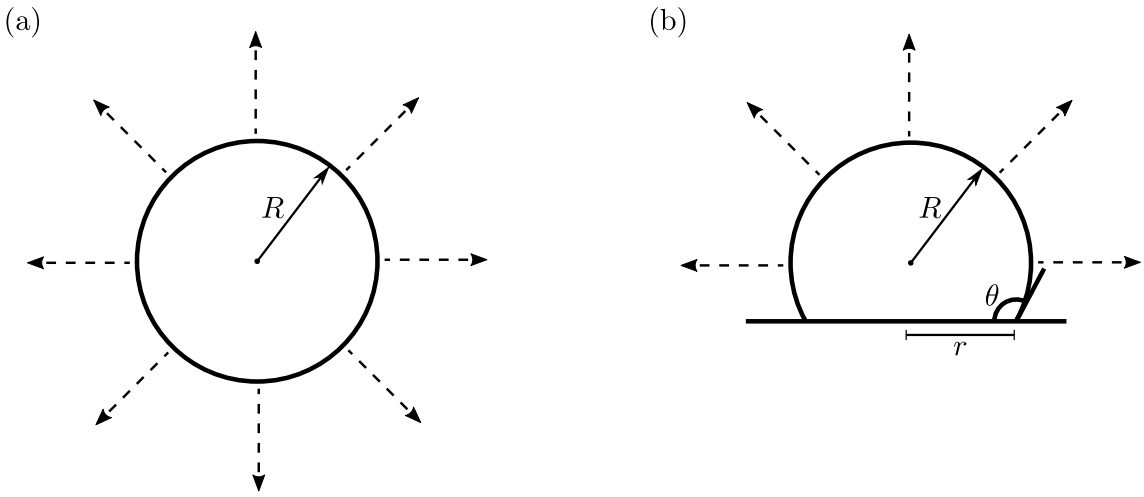

Figure 2.12: (a) A sphere of liquid in free space. (b) A spherical cap of liquid on a surface. At angles other than $\theta = 90°$ the vapour gradient becomes more complex, discussed in section 2.3.2.

2.3.2 Model of Diffusion-limited Evaporation

Geometric Description of Evaporating Sessile Droplets

If the droplet is placed on a pinning-free surface where the spreading coefficient $S < 0$, and the droplet is below the capillary length κ^{-1}, the droplet will adopt an axially symmetrical spherical cap shape with well-defined geometric parameters that can be measured from side profile images. These parameters include the spherical cap radius R, contact radius r, contact angle θ and droplet height h. The relationship between these parameters can be defined as

$$R = \left(\frac{3\Omega}{\pi(2 - 3\cos\theta + \cos^3\theta)} \right)^{1/3}$$

$$h = R(1 - \cos\theta)$$

$$r = R\sin\theta$$

$$\tan\left(\frac{\theta}{2}\right) = \frac{h}{r}$$

The presence of the solid surface limits the diffusion of the droplet as shown in figure 4.16 (b). The concentration gradient is assumed to be radially outward and equal to $(c_\infty - c_0)/R$ where c_∞ and c_0 are the vapour concentrations of the vapour far removed from the droplet and close to the droplet. Combining the geometrical assumptions with the concentration gradient model (2.11),

the evaporation rate can be expressed as

$$\frac{d\Omega}{dt} = -2\lambda R f(\theta) \tag{2.14}$$

where

$$\lambda = \frac{2\pi D(c_s - c_\infty)}{\rho} \tag{2.15}$$

$f(\theta)$ is a complex function of the contact angle the droplet makes with the surface.

Ideal Modes of Evaporation

In practice, sessile drop evaporation is subject to contact-line pinning to some extent. Picknett & Bexon provided an analytical model describing the ideal case of diffusion-limited evaporation of a sessile droplet in the absence of gravity, including an exact solution for the complex function of the contact angle $f(\theta)$ and a polynomial interpolation of their solution [67]. Their analysis identified two ideal modes of evaporation [67]. The first corresponds to a Constant Contact Radius (CCR) mode, where the apparent contact angle decreases during evaporation. Since the CCR mode of evaporation requires complete pinning of the contact line, it can be achieved experimentally and has been widely studied [68]. The second mode is a Constant Contact Angle (CCA) mode evaporation, where the contact angle is expected to retain a constant value approximating the contact angle predicted by Young's law whilst the square of the base radius of the droplet decreases linearly in time.

The observation of the CCA mode evaporation on a smooth (non-textured) flat solid surface remains elusive because it requires complete mobility of the contact line, and the roughness of ordinary flat solid surfaces always results in some contact line pinning. Instead, many experimental studies have reported a stick-slip mode of evaporation, whereby the droplet's contact line is repeatedly pinned until the force from the out-of-equilibrium contact angle increases sufficiently and a de-pinning event and rapid contact line motion occurs. Stauber et al. add further understanding describing another mode of evaporation known as stick-slide mode of evaporation, where the contact line and contact angle decrease at the same time. They provide a model to predict the

lifetime of evaporating drops in stick-slide mode evaporation [69]. Recent comprehensive reviews of sessile drop evaporation are given by Erbil [6], Cazabat & Guéna [65] and Larson [66].

Attempts to experimentally observe the CCA mode of evaporation have included the use of super-hydrophobic surfaces and SLIPS, a type of LIS [47, 48]. Super-hydrophobic surfaces take advantage of surface texture to suspend droplets in a Cassie-Baxter state [17] on a small solid surface fraction thereby reducing the droplet-solid contact area, increasing its contact angle and reducing contact-angle hysteresis [38]. McHale et al. [70] reported the first experiments of this type using SU-8 textured surfaces with water droplets initially evaporating in CCR mode evaporation, before retreating in a step-wise fashion as the droplet jumps between micro-pillars and ultimately converting into a Wenzel state where the droplet is impaled in the texture with a completely pinned contact line [18]. Since then, many works studying evaporation on super hydrophobic surfaces and the effect of contact-angle hysteresis has been reported [71–76]. In all of these studies, the surface is no longer smooth, but is textured or rough and hydrophobic, with a contact angle far from the value given by Young's law for a smooth non-textured solid surface.

A second approach to observing a CCA mode of evaporation was introduced by Guan *et al.* who used a SLIPS approach, with a lubricant oil impregnated into a hydrophobic SU-8 textured surface [77]. The lubricant oil completely coats the solid and is immiscible to water, therefore is not displaced by it. SLIPS enables droplets to slide at tilt angles of less than 1°. However, the high mobility of droplets on SLIPS arises by the replacement of the droplet-solid interface by a droplet-lubricant interface and the removal of all direct contact between the droplet and the solid. On SLIPS, contact angles and contact radii have to be interpreted as apparent contact angles and apparent contact radii from the change in slope of the droplet close to the surface. Guan *et al.* were able to observe the pinning-free evaporation of water droplets on SLIPS and interpret their evaporation using the Picknett & Bexon diffusion-limited model, modified for the presence of a wetting ridge of the impregnated oil which surrounds the droplet's base [77]. Ultimately, neither of these two approaches have provided observation of the evaporation of sessile droplets on flat smooth (non-textured) solid surfaces without contact line pinning. A key challenge remains the ability to remove contact line pinning during evaporation of sessile droplets from non-textured solid surfaces.

Model of Constant Contact Angle Mode Evaporation

Now focusing specifically on the model of constant contact angle mode evaporation. An exact solution for $f(\theta)$ was derived by Picknett & Bexon [67] and they gave a numerically accurate polynomial interpolation for $f(\theta)$ covering the entire contact angle range,

$$f_{PB}(\theta) = \begin{cases} \frac{1}{2}(0.6366\theta + 0.09591\theta^2 - 0.06144\theta^3) & 0^\circ < \theta \leq 10^\circ \\ \frac{1}{2}(0.00008957 + 0.6333\theta + 0.116\theta^2 - 0.08878\theta^3 + 0.01033\theta^4) & 10^\circ < \theta \leq 180^\circ \end{cases} \tag{2.16}$$

where θ in the series is radians. Geometrically the volume Ω can be defined as

$$\Omega = \frac{\pi\beta(\theta)R^3}{3} \tag{2.17}$$

where,

$$\beta(\theta) = (1 - \cos\theta)^2(2 + \cos\theta) \tag{2.18}$$

looking at side profile images of sessile droplets it is often easier to measure the contact radius, r, as opposed to the spherical radius, R, therefore substituting R^3 for $\frac{r^3}{\sin^3\theta}$ gives

$$\Omega = \frac{\pi}{3}\frac{\beta(\theta)r^3}{\sin^3\theta} \tag{2.19}$$

To look at the loss of volume in time due to evaporation during constant contact angle evaporation, we first integrate 2.19 with respect to time

$$\frac{d\Omega}{dt} = \frac{\pi\beta(\theta)r^2}{\sin^3\theta}\frac{dr}{dt} \tag{2.20}$$

R in equation 2.14 can be substituted for $r/\sin\theta$

$$\frac{d\Omega}{dt} = -\frac{2\lambda r}{\sin\theta} f(\theta) \tag{2.21}$$

rearranging 2.20 for dr/dt and substituting $d\Omega/dt$ for 2.21

$$\frac{dr}{dt} = \frac{sin^2\theta}{\pi\beta(\theta)} \frac{1}{r} \left(-2\lambda f(\theta)\right) \tag{2.22}$$

$$\frac{d(\pi r^2)}{dt} = -\frac{2\lambda \sin^2\theta f(\theta)}{\pi\beta(\theta)} \tag{2.23}$$

Integrated to give r^2

$$\pi r^2 = -\frac{D\Delta c f(\theta)}{\rho\beta(\theta)} t + \text{constant} \tag{2.24}$$

when $\pi r^2/t = \text{m}$ is the gradient of a straight line. This result shows the contact area of the droplet evaporating in constant contact angle mode evaporation decreases linearly in time.

Calculation of the Diffusion Coefficient

It is possible to calculate the diffusion coefficient from experiments observing evaporating sessile droplets in constant contact angle mode evaporation, measuring the decrease in contact radius (or contact area) in time. Equation 2.24 can be rearranged for D to give the following

$$D = \frac{\text{m}\rho\beta(\theta)}{8\Delta c f(\theta)} \tag{2.25}$$

c_0 is obtained from *Kaye and Laby Tables of Physical and Chemical Constants* [12] A polynomial fit of this data gives a calculated relationship between saturation vapour density to be

$$\text{Saturation vapour density} = 0.0004T^3 + 0.0053T^2 + 0.3759T + 4.7736$$

The actual vapour density is calculated using the following relationship

$$\text{Relative humidity} = \frac{\text{Actual vapour density}}{\text{Saturation vapour density} \times 100\%}$$

Similar to saturation vapour density, the literature value for the diffusion coefficient can be taken from the *CRC handbook of chemistry and physics constants* [10] and a relationship be given as

$$D = 0.0024T - 0.4677$$

2.3.3 Droplet Lifetime Dependence on Contact Angle in Constant Contact Angle Mode Evaporation

The lifetime of drying droplets is important for many applications including heat exchange [8], particle deposition [63] and inkjet printing [7]. Understanding how the contact angle of the droplet may effect time lifetime of the droplet is therefore important. For example, in inkjet printing when multiple droplets are deposited in the same location to increase the thickness of deposited material while keeping the increase of the width to a minimum, the subsequent drop should impact after the former drop has evaporated. To understand this dependence we can look at the rate of change in the contact area in time.

$$\frac{d(\pi r^2)}{dt} = -\frac{4\lambda \sin^2(\theta_c) f(\theta_c)}{\beta(\theta_c)} \tag{2.26}$$

where θ_c is the constant contact angle, that is the contact angle does not change during the droplet lifetime. Because the contact angle is constant, the contact area change in time is linear, this is determined by its initial value $\pi r_i^2(t_f = 0)$.

$$\pi r(t)^2 = \pi r_i^2 - \frac{4\lambda \sin^2(\theta_c) f(\theta_c) t}{\beta(\theta_c)} \tag{2.27}$$

The droplet lifetime is defined as the time when the contact area vanishes i.e. the value of t_f for

which $\pi r^2(t_f) = 0$ and can be written from (2.27) as

$$t_f(\theta_c, r_i, \lambda) = \frac{\pi r_i^2 \beta(\theta_c)}{4\lambda f(\theta_c)} \tag{2.28}$$

The droplet lifetime can also be defined by the volume using the relation between the volume and contact radius

$$t_f(\theta_c, \Omega_i, \lambda) = \frac{3}{4\lambda f(\theta_c)} \left(\frac{\pi \beta(\theta_c) \Omega_i^2}{c} \right)^{2/3} \tag{2.29}$$

The total lifetime of the droplet during constant contact angle evaporation of a spherical cap shaped sessile droplet depends on the value of the contact angle and the initial contact radius (or volume), and a parameter λ, combining the diffusion coefficient, density of liquid vapour concentration difference.

2.4 Electrowetting

In previous sections modification of a surface has been discussed to obtain different wetting properties. However it is possible to modify the apparent wettability though the application of an electric field. Electrowetting is a widely used tool that allows for the manipulation of droplets on surfaces. In particular Electrowetting-on-Dielectric (EWOD) where the solid-liquid contact area of a sessile droplet acts as one electrode in a capacitive sandwich structure thereby allowing the contact angle to be reduced by the application of a voltage. [78, 79] Electrowetting can manipulate and control droplets and has applications including, e.g., microfluidics, [80–82] liquid lenses [83] and optofluidics, [84] but often the surface properties of the dielectric and its hydrophobic coating causes contact line pinning. This can be overcome using a SLIPS coating as shown by a number of authors (e.g. [85, 86]).

2.5 Electrocapillarity and Electric Double Layer Theory

The field of electrowetting finds its origins in the late nineteenth century with the discovery of electrocapilarity by Gabriel Lippmann. He performed a series of experiments investigating the

capillary rise of mercury in glass capillary tubes (figure 2.13).

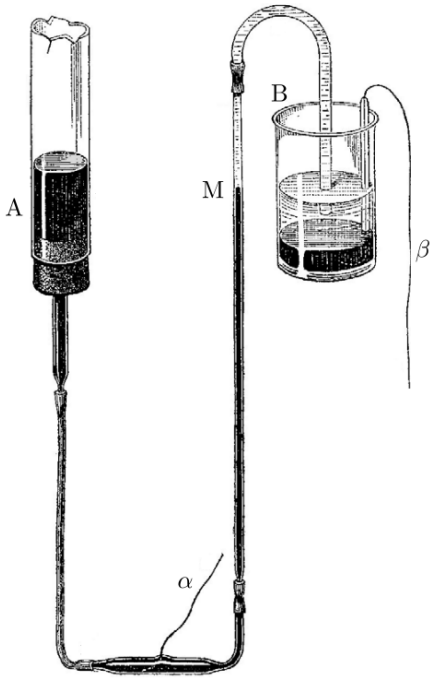

Figure 2.13: Lippmann's electrocapilarity experiment: (A) Reservoir of mercury, (B) electrolytic solution of water and sulphuric acid with mercury at the bottom of the beaker, (M) position of mercury meniscus in glass capillary and (α and β) platinum probes to voltage source. Figure Adapted from Lippmann (1845). English translation in Mugele *et al.* (2005).

He found that by applying a voltage between the mercury and an electrolytic solution the meniscus height varied with voltage. From these measurements he deduced the electrocapillary equation known as Lippmann's equation. It relates the charge density at the interface of the mercury and electrolytic solution, σ to the voltage, V dependence of the surface tension, γ,

$$\sigma = -\frac{d\gamma}{dV} \tag{2.30}$$

When a solid electrode is submerged in an electrolytic solution and a voltage is applied, ions of opposite charge in the solution redistribute and are attracted to the electrode while ions with the same charge are repelled. The ions that are attracted to the electrode form what is known as an Electric Double Layer (EDL) whose thickness is typically of the order of a few nanometres. The EDL continues to form and grow until the electric field vanishes in the bulk of the electrolyte due to the screening [87]. However, application of more than a few millivolts will cause an electrical current that degrades the system and electrolysis of the solution. The failure of the system in this way is the motivation for EWOD.

2.5.1 Standard Model of Electrowetting on Dielectric (EWOD)

In modern electrowetting, a dielectric is used to protect the device from short circuits a common issue in electrowetting on a conductor [79]. This is completed by using a conductive surface layered with a solid insulator, then using a conducting liquid drop (figure 2.14). The liquid-solid contact area acts as a capacitor, as a voltage is applied, the surface energy increases. This causes a spreading of the drop as it attempts to reduce the free energy of the system. A limitation with EWOD is the limit where the droplet will spread no further, meaning films of liquid cannot be induced [79]. However, recently Xiangming *et al.* report a lower-than-saturation contact-angle can be achieved by reversing the polarity of the applied voltage in a well-modulated way that charges and discharges the trapped potential [88]. The quasi-static contact angle made between the surface and the droplet is defined as a function of the applied voltage dependant on the dielectric properties and thickness of the insulating layer (eq.2.31) [79].

$$\cos\theta(V) = \cos\theta_e + \frac{\epsilon_0\epsilon_d}{2d\gamma_{lv}}V^2 \tag{2.31}$$

where V is the applied voltage, θ is the contact angle, θ_e is the equilibrium contact angle at $V = 0$, ϵ_0 is the permittivity of free space, ϵ_d is the dielectric constant of the insulator, d is the insulator thickness and γ_{lv} is the liquid-vapour surface tension. The dielectric properties can also be written as the capacitance per unit area $c_d = \epsilon_0\epsilon_d/d$.

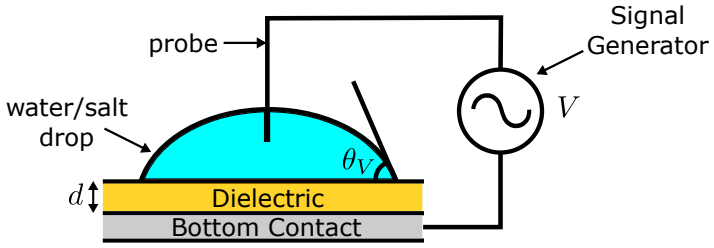

Figure 2.14: A water/ salt solution droplet in a EWOD configuration. d is the dielectric thickness and θ_V is the contact angle under applied voltage, V.

For the previously described contact-angle voltage relationship are based on a static relationship. When the voltage is adjusted slowly, the contact-angle can follow closely. In AC EWOD, if the frequency of the signal is greater than the hydrodynamic response of the droplet, the liquid

responds to RMS of the applied voltage and therefore, RMS is used in equation 2.31.

Frequency-Dependant Electromechanics of Droplet Electrowetting Behaviour

The standard Young-Lippmann equation (2.31) does not depend on the sign of the signal nor the AC frequency. If the frequency of the applied AC signal is modulated, the response that is observed depends on the frequency range [87]. There are two characteristic frequency regimes in electrowetting; hydrodynamic resonant frequency and electrical transition frequency. For typical drop sizes in electrowetting (microlitre), the hydrodynamic resonant frequency is in the range of tens to hundreds of Hz. In this frequency regime the droplet contact angle and shape will follow the predicted behaviour quasi-statically. The electrical transition frequency is where the droplet transitions from a perfect conductor behaviour, to a dielectric. This behaviour is dependant on the conductivity, dielectric constant and geometry of the droplet. This is typically in the range of several tens to hundreds of kHz. Below this critical frequency, the droplet responds to the time average of the applied voltage. For a sine wave voltage $V(t) = V_{pp} \sin \omega t$ where $\omega = 2\pi/\tau$ and V_{pp} is the peak-to-peak applied voltage. The Young-Lippmann equation for time-averaged apparent contact angle is therefore,

$$\cos\theta_{RMS}(V_{RMS}) = \cos\theta_e + \frac{\epsilon_0\epsilon_d}{2d\gamma_{lv}}V_{RMS}^2 \tag{2.32}$$

Because the AC Young-Lippmann equation is the same as the DC Young-Lippmann equation except the RMS voltage is used instead of peak-to-peak voltage, the RMS subscript is often omitted in the literature. However, as the frequency of the signal approaches the electrical transition frequency, the contact angle increases for a fixed voltage at increasing frequency [89]. Beyond this critical value, as the droplet behaves like a dielectric and begins to increase in resistivity, the temperature of the droplet can begin to increase [90,91]. Jones & Wang investigate the electrowetting response in the high frequency regime and provide a simple RC circuit model to predict the frequency dependant behaviour [92]. Ying-Jia *et al.* show experimentally the frequency dependence in high frequency electrowetting [93].

2.5.2 Dielectrowetting

The issue of contact angle saturation can be overcome using dielectrowetting [84, 94–97]. This involves placing a dielectric droplet onto a structure of interdigitated electrodes (figure 2.15). When a voltage is applied to this surface, a non uniform electric field is generated, which polarises dipoles within the liquid close to the liquid solid interface. This energy imbalance causes the liquid to spread with the increasing voltage. In this technique, liquid films can be induced.

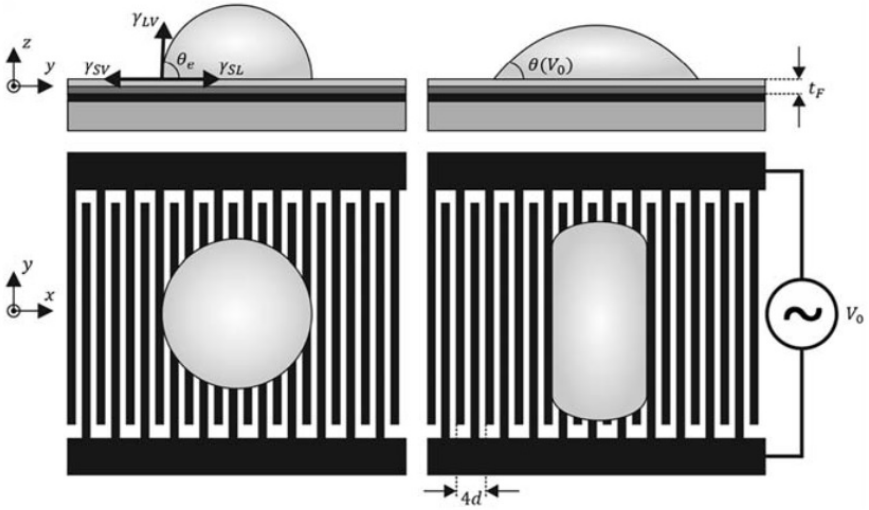

Figure 2.15: A droplet sat on top of a dielectrowetting surface, on the left, is a droplet in equilibrium, where $V = 0$. Right is a droplet after a voltage is applied. The droplet spreads along the electrodes. Diagram taken from (Edwards et al. 2018).

The cosine of the contact angle the liquid makes with the surface is again a function of the applied voltage-squared V^2 (eq.2.33), as with electrowetting. However rather than a dependence on the insulator thickness, such as in electrowetting , it is dependant on the penetration depth of the non-uniform electric field, δ, into the liquid. The penetration depth is related to the width and gaps between the interdigitated electrodes, d by $\delta = 4d/\pi$ [84].

$$\cos\theta(V) = \cos\theta_V + \frac{\epsilon_0(\epsilon_l - 1)}{2\gamma_{lv}\delta}V^2 \tag{2.33}$$

where ϵ_l is the dielectric constant of the liquid. A limitation of both electrowetting and dielectrowetting is high contact angle hysteresis. That is the droplet getting pinned as it moves across the surface causing changes in the contact angle between the solid and the liquid. Recently progress has been made to overcome this pinning, using SLIPS to reduce or even remove the contact angle

hysteresis [98].

2.6 Quartz Crystal Microbalance QCM

QCM is a method of measuring small mass changes per unit area on a surface by measuring the change in resonant frequency of a quartz crystal resonator. Quartz is a crystalline material which can experience the piezoelectric effect. The piezoelectric effect is the accumulation of electric charge in certain materials as a response to mechanical charge. in QCM this effect is utilised by applying an alternating current to electrodes on a quartz crystal which will induce thickness shear mode vibrations. These vibrations can be extremely stable and accurate, allowing precise measurement of the resonance frequency. The resonant frequency of the quartz crystal resonator is dependant on the intrinsic properties of the crystal with most equipment able to measure the accuracy of this to within a resolution of Hz for crystals of fundamental resonant frequency of $5\,\mathrm{MHz}$. If a mass is added to the quartz crystal resonator then the resonant frequency will shift. The Sauerbrey equation is used to to convert the change in resonant frequency to a change in mass [99].

$$\Delta f = -\frac{2f_0^2}{A\sqrt{\rho_q \mu_q}\Delta m} \tag{2.34}$$

where, f_0 is the resonant frequency of the unloaded crystal, Δf is the frequency change (Hz), Δm is the change in mass (g), A is the area between the electrodes (cm^2), ρ_q is the density of quartz ($2.646\,\mathrm{gcm}^{-3}$) and μ_q is the shear modulus of quartz ($2.947 \times 10^{-10}\,\mathrm{gcm}^{-1}\mathrm{s}^{-2}$). Sauerbrey's equation only applies to systems where the mass is rigid, evenly distributed and $\Delta f/f < 0.05$. Kanazawa and Gordon describe frequency shift and damping when the QCM is in contact with a liquid [100]. This sensitivity to mass deposition allows deposition of monolayers and (potentially) adsorbed mass to be monitored and measured. typically QCM measurements are taken in a humidity and temperature controlled environment so there is no expected change in behaviour due to temperature increase caused by the resonance of the crystal.

2.7 Conclusion

This chapter has given an overview of concepts and theories on how liquids interact with solid surfaces. This included how the balance of the surface tensions of the three phases define the shape of sessile droplets in the ideal case. It highlights a critical issue of contact-line pinning, that prevents the ideal Young's contact angle being achieved in various applications. A review of three surfaces that look to prevent contact line pinning are given, superhydrophobic, SLIPS and SOCAL surfaces. The theory of evaporation for both aerosol droplets and sessile droplets resting on a solid surface. The model of diffusion limited evaporation and the droplet lifetime dependence on contact angle is shown. The basic model of EWOD. These concepts together with the literature detailed in this section are the foundation of the work presented in this thesis. The next chapter details the experimental methods and techniques used to study sessile droplet evaporation on pinning-free surfaces from manufacture and characterisation of the surfaces, to measurements of there geometry during evaporation in controlled environments and with added potential difference through electrowetting.

Chapter 3

Materials & Experimental Techniques

This chapter describes the methods used to make and characterise a surfaces repellance to liquids, more specifically in this thesis the liquid to be repelled is water. The standard technique to characterise a surfaces properties is through contact-angle hysteresis measurements and sliding angles. Surface roughness can be measured through the use of profilometry. The adsorption of a liquids to a solid surface can be measured using QCM. Once these standard techniques are understood then the manufacture of slippery surfaces can be studied, using the aforementioned techniques to quantify their liquid shedding properties. Once slippery surfaces have been made and have been characterised to have good liquid shedding properties, experimental design and setup is discussed. This includes the creation of a bespoke humidity chamber. This is used both in the manufacture of SOCAL and to allow the observation of slow evaporation in a high humidity environment. The symmetrical nature of sessile droplets allows for useful information to be obtained from side profile images. Finally this chapter concludes with the basic electrowetting experimental setup.

3.1 Surface Characterisation

3.1.1 Inflation/ Deflation Contact-Angle Hysteresis

As previously described, a sessile droplet in thermodynamic equilibrium will form a contact angle, θ_e based on the three interfacial tensions (2.6). This contact angle is rarely observed in practice

due to contact-line pinning. Consider a sessile droplet on a surface with a thin capillary needle place in the centre of the droplet (figure 3.1 (a)).

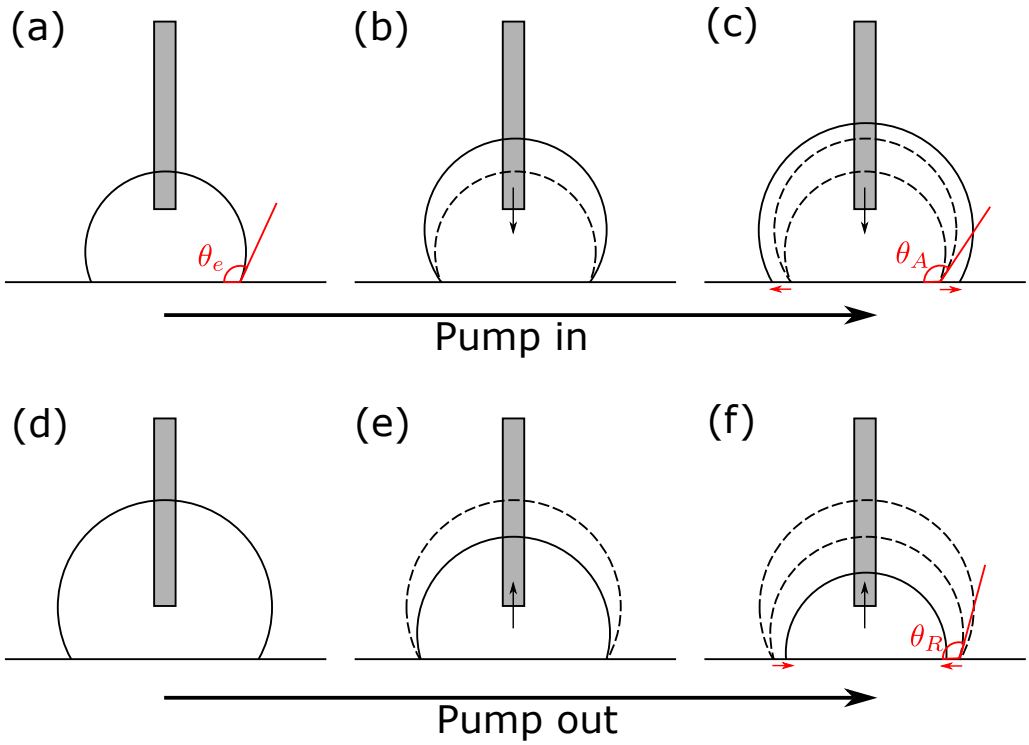

Figure 3.1: contact-angle hysteresis measurement stages:(a) Droplet in thermodynamic equilibrium with a thin needle inserted into centre. (b) Same liquid as droplet pumped in, Contact angle increases, base radius constant. (c) θ_A taken as angle instantly before radius increases.(d) Droplet in thermodynamic equilibrium with a thin needle inserted into centre.(e) Liquid pumped out, Contact angle decreases, base radius constant. (f) θ_R taken as angle instantly before radius decreases.

If liquid from the needle is dispensed into the droplet the contact angle observed would begin to increase while the base radius remains pinned (figure 3.1 (b)). At some point the radius of the droplet would begin to advance (figure 3.1 (c)). The contact angle at the moment the contact line begins to move is known as the advancing angle θ_A. This is the largest angle a droplet can sit on a surface without the contact line moving to try and return to equilibrium. To observe the smallest angle a droplet can take on a surface without the movement of the contact-line, again a droplet is placed on a surface with a thin needle in its centre (figure 3.1 (d)). This time liquid is pumped out of the droplet causing the contact angle to decrease while the contact line remains pinned (figure 3.1 (e)). Eventually the contact line will de-pin causing the droplet to begin to retract across the surface, the contact angle just before the contact line begins to move is known as the receding angle, θ_r (figure 3.1 (f)).

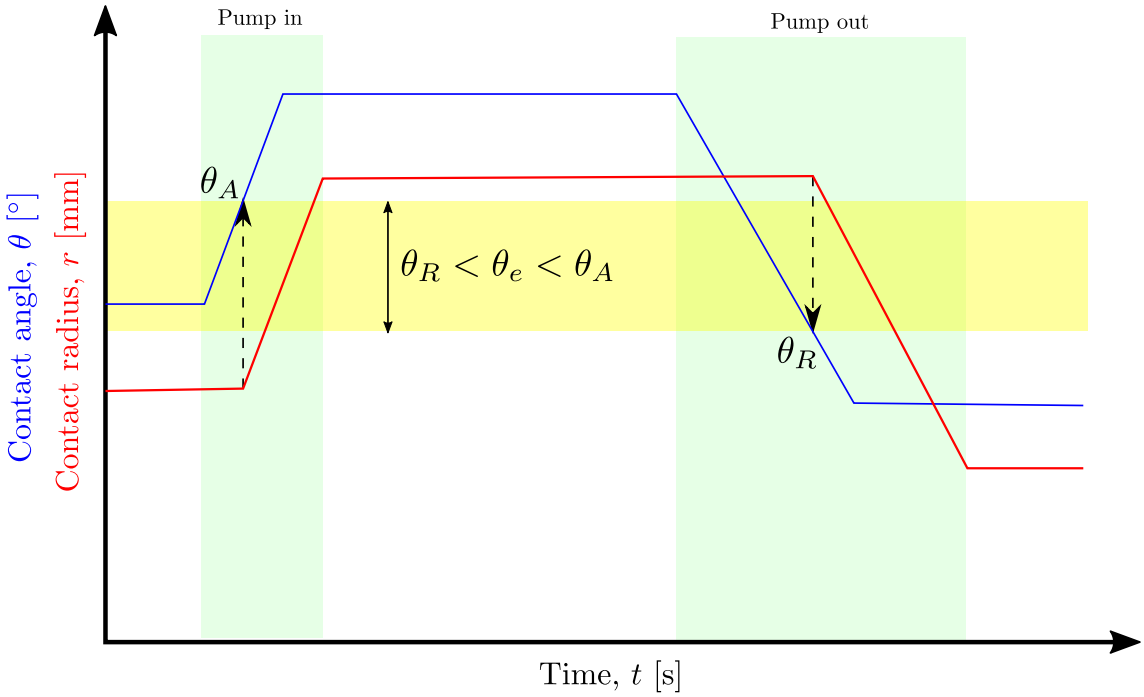

Figure 3.2: contact-angle hysteresis measurement plot of contact angle and contact radius in time

In practice the contact-angle of a stationary droplet on a surface will be between the bounds of the advancing and the receding angle. The difference between the two is known as the contact-angle hysteresis, $\Delta\theta_{CAH}$. The larger the contact-angle hysteresis, the more difficult it is to move a droplet [3, 27, 31]. A drop must distort from the spherical cap shape in order to move if there is any difference between θ_A and θ_R. Distorting the droplet requires the application of a force [101].

$$F = 2r\gamma_{lv}(\cos\theta_R - \cos\theta_A) \tag{3.1}$$

where F is the dissapative force acting on the droplet and r is the droplet radius. Contact-angle hysteresis makes it difficult to observe the true equilibrium contact angle as defined by the three surface tensions, θ_e. The true value of θ_e lies between the advancing and receding angle $\theta_R < \theta_e < \theta_A$. As contact-angle hysteresis reduces, the envelope of angles a droplet can sit on a surface in equilibrium reduces, until there is only a single angle a droplet can take with a surface θ_e. This can be seen visually on a plot of the contact angle and radius in time of the contact-angle hysteresis measurement (figure 3.2).

3.1.2 Sliding Angle

While contact-angle hysteresis is a useful measurement, it is not always possible to take clear side profile measurements of a droplets contact angle. On SLIPS when there is an excess of oil, a wetting ridge is visible. This wetting ridge makes it difficult to measure the contact angle. The sliding angle, α is characterised as the angle at which a droplet first begins to slide on a surface [101, 102]. A droplet of a fixed volume is placed on a surface, the surface is then very accurately ($\pm 0.2\,\mathrm{degrees}$) tilted, the angle where the droplet begins to move continuously is measured as the sliding angle. As the force acting upon the droplet is a component of the gravitational force, it changes with with mass, m, $F = mg\sin\alpha$ [30], it is important to consistently use the same volume droplet, unlike contact-angle hysteresis measurements, which do not depend on volume.

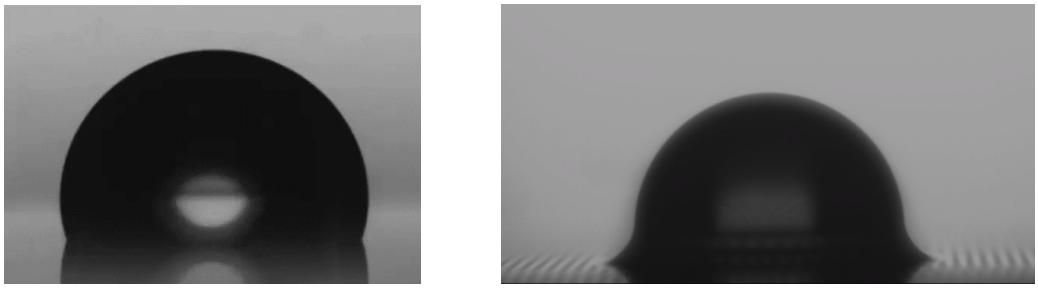

(a) (b)

Figure 3.3: Side profile image of a water droplet on (a) SOCAL, where a defined contact angle with the solid surface is clearly visible (b) SLIPS, where a wetting ridge is present preventing direct measurement of the contact angle. SLIPS image from Guan *et al.* (2015).

3.2 Materials & Surfaces

There are two types of surface used in this thesis to remove contact line pinning SOCAL and SLIPS. In this section the manufacture and characterisation of these surfaces is detailed.

3.2.1 Glass Cleaning Method

To produce samples on glass slides, it is important to thoroughly clean the glass before adding the SOCAL or SLIPS layer. This ensures the glass substrates are free from contaminants and are beginning with the same initial conditions when the surface is prepared. New glass slides are removed from their plastic wrapper and are rinsed with De-ionised (DI) water to remove any large debris. 20 glass slides ($25 \times 75\,\mathrm{mm}$) are placed into bespoke designed 3D printed glass slide holder

that fits into a standard $500\,\mathrm{mL}$ laboratory beaker. The glass slide holder is designed in such a way to grip the slides at the bottom maintaining minimal contact to ensure effective cleaning of the entire face of the slide (figure 3.4). The slides in the slide holder are submerged in DI water in the $500\,\mathrm{mL}$ beaker. 3% Decon90 (Decon Laboratories Limited) is added to the DI water, the mixture is then sonicated in a sonic bath (Fisherbrand™ S-Series) at room temperature for 30 minutes as per the Decon90 manufacturer guidelines. Decon90 is used to remove smaller contaminants that may not have been removed by the DI water rinse. The sonic bath is used to agitate the samples to further promote removal of contaminants. After this time, the glass slide holder is lifted out of the beaker and again rinsed with DI water to remove any remaining Decon90. The glass slide holder is then placed in a fresh beaker of DI water without Decon90 and sonicated again for an additional 30 minutes. This removes any excess cleaning agent from the glass slides. The glass slides are then removed from the holder and rinsed with acetone (Fisher Chemical) then immediately after with Isopropyl Alcohol (IPA) (Fisher Chemical). Acetone can leave a residue when dried which the IPA removes. This solvent rinse step is an additional measure to remove any remaining Decon90 mixture. The glass slides are then air dried in a fume cupboard until IPA has visibly evaporated (within a few seconds) as opposed to using compressed air which can reintroduce dust and debris onto the surface. The glass slide is then inspected and the solvent rinse step is repeated if the glass is streaky. Once complete, the glass slides are stored in individual plastic petri dishes until they are to be coated. While SOCAL could be prepared on glass slides which have been cleaned via less rigorous methods, any surfactants on the surface can present issues in coating uniformity so a thorough cleaning regime is recommended.

3.2.2 Preparation of SOCAL

SOCAL was first created by Wang & McCarthy in 2016 [3]. Since then, at the time of writing, this article has received over 125 citations, highlighting its significance. Of those citations, only six have reported successful creation of SOCAL surfaces and even then, with varying success [3, 31, 56, 58–60]. To make SOCAL surfaces for the experiments in this thesis, Wang & McCarthy's method was adapted to specific equipment available and with process parameters iteratively developed until a reproducible and low contact-angle hysteresis method was achieved. Glass slides which had been cleaned by the above method are placed into a Henniker plasma cleaner (HPT-100) at $30\,\mathrm{W}$ power for $20\,\mathrm{min}$. This step adds Oxygen-Hydrogen (OH) radicals to

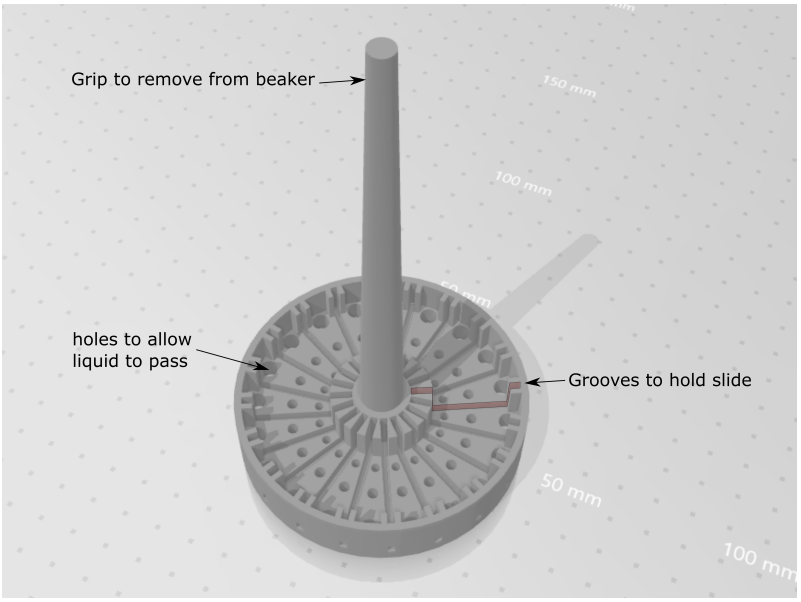

Figure 3.4: 3D printed slide holder: the grooves at the base hold the slides securely without obstructing the face of the slide where the surface will be coated.

the surface, which will allow the PDMS chains to attach and grow to the surface. The effect of changes to the plasma time and power are studied and detailed in the subsequent sub-sections. The slide was then dipped into a reactive solution of IPA, dimethyldimethoxysilane (Sigma Aldrich), and sulphuric acid (Fisher Chemical)(90, 9, and $1\,\%$ wt.) for $5\,\mathrm{s}$, and then slowly withdrawn (figure 3.5 (a)). The choice of solvent, acid and silane and their concentrations is studied in depth by Wang & McCarthy and characterise the SOCAL by the contact-angle hysteresis and coating thickness. For the method used in this thesis, the recipe with the lowest contact-angle hysteresis has been used. The OH radicals also increase the surface free energy, allowing liquids to wet more easily to the surface. This allows a film of liquid to form on the surface more easily. It is observed that with inadequate plasma cleaning power or time, the reactive solution can visibly de-wet from the surface after dip coating. This prevents a homogeneous reaction occurring across the entire surface, which is undesirable. The slides were then placed in a bespoke humidity-controlled environment at $60\,\%$ Relative Humidity (RH) and $25\,^{\circ}\mathrm{C}$ for $20\,\mathrm{minute}$. During this step, an acid-catalyzed graft polycondensation of dimethyldimethoxysilane creates a homogeneous layer of PDMS grafted to the surface (figure 3.5 (b)). The relative humidity during the reaction process is studied by Wang & McCarthy for relative humidities of 12, 30, 55 and 65%. As their results show large variations of contact-angle hysteresis with changing relative humidity ($1^{\circ} < \Delta\theta_{CAH} < 20^{\circ}$), the effect of relative humidity on contact-angle hysteresis is studied in the subsequent sub-section. Unreacted

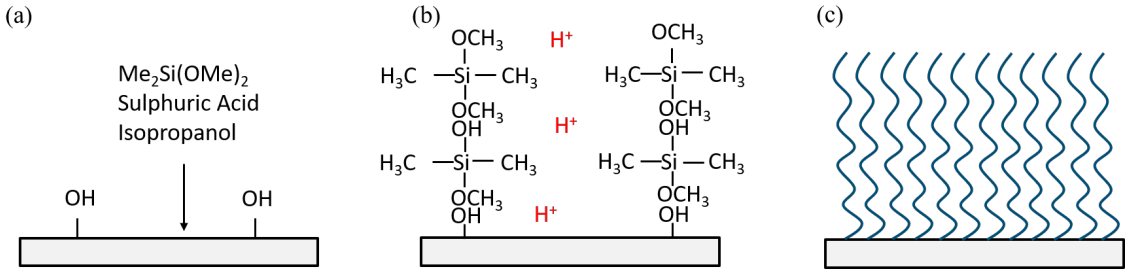

Figure 3.5: SOCAL preparation method: (a) plasma treated clean glass slide dipped in reactive solution, (b) PDMS chains grow in high humidity environment, (c) un-reacted solution rinsed off aft 20 min leaving uniform even coating of SOCAL. Figure adapted from Wang & McCarthy (2016).

material was then rinsed away with DI water, then IPA, and then toluene (Fisher Chemical) (figure 3.5 (c)).

As dimethyldimethoxysilane is hygroscopic, the reactive solution was prepared in 100 mL wide-mouthed screw top bottles, that allow dipping of the glass slides directly without the need to decant, limiting the reactive solutions exposure to moisture in the air. Should the solution expire, it visibly de-wets from the surface of the dipped glass slide rather than producing a desired uniform thin film. To prevent expiration of the solution, new solution to make samples was prepared approximately every two months. To prepare the reactive solution 91.45 mL IPA is poured into screw cap bottle measured using 100 mL graduated cylinder. 8.16 mL dimethyldimethoxysilane is measured using a syringe to the IPA and mixed using glass stirrer for 30 s. A volumetric pipette is used to slowly add 390 µL sulphuric acid while stirring with glass stirrer. These give the volumes of each chemical as reported by Wang & McCarthy. The solution was left to stand for 30 min at room temperature before being used. It is important to note the reactive solution must be mixed in the above stated order (IPA, dimethyldimethoxysilane, sulphuric acid) to prevent exothermic reaction of the IPA and sulphuric acid.

Characterisation of Contact-Angle Hysteresis

To characterise the SOCAL, an inflation/ deflation contact-angle hysteresis method was used. Contact-angle measurements were carried out using a Krüss Drop Shape Analyzer (DSA 30) and Krüss DSA4 software. A 4 µL droplet of DI water was dispensed onto the surface at room temperature (20-25 °C). A video sequence at 5 frames per second captured the inflation and deflation of the droplet to determine advancing and receding contact angles. The droplet was inflated by

$2\,\mu L$ at $20\,\mu L\,min^{-1}$, left to stabilize for $5\,s$, and then, $2\,\mu L$ was withdrawn at $1\,\mu L\,min^{-1}$. A slow withdrawal speed was used for contact-angle hysteresis measurements to limit the risk that the measured angles were dynamic angles. In all reported measurements, the advancing angle, θ_A, is the angle immediately before the droplet radius begins to increase. Similarly, the receding angle, θ_R, is the angle immediately before the droplet radius begins to decrease. Each reported contact-angle hysteresis value, $\Delta\theta_{CAH} = (\theta_A - \theta_R)$, is the average of contact-angle hysteresis values measured at three different locations on the SOCAL-treated glass slide. The error bars on these measurements is the standard deviation, this is inline with how Wang & McCarthy report the contact-angle hysteresis to allow a direct comparison of their surfaces and the ones produced for this thesis. It must be noted however, this does not account for errors in fitting methods and errors in the base radius so there is a larger level of uncertainty which is discussed in section (3.3.2).

Reaction Parameters

To produce SOCAL reliably and consistently with low contact-angle hysteresis, the following parameters need to be controlled and optimised: plasma exposure time; the relative humidity the reaction takes place, and the reaction time. With the plasma cleaner set to $100\,Watt$ power and varying the treatment duration from $30\,s$ to $30\,min$, a minimum in the contact-angle hysteresis occurs at $5\,min$ plasma time ($\Delta\theta_{CAH} = 1.8 \pm 0.7°$) shown in figure 3.6 (a). Although very low, this contact-angle hysteresis is larger than previously reported by Wang & McCarthy [3]. By reducing the plasma power to $30\,W$, the time sensitivity of the contact-angle hysteresis is reduced to achieve ($\Delta\theta_{CAH} = 0.9 \pm 0.3°$) with $20\,min$ plasma cleaning time (figure 3.6 (b)). To assess the reproducibility and the uniformity of results across a surface, the contact-angle hysteresis for each change in the process parameter was assessed using advancing and receding contact-angle measurements taken at three different locations on the surface; the average of the results across all the three locations is reported with its standard deviation.

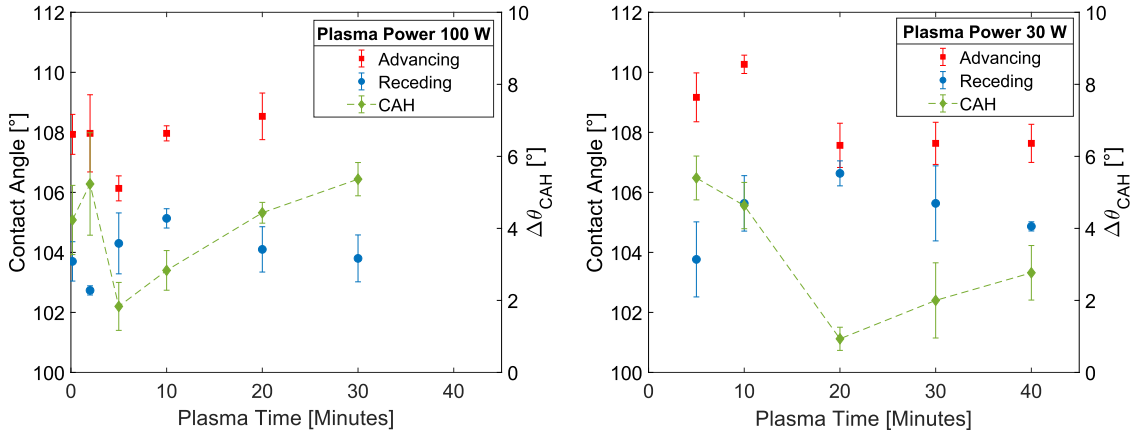

(a) (b)

Figure 3.6: Contact-angle hysteresis as a function of plasma power and time, (a) 100 W plasma power and (b) 30 W plasma power. The error bars represent the standard deviation of the advancing angle, receding and and contact-angle hysteresis separately.

With an optimum plasma power and time found at 30 W and 20 min, the relative humidity within the reaction chamber was varied to find the value which yielded the lowest contact-angle hysteresis (figure 3.7). A relative humidity of 60% gives $\Delta\theta_{CAH} = 0.4 \pm 0.2°$. To confirm reproducibility a further six samples are made using the same optimised parameters and characterised using contact-angle hysteresis (Table 1). The average contact-angle hysteresis of the samples using this recipe gives $\Delta\theta_{CAH} = 1.2 \pm 0.5°$ showing a reliable and reproducible low contact angle hysteresis.

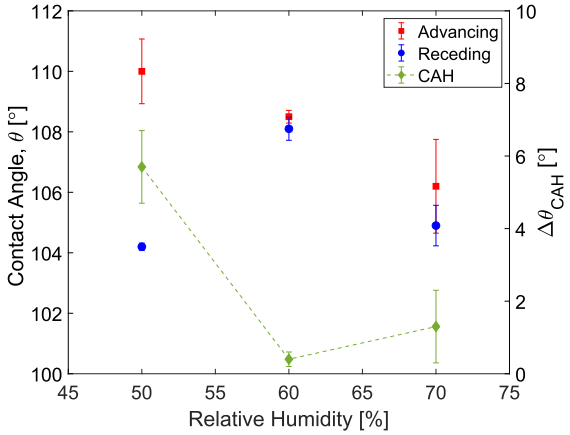

Figure 3.7: Contact-angle hysteresis as a function of contact angle as a function of relative humidity during the reaction process.

Table 1: Contact-angle hysteresis results for six SOCAL samples made using: 30 W plasma power, 30 min plasma time, 20 min reactive solution drying time and 60% reactive solution drying relative humidity. Adv. is the advancing angle, Rec. is the receding angle, Av. is average, S.D is standard deviation.

Sample	Repeat	Adv. Angle	Rec. Angle	$\Delta\theta_{CAH}$	$\Delta\theta_{CAH}$ Av.	$\Delta\theta_{CAH}$ S.D.	Adv. Av.	Adv. S.D.	Rec. Av.	Rec. S.D.
	1	107.9	106.3	1.6						
1	2	104.9	103.4	1.5	1.5	0.1	106.6	1.5	105.1	1.5
	3	106.9	105.5	1.4						
	1	108.7	106.1	2.6						
2	2	106.4	106.0	0.4	1.4	1.1	107.0	1.5	105.6	0.8
	3	105.9	104.6	1.3						
	1	108.3	107.9	0.4						
3	2	108.1	107.6	0.5	0.7	0.5	108.0	0.3	107.3	0.8
	3	107.7	106.4	1.3						
	1	108.0	106.5	1.5						
4	2	108.0	105.0	3.0	2.2	0.8	107.9	0.2	105.6	0.8
	3	107.6	105.4	2.2						
	1	107.3	106.5	0.8						
5	2	108.4	107.1	1.3	0.9	0.3	107.6	0.7	106.6	0.4
	3	107.0	106.3	0.7						
	1	108.7	108.5	0.2						
6	2	108.3	107.9	0.4	0.4	0.2	108.5	0.2	108.1	0.4
	3	108.4	107.8	0.6						
					1.2	0.5	107.6	0.8	106.4	0.8

Future Characterisation

While the aim of this study into the parameters was designed in such a way to achieve low hysteresis surfaces reliably and reproducibly, there are still many aspects of SOCAL surfaces that can be characterised and studied. Wang & McCarthy show with ellipsometry that the thickness of the SOCAL layer increases with longer reaction times [3]. For the reaction parameters used in this thesis, the expected SOCAL layer thickness is $4\,\mathrm{nm}$. Further work could be done to understand how the other parameters can affect the film thickness such as relative humidity and dip withdrawal speed. The uniformity of the coating can be analysed with Atomic Force Microscopy (AFM), determining whether pinholes are present.

3.2.3 Preparation of SLIPS

The preparation of SLIPS has been widely documented and has been easily reproduced in the literature [47, 77, 103, 104]. A common method is to use a pillared SU-8 surface for the oil to

wick into. The pillared structure is often coated with a chemically hydrophobic layer such as octadecyltrichlorosilane (OTS) [105] or Teflon [106], this makes the structure superhydrophobic. Creating a superhydrophobic surface reduces the surface affinity for water preventing the imbibing oil from being as easily displaced. If a water droplet was deposited on the superhydrophobic surface it would sit on top of the pillars in a Cassie-Baxter state with a large $> 150^\circ$ contact angle. With a pillared structure, the surface must be created on a flat surface on a small scale, which reduces the possibility of industrial or commercial applications. If photolithography is used to create the pillared structure, it can be expensive and time consuming. If the oil thickness or the pillar spacing is too great, a visible oil ridge between the droplet and lubricating layer observed, this makes characterisation of contact-angle hysteresis difficult. Recently the use of hydrophobic nanoparticles has allowed for conformal SLIPS where the excess oil can be shed until no visible wetting ridge is present [44, 107–109]. In this thesis, a GLACO™ coating is used with a silicone oil lubricating layer to make SLIPS. GLACO™ is a silica nanoparticle coated with a hydrophobic chemical coating. The nanoparticles are sprayed onto a surface out of a can using propellants and IPA. When the IPA evaporates, a porous nano-structure of particles is left.

Super-hydrophobic Characterisation

The glass substrates are first cleaned using the method detailed in section 3.2.1. In a fume cupboard, the glass slide is placed flat on a paper towel. The GLACO™ is then sprayed uniformly across the entire surface. The slide is then gently blown with compressed air until the IPA in the GLACO™ evaporates. This step is repeated for a total of 5 times, then the surface preparation is complete. To confirm the application was successful, the surface is now tested for superhydrophobic properties, static contact angle $\theta_s > 150^\circ$ and low contact-angle hysteresis $\Delta\theta_{CAH} < 10^\circ$ [16]. An alternative but equally effective method of applying the GLACO™ nanoparticles is to spray coat the glass slides while they are held at a 45° incline, then remove any excess liquid at the bottom of the slide using a paper towel. There are then two choices for the drying stage, at either high or low temperature. At room temperature, the coated slide can be left to air dry for 1 to 3 hours. The slide can be left to dry in an oven for $30\,\mathrm{min}$ at $250\,^\circ\mathrm{C}$. Each method requires 5 coats to provide the lowest contact-angle hysteresis as shown in previous studies [44, 109, 110].

Lubricant Imbibition

Once the superhydrophobic coating is confirmed it is then imbibed with silicone oil. Various imbibition techniques are reported in the literature for creating SLIPS using a GLACO™ porous texture. Orme *et al.* use dip coating at various speeds to tune the thickness of the oil layer [108]. Goodband *et al.* take a $500\,\mu\mathrm{L}$ drop of $20\,\mathrm{cSt}$ silicone oil placed at the center of the slides and immediately spin coat at $1000\,\mathrm{rpm}$ for $1\,\mathrm{min}$, then $500\,\mathrm{rpm}$ for $1\,\mathrm{min}$ [110]. Keiser *et al.* simply introduce the surface to a bath of oil where it spontaneously fills the textures ensuring overfilling does not occur [111]. An excess of oil is often undesirable, the water droplets can remove excess oil as they move across the surface, resulting in changing properties of the surface over time. McHale *et al.* show that the excess oil on an oil infused GLACO™ surface can be removed down to a conformal layer by rinsing the excess of oil from dip coating, this allows the observation of an apparent contact angle without a visible wetting ridge [107]. This is the technique used for studies in this thesis.

When dip coating a solid surface by withdrawal at a constant speed,U, from a bath of the liquid, the liquid will form a film on the surface of the solid of uniform thickness, h_d. The film thickness can be calculated by balancing the viscous forces responsible for the coating with the opposing capillary forces which yields the Landau–Levich–Derjaguin (LLD) equation [112, 113]

$$h_d \approx 0.94\sqrt{\frac{\gamma_{lv}}{\rho g}}Ca^{2/3} \tag{3.2}$$

where $Ca^2/3 = \eta U/\gamma_{lv}$ is the capillary number and η is the viscosity. For a textured solid, Seiwert *et al.* propose a modified LLD equation which accounts for the texture entrapping some liquid by [114]. As GLACO™ coatings are built on a surface via multiple spray coatings until it resembles a flat layer, the standard LLD equation can be used [108].

Characterisation

Previous literature has defined SLIPS water shedding ability only by sliding angle [44, 47, 108, 109]. However, creation of a conformal SLIPS allows for a clearly defined apparent static, advancing and receding contact angles without the lubricant ridge (as well as characterisation of the apparent contact angle hysteresis). Characterisation of a conformal SLIPS gives $\Delta\theta_{CAH} =$

$0.4 \pm 0.4°$ (table 2).

Table 2: Contact-angle hysteresis of a conformal SLIPS with a GLACO™ porous layer.

Repeat	Advancing Angle	Receding Angle	$\Delta\theta_{CAH}$
1	109.7	109.5	0.2
2	109.5	109.5	0.0
3	109.7	108.8	0.9
	$109.6 \pm 0.1°$	$109.2 \pm 0.3°$	$0.4 \pm 0.4°$

Ageing of SLIPS surfaces

SLIPS have a broad range of potential applications due to their water shedding properties discussed in section 2.2. However, the ageing of the surface is often overlooked, despite it being one of the biggest problems of self-cleaning surfaces [115]. Previous studies have looked at static storage in air as the mechanism for oil loss [108, 116], or under external perturbations on a freshly made surface [117–120]. Durability is assessed in terms of recovery after damage incidents [121–123]. As long as the oil layer is not depleted, SLIPS will retain their slippery properties [124–126]. It is possible for surfaces to regain their slippery properties if re-imbibed with oil [127].

To understand the ageing effect on the GLACO™ SLIPS used in this thesis, a systematic study is conducted on the ageing process. This is achieved by immersion into an aqueous solution of either DI water or $0.6\,\mathrm{mol}$ NaCl solution, then sonicated in an ultrasonic bath to ensure a reproducible but accelerated ageing compared to ambient laboratory conditions. This strategy enables the identification some of the mechanisms responsible for the oil loss and degradation of the porous layer, including the impact of dissolved salt ions in the aqueous solution that are in contact with the surface. The ageing of the surface is tracked and linked to nanoscale changes that occur within the different components. This is achieved by combining macroscopic contact angle and contact-angle hysteresis measurements. This approach allows for a systematic study into the effects of ageing across different length scales. The GLACO™ SLIPS surfaces are compared to a flat smooth dichlorodimethylsilane (DMS)-functionalized surface, imbibed with oil as a reference to single out the effect of porosity on oil retention. The two surfaces are left in ambient conditions with periodic measurements of weight and static contact angle (Figure 3.8). The thickness of the silicone oil layer decreases in time because of the losses to the environment (Figure 3.8(a)).

The loss is significantly more pronounced for the DMS-LIS, which depletes to below an oil layer thickness of $2\,\mu\mathrm{m}$ within 15 days. Static contact angle measurements (3.8(b)) show no evolution over the GLACO™ SLIPS, but a progressive return to oil-free values for the DMS-LIS. This is consistent with the almost complete oil depletion measured in figure 3.8(a).

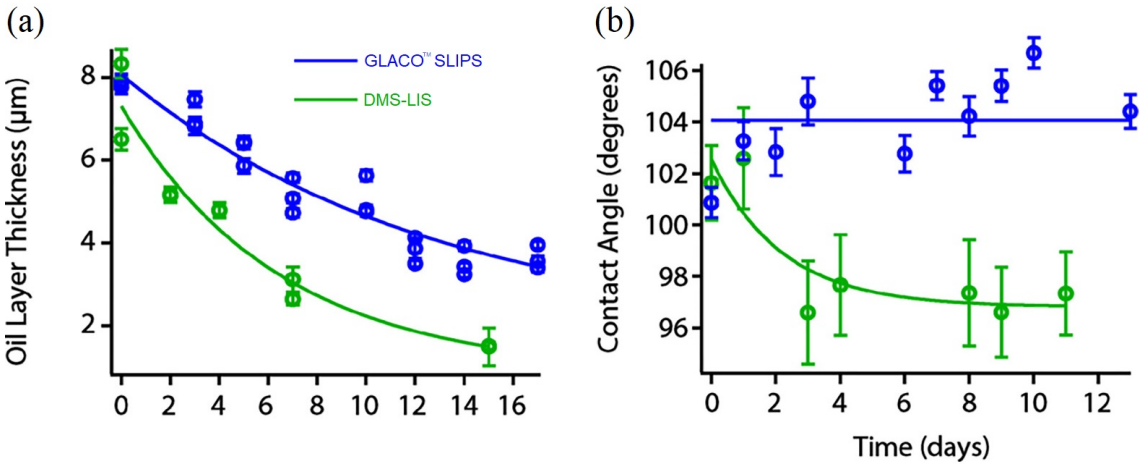

Figure 3.8: Oil retention ability of the DMS-LIS (Green) and GLACO™ SLIPS (Blue) in air under ambient laboratory conditions compared to the static contact angle: (a) Oil layer thickness as a function of time and (b) Static contact angle measurements. The two data sets are independent and were taken on different samples but placed together for comparison. Each point represents an average of 3 measurements with its standard error. The solid lines in (a,b) serve as eye guides. Figure adapted from Goodband *et al.* (2020).

To assess the impact of ageing in accelerated conditions, the GLACO™ SLIPS samples were immersed in aqueous solutions containing either DI water or a $0.6\,\mathrm{mol}$ NaCl (saline) solution and exposed to pressure waves by ultrasonication. The choice of the saline solution is to mimic conditions in a number of SLIPS applications, such as for medical devices, transport vehicles, and underwater structures. The ageing process used here is harsher than most natural conditions and can be seen as accelerated ageing. In both liquids, the average contact angle remains unchanged within error as the infused oil layer thickness decreases figure 3.9(c), but the spread of the contact angle values increases rapidly past $8\,\mathrm{min}$ of sonication (green dashed line). This indicates significant fluctuations arising with time, presumably due to pinning effects as the oil layer progressively becomes patchy. The oil layer thickness figure 3.9(c) was deduced from weight measurements taken every $30\,\mathrm{s}$ ($<5\,\mathrm{min}$) or every $60\,\mathrm{s}$ ($>5\,\mathrm{min}$) This is despite an exponential decay in the oil layer's thickness (Figure 3.9(c)). Both solutions exhibit a large spread of measured contact angle values with a rapid increase past $8\,\mathrm{min}$ of sonication. This transition approximately coincides with the

point where the oil layer thickness starts to plateau after an initial rapid decrease shown in figure 3.9 (c). This behaviour suggests the appearance of defects in the oil layer, with possible localized exposure of the GLACO™ SLIPS surface underneath. This exposure is localized enough not to affect the contact angle value on average, but sufficient to induce droplet pinning and a higher contact angle variability. Overall, this study shows that the ageing effect on GLACO™ SLIPS can be significant when exposed to non-ideal environmental conditions. This is a part of a larger study on LIS which also tracks the changes to the nanoscale structure [110].

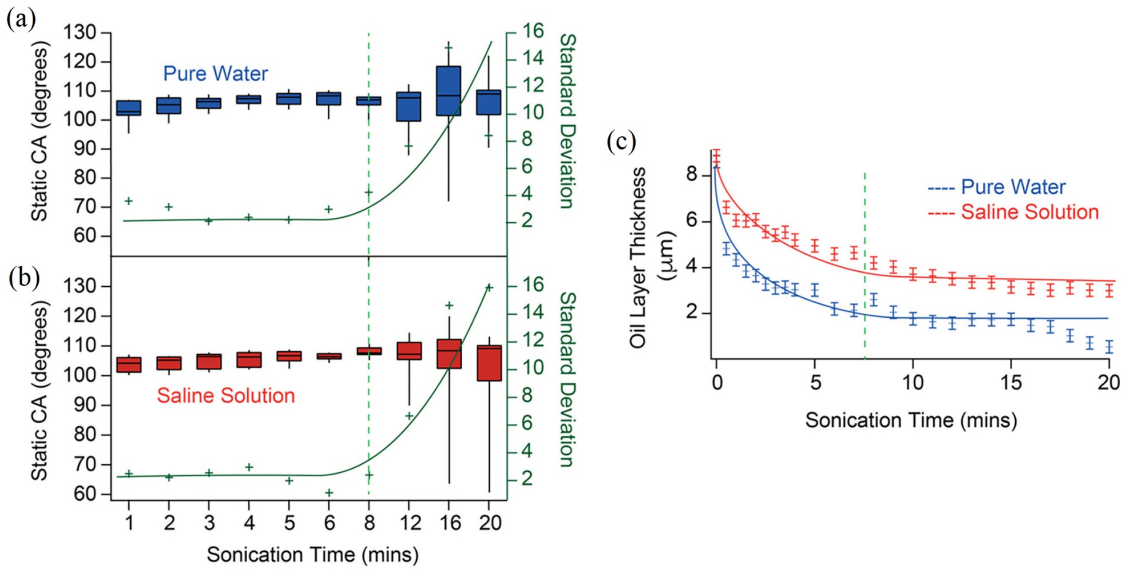

Figure 3.9: Accelerated ageing of the model LIS under ultrasonication in DI water and in a $0.6\,\mathrm{mol}$ NaCl (saline) solution. For both DI water (a) and saline solution (b), the evolution of the contact-angle hysteresis is presented in box and whisker plots (black) showing the median value and the upper and lower quartiles. The standard deviation (green) is shown as a function of sonication time with a fitted curve serving as an eye guide. Separate samples were used for the contact-angle hysteresis data (a,b) and the weight measurements in (c) to avoid the extended time periods necessary to take contact-angle hysteresis hysteresis measurements between weight measurements. The data represents 20 CA measurements taken over 5 different locations for each sample and at each time step for the box plots (a,b). Figure adapted from Goodband *et al.* (2020).

3.3 Experimental Design and Setup

3.3.1 Humidity Chamber

Evaporation of sessile water droplets are sensitive to their environment. Often laboratories are temperature controlled to maintain consistent experimental conditions. However, humidity is less often controlled. To ensure repeatability of experiments and because of the sensitivity of the

SOCAL manufacture process on humidity, a humidity controller was created for experiments. Compressed air, between $0.5 - 1.5\,\mathrm{bar}$ is introduced to the system. Two stepper motors open and close the *wet-line* (figure 3.10 (a)) and *dry-line* (figure 3.10 (b)) valves proportionally depending on the difference between the target humidity and actual humidity. The air in the *wet* line is saturated by two gas washing bottles, the first forces the air through water, where it picks up moisture, the second prevents large droplets being blown into the chamber (figure 3.10 (c)). A Raspberry Pi micro computer to read the input of real time temperature and humidity data in the chamber where the experiment is being carried out (figure 3.10 (d)). The Raspberry Pi also has a $9\,\mathrm{inch}$ touch screen which allows the user to change the target humidity, calibrate the sensitivity of the proportional control and view a plot of the humidity and temperature on a scrolling 5 minute plot. The humidity controller has a 2% dead band where both valves are closed and the humidity is considered at the target value. The deadband prevents overshoot of the control in place of full Proportional Integral Differential (PID) control. This system can control relative humidity to within $\pm 1\%$ of the target value with a range of $10 - 80\%$ RH. The range can be further extended with either additional water reservoirs in the chamber to increase relative humidity or silica beads to reduce relative humidity.

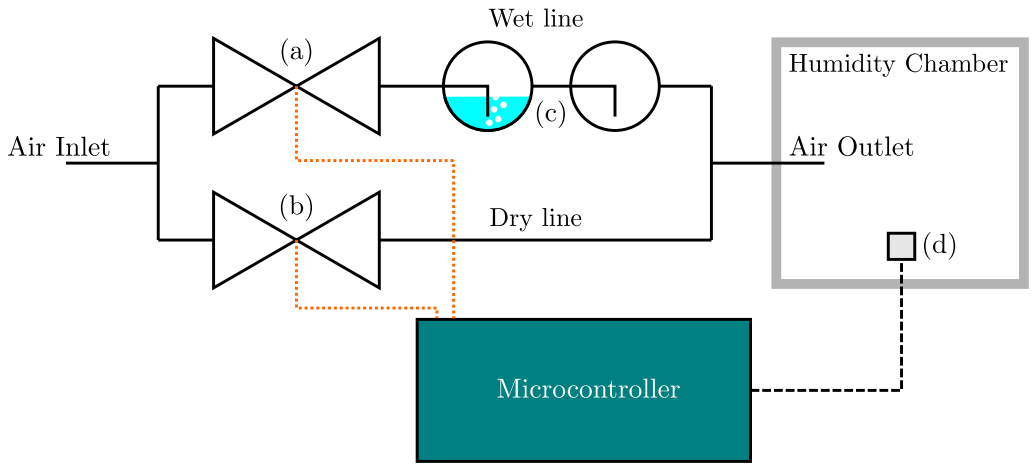

Figure 3.10: Schematic of humidity control setup: (a) Saturated air line control valve and stepper motor, (b) dry air line control valve and stepper motor, (c) gas washing bottles to saturate the air and to catch larger droplets, (d) temperature and humidity sensor for feedback control.

3.3.2 Image Analysis

To study sessile droplets on surfaces, side profile images can be taken, the droplet radius and contact angle can be measured. There are different challenges to overcome to do this. As water is

transparent, light will reflect and refract around the droplet making the shape of the droplet difficult to determine. By using a small aperture light, a shadow can be cast around the droplet, creating a sharp contrast of the droplet and background allowing for easier analysis. For this thesis, two software solutions were used for the measurement of droplets. Krüss Drop Shape Analysis (DSA) commercial software and pyDSA python freeware program [128]. The Krüss DSA commercial software has a stated resolution of $0.01°$ [129].

When analysing images using the pyDSA software, the first stage of analysis is to take a side profile image of the droplet, such as in figure 3.11 (a). To accurately measure lengths in the images, an object of known length is used to calibrate how many pixels represent a given length. As the pixels are square, calibrating an image with a horizontal length will allow measurements in all directions to be carried out. The needle used in experiments is of a known gauge and has a well defined outer diameter which can be used to scale the image, in figure 3.11 the needle is a 22 gauge needle, which gives an outer diameter of $0.72 \pm 0.01\,\mathrm{mm}$ according to the Birmingham gauge scale [130]. The baseline is set manually to the point the droplet meets the surface, the reflection of the droplet contact angle from the surface is a good visual cue to this point. Contact angles close to $90°$ may be difficult to determine so care must be taken to select the baseline from an image within an image sequence away from this value. Vuckovac *et al.* discuss the importance of good baseline fitting and resolution of images on the uncertainties in contact angle goniometry, where a single pixel error can lead to errors of $\pm 0.5°$ to $\pm 1°$ for contact angles up to $150°$ [131]. The edge detection of the droplet will pick up the syringe needle, preventing an accurate polynomial fit. The region of interest is selected to remove the needle while keeping the majority of the droplet in view.

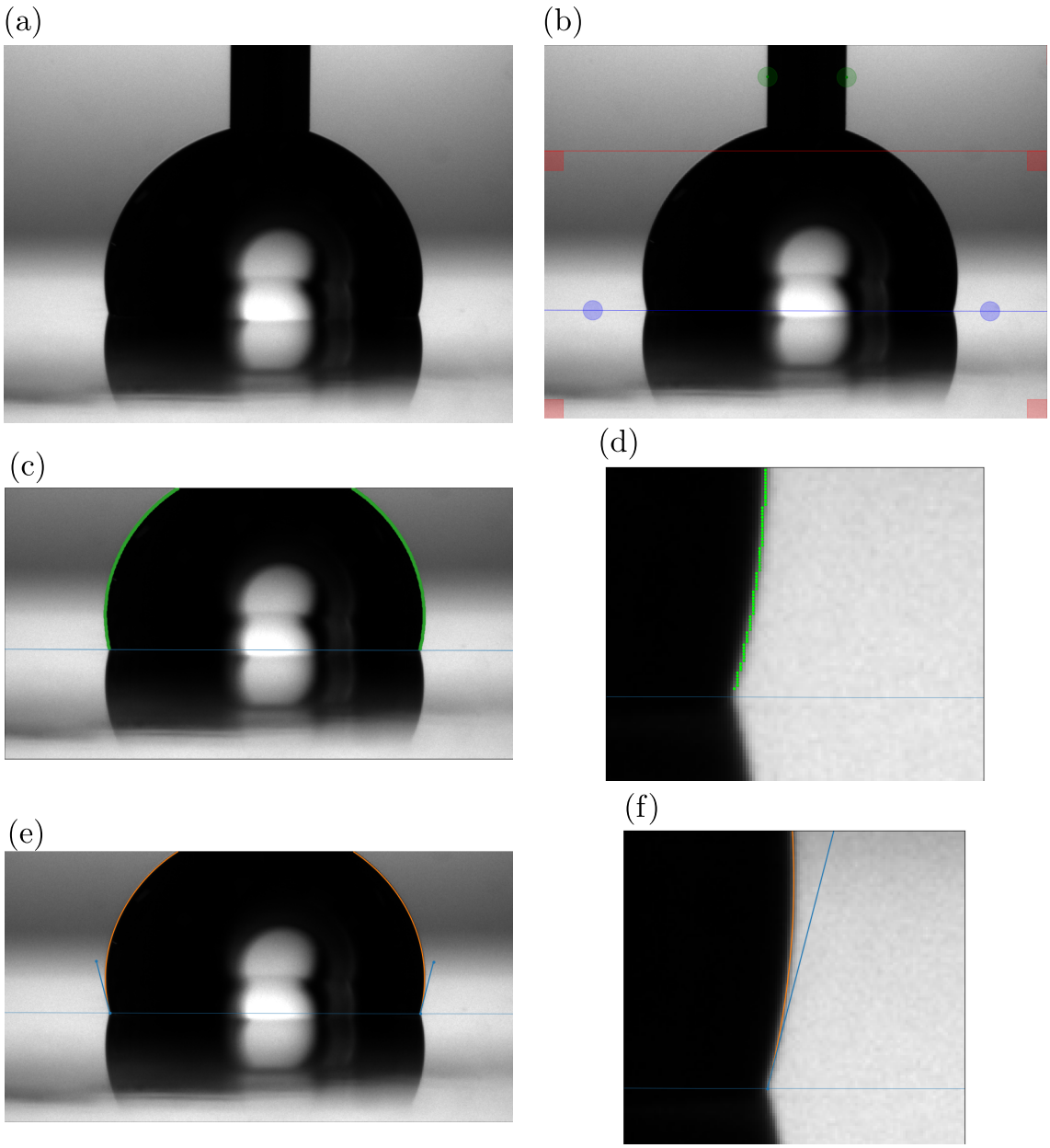

Figure 3.11: PyDSA Image analysis steps: (a) Side profile shadowgraph image taken of droplet, (b) baseline (blue line), region of interest (red box) and scale (green circles) are manually selected, (c) droplet contour detected, (d) close up of detected contour showing discrete points, (e) $3^r d$ order polynomial fit of droplet curve from contour points and (f) close-up of contact angle from where $3^r d$ order polynomial fit intersects baseline .

Open Source Computer Vision Library (OpenCV) Canny edge detection function is used to detect the edges of the droplet. This is a multi stage algorithm developed by John Canny in 1986 which detects the edge between two threshold values while filtering noise to give a single smooth edge [132]. In the pyDSA software, this returns an array of coordinates of where the edge is detected (figure 3.11 (c) and close up (d)). These coordinates are discrete positions, in order to

obtain the position of the triple-phase point and contact angle a fit of this discrete data is made. A polynomial fit is made to obtain these values, taking the contact angle from the tangent of the intersection between the fitted curve and the baseline (figure 3.11 (e) and close up (f)). The accuracy of the fitting used to measure contact angles of sessile droplets is the subject of research interest [133, 134]. Quetzeri-Santiago *et al.* consider the optimal order polynomial for the fitting of impacting droplets, and find a quadratic fit provides the most consistent results [135]. This analysis is automated to measure contact angles and droplet radius for entire image sequences, this information is then exported for further analysis.

3.3.3 Electrowetting

Section 2.4 describes the basic theoretical principles of EWOD. Experimentally, an AC system using a signal generator (TTi Instruments TGA1244) to generate a sinusoidal wave with programmable frequency ($1\,\mathrm{Hz}$ to $50\,\mathrm{kHz}$) which is then amplified (Trek PZD700A) as a programmable root mean square (rms) voltage, V, with a range of 0 to $600\,\mathrm{V}$ (figure 3.12). A second channel with a triangle wave can be used to modulate the signal amplitude to allow sweeping voltages at a constant $\mathrm{V\,s^{-1}}$ rate. This functionality allows observation of dynamic contact angles during changing voltages. The amplified signal is then applied to an aluminium-coated glass slide ($100\,\mu\mathrm{m}$, vapour deposited) as one electrode and a thin metal, $0.2\,\mathrm{mm}$ diameter, in the centre of the droplet, as the second electrode.

Different dielectrics such as Teflon™, SU-8, S18-13 and glass are used to alter the electrowetting properties (discussed in section 5.1). A slippery layer of either SLIPS or SOCAL can be added to the dielectric layer by the aforementioned methods. This is discussed in more detail in chapter 5. The droplets of deionized water used in the experiments had KCl and NaCl salts added to ensure the electrical conductivity required for electrowetting (section 5.2). The thin metal electrode is lowered into the centre of the droplet after deposition. experiments are conducted at room temperature ($22 \pm 2\,^{\circ}\mathrm{C}$) within a transparent chamber with the ability to control the relative humidity to regulate the conditions local to the droplet. The chamber also shields the droplet from the presence of air draughts which might effect the droplet or surface. electrowetting sequences are recorded using a camera. Contact radius, r, and contact angle, θ, measurements are then determined using open-source pyDSA software. Experimentally, profiles of the droplet are accurately described by

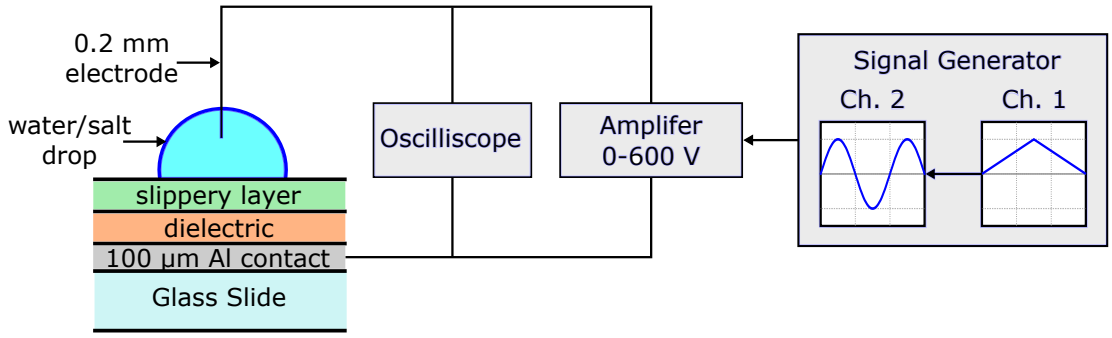

Figure 3.12: Electrowetting setup schematic: 2 channel input signal with triangle and sine wave sends a rate programmable signal into a 0-600 V amplifier. The amplified signal goes to the $0.2\,\mathrm{mm}$ probe and the Aluminium contact.

a spherical cap to within a slight distortion around the electrode needle.

3.4 Conclusion

This chapter gives an overview of that standard experimental techniques to create and characterise slippery surfaces. This includes the inflation/ deflation contact-angle hysteresis measurement method and sliding angles. Surface preparation including a process for cleaning glass substrates is detailed. Preparation of SOCAL, including optimisation of the the process to get consistently low hysteresis surfaces. A method of preparing SLIPS surfaces using nano-particle based GLACO™ is detailed, including a review of different techniques used in the literature to imbibe with silicone oil. This technique results in the capability to create a conformal SLIPS without a visible wetting ridge, the significance of this result is the ability to characterise the SLIPS surface using the inflation/ deflation method as opposed to sliding angle characterisation.

Experimental setups and methods have also been detailed. A bespoke humidity controller has been made to control the environmental conditions of the experiments. Image analysis of side profile sessile droplets has been detailed. The electrowetting on dielectric setup has been detailed with the ability to modulate the signal to allow the rate of change in voltage to be studied along with fixed voltage experiments. With these materials and experimental techniques and the theoretical underpinning of the previous chapter, evaporation of sessile droplets on SOCAL surfaces can now be studied.

Chapter 4

Evaporation on SOCAL Surfaces

Previous chapters describe the theory of sessile droplet evaporation (section 2.3) and the difficulty in observing the ideal CCA mode evaporation (section 2.3.2). A key challenge remains the ability to remove contact line pinning during evaporation of sessile droplets from non-textured solid surfaces. In this chapter, experiments of the evaporation of sessile droplets of water on SOCAL-coated glass surfaces with contact-angle hysteresis of less than 1° over a wide range of relative humidity from 10 to 70% are reported. CCA mode evaporation for small sessile water droplets is observed; confirmed with the linearity of the contact area decrease in time. Images are taken above the droplet evaporation also confirm qualitatively the removal of pinning. Contact angles are consistently measured close to the static values, and within the bounds expected from the measured and extremely low contact-angle hysteresis. The entire evaporation sequence including a step change in the observed value of the CCA that occurs at RH between 30 and 40%. The step change is reminiscent of a type V adsorption isotherm. To investigate the source of the step-change, mass change in humidity is studied using QCM and DVS. Finally, the Picknett and Bexon model is used to analyse the evaporation of individual droplets and provide a set of estimates of the diffusion coefficient. By comparing the evaporation rate to the RH across all experiments, a second estimate of the diffusion coefficient is obtained. Both types of estimate are within 2% of the literature value and show how SOCAL surfaces, which are omniphobic, provide a simple but accurate methodology to determine the diffusion coefficient of volatile liquids.

4.1 Experimental Setup

Small ($4.0 \pm 0.3\,\mu L$) droplets of room-temperature DI water (type III, purified in an Elga PURELAB Option-Q lab water purification system) are deposited on a SOCAL-treated glass slide (SOCAL manufacture method detailed in section 3.2.2), in a commercial humidity and temperature-controlled chamber (TC30) that had been equilibrated at $25.0 \pm 0.1\,°C$, attached to a Krüss (DSA 25)(figure 4.1). The evaporation of the droplets is observed for a range of RH from 10 to 70% ($\pm 0.5\%$) in intervals of 10%. A further sequence of evaporation experiments refined the RH range between 30 and 40% in steps of 2%. The evolution of the contact angle and the contact radius as a function of time are recorded with time-lapse image capture at $10\,s$ intervals. The data and images for each evaporation sequence are analysed individually to verify the absence of contact-line pinning.

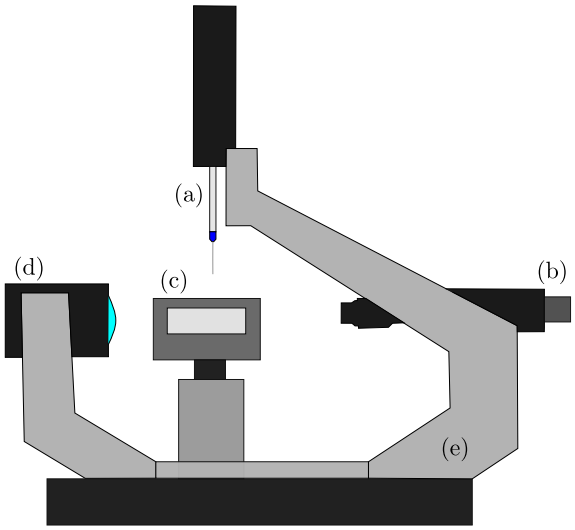

Figure 4.1: Krüss DSA 25: (a) Automatic syringe dosing unit, (b) Camera with macro lens and barrel, (c) Humidity and temperature-controlled chamber (TC30), (d) Light-emitting diode backlight and (d) Krüss DSA 25 chassis

The contact radius is calculated by identifying the contact base line by eye; the Krüss Advance software package then tracks the drop radius throughout the evaporation. The contact angle is then evaluated using an elliptical fit in the Krüss Advance software, which uses the tangent of the ellipse intersecting the contact base line. This gives a mean contact angle from the average of the left and right contact angle. Because SOCAL is a transparent coating, it is possible to confirm that droplets on the surfaces retain an axisymmetric shape during evaporation by conducting control experiments using the simultaneous side profile and bottom up views. Data presented in this

chapter show typical curves for each RH obtained from the average of three repeated evaporation sequences. The data for each RH is averaged into 100 equally spaced bins for each measured quantity (elapsed time, contact angle, contact radius). All of the experiments are carried out on five separately made SOCAL-treated glass slides at various locations on the slides. The different humidity experiments were carried out non-sequentially to ensure that no ageing effects are observed.

4.2 Typical Evaporation Sequence

Figure 4.2 shows the contact angle, θ, and contact area, πr^2, as a function of time, t, during a typical sessile droplet evaporation sequence. After short initial relaxation, when a droplet is deposited, a CCA is observed for the majority of the evaporation time. During the CCA period, the contact area reduces linearly with time. The short initial relaxation is likely to be due to the droplet equilibrating to the surface, temperature, and RH (see McHale *et al.* [136]). The final stage of evaporation appears to be correlated to the observation of mineral deposit formation when the droplet radius reduced to $0.5\,\mathrm{mm}$, which is the radius at which the contact angle first begins to decrease.

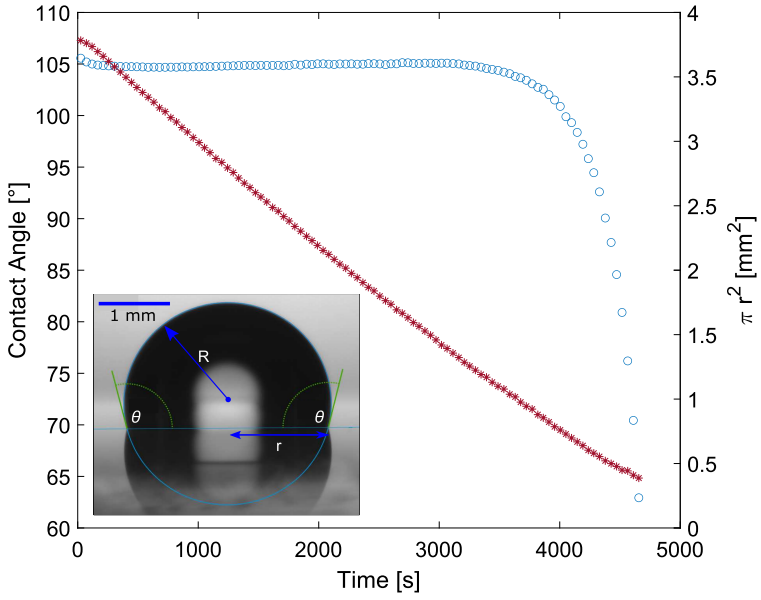

Figure 4.2: Typical evaporation showing the contact-angle,$theta$ (ooo) and contact area, πr^2 ($***$) as a function of time. The conditions of this typical evaporation are a $4\,\mu\mathrm{L}$ droplet of DI water, $25°$, and 70% relative humidity. The inset shows the ellipse fitting of the droplet to measure the contact angle, θ, contact radius, r, and spherical radius, R.

4.3 Axisymmetric Evaporation

To confirm the no pinning was present throughout the entirety of the evaporation, top down images were taken during an evaporation (figure 4.3). Inspecting the images the droplet remains visibly axisymmetric throughout the entire evaporation sequence.

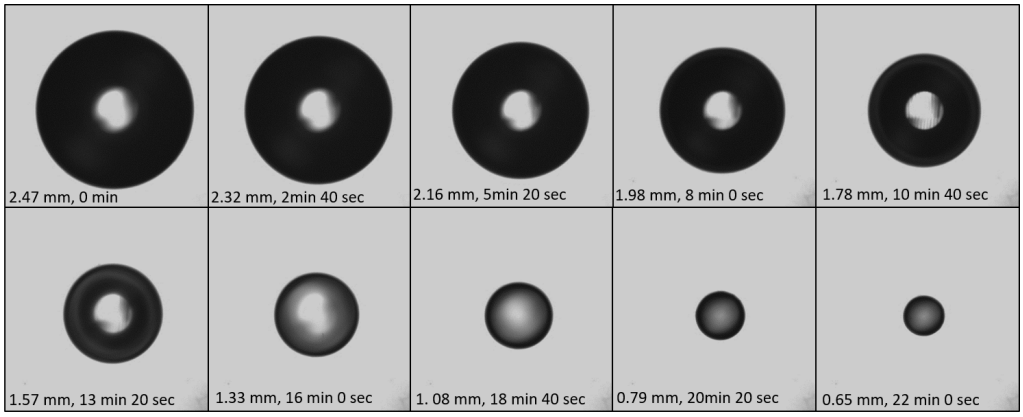

Figure 4.3: Top down view of sessile droplet evaporation sequence of a $4\,\mu$L droplet of DI water.

The spherical radius, R, of the droplet can be measured throughout the evaporation sequence and plotted as cross sectional area, πR^2, as a function of time, t (figure 4.4). The result of which, shows a linear decrease in the cross sectional area in time depicted by the dashed line. Through geometry this shows a constant contact angle evaporation, and the analysis of the evaporation sequences of side view images can be assumed to form a spherical cap and be treated using the geometric relations detailed in section2.3.2.

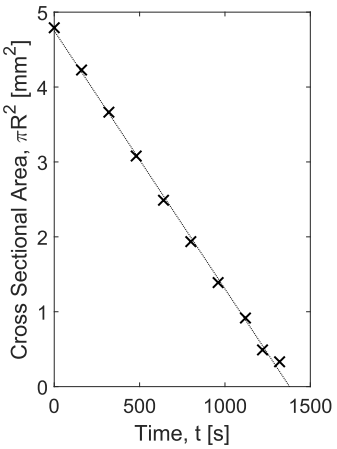

Figure 4.4: plot of the spherical cross sectional area, πR^2 in time from images in figure 4.3 where the dotted line is the linear fit through the data.

4.4 Initial Relaxation

The qualitative features of typical evaporation sequences are focused on first. After a droplet is deposited, there is an immediate and short duration initial relaxation of the contact angle. The decrease in the contact angle could be due to changes in temperature as evaporation establishes itself and evaporative cooling of the droplet and substrate occurs. For isolated evaporating spherical drops, the cooling is determined by the evaporation rate [137], and this will also occur for sessile droplets with the evaporative cooling correlated to the RH, which controls the rate of evaporation. In addition, thermal properties of the substrate will influence how effectively thermal energy can be supplied to maintain the temperature of the substrate surface. For example, David *et al.* show a link between the cooling effect on a droplet and the thermal properties of the substrate [138]. A further possibility is that evaporation creates a local RH which, given the contact angle is over $90°$, may be important for the precise value of the contact angle because of the confined wedge space defined by the droplet and the substrate near the contact line. The simplest interpretation is that, although the contact-angle hysteresis is very small, an evaporating droplet is simply adopting a receding contact angle, which is slightly lower (1 to 2 °C) than its initial value on deposition. The initial relaxation is then followed by a CCA period that dominates the overall evaporation time.

4.5 Effect of Relative Humidity

The CCA mode of evaporation occurs across a broad range of RH ($10 - 70\%$). Figure 4.2 illustrates a typical evaporation at the lowest and highest values of RH. Even though these extremes in RH result in significantly different total evaporation times of $23\,\mathrm{min}$ and $2\,\mathrm{h}\ 15\,\mathrm{min}$, the droplet evaporation sequences demonstrate the same behaviour. The presence of the syringe (seen at the top of each image in Figure 4.2) illustrates that an evaporating droplet remains centred, close to the initial deposition location, from the start to end of their evaporation. This provides confidence that the droplet contact line is completely mobile and free from pinning at all locations around the droplet.

Figure 4.6 shows a full set of sessile droplet evaporation sequences across the range of RH from 10 to 70% in steps of 10% and using the volume as the horizontal axis to collapse all the data

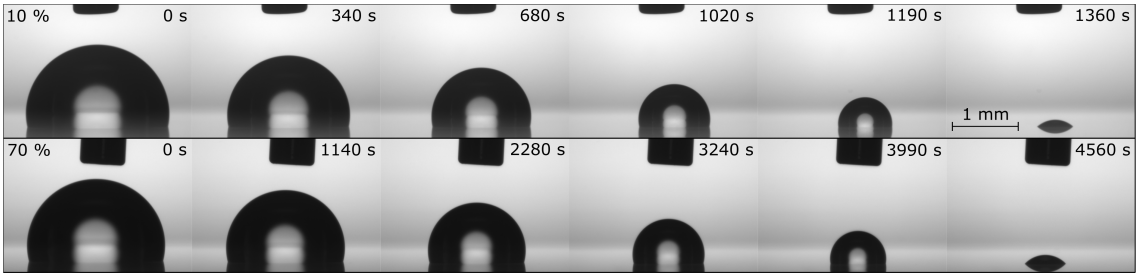

Figure 4.5: Evaporation time lapse at 10 and 70% relative humidity. The syringe needle is kept in the image to show the droplets evaporate, moving radially inward in all directions.

onto a single plot. The central inset in figure 4.2 reveals that the CCA during evaporation has two distinct values. The contact angle in the range of the RH of $10 - 30\%$ is $101°$ while in the range of the RH of $30 - 40\%$, there is a sharp rise in the CCA to $104.5°$, which remains the value observed for the range from 40 to 70%. The step nature of this transition is further detailed in figure 4.7 (a), which presents data for the RH range $30 - 40\%$ using steps in the RH of 2%. Advancing angle measurements were carried out at each RH value to confirm the surface retained low contact-angle hysteresis despite this step change in the contact angle. Evaporation causes the contact line to retreat slower than a needle withdrawing liquid; therefore, the receding angle at a given RH is the angle observed during evaporation of liquid at that RH. Contact-angle hysteresis estimated using the constant receding angle during evaporation and the measured advancing contact angle prior to evaporation was largest at RH = 34% with $\Delta\theta_{CAH} = 1.09 \pm 0.27°$ and lowest at RH = 60% with $\Delta\theta_{CAH} = 0.41 \pm 0.16°$. Figure 4.7 shows $\Delta\theta_{CAH}$ remains low for both contact angle regimes with $\Delta\theta_{CAH} < 2°$.

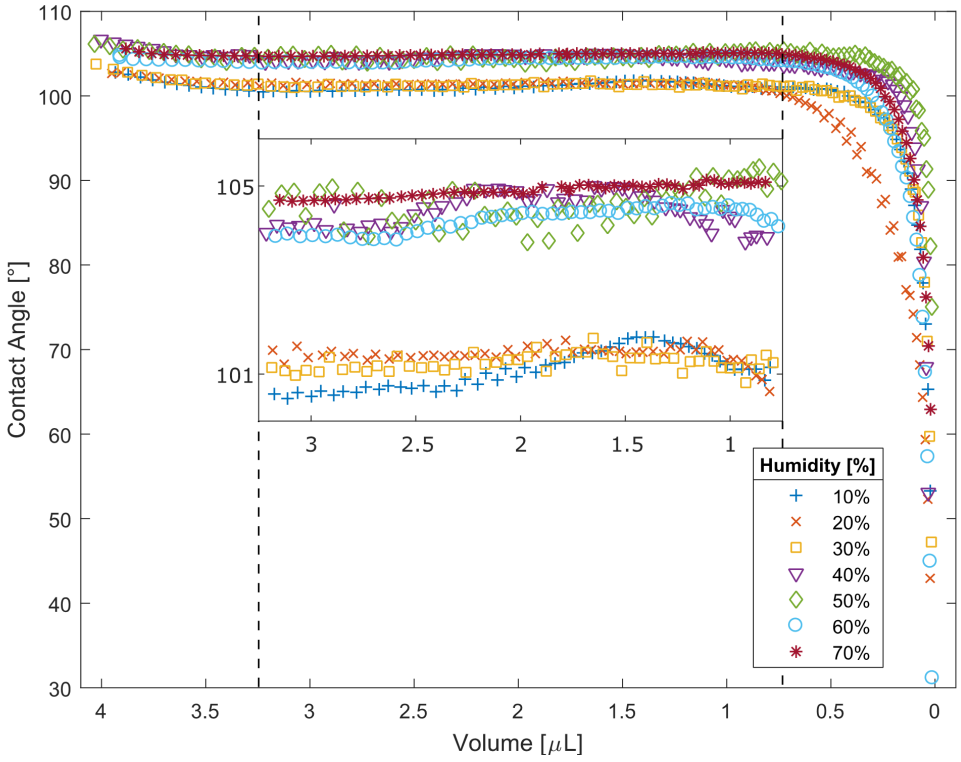

Figure 4.6: Contact angle as a function of volume: The dashed lines indicate the constant contact angle mode of evaporation. The central inset is a magnification of the CCA mode evaporation, showing the two contact angles for low ($10-30\%$) and high ($40-70\%$) relative humidity. Each data series is a binned average of three experiments, the standard deviation of each marker is typically $0.5°$.

4.5.1 Step-Change in Contact Angle

An unexpected feature in the data is the apparent separation into two distinct values of the CCA of $101°$ and $104.5°$ for this CCA evaporation mode. This step change for RH between 30 and 40% is shown in Figure 4.7 and is reminiscent of the shape of a type V adsorption isotherm [139]. These two contact angle values can be compared to the $0.6°$ increase in contact-angle hysteresis at the lower RH values quantified using measurements via addition and withdrawal of liquid to a droplet.

The possible origins of the step change can be considered using Young's law (2.6), for which there are two interfacial tensions, γ_{lv} and γ_{sv}, that depend on the vapour. The first of these, the surface tension γ_{lv}, is known from pendant drop measurements to have a smooth change with temperature and RH over the range used in the experiments (72.2-$75.5\,\mathrm{mN\,m^{-1}}$) [140, 141]. However, the second of these, the solid-vapour interfacial tension γ_{sv}, is a candidate for the origin of a step

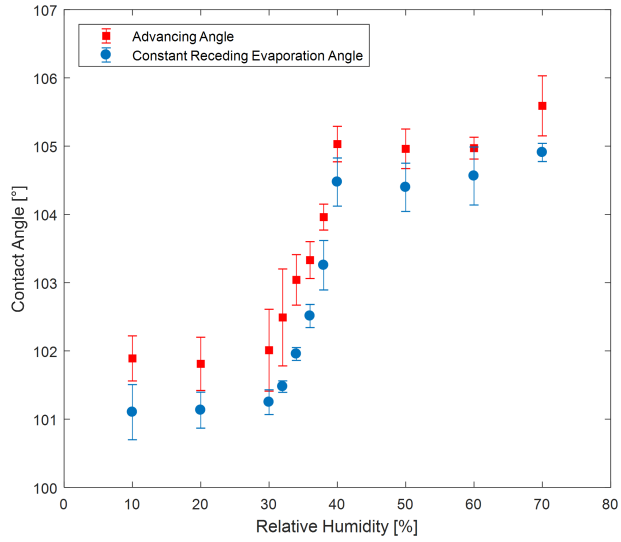

(a)

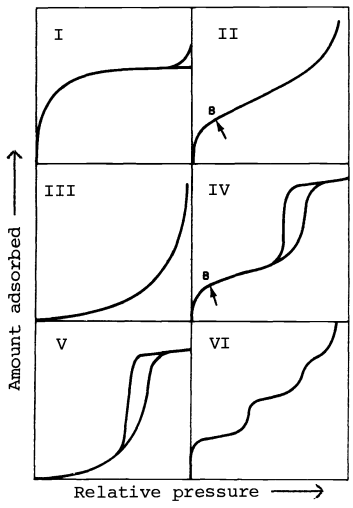

(b)

Figure 4.7: (a) Step change in the value of the constant contact angle for evaporation at different relative humidity reminiscent of a type V adsorption isotherm, (b) Types of adsorption isotherms (from Sing *et al.* 1985).

change in the observed contact angle. This might occur if a film of vapour condensed on the solid over the narrow $30-40\%$ range of RH, thereby replacing the solid-vapour interface by solid-liquid and liquid-vapour interfaces.

4.5.2 Dynamic Contact Angle

Droplets in lower humidity environments evaporate faster than those in high humidity because the vapour is able to diffuse easier into surroundings that are not already saturated with the vapour of the same liquid. The data from the evaporation experiments can be plotted in terms of contact line velocity during the constant contact angle evaporation regime, taken from the change in contact radius in time from the image sequence, and the corresponding contact angle (figure 4.8). There is an apparent overlap in contact line velocity in the 40 and 50% relative humidity evaporations and that of 30 and 20% however there is no obvious relationship between the contact line velocity and the contact angle. This rules out the step change in contact angle cause as a result of the contact line moving quicker in low humidity.

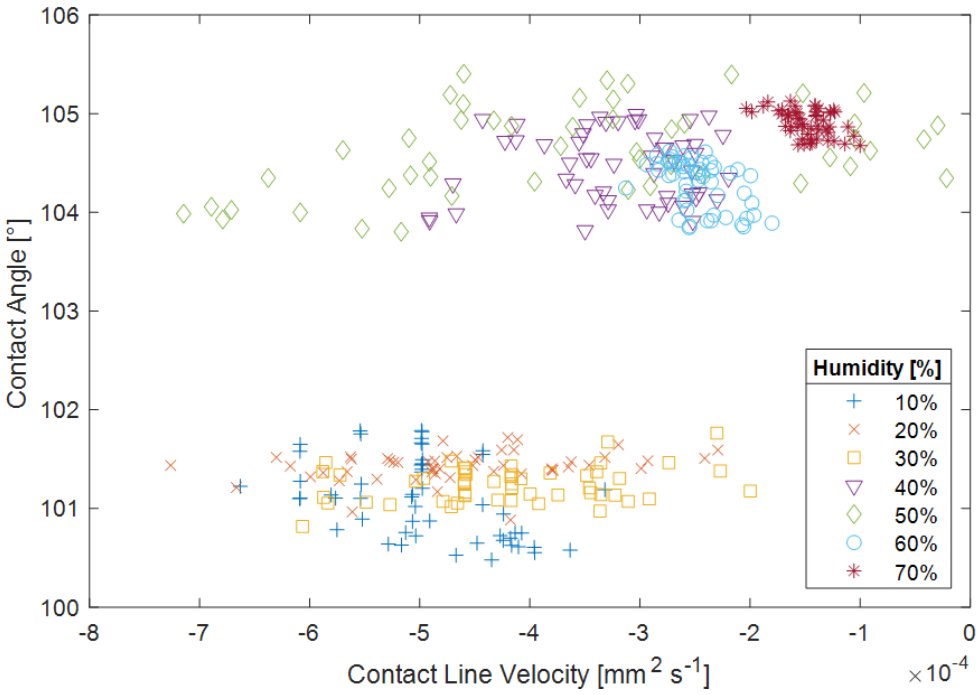

Figure 4.8: Plot of contact angle as a function of contact line velocity for evaporating sessile DI water droplets at 10 to 70% relative humidity

4.5.3 Adsorption Characterisation

A possible explanation for the step change in contact angle is that the solid-vapour interfacial tension changes because of the adsorption of a monolayer of vapour at a threshold humidity. This could cause an increase in the contact angle as the RH increases, as observed experimentally, because of increased cohesion of the water molecules and, hence, a decrease in the solid-vapour interfacial tension γ_{sv}. It is important to understand the distinction between adsorption and the similarly named, more familiar phenomena, absorption. The left-hand-side image in figure 4.9 shows molecules in a vapour moving into the bulk of a liquid phase, this is known as absorption. The right-hand-side shows molecules moving within a liquid and attaching to the surface of a solid, known as adsorption. The attachment of these molecules could occur from a vapour or a liquid.

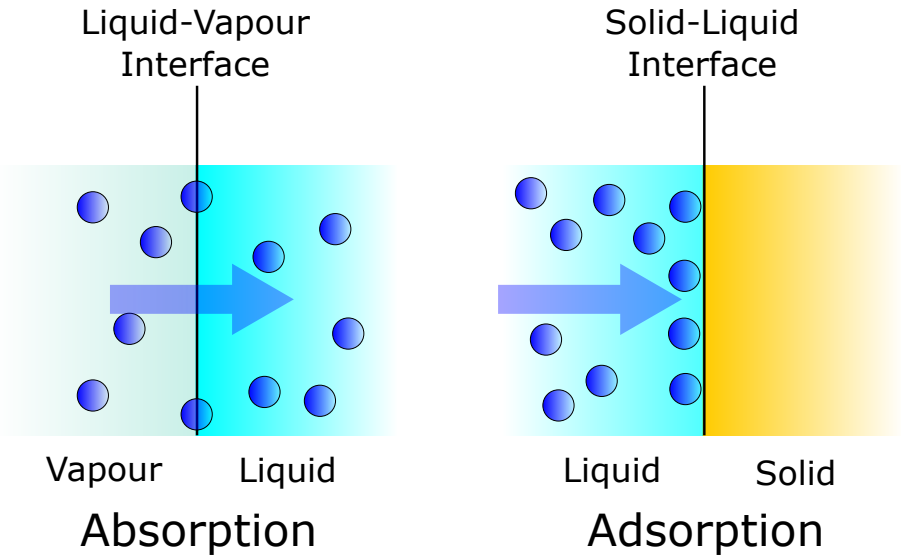

Figure 4.9: Diagram showing the key difference between absorption and adsorption.

Dynamic Vapour Sorption (DVS)

To consider this possibility that the solid-vapour interfacial tension changes because of the adsorption of a monolayer of vapour, experiments are conducted to measure mass change on a SOCAL-coated glass surface using a DVS method. Initially, experiments were carried out at $25\,^{\circ}\mathrm{C}$ with the machine cycling through each relative humidity (0-90%) moving onto the next humidity when the measured change in mass was smaller than $dm/dt < 0.0001$. Because the mass of the adsorbed layer would be so low in comparison to the sample the machine only ran until it reached the set-point humidity, and the mass for each humidity does not have time to adjust (figure 4.10 and 4.11).

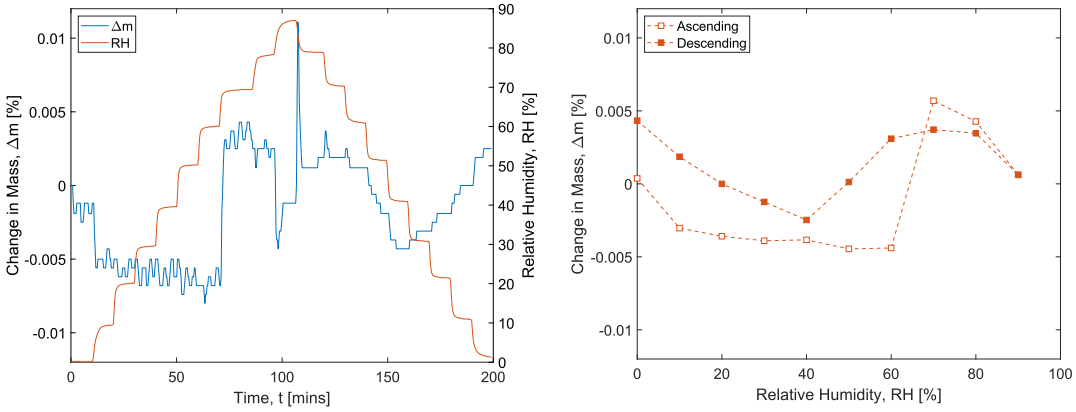

(a) (b)

Figure 4.10: DVS measurements of SOCAL mass change as a function of relative humidity: (a) the relative humidity and mass plotted as a function of time over the entire experiment and (b) The change in mass as a function of the relative humidity taken when the setpoint humidity was reached and $dm/dt < 0.0001$

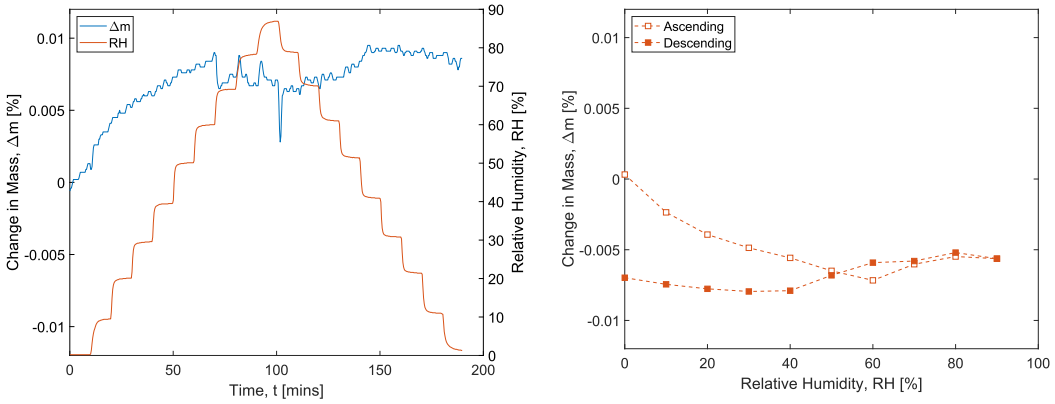

(a) (b)

Figure 4.11: DVS measurements of SOCAL mass change as a function of relative humidity: (a) the relative humidity and mass plotted as a function of time over the entire experiment and (b) The change in mass as a function of the relative humidity taken when the setpoint humidity was reached and $dm/dt < 0.0001$

As the change in mass was so small, humidity was fixed for 2 hours in hopes that the humidity would settle to a fixed value (figure 4.12). Again no trend was apparent in these experiments. Again with the conclusion that the adsorption would be such a low amount, it is not visible within the resolution of the machine.

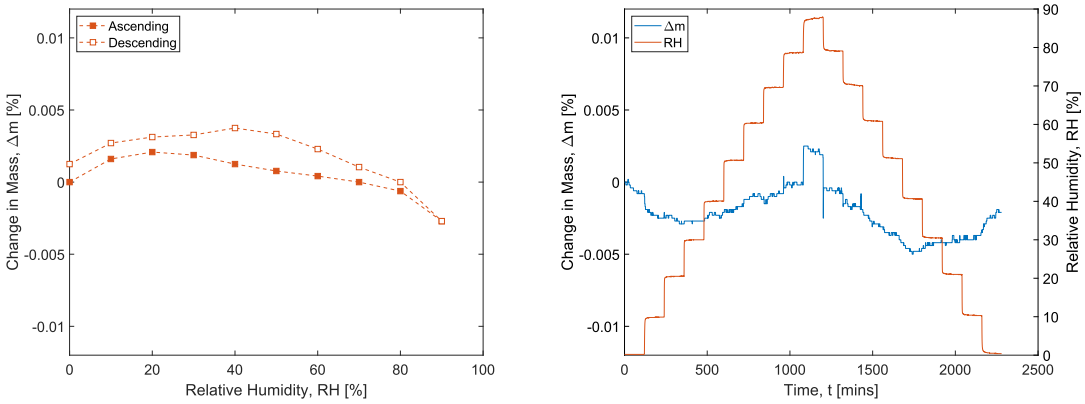

(a) (b)

Figure 4.12: DVS measurements of SOCAL mass change as a function of relative humidity: (a) the relative humidity and mass plotted as a function of time over the entire experiment and (b) The change in mass as a function of the relative humidity taken 2 hours after the set point humidity was reached.

Quartz Crystal Microbalance (QCM)

QCM is another technique that is used to attempt to measure if any mass change occurs on the surface at increased relative humidity. A quartz glass crystal (figure 4.13 (a)) were coated with SOCAL and placed in a humidity control chamber. The QCM Measures the resonant frequency for each relative humidity and the phase shift is recorded and plotted as a function of relative humidity compared to the uncoated quartz glass (figure 4.13 (b)). Comparing both coated and uncoated, there appears to be no change in the behaviour of the mass change in increasing relative humidity.

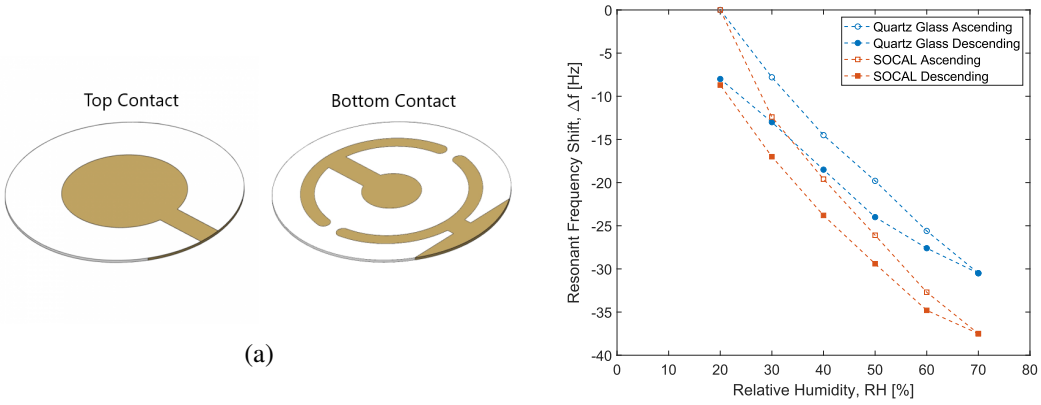

(a)

(b)

Figure 4.13: (a) Image of quartz glass used in QCM. The SOCAL coating is applied to the top contact (b) plot of resonant frequency shift as a function of relative humidity for quartz glass and SOCAL coated quartz glass.

The nature of the step change remains elusive, however the explanation that the step change being due to adsorption of molecules remains plausible and requires further investigation. It could be possible to attempt to measure the adhesion forces of water molecules to the surface at different humidities using AFM.

4.6 Salt Deposits

In the very final stages of evaporation, the contact angle reduces rapidly and after the droplet had completely evaporated, deposits are observed over an area corresponding to that at which the contact angle first began to reduce. Energy-dispersive X-ray spectroscopy and scanning electron microscopy analysis of these deposits showed them to be composed of NaCl, AlCl, MgCl, and KCl. This suggests trace amounts of salts precipitated out of water at a volume of 0.6 ± 0.1 µL, and their deposition on the SOCAL-coated glass surface then created a self-pinning effect (figure 4.14). This figure is a single experiment, unlike figure 4.6 which is a binned average of three repeats, this is to directly compare the pinning radius to that of the salt deposit. This was conducted on a drop-shape analyser without temperature and humidity control. These two factors likely account for the different scatter and slope in the contact angle compared to that of the previous study. To understand this behaviour in more detail, a more thorough and robust study using many droplets should be conducted in future work.

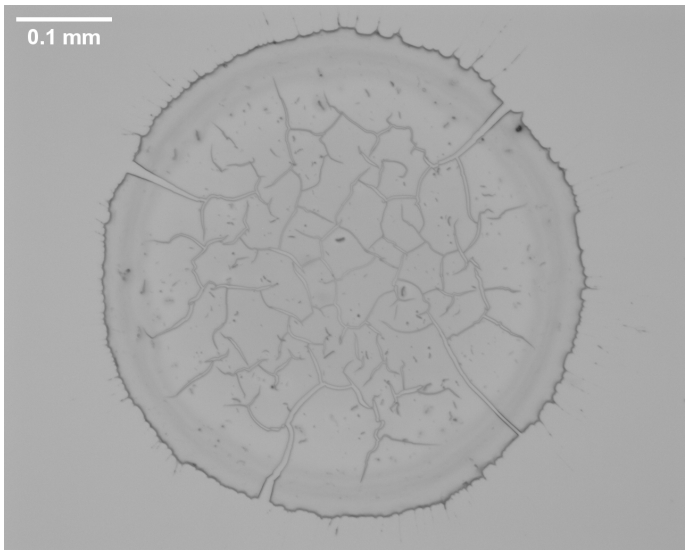

(a)

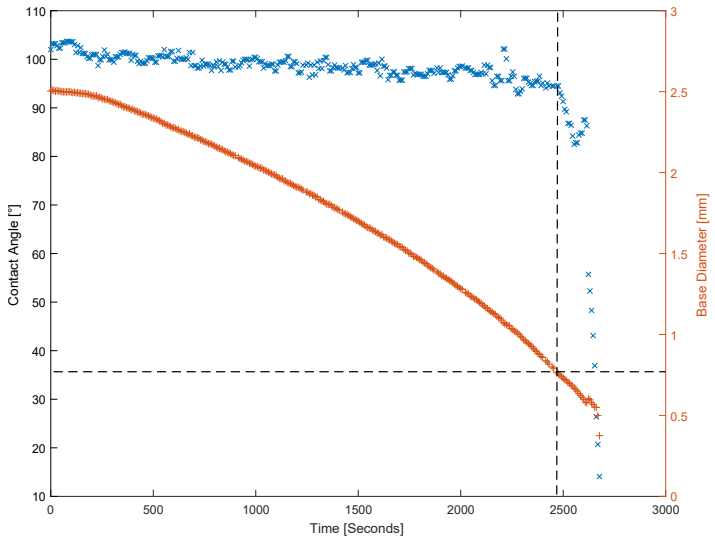

(b)

Figure 4.14: Salt deposit from water droplets on SOCAL: (a) microscope image of salt deposit and (b) contact angle measurement and base radius of an evaporating droplet with the dashed lines highlighting the diameter of the salt deposit.

4.7 Diffusion Coefficients

Previously in section 2.3.2, an exact solution for sessile droplets evaporating in a CCA mode evaporation is given. Because the droplets in the experiments conform to spherical caps, and unlike the previous work of Guan *et al.*, observing sessile droplet evaporation on SLIPS [77], there is no wetting ridge present, these equations can be used directly to analyse the data. For

the CCA mode with side profile observations providing both contact angle and contact radius, equation (2.23) is most appropriate. As the right-hand side of (2.23) does not depend on time for CCA mode of evaporation, the contact area should reduce linearly with time.

Figure 4.15 shows representative data for sessile droplet evaporation on SOCAL surfaces for each value of RH (10-70%) and each can be seen to provide excellent agreement with a linear fit; the inset in figure 4.15 illustrates the time range used to define the CCA range (dashed lines). From the slopes in figure 4.15, the diffusion coefficient for each RH, D_{RH}, has been calculated using equation (2.23) and is shown in Table 3. These values of D_{RH} range from 2.31×10^{-5} to $2.87 \times 10^{-5}\,\mathrm{m^2\,s^{-1}}$ with an average of $(2.58 \pm 0.20 \times 10^{-5}\,\mathrm{m^2\,s^{-1}}$, which compares well to the literature value of $2.48 \times 10^{-5}\,\mathrm{m^2\,s^{-1}}$. Figure 4.15 provides confidence that we have observed CCA mode evaporation, which is diffusion-limited, and Table 3 confirms that the extracted diffusion coefficients from each RH are consistent with the literature values. However, because the diffusion coefficient should not depend on the RH, rearranging (2.23) and relating the RH to vapour concentration by $\Delta c = c_0((RH/100) - 1)$, allows a single estimated diffusion coefficient, D_E, to be calculated using all experiments across the range of RH 10-70%.

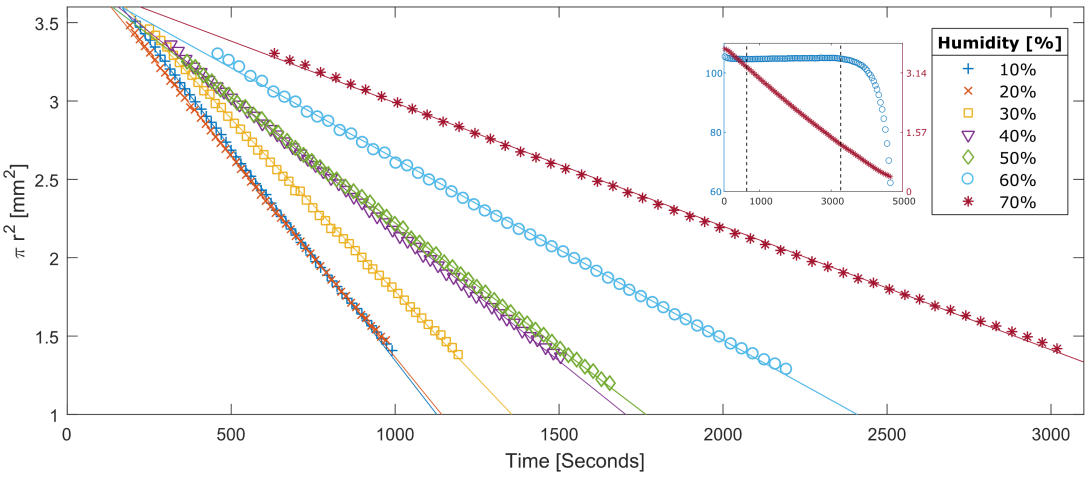

Figure 4.15: Contact area πr^2 as a function of time for evaporations at relative humidity 10-70%: The line through each data set represents the linear fit used to calculate D_{RH}. The inset shows the representative contact angle and contact area as a function of time, where the data between the dashed lines show the section of the evaporation that is the CCA mode.

Table 3: Calculated diffusion coefficient for each relative humidity compared to the literature value.

RH [%]	$d\pi r^2/dt$ [$\mathrm{mm^2\,s^{-1}}$]	D_{RH} [$10^{-5}\,\mathrm{m^2\,s^{-1}}$]	D Literature [$10^{-5}\,\mathrm{m^2\,s^{-1}}$]
10	-0.002699	2.47	2.48
20	-0.002513	2.58	2.48
30	-0.002202	2.58	2.48
40	-0.001678	2.44	2.48
50	-0.001640	2.87	2.48
60	-0.001297	2.82	2.48
70	-0.000754	2.31	2.48
	Average:	2.58 ± 0.20	2.48

Figure 4.16 shows data from figure 4.15 plotted using (2.23), and the gradient from this gives an estimate of the diffusion coefficient of $D_E = 2.44 \pm 0.48 \times 10^{-5}\,\mathrm{m^2\,s^{-1}}$, which is an improved estimate compared to the single RH estimates and which is within 2% of the literature value. Finally, because Wang and McCarthy have reported that SOCAL surfaces are omniphobic and have low contact-angle hysteresis to a wide range of liquids, including diiodomethane, toluene, hexadecane, cyclohexane, decane, and hexane [3] the accuracy of our evaporation method of determining the diffusion coefficient for water suggests that a SOCAL-coated glass surface could be used to determine the diffusion coefficients for a wide range of other liquids.

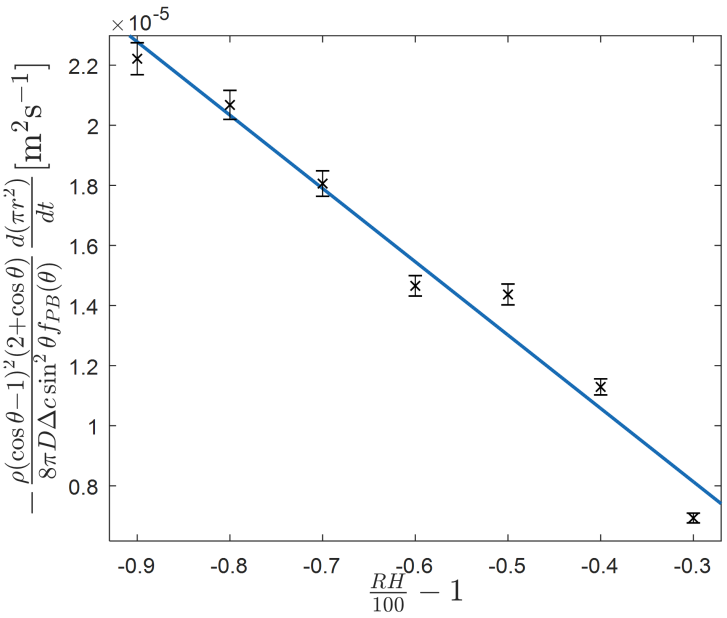

Figure 4.16: Contact area as a function of relative humidity. The gradient of the plot gives the calculated diffusion coefficient D_E.

4.8 Conclusion

This chapter has shown it is possible to observe the CCA evaporation mode on a flat smooth (non-textured) solid surface by creating SOCAL-coated surfaces with extremely low contact-angle hysteresis. This differs from previous attempts to observe the CCA mode, which have relied on the use of textured solid surfaces, or a lubricant oil that removes all contacts with a solid surface. A step change in the CCA value is observed, occurring in a narrow range of RH (30-40%), which is indicative of the adsorption of water vapour on the surface and reminiscent of a type V isotherm. The value of the CCA during evaporation has been shown to be consistent with the ideal contact angle from Young's law estimated by using independent measurements of the advancing and receding contact angle. Quantitative analysis of the sessile droplet evaporation sequences provides accurate measurements of the diffusion constant of the evaporating liquid. Hence, this methodology can provide a simple and reliable way to characterise the volatility of a wide range of other liquids.

Chapter 5

Electrowetting on SOCAL

In this chapter the development of Electrowetting on SOCAL is detailed. The function of the electrowetting setup is first verified by conducting an electrowetting experiment on PTFE and recovering the Young-Lippmann relationship between the contact angle of the droplet and the applied voltage. This highlights the effect of hysteresis of even a hydrophobic material such as PTFE and therefore the necessity for pinning-free surfaces such as SOCAL surfaces. As SOCAL needs to be supported by a substrate. Glass is suitable substrate which can also be used as a dielectric. A glass dielectric is used with thin enough thickness so to the actuation voltage required is lower than the limits of the equipment used while thick enough to not experience dielectric breakdown. The performance of electrowetting on SOCAL coated glass dielectrics by studying the effect of salt type and concentration on the electrowetting, the rate of change of voltage and, the effect of subsequent cycles on the contact angle.

5.1 EWOD Development

There are many practical considerations when designing an electrowetting system. The materials and design of an electrowetting on dielectric system can cause experimental results which deviate from the expected performance of the ideal Young-Lippmann contact angle-voltage relationship. The parameters which the relationship depends upon are: the permittivity of the dielectric, ϵ_d, the dielectric thickness, d, The liquid-vapour surface tension, γ_{lv} and the applied voltage. Dielectrics also have a breakdown voltage, V_{bd} depending on the thickness of the dielectric, and the

permittivity.

$$V_{bd} = E_{ds} \cdot d \tag{5.1}$$

where E_{ds} is the dielectric strength measured in [$\mathrm{V\,m^{-1}}$] which is related to the dielectric permittivity $E_{ds} = \epsilon_0/\epsilon_d$. If the breakdown voltage for a given thickness dielectric is lower than the required voltage to actuate the droplet contact angle, then the voltage will punch-through the dielectric, creating a short circuit and a device failure. A thicker dielectric will increase the breakdown voltage, however it will also increase the actuation voltage. For a desired change in contact angle $\Delta\theta$, the Young Lippmann equation (2.31) can be rearrange to give the actuation voltage$V_{\Delta\theta}$ as

$$V_{\Delta\theta} = \sqrt{\frac{2d\gamma_{lv}\alpha}{\epsilon_0\epsilon_d}} \tag{5.2}$$

where $\alpha = \cos\theta - \cos\theta_E = 2\cos(\theta + \theta_E/2)\cos(\theta - \theta_E/2)$. When $V_{\Delta\theta} < V_{bd}$, the device will be able to reach the desired contact-angle of the droplet without damaging the device. If voltage breakdown occurs, a leakage current can cause gas bubbles in the water to be observed as electrolysis takes place at the electrode, which will permanently destroy the device.

Contact-angle hysteresis can cause electrowetting behaviour to deviate from the expected theory. This can be demonstrated experimentally using a PTFE dielectric. An aluminium coated glass slide acts as a bottom contact, this is covered with PTFE tape of $\sim 75\,\mu\mathrm{m}$ thickness. A $4\,\mu\mathrm{L}$ salt/water solution droplet ($0.01\,\mathrm{mol}$) with a thin metal probe $0.2\,\mathrm{mm}$ diameter. The device is connected to a function generator, amplifier and oscilloscope as the experimental setup in figure 3.12. The droplet contact angle can be viewed captured and measured using shadowgraph and image analysis techniques detailed in section 3.3.2. Images are taken of the droplet at $50\,\mathrm{V}$ intervals of increasing then decreasing fixed-voltage between $0 - 500\,\mathrm{V}$. Figure 5.1 (a) shows the contact angle as a function of voltage on a PTFE dielectric device. The blue circles represent the voltage increasing, figure 5.1 (b) shows the relationship for $\Delta\cos\theta/V^2$ is linear which is expected by the theory. However, when the voltage decreases (orange squares), the contact angle does not follow the same path as the increasing voltage, in-fact the contact angle appears to still decrease with decreasing voltage, which is unlike the theory. This is due to the contact-angle hysteresis, when a droplet is spread via electrowetting below the receding angle, and the voltage is then removed, the contact angle is expected to increase until it reaches the receding angle, where it is in equi-

librium. For the voltage applied in the experiment, it is likely the receding angle was not reached and therefore as the experiment continued, and the droplet evaporated during the experiment, it continued to reduce the contact angle. This experiment illustrates several considerations in design of an electrowetting device. Lower contact-angle hysteresis will allow the droplet contact angle to return closer to the equilibrium contact angle. If several cycles are to be performed, the contact angle at $0\,\mathrm{V}$ after the first cycle would considered the initial contact angle and the contact angle would then follow the theory for both increasing and decreasing voltage. If a pinning-free coating was used, then the contact angle would be reversible from the first cycle.

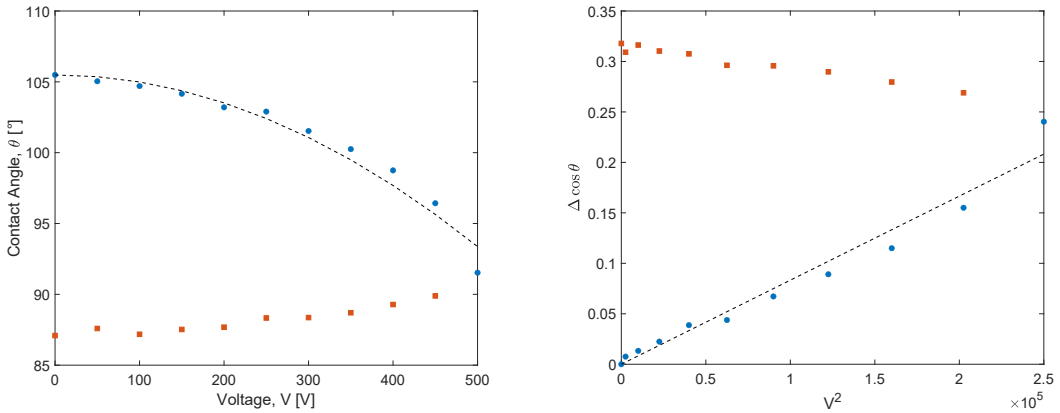

(a) (b)

Figure 5.1: Electrowetting on PTFE: (a) Contact angle, θ as a function of Voltage, V and (b)$\Delta\cos\theta$ as a function of V^2. Blue circles represent the contact angles at increasing voltage, orange squares represent the contact angle at decreasing voltage and the dashed line represents the Young-Lippmann Contact angle-voltage relationship based on the fit of contact angles for increasing voltage in (b).

The evaporation of the conducting liquid also creates issues of the droplet evaporating to the receding angle. To mitigate the effects of droplet evaporation, higher relative humidity can be used, lower ambient temperature, larger droplets and a faster experiment. To help improve the electrowetting device performance, a glass dielectric of $170\,\mu\mathrm{m}$ thickness is coated with SLIPS using the method detailed in section 3.2.3 as the dielectric layer. The SLIPS layer acts to reduce contact-angle hysteresis allowing the contact angle to reversibly follow the theory. The thick glass dielectric acts to prevent dielectric breakdown. In the previous experiment the voltage is set manually, then an image is taken before moving to the next voltage. This means the total experiment length is uncontrolled, therefore the total evaporated volume is uncontrolled. To improve the experiment

a $600\,\mathrm{V}$ sine wave is modulated with a triangle wave of frequency $0.017\,\mathrm{Hz}$. This translates to a voltage rate of change $20\,\mathrm{V\,s^{-1}}$. The experiments are also performed in a humidity chamber at $70\,\%$ relative humidity to reduce the evaporation during the experiment time.

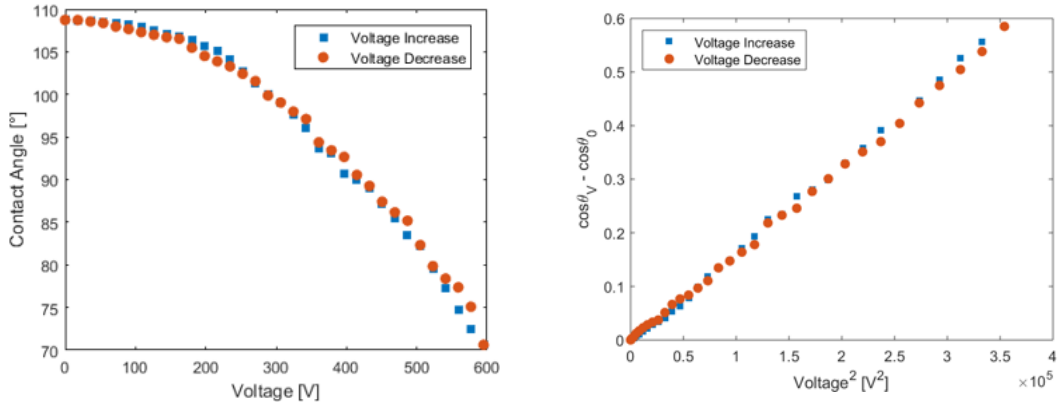

(a) (b)

Figure 5.2: Electrowetting on SLIPS coated $170\,\mu\mathrm{m}$ glass dielectric: (a) Contact angle, θ as a function of Voltage, V and (b)$\Delta\cos\theta$ as a function of V^2. Blue circles represent the contact angles at increasing voltage, orange squares represent the contact angle at decreasing voltage.

Figure 5.2 shows electrowetting on SLIPS to follow the theory for both increasing voltage and decreasing voltage. This is confirmed by the linear $\Delta\cos\theta$ as a function of V^2 plot in figure 5.2 (b). This confirms the electrowetting experimental setup is working as expected. Recovery of the initial contact angle during electrowetting was first performed by Brabcova *et al.* [95]. To investigate whether the electrowetting theory can be recovered for SOCAL coated glass cover slips the experiment is repeated but now with a SOCAL coating instead of a SLIPS coating. The coating is prepared using the method detailed in section 3.2.2. Figure 5.3 shows the electrowetting curve for SOCAL does not follow the expected theory. One possible explanation is the contact line cannot move quickly enough to follow the voltage. To investigate this further experiments in section 5.4 look at how the rate of change in voltage changes the expected contact angle-voltage behaviour.

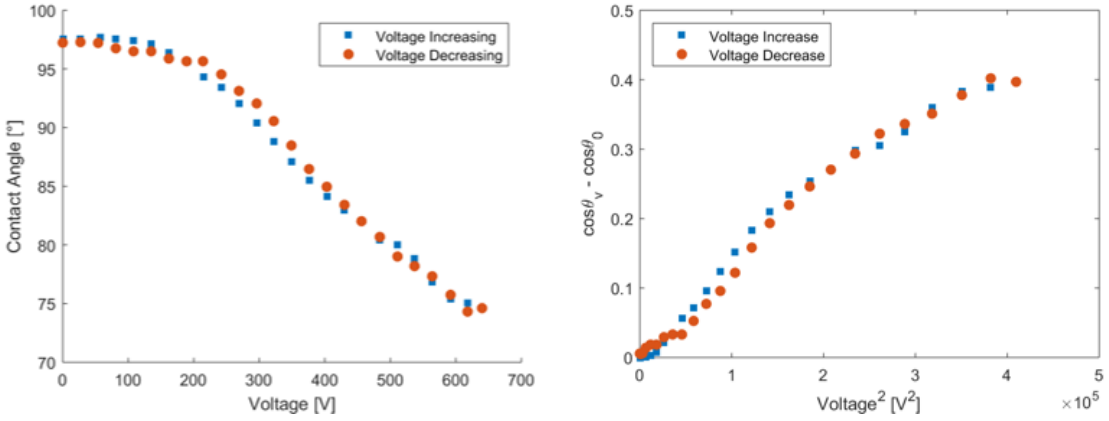

(a) (b)

Figure 5.3: Electrowetting on SOCAL coated $170\,\mu\text{m}$ glass dielectric: (a) Contact angle, θ as a function of Voltage, V and (b)$\Delta\cos\theta$ as a function of V^2. Blue circles represent the contact angles at increasing voltage, orange squares represent the contact angle at decreasing voltage.

In both series of experiments, contact angle saturation is not reached. Contact angle saturation is the experimental observation of a limit where the contact angle will no longer change with increasing voltage. Contact angle saturation is often observed between $60 - 80°$ [87]. The equipment used in these experiments is limited to a maximum output contact angle of $600\,\text{V}$, so it is not possible to reach saturation in this current setup. The thickness of the selected dielectric can be modified to obtain lower contact angles for the same voltage. The slope of the plot in figure 5.2 (b) gives $\epsilon_0\epsilon_d/2d\gamma_{lv} = 1.71 \times 10^{-6}\,\text{V}^{-1}$. As the value for each of the variables are known, the effect of using different thickness dielectrics of the same material can be plotted to help inform experiments. Figure 5.4 shows the theoretical EWOD curves for three different thicknesses, $170\,\mu\text{m}$, the thickness used in the experiments of figure 5.2, which is used to calculate 80 and $120\,\mu\text{m}$. $80 - 120\,\mu\text{m}$ is the range of thickness stated in a pack of precision glass cover slips (Thorlabs CG00K1). Figure 5.4 for the range of available cover slip thicknesses contact angle saturation should be possible.

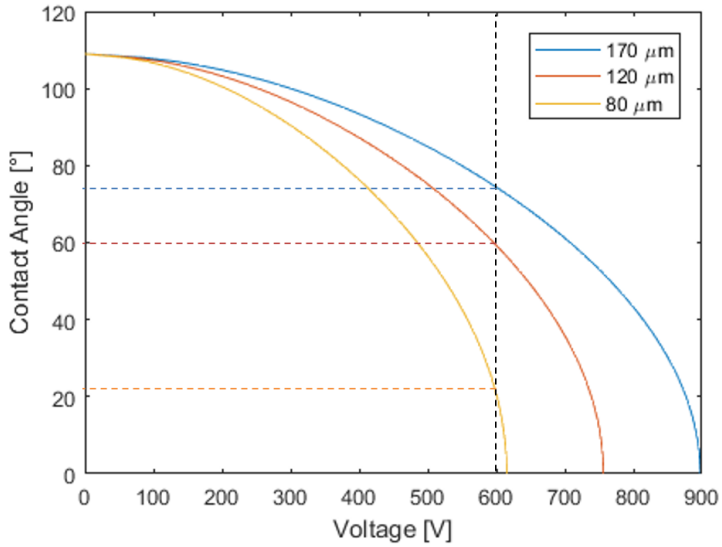

Figure 5.4: Electrowetting performance as a function of glass dielectric thickness:(a) Contact angle, θ as a function of Voltage, V for $170\,\mu\mathrm{m}$ (blue), $120\,\mu\mathrm{m}$ (orange) and $80\,\mu\mathrm{m}$ (yellow) dielectric thicknesses. Dashed lines show minimum achievable contact angle - disregarding contact angle saturation - at $600\,\mathrm{V}$(maximum voltage for equipment).

As $600\,\mathrm{V}$ is the maximum limiting voltage of the available equipment, equation (5.2) can be rearranged and plotted to show the lowest achievable contact angle at as a function of dielectric thickness at fixed voltage. Figure 5.5 shows that using a glass dielectric of thickness $< 125\,\mu\mathrm{m}$ will allow contact angles down to saturation ($\sim 60°$).

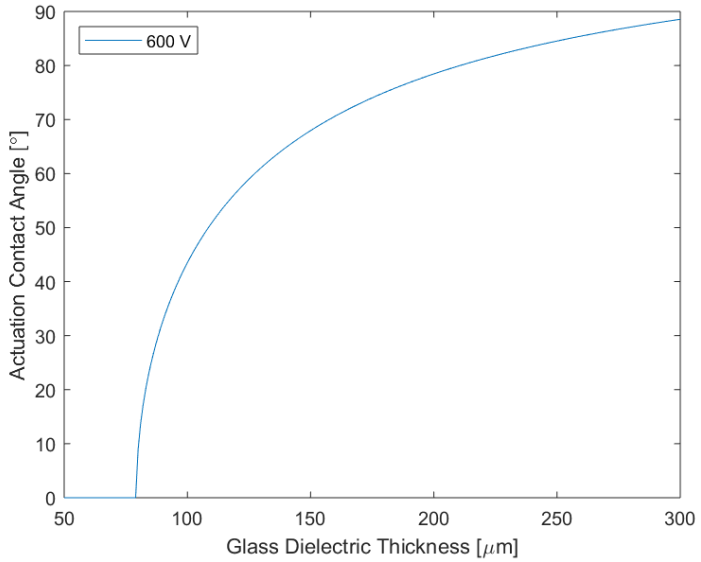

Figure 5.5: Actuation Voltage at $600\,\mathrm{V}$ for changing dielectric thickness.

From the initial experiments thinner coverslips were procured to assure actuation to the saturation contact angle. These coverslips were placed on an aluminium coated glass slide to provide the bottom contact. To control the rate of change in the voltage the signal was modulated with a triangle wave with a $60\,\mathrm{s}$ period. This gives a rate of change in the voltage of $20\,\mathrm{V\,s^{-1}}$. Figure 5.6 shows the contact angle as a function of time for $600\,\mathrm{V}$, $10\,\mathrm{kHz}$ AC on $100\,\mu\mathrm{m}$ glass dielectric, using a $8\,\mu\mathrm{L}$ droplet of DI water with $0.1\,\mathrm{mol}$ KCl. These results shows a different behaviour of the contact angle for increasing/ decreasing voltage. This could be due to the slow moving contact line observed on SOCAL. There is also an unexpected hysteresis from the initial angle to the angle the droplet returns to. The droplet is left to relax at the end of the experiment which suggests a slow moving contact line. Another possible explanation is the addition of salt to the water, which is necessary for better conduction within the droplet. To further investigate, studies of the effect of salt concentration and rate of change of voltage are conducted.

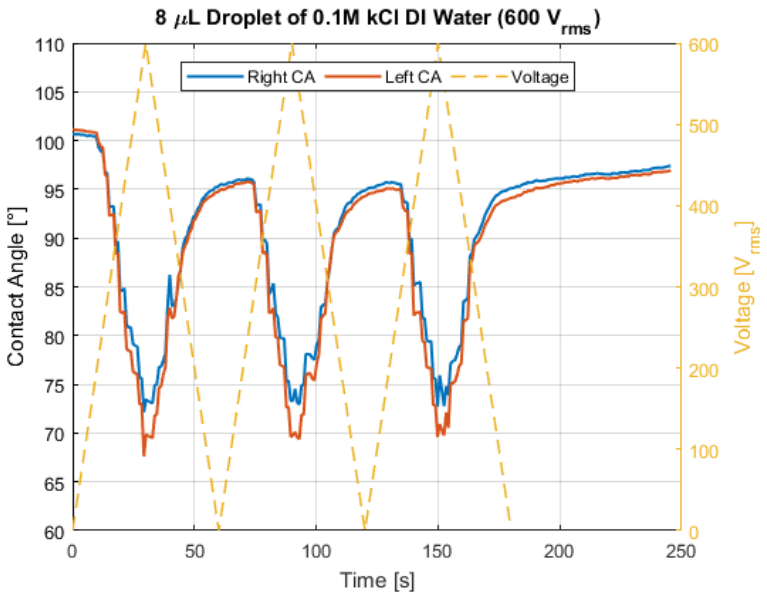

Figure 5.6: Contact angle as a function of time of $8\,\mu\mathrm{L}$ DI water with $0.1\,\mathrm{mol}$ KCl on a SOCAL coated $100\,\mu\mathrm{m}$ glass coverslip actuated between 0-600 V at a rate of $20\,\mathrm{V\,s^{-1}}$ for 3 cycles then left at $0\,\mathrm{V}$ to allow the contact line to relax.

5.2 Effect of Salt Type and Concentration

To investigate whether the unexpected hysteresis on SOCAL was due to the salt used in the DI water, contact-angle hysteresis measurements were taken of varying concentration of monovalent KCl and divalent $CaCl_2$ (Table 5). $100\,\mathrm{mL}$ salt solutions were prepared with the two salt types. Table 4 shows the mass of salt [g] required to be added to $100\,\mathrm{mL}$ to achieve a specific concentration [mol]. The salt is weighed on a micro-balance, then $100\,\mathrm{mL}$ water is added, the solution is then stirred using a glass stirring rod for $60\,\mathrm{s}$ to ensure it is completely diluted. The solution is then decanted into smaller $20\,\mathrm{mL}$ scintillation vials for use.

Table 4: Required mass of KCl and $CaCl_2$ per $100\,\mathrm{mL}$ water to give a set concentration.

Concentration [mol]	KCl [g]	$CaCl_2$ [g]
0	0.000	0.000
0.01	0.075	0.111
0.1	0.075	1.110
0.2	1.491	2.220

To confirm whether the salt was the cause of the unexpected hysteresis on SOCAL in the electrowetting experiments, contact-angle hysteresis measurements are carried out on SOCAL coated coverslips following the method detailed in section 3.1.1. For DI water on the glass coverslips the contact-angle hysteresis is measured as $\Delta\theta_{CAH} = 2.6 \pm 0.4°$, slightly larger than that measured on glass slides ($\theta_{CAH} = 1.2 \pm 0.5°$), this could be due to the roughness of the coverslip compared to the glass, however the measured contact angles are still lower than the $\sim 95°$ contact angle the droplet returned to after an electrowetting cycle. On average $CaCl_2$ has a lower contact-angle hysteresis than KCl for both $0.01\,\mathrm{mol}$ and $0.2\,\mathrm{mol}$. KCl also has a higher standard deviation than either $CaCl_2$ or DI water, this makes it unsuitable for electrowetting on SOCAL. It is also noted that both salt types have a higher receding angle than the observed $\sim 95°$ contact angle the droplet returned to after an electrowetting cycle.

Table 5: contact-angle hysteresis measurements of salt solution water on SOCAL.

Salt Type	Concentration [mol]	Repeat	Advancing	Receding	$\Delta\theta_{CAH}$	Av. $\Delta\theta_{CAH}$	Standard Deviation
DI Water	0	1	105.6	103.2	2.4	2.6	0.4
		2	106.4	103.3	3.1		
		3	105.6	103.2	2.4		
$CaCl_2$	0.01	1	106.7	102.3	4.4	3.3	0.9
		2	105.8	102.9	2.9		
		3	106.1	103.4	2.7		
$CaCl_2$	0.2	1	106.7	103.5	3.2	2.6	0.8
		2	106.4	104.7	1.7		
		3	106.5	103.6	2.9		
KCl	0.01	1	106.3	103.5	2.8	3.8	1.5
		2	106.0	100.4	5.6		
		3	105.5	102.4	3.1		
KCl	0.2	1	106.2	103.9	2.3	3.7	1.8
		2	107.6	104.5	3.1		
		3	106.1	100.3	5.8		

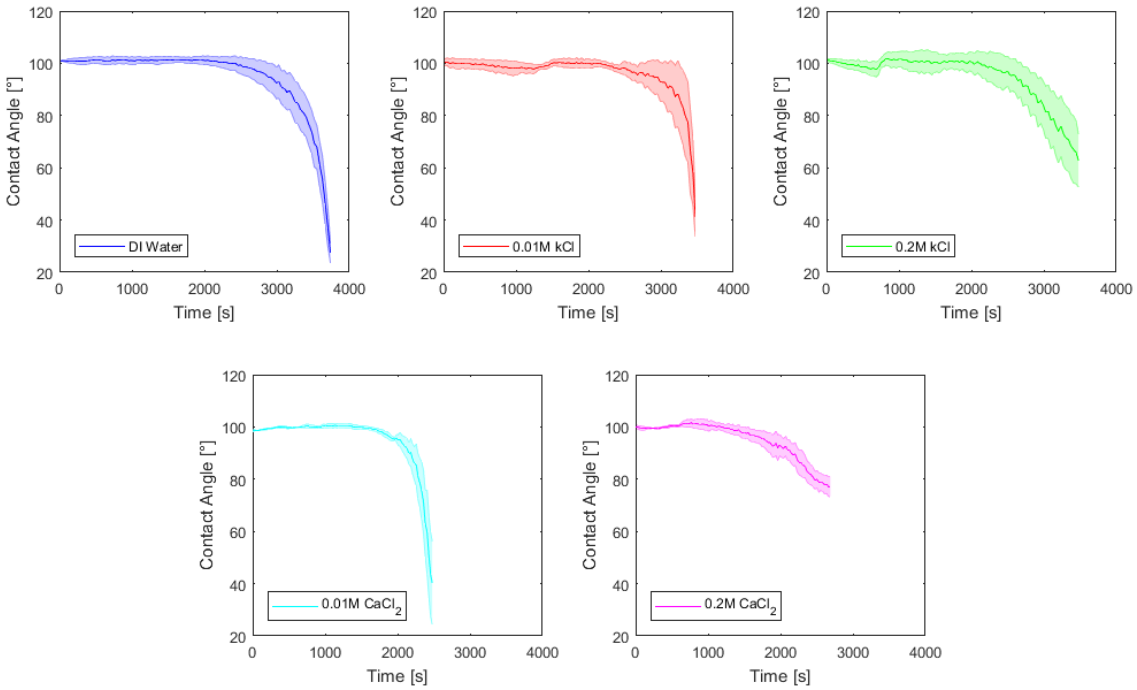

Figure 5.7: Contact angle as a function of time of droplets evaporating on SOCAL with different initial salt concentrations. Solid line shows the average contact angle of three evaporation experiments. The shaded area shows the standard deviation of the contact angle of the experiments

Droplets of these different concentrations were then evaporated at 40% RH and 25 °C to confirm whether constant contact angle evaporation was still present (Figure 5.7). DI water, (blue), shows

a typical evaporation sequence as expected from the results of chapter 4, where a constant contact angle is observed for the majority of the evaporation, with a drop in the contact angle at the end of the evaporation. $0.01\,\mathrm{mol}$ KCL salt/water solution droplet evaporation (red), again shows constant contact angle evaporation. $0.2\,\mathrm{mol}$ KCL (green) shows constant angle evaporation but with a larger standard deviation. The decrease in the contact angle at the end of the evaporation occurs sooner than the $0.01\,\mathrm{mol}$ solution and a large salt deposit is visible at the end of the evaporation. $0.01\,\mathrm{mol}$ $CaCl_2$ appears to give the constant contact angle evaporation with the lowest standard deviation. $0.2\,\mathrm{mol}$ $CaCl_2$ on the visually appears the least like the expected constant contact angle evaporation with a decreasing contact angle for the majority of the evaporation. This is an unexpected result as the $0.2\,\mathrm{mol}$ $CaCl_2$ had the lowest of any of the salt/water solutions tested. The was also a visible large salt deposit at the en of the evaporation which explains why the contact angle plateaus at a larger value than the other evaporations. Although these experiments do not explain the low returning contact angle in the SOCAL electrowetting experiments, they help inform which salt concentration gives the most consistent results. For these experiments, $0.01\,\mathrm{mol}$ $CaCl_2$ is used for any electrowetting experiments conducted here out.

5.3 Comparison of AC Frequency

The standard theory of electrowetting does not depend on sign or frequency of the applied voltage [87]. For AC electrowetting, there is a range of frequencies in the order of tens to hundreds of kHz where typical electrowetting experiments are conducted with the lower and upper limits between causing undesired behaviour as described previously in section 2.4. Tests to observe the optimum frequency for electrowetting on SOCAL coated glass dielectrics are conducted. An $8\,\mu\mathrm{L}$ droplet is place on the electrowetting device and an applied voltage is cycled three times (0-$600\,\mathrm{V}$ at $20\,\mathrm{V\,s^{-1}}$) at varying frequency (1-$50\,\mathrm{kHz}$). Figure 5.8 (a) shows contact angle as a function of time at $1\,\mathrm{kHz}$ frequency. The contact line pins on the left side of the droplet as the voltage decreases at the end of each cycle. This could be the upper limit of the hydrodynamic resonant frequency, where the droplet would follow the AC signal transitioning to the time-average apparent contact angle. Any lower frequency, the contact-angle is observe to be following the frequency of the applied signal. This could be a source of the pinning. (b) $10\,\mathrm{kHz}$ looks to be the optimum frequency of the trialled frequencies, there is the least deviation between the left

and right contact angle and the least visible pinning. This is likely between the hydrodynamic resonant frequency and the electrical transition frequency. Within this range, the droplet is acting as a perfect conductor and therefore no heating is expected. There is still a decrease from the initial contact angle to the $0\,\mathrm{V}$ contact angle after the first, second and third cycle. (c) $20\,\mathrm{kHz}$ is similar to $10\,\mathrm{kHz}$ except there is a larger variation in the contact angle at $0\,\mathrm{V}$ contact angle after the first, second and third cycle. The lower minimum contact angle than the $10\,\mathrm{kHz}$ may be explained by a similar phenomenon to that witnessed by Li *et al.* where the frequency of modulating the signal can cause charge-trapping to charge and discharge, allowing a lower contact angle [93]. While this could be an explanation further study would be required to fully understand this phenomenon. (d) $50\,\mathrm{kHz}$ appears to have the most pinning and variation throughout the three cycles. This regime must be reaching the electrical transition frequency, where the saturation angle is increased which is visible between 500-600 V. In this regime, some heating of the droplet could be expected as the droplet transitions from a perfect conductor to dielectric and a resistance begins to occur. From these experiments $10\,\mathrm{kHz}$ gives the lowest pinning, however all frequencies still observe the lower contact angle after the initial cycle.

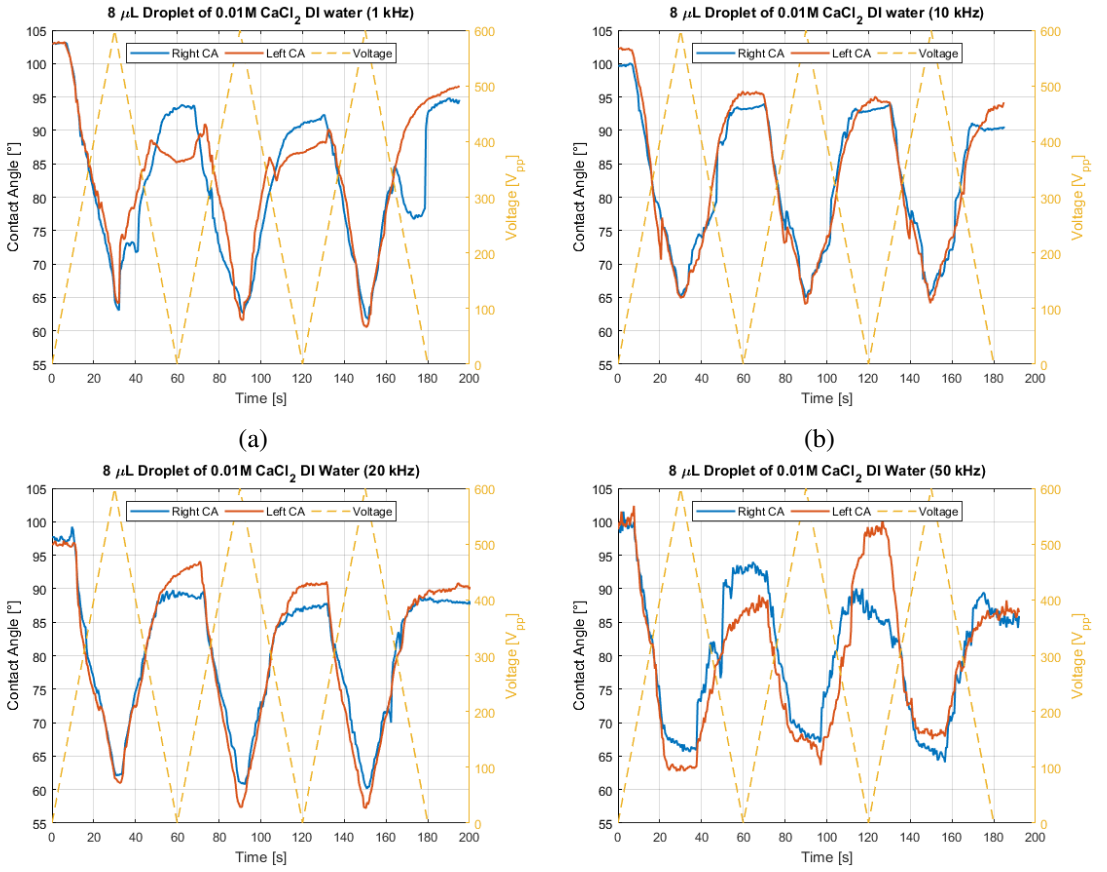

Figure 5.8: Contact angle as a function of time of 8 µL DI water with 0.01 mol $CaCl_2$ on a SOCAL coated 100 µm glass coverslip actuated at a rate of 20 V s^{-1} between 0-600 V. The frequency of the actuated signal is varied between (a) 1 kHz, (b) 10 kHz, (c) 20 kHz and (d) 50 kHz.

5.4 Rate of Change of Voltage

To elucidate the origin of the reduced contact angle experiments are conducted to observe the effect the rate of change in voltage has on the contact angle for electrowetting droplets on SOCAL coated glass coverslips. An 8 µL droplet of 0.01 mol $CaCl_2$ DI water is placed on a 100 µm SOCAL coated glass coverslip on an electrowetting setup as previously described. A 10 kHz AC signal is modulated with a triangle wave to ramp the signal 0-600-0 V at a set rate. The voltage is cycled four times then left to observe if the contact angle relaxes back to the original value. The experiments are conducted in a humidity controlled environment to reduce the evaporation occurring during the experiments.

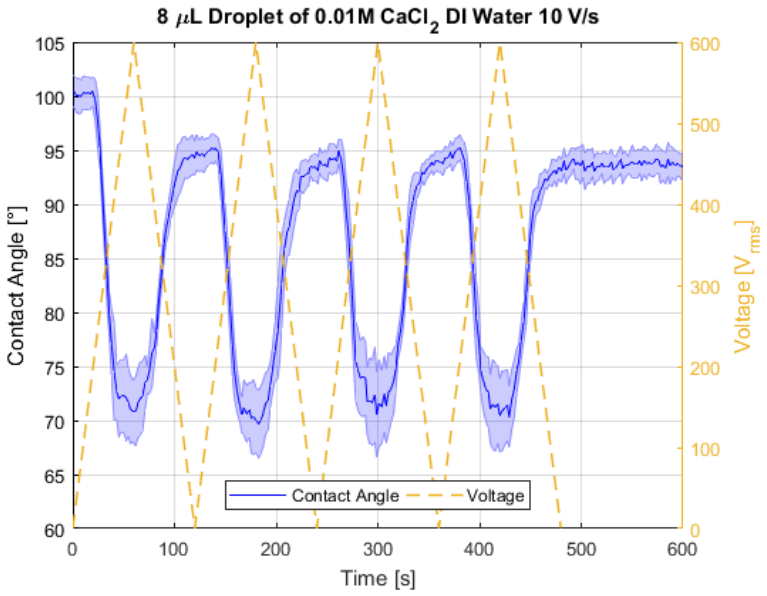

(a)

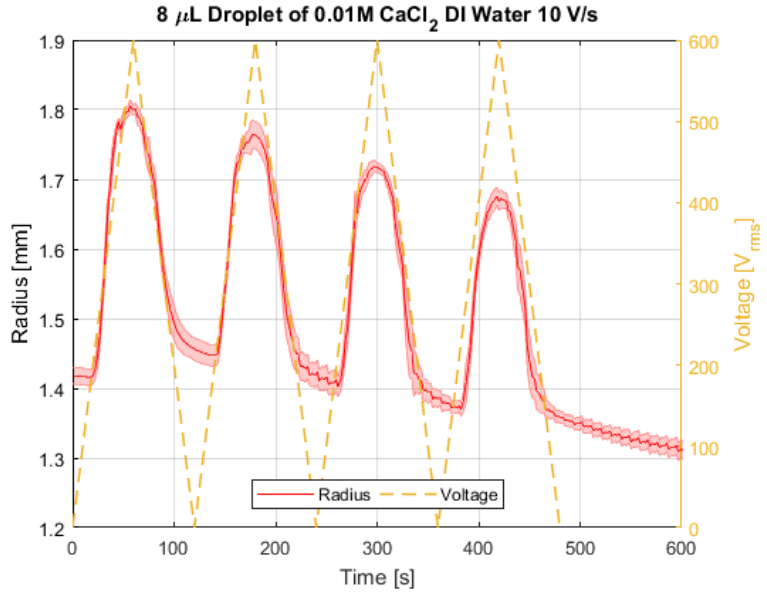

(b)

Figure 5.9: $10\,\mathrm{V\,s^{-1}}$ Voltage rate change experiments: $8\,\mu\mathrm{L}$ droplets of $0.01\,\mathrm{mol\ CaCl_2}$ DI water for cycles of 0-600 V at a rate of $10\,\mathrm{V\,s^{-1}}$ (a) Contact angle as a function voltage (b) Radius as a function of voltage. Shaded area shows standard deviation of 3 repeated and averaged experiments and yellow dashed line shows voltage in time.

Figure 5.9 (a) shows the contact angle change at a voltage rate of $10\,\mathrm{V\,s^{-1}}$. The contact angle decreases from $100°$ to $95°$ between the initial angle and the end of the first cycle. When returning from 600 to $0\,\mathrm{V}$, the contact-angle in time is asymmetric, the contact angle still increases when the voltage first begins to increase again, this suggests the contact angle is not able to move as fast

as the voltage changes. The contact angle then returns to $95°$ every subsequent cycle. The contact angle remains constant after the three cycles at $95°$, showing the receding angle to be altered from previous hysteresis results. Figure 5.9 (b) shows the radius change at a voltage rate of $10\,\mathrm{V\,s^{-1}}$. The rate of change in the radius appears linear for the majority of a cycle. The rate of change in the radius slows down when $V > 500\,\mathrm{V}$ and when $V < 250\,\mathrm{V}$. A possible explanation is that at $V > 500\,\mathrm{V}$ the droplet is nearing contact-angle saturation and is unable to spread further.

Figure 5.9 (b) shows the contact angle change at a voltage rate of $2\,\mathrm{V\,s^{-1}}$. Unlike the $10\,\mathrm{V\,s^{-1}}$, The contact angle follows the voltage from $100 - 600 - 100\,\mathrm{V}$, this is also seen in the radius. At low voltage, the contact angle still appears slightly asymmetric, suggesting $2\,\mathrm{V\,s^{-1}}$ is still faster than the contact line can move over the SOCAL.

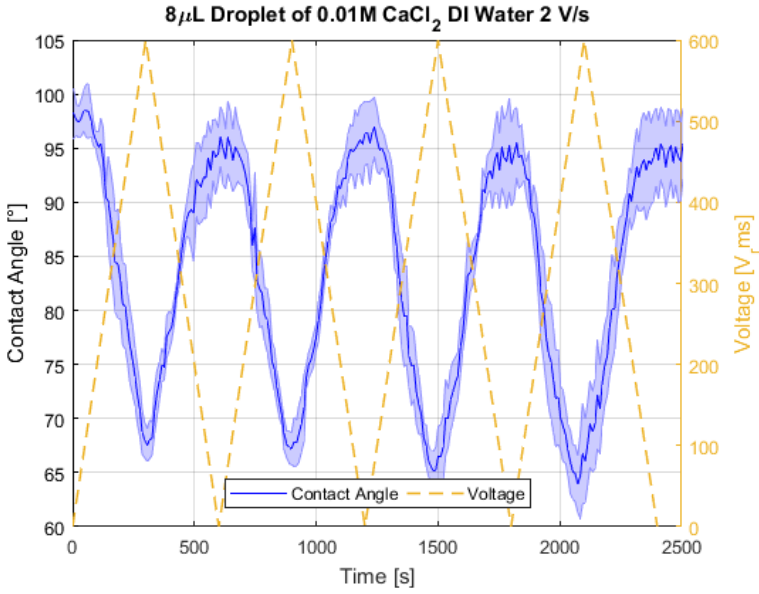

(a)

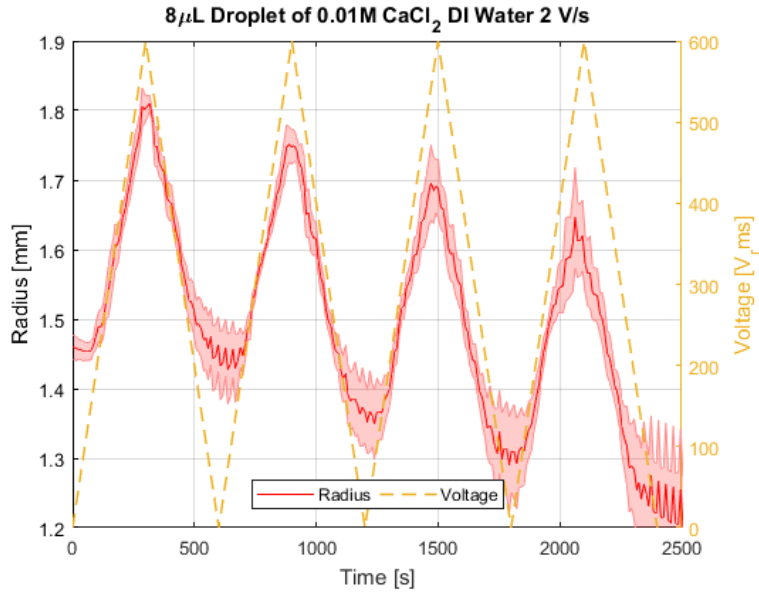

(b)

Figure 5.10: $2\,\mathrm{V\,s^{-1}}$ Voltage rate change experiments: $8\,\mu\mathrm{L}$ droplets of $0.01\,\mathrm{mol\ CaCl_2}$ DI water for cycles of 0-600 V at a rate of $2\,\mathrm{V\,s^{-1}}$ (a) Contact angle as a function voltage (b) Radius as a function of voltage. Shaded area shows standard deviation of 3 repeated and averaged experiments and yellow dashed line shows voltage in time.

Further comparisons between $10\,\mathrm{V\,s^{-1}}$ and $2\,\mathrm{V\,s^{-1}}$ by taking the average of the 2^{nd}, 3^{rd} and 4^{th} cycle, and plotting them against the voltage (figure 5.11). $10\,\mathrm{V\,s^{-1}}$ shows no movement in the contact angle or base radius from 0-200 V. This could be interpreted as a threshold voltage that is required to be overcome before the contact line begins to move, however, at the slower $2\,\mathrm{V\,s^{-1}}$, the

contact angle changes in this region. Another explanation is that as the contact angle is still trying to relax from the previous cycle and the competing forces are preventing the movement.

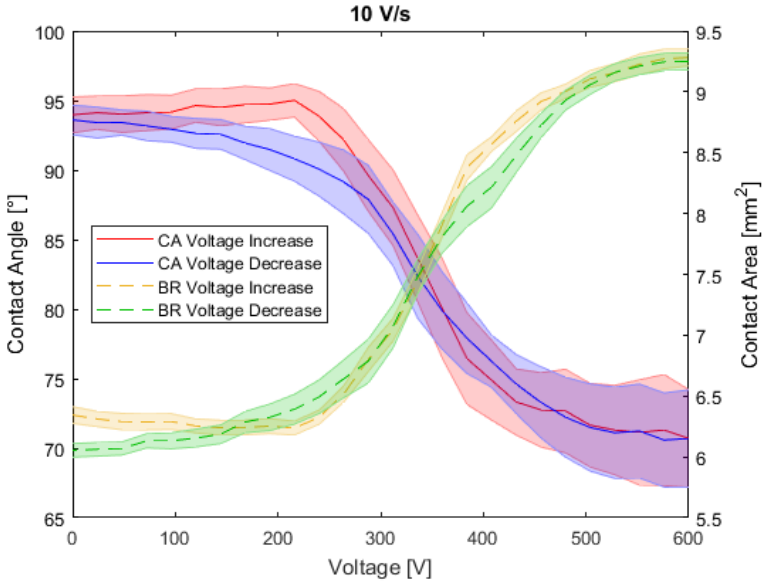

(a)

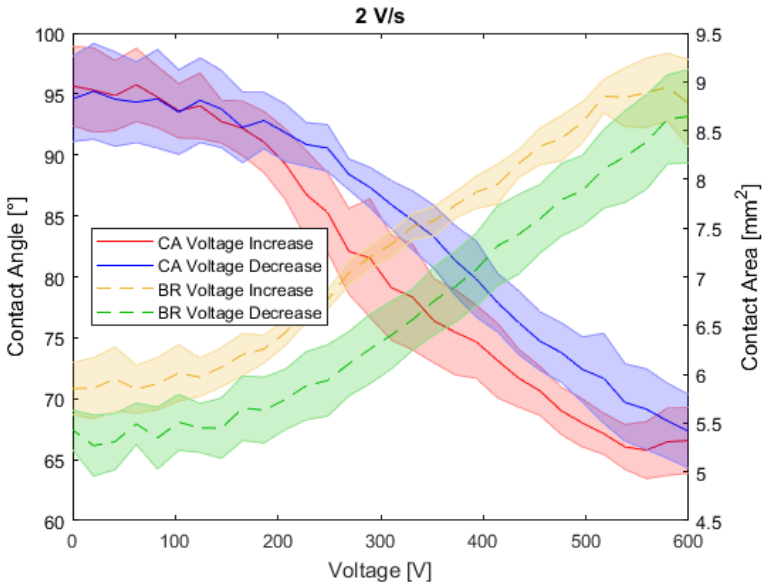

(b)

Figure 5.11: Contact angle and base radius as a function of Voltage for 2^{nd}, 3^{rd} and 4^{th} cycles of voltage rate: (a) $10\,\mathrm{V\,s^{-1}}$ and (b) $2\,\mathrm{V\,s^{-1}}$.

Plotting the contact angle as a function of time while varying the frequency of the triangle wave (which amplitude modulates the rate of change in the voltage), the contact angle as a function of frequency can be plotted. This shows how the contact angle varies with frequency. Figure 5.12 shows a decrease in the contact angle at 0 V after a cycle, θ_0 and an increase in the minimum

contact angle at $V = 600\,\mathrm{V}$, θ_{Vmax}. In order to observe the quasi-static contact angle voltage relationship expect from theory, one can evaporate the droplets at fixed voltage for a range of voltages. This will be explored in the next chapter.

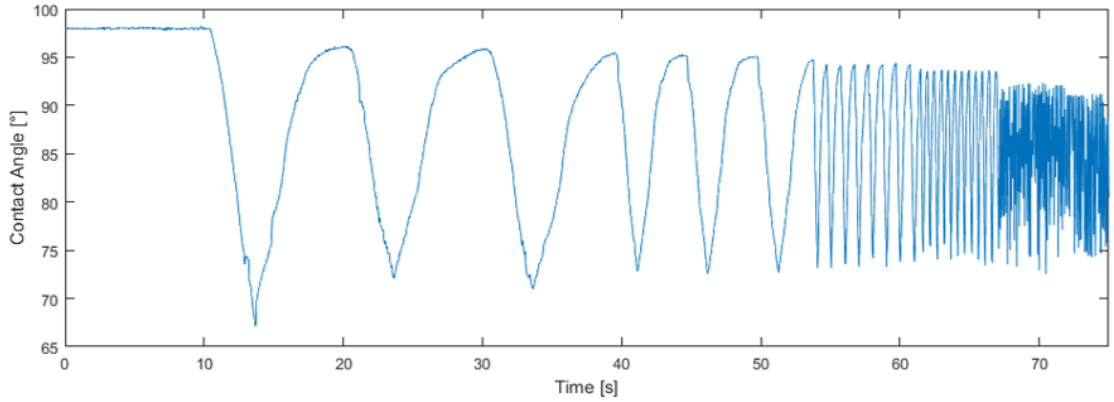

(a)

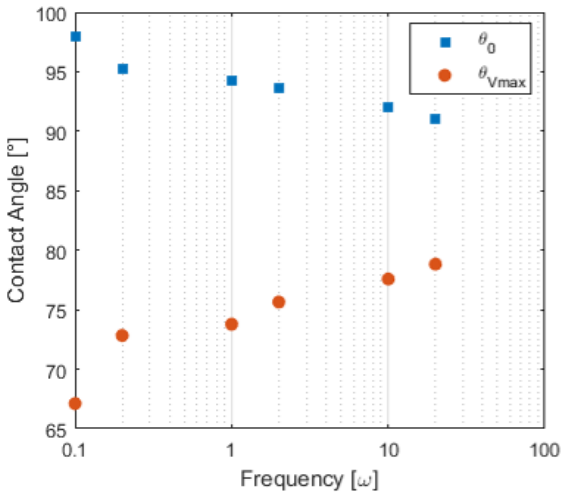

(b)

Figure 5.12: Contact angle as a function of voltage rate: (a) contact angle in time throughout experiments and (b) Maximum and minimum contact angle as a function of frequency.

5.5 Conclusion

This chapter has detailed the experiments conducted to setup and calibrate electrowetting experiments on SOCAL. This has included preliminary tests on PTFE to recover the Young-Lippmann theory. This experiment also highlights how hysteresis prevents reversible electrowetting modulation of the contact angle. Experiments using coverslips and SLIPS replicate the hysteresis free electrowetting results of Brabcova *et al.* [98]. These experiments inform of the appropriate

thickness of glass dielectric, while preventing dielectric breakdown, and allowing actuation of the contact angle of the droplet to the limit of contact angle saturation within the maximum voltage of the available equipment. Experiments on glass covered dielectrics show an unexpected behaviour where the contact angle does not follow the theory. To investigate further, the effect of the salt type on the contact-angle hysteresis. What salt type and concentration do appear to have an impact, the effect is minimal compared to the contact-angle hysteresis observed in electrowetting experiments. The effect of frequency on the system is also studied, which informs the best frequency for the experiments. The rate of change in voltage is also varied to study the effect. This does appear to increase the hysteresis and deviation from the theory, however, within the experiments conducted they are still not slow enough to recover the theory. The slowest possible movement is to evaporate the droplet at high humidity and observe whether the constant contact angle evaporation of droplets, while under an applied electrowetting voltage, will recover the Young-Lippmann theory. This will be detailed in the next chapter.

Chapter 6

Tunable Evaporation on Slippery Surfaces

Sessile droplet evaporation underpins a wide range of applications from inkjet printing to coating. However, drying times can be variable and contact-line pinning often leads to undesirable effects, such as ring stain formation. Here, voltage programmable control of contact angles during evaporation on two pinning-free surfaces is shown. This is achieved using an electrowetting-on-dielectric approach and SLIPS or SOCAL surfaces to achieve a constant contact angle mode of evaporation. Evaporation sequences and droplet lifetimes across a broad range of contact angles from $105°-65°$ are studied. The values of the contact angles during evaporation are consistent with expectations from electrowetting and the Young-Lippmann equation. The droplet contact areas reduce linearly in time and this provides estimates of diffusion coefficients close to the expected literature value. Further findings show that the total time of evaporation over the broad contact angle range studied is only weakly dependent on the value of the contact angle. It is concluded that on these types of slippery surfaces droplet lifetimes can be predicted and controlled by the droplet's volume and physical properties (density, diffusion coefficient, and vapour concentration difference to the vapour phase) largely independent of the precise value of contact angle. These results are relevant to applications, such as printing, spraying, coating and other processes, where controlling droplet evaporation and drying is important.

6.1 Experimental Setup

The experiments require surfaces that are both free of contact line pinning and which have contact angles that can be adjusted to different constant values. To do this, two types of surfaces are used, SOCAL and SLIPS, as slippery layers on a glass substrate (as the dielectric) in an electrowetting configuration as described below (Figure 6.1). The electrowetting configuration allows the initial contact angle determined by the droplet-solid, droplet-lubricant and other interfacial tensions to be reduced in a programmable manner by application of a voltage.

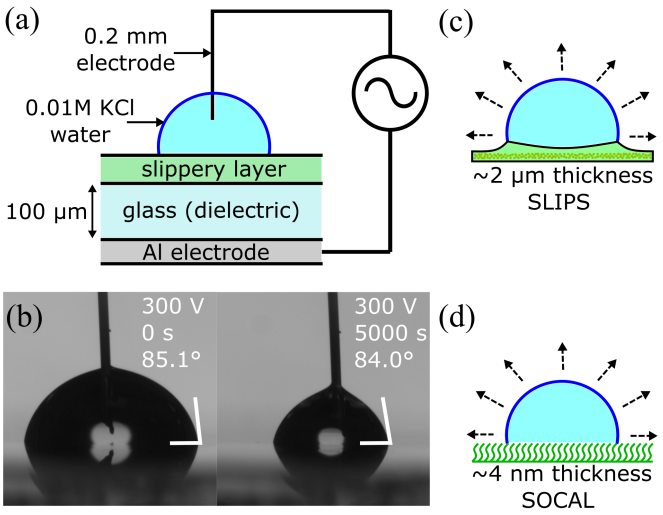

Figure 6.1: Electrowetting and evaporation on slippery surfaces: (a) Schematic of droplet in an electrowetting setup with a glass dielectric substrate and a slippery top layer. (b) example images of droplets evaporating under fixed rms voltage (300 V) at constant angle on SOCAL. Sketches of the two types of slippery top-layers (c) droplet on hydrophobic nano-particle SLIPS, and (d) droplet on SOCAL.

The electrowetting configuration to investigate evaporation at different constant contact angles on these surfaces is shown in figure 6.1(a) with example evaporation images in figure 6.1(b) and the schematics showing the two types of slippery surfaces in figure 6.1(c) and figure 6.1(d). An AC system using a signal generator (TTi Instruments TGA1244) to generate a $10\,\mathrm{kHz}$ sinusoidal wave which was then amplified (Trek PZD700A) as a programmable root mean square (rms) voltage, V, within the range 0 to 450 V. The amplified signal was then applied to an aluminium-coated glass slide ($100\,\mu\mathrm{m}$, vapour deposited) as one electrode and a thin metal, $0.2\,\mathrm{mm}$ diameter, in the centre of the droplet, as the second electrode. The cross sectional area of the needle is $0.13\,\mathrm{mm}^2$, compared to the surface area of a $8\,\mu\mathrm{L}$ droplet with $105°$ contact angle which is $15.6\,\mathrm{mm}^2$ which

is less than 1% of the total surface area, the needle is therefore not expected to have a significant effect on the spherical cap shape during the evaporation. The $100\,\mu\mathrm{m}$ thick glass cover-slip on which the slippery coating (SOCAL or SLIPS) was attached acts as a dielectric enabling storage of capacitive energy and allowing the contact area, and hence contact angle, to be adjusted by altering the balance between capacitive and interfacial energies. The droplets of deionized water used in the experiments had a volume of $8\,\mu\mathrm{L}$ and $0.01\,\mathrm{mol}$ KCl was added to ensure the electrical conductivity required for electrowetting. Although the findings of the previous chapter show $CaCl_2$ shows more consistent results, KCl was more readily available and the difference between two salts although measurable, small enough to be negligible. The thin metal electrode was lowered into the centre of the droplet after deposition and evaporation experiments were conducted at room temperature ($22 \pm 2\,^{\circ}\mathrm{C}$) at a controlled relative humidity of 70% within a transparent chamber to regulate the conditions local to the droplet. The chamber also shields the droplet from the presence of air drafts which might otherwise entrain the lubricant from a SLIP surface over an evaporating droplet [104]. Droplet evaporation sequences were recorded using a camera at 0.05 frames per second and contact radius r and contact angle θ measurements were determined using open-source pyDSA software. Experimentally, profiles of the droplet are accurately described by a spherical cap to within a slight distortion around the electrode needle, however, further improvements could be made in future EWOD designs by using a co-planar electrode whereby the probe is replaced with an in plane electrode [142]. Such a design would require further work to apply SOCAL to the electrode to prevent pinning. The volume of the droplet during evaporation was calculated using the contact radius and contact angle. The data set presented in this chapter is a representative sample of wider body of experiments, and each evaporation at a fixed voltage for each surface is the average of three evaporation sequences.

The first type of slippery surface used SLIPS samples prepared by taking new glass cover-slips (Thorlabs, CG00K1) of thickness $100 \pm 5\,\mu\mathrm{m}$, coating them with 5 layers of GLACO™ Mirror Coat (Nippon Shine) to create a nanoparticle-based superhydrophobic porous structure and then infusing a layer of lubricant by withdrawal from a bath of $20\,\mathrm{cSt}$ silicone oil (Sigma Aldrich, 378348) at $0.1\,\mathrm{mm\,s^{-1}}$. Excess oil is rinsed off to ensure only a thin conformal oil layer remained on the surface so that there is no visible wetting ridge of oil on subsequent sessile droplets. The water contact-angle hysteresis $\Delta\theta_{CAH}$ was determined by measuring advancing contact angle θ_A

and receding contact angle θ_R through the average of three droplet inflation/deflation experiments in different locations on the substrate ($\Delta\theta_{CAH} = 0.4 \pm 0.3°, \theta_A/\theta_R = (109.6°)/(109.2°)$). Sliding angles, α, were also measured by placing a 20 µL droplet of deionized water on the surface and tilting the substrate until the droplet begins to slide, and the average of three measurements gives $\alpha_{(20\mu L)} = 0.2 \pm 0.2°$. The measured contact angle is consistent with theoretical expectations of $108°$ based on a liquid-form of Young's law (eq. 4 in [107]) using an effective droplet-vapour interfacial tension as sum of the droplet-oil and oil-vapour interfacial tensions and indicates silicone oil should cloak the droplet-vapour interface despite the absence of a visible wetting ridge at the contact line [53, 107]. The second type of slippery surface used, smooth liquid-like SOCAL surfaces, are prepared on glass samples (see references [3, 143] and section 3.2.2). New glass cover-slips of thickness of $100 \pm 5\,\mu\mathrm{m}$ were exposed to air plasma in a (Henniker HPT-100) at $30\,\mathrm{W}$ for $20\,\mathrm{min}$. The cover-slips were then dipped in a reactive solution of $91.45\,\mathrm{mL}$ isopropyl alcohol ($\leq 99.7\%$, Sigma Aldrich, 292907), $8.16\,\mathrm{mL}$ dimethyldimethoxysilane (95%, Sigma Aldrich, 104906) and $0.39\,\mathrm{mL}$ sulphuric acid (95.0-98.0%, Sigma Aldrich, 258105) for 5-10 s and then slowly removed. These coated glass slides were subsequently placed in a bespoke humidity chamber for $20\,\mathrm{min}$ at $60 \pm 2\,\%$ relative humidity to allow the acid-catalysed polycondensation to take place. After this time, the surface was rinsed with isopropyl alcohol, toluene ($\leq 99.5\%$, Sigma Aldrich, 179418), and deionized water (type III, purified in an Elga PURELAB Option-Q lab water purification system) to remove any remaining reactive solution. This creates flexible polydimethylsiloxane chains approximately $4\,\mathrm{nm}$ in length, that allow mobility of the droplet contact-line thereby minimizing contact line pinning [3]. To confirm successful and homogeneous coating, contact-angle hysteresis and sliding angles were measured in the same manner as for the first surface and determined to be ($\Delta\theta_{CAH} = 1.0 \pm 0.5°, \theta_A/\theta_R = (105.7°)/(104.7°)$) and $\alpha_{(20\mu L)} = 5.6 \pm 0.4°$. These values are in good agreement with Wang & McCarthy who reported ($\Delta\theta_{CAH} = 1.0°, \theta_A/\theta_R = (104.6°)/(103.6°)$) and $\alpha_{(20\mu L)} = 4°$ for droplets of water. Using the same interfacial tensions as for the silicone oil in the SLIPS, but assuming the PDMS chains on a SOCAL surface cannot cloak the droplet-vapour interface, the liquid-form of Young's law suggests the water droplet should have a contact angle on SOCAL of $104°$ and this is consistent with the measured value.

6.2 Diffusion Coefficient Calculation

First the qualitative features of the droplet evaporation is discussed. It is observed that after a brief initial period (corresponding to a volume reduction from $8\,\mu L$ to $7\,\mu L$), the contact angle remained approximately constant during the evaporation for most of the evaporation period on both types of slippery surfaces (Figure 6.2). Focusing on SLIPS, the droplet evaporation sequences was consistent with prior literature [77]. However, because the samples here use thin conformal SLIPS layers based on a hydrophobic nanoparticle coating, rather than lithographically produced micro-pillar textures with thicker layers of lubricant, there were no visible wetting ridges around the contact line. This is an improvement for evaporation studies since the oil in a wetting ridge removes some of the droplet-vapour surface area for evaporation. The application of a constant amplitude electrowetting voltage reduced the initial contact angle in a reproducible manner over many voltage cycles on the SLIPS consistent with previous reports [98]. Figure 6.2(a) provides the first reports of droplet evaporation sequences with voltage selectable constant contact angle (70° to 105°) on SLIPS and covers the voltage range up to the saturation region well-known for electrowetting (see reference [87]). Greater voltage than the $450\,V$ would be required to observe contact-angle saturation, however the voltages were kept consistent with the SOCAL experiments for comparison. The added dielectric thickness of the GLACO™ on the SLIPS surface increases the required voltage to reduce the contact-angle. In addition, when comparing directly to SOCAL, SLIPS has a marginally larger equilibrium angle, requiring a greater voltage to reduce to the same contact-angle as SOCAL. Focusing now on SOCAL surfaces, the evaporation sequences were observed to be consistent with that on the SLIPS surfaces and at zero applied voltage, consistent with the study of CCA mode evaporation on SOCAL in chapter 4. the contact angle was able to be reduced by the application of the electrowetting voltage and observe, for the first time, evaporation sequences with voltage selectable constant contact angle (67°-105°) on SOCAL (Figure 6.2(b)). When repeatedly cycling the electrowetting voltage the contact angle increased to $3.6 \pm 0.4^\circ$, which nonetheless remains low compared to other hydrophobic coatings. In such experiments, the contact angle measured during the constant contact angle period of evaporation at zero voltage after the first was cycle was reduced from $102.1 \pm 1.2^\circ$ to $94.9 \pm 1.5^\circ$. However, it was possible to apply a constant electrowetting voltage to a freshly deposited droplet on different areas of a SOCAL surface and observe smoothly receding contact lines as the droplets evaporated. Figure

6.2(b) shows such data with each data point an average of three droplets on a sample and shows constant contact angles of $102.1 \pm 1.2°$ to $67.2 \pm 0.3°$ for voltages with rms values between 0-450 V. The corresponding contact areas of droplets decreases linearly in time during the constant contact angle period of the evaporation (Figure 6.2(a) inset).

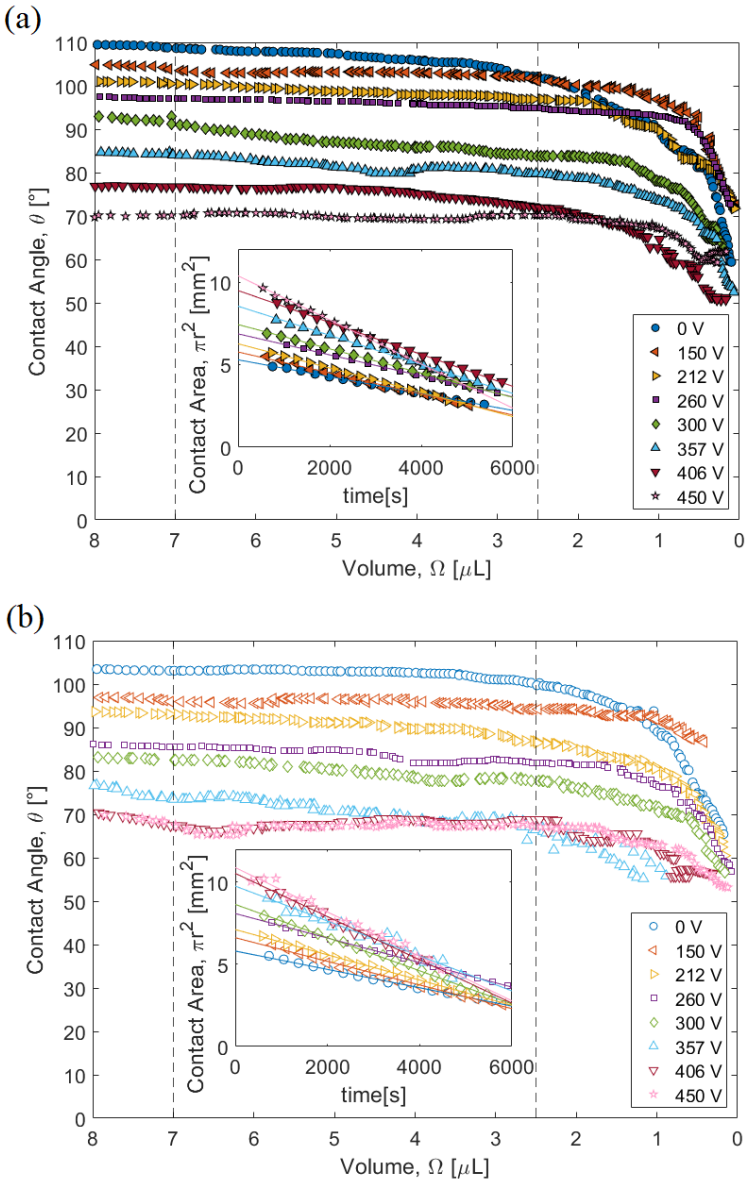

Figure 6.2: Contact angle as a function of reducing volume for $0.01\,\mathrm{mol}$ KCl deionized water droplets evaporating at fixed electrowetting voltages on: (a) SLIPS and (b) SOCAL surface. Inset shows contact area as a function of time for the constant contact angle regime indicated by dashed lines.

Quantitative analysis of the constant contact angle regime is now considered for both types of slippery surfaces to confirm the absolute slopes from the data in Figure 6.2 are physically reasonable.

Rearranging (2.27), the diffusion coefficient can be determined from the evaporation of a droplet using the average rate of change in contact area (slope in the insets to Figure 6.2), i.e.

$$D = -\frac{\rho\beta(\theta)}{8\pi(c_s - c_\infty)\sin^2\theta f_{PB}(\theta)}\frac{d(\pi r^2)}{dt} \tag{6.1}$$

where $f(\theta)$ is evaluated using the Picknett & Bexon interpolation formula (eq. 2.16). Table 6 shows these calculated diffusion coefficients across the electrowetting voltage range (prior to contact angle saturation) is in good agreement with the literature diffusion coefficient. On the SLIPS, the average diffusion coefficient measured experimentally is $D_{Exp} = 2.06 \pm 0.26 \times 10^{-5}\,\mathrm{m^2\,s^{-1}}$ compared to the literature value of $D_{Lit} = 2.41 \pm 0.05 \times 10^{-5}\,\mathrm{m^2\,s^{-1}}$ On the SOCAL surfaces, the experimental average was found to be $D_{Exp} = 2.14 \pm 0.21 \times 10^{-5}\,\mathrm{m^2\,s^{-1}}$ and using data for droplets on both types of surface the experimental average was $D_{Exp} = 2.10 \pm 0.24 \times 10^{-5}\,\mathrm{m^2\,s^{-1}}$.

The rate of change in contact area in time for constant contact angle evaporation (2.26), can be arranged to give the rate of change in volume and be expressed in terms of the instantaneous volume and the constant contact angle

$$\frac{d\Omega}{dt} = -2\lambda\left(\frac{3\Omega}{\pi\beta(\theta_c)}\right)^{1/3} f(\theta_c) \tag{6.2}$$

and this integrates to give a $2/3^{rd}$ power law for the volume,

$$\Omega(t)^{2/3} = \Omega_i^{2/3} - \frac{4\lambda}{3}\left(\frac{3\Omega}{\pi\beta(\theta_c)}\right)^{1/3} f(\theta_c)t \tag{6.3}$$

where Ω_i is the initial droplet volume $t = 0$. The $2/3^{rd}$ power law for the drop volume is verified experimentally and the slopes from the analysis are also given in Table 6 along with the value determined for the constant contact angle and the droplet lifetime (see section 2.3.3). These results also support the assumption that electrowetting does not significantly alter the evaporation of sessile droplets from these surfaces. Any significant heating caused from the AC voltage would increase the evaporation rate and effect the experimentally obtained evaporation rate.

Table 6: Experimentally Determined Diffusion Coefficients

Slippery layer	rms Voltage [V]	Constant Contact Angle, θ_c [°]	d(πr^2)/dt $[10^{-4}\,\mathrm{mm\,s^{-1}}]$	d$\Omega^{2/3}$/dt $[10^{-3}\,\mu\mathrm{L\,s^{-1}}]$	Total evaporation time, t_f [s]	D_{Exp} $[10^{-5}\,\mathrm{m^2\,s^{-1}}]$
SLIPS	0	105.3±1.6	-5.18±0.03	-4.49±0.03	8034±960	1.84±0.06
	150	102.5±2.6	-6.60±0.09	-4.43±0.05	7877±940	2.17±0.07
	212	98.2±2.2	-7.31±0.05	-4.97±0.04	9416±1100	2.28±0.08
	260	95.8±0.4	-6.42±0.02	-3.98±0.02	8698±1040	1.89±0.05
	300	86.3±3.6	-7.15±0.06	-4.25±0.04	10876±1300	1.76±0.09
	357	81.0±6.0	-8.70±0.09	-4.35±0.02	9255±1100	1.95±0.16
	406	74.6±2.2	-9.83±0.05	-4.46±0.02	9004±1070	2.03±0.09
	450	70.1±1.4	-13.27±0.12	-5.12±0.05	10151±1210	2.54±0.11
SOCAL	0	102.1±1.2	-5.76±0.06	-4.10±0.02	7806±930	2.06±0.06
	150	95.5±2.8	-7.41±0.10	-4.09±0.04	9692±1160	2.17±0.09
	212	89.8±3.6	-7.68±0.08	-4.34±0.03	9779±1170	2.06±0.10
	260	83.3±2.8	-7.43±0.06	-3.89±0.03	10323±1230	1.78±0.07
	300	79.4±3.6	-9.88±0.08	-4.27±0.04	10712±1280	2.23±0.11
	357	70.3±2.2	-10.29±0.30	-4.83±0.07	8560±1020	2.00±0.10
	406	67.7±2.4	-13.43±0.26	-5.72±0.04	8810±1050	2.44±0.12
	450	67.2±3.0	-13.57±0.29	-4.54±0.08	10252±1220	2.35±0.13

6.3 Contact Angle Dependence on Voltage

The consistency of the observed voltage-selected contact angles with expectations from the theory of electrowetting is now evaluated. In the absence of contact line pinning, the initial contact angle without an applied voltage is assumed to be given by Young's law. The effect of applying a voltage and charging a dielectric using the contact area of a droplet as one electrode is to introduce a capacitive energy in addition to interfacial energies. This causes a voltage dependent contact angle, $\theta(V)$, described by the Young-Lippmann equation, (2.31). A quadratic power law is expected, with dependence of $\cos\theta$ on the voltage and this is confirmed for both the SLIPS and SOCAL surfaces by figure 6.3. The insets in figure 6.3 show a linear plot of the $\Delta\cos\theta$ with V^2 and the saturation effect of wetting is clearly visible for the SOCAL surface.

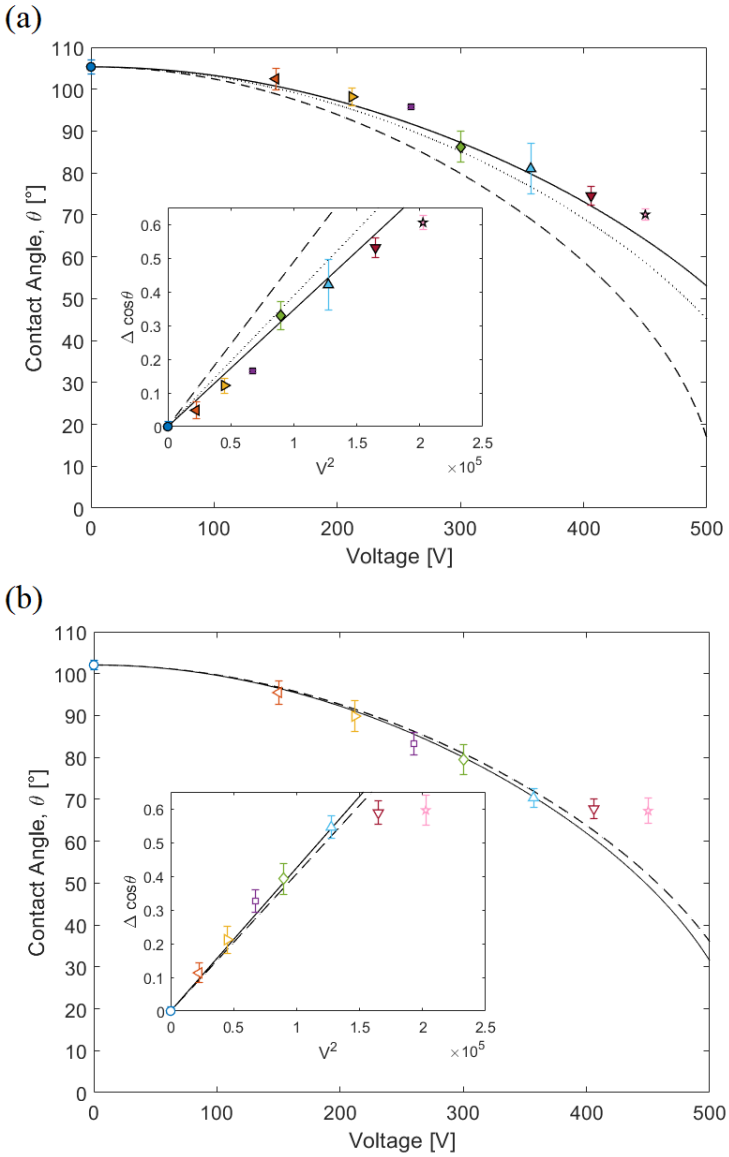

Figure 6.3: Cosine of average contact angle during evaporation (constant contact angle regime) as a function of voltage: (a) SLIPS and (b) SOCAL. Inset shows $\Delta \cos\theta$ as a function of V_{rms}^2 fit (solid line) before saturation (voltage rms$<$400 V). The dashed and dotted lines for SLIPS are predictions from theory assuming the droplet is cloaked and not cloaked in oil, respectively. The dashed lines for SOCAL are predictions from theory.

To compare quantitatively to the theoretical expectations from (6.3), the slippery SOCAL layer is considered. This has a sufficiently small thickness ($\sim$4 nm) to be a negligible correction to the dielectric thickness due to the 100 µm thick glass substrate and the covalently attached PDMS chains mean there is no cloaking of the droplet-vapour interface. The glass has a manufacturer-stated relative permittivity $\epsilon_{glass} = 6.7$, and so using a surface tension for water of $\gamma_{lv} = 72.8\,\mathrm{mN\,m^{-1}}$ gives $\epsilon_0\epsilon_d/2\gamma_{lv}d = 4.07 \times 10^{-6}\,\mathrm{V^{-2}}$. This can be compared to the slope $\Delta\cos\theta/V^2$ in the inset in fig-

ure 6.3(b) for the experimental data for SOCAL. The experimental result of $4.20 \pm 0.10 \times 10^{-2}\,\mathrm{V}^{-2}$ using data below the contact angle saturation voltage of $400\,\mathrm{V}$ is in excellent agreement with the theoretical value.

We now consider the consistency theory between the theory and the experimental results for droplets on SLIPS. In this case, the glass substrate and the SLIPS layer is regarded as a series capacitive combination of the glass with the SLIPS layer so that the relative dielectric thickness is $(d/\epsilon_r)_{total} = (d/\epsilon_r)_{glass} + (d/\epsilon_r)_{SLIPS}$. The major contribution to the capacitance is therefore from the glass substrate and this gives an order of magnitude estimate consistent with the experimental data. (2.31)To estimate the small correction due to the SLIPS, The thickness of the porous GLACO™ layer $\sim 2\,\mu\mathrm{m}$ was used, infused with silicone oil with excess oil remove through rinsing as the thickness of the SLIPS. Moreover, since the relative permittivity of the silica nanoparticles ($\epsilon_r = 2.5 - 3.5$) and oil ($\epsilon_r = 2.68$) in the SLIPS layer are similar and the layer is a small correction, it is approximate to a uniform dielectric layer with $\epsilon + r \sim 2.68$. This provides an estimate of $(d/\epsilon + r)_{SLIPS} = 6.38 \times 10^{-4}\,\mathrm{m}$. In addition to these dielectric considerations, it is expected that the droplet-vapour interface is cloaked so that an effective interfacial tension should be used in equation (2.31) replacing γ_{lv} by $\gamma_{Eff} = \gamma_{WO} + \gamma_{OA}$, where γ_{WO} and γ_{OA} are the water-oil and oil-air interfacial tensions, respectively. Using the interfacial tension data from Banpurkar *et al.* [144], the water-oil interfacial is estimated at $\gamma_{WO} = 38\,\mathrm{mN\,m^{-1}}$ and from the data of McHale *et al.* [107] the oil-air interfacial tension is $\gamma_{OA} = 19.8\,\mathrm{mN\,m^{-1}}$ giving an effective interfacial tension of $\gamma_{Eff} = 57.8\,\mathrm{mN\,m^{-1}}$. Including this cloaking effect gives $\epsilon_0\epsilon_d/2\gamma_{Eff}d = 4.89 \times 10^{-6}\,\mathrm{V}^{-2}$ and so over-estimates the contact angle changes compared to the experimental data (dashed line compared to symbols in figure 6.3(a)). However, we note that assuming oil does not cloak the droplet-air interface gives $\epsilon_0\epsilon_d/2\gamma_{Eff} = 3.88 \times 10^{-6}\,\mathrm{V}^{-2}$, where $\gamma_{lv} = 72.8\,\mathrm{mN\,m^{-1}}$, and this is closer to the fit to the data which is $\epsilon_0\epsilon_d/2\gamma_{Eff} = 3.47 \pm 0.11 \times 10^{-6}\,\mathrm{V}^{-2}$ (dotted lines compared to solid lines in figure 6.3(a)). To fit the curve using equation (2.31) and an oil-cloaked droplet-air, would require a significantly smaller value of the relative permittivity ($\sim 75\%$) than the manufacturer provided value and/or a significantly thicker ($\sim 40\%$) glass substrate.

6.4 Evaporation Time Dependence on Contact Angle

The extent to which the lifetime of an evaporating droplet, t_f, depends on its initial contact angle is now considered. From the fits to the contact area for each evaporating droplet sequence the lifetime was determined (figure 6.2 inset) and these values are given in Table 6 for each surface. To show the scaling dependence, figure 6.4 shows the contact area normalized by the initial contact area (using the intercepts in the insets in figure 6.2) as a function of time normalized by total evaporation time for droplets on each surface. The secondary y-axis in each figure shows the contact angle normalized by the constant contact angle. A similar collapse of data onto a single scaling curve can be observed by for the $2/3^{rd}$ power law for the drop volume and this illustrates the good agreement with the power law on these slippery surfaces (insets in figure 6.4). Equation (2.29) shows that the lifetime is a separable product of three functions involving the constant contact angle, θ_c, the initial droplet volume, Ω_i, and the parameter λ which incorporates the density, ρ, difference in vapour concentration Δc, and diffusion coefficient, D, i.e.

$$t_f(\theta_c, \lambda, \Omega_i) = \tilde{t}(\theta_c)\xi(\lambda)\Omega_i^{2/3} \tag{6.4}$$

where the contact angle dependent factor is,

$$\tilde{t}(\theta_c) = \frac{\beta^{1/3}(\theta_c)}{2^{4/3} f(\theta_c)} \tag{6.5}$$

and various other dependencies have been grouped together as,

$$\xi(\lambda) = \frac{4(18\pi)^{1/3}}{\lambda} = \frac{2(18\pi^2)^{1/3}\rho}{D(c_s - c_\infty)} \tag{6.6}$$

According to Stauber *et al.* the droplet lifetime in the constant contact angle mode of evaporation has a maximum at $\cos\theta = 0$ [145]. This is illustrated by the solid curve in Figure 6.5 showing a plot of equation (6.5) over the full contact angle range from a film with $\cos\theta = 1$ to a spherical sessile droplet with $\cos\theta = -1$ using the Picknett & Bexon polynomial interpolation for $f(\theta)$ in equation (6.5). Expanding Stauber et al.'s formula analytically (or, equivalently, numerically fitting the Picknett & Bexon formula) gives a quadratic expansion approximation around the maximum

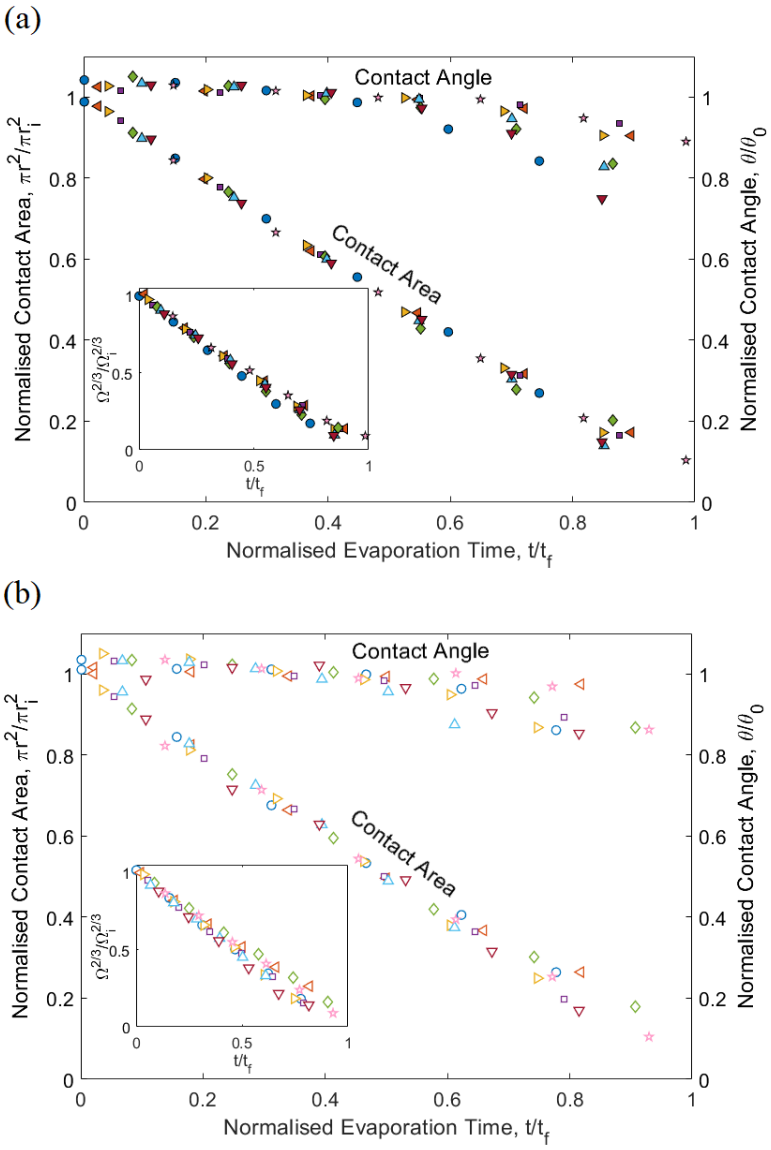

Figure 6.4: Scaling of evaporation measurements with droplet lifetime. Normalised contact area, $\pi r^2/\pi r_i^2$ as a function of normalised time, t/t_f and normalized contact angle, θ/θ_c as a function of normalised time t/t_f. Insets: normalised volume $\Omega^{2/3}/\Omega_i^{2/3}$ as a function of normalised time, t/tf. Data presented is every 50^{th} data point for clarity of presentation.

of,

$$\tilde{t}(\theta) \approx 1 - \frac{(9\pi - 32)(\theta - \pi/2)^2}{6} \tag{6.7}$$

where θ is in radians. From the full plot in figure 6.5, the contact angle dependence is predicted to be relatively insensitive to the precise value of θ and remains within 10% of the maximum value over the contact angle range from $40°$ to $180°$. In experiments using smooth surfaces, i.e. not superhydrophobic, the maximum achievable contact angles with surface chemistry is $\sim 115°$

rather than the parameter maximum of $180°$ in the theory. The inset in figure 6.5 shows the more limited range bounded by the lower limit due to contact angle saturation in electrowetting $(\sim 67°)$ and the maximum achievable contact angle $(105°)$ on our smooth surfaces; this covers a wide range of $\cos\theta$ from 0.39 to -0.26.

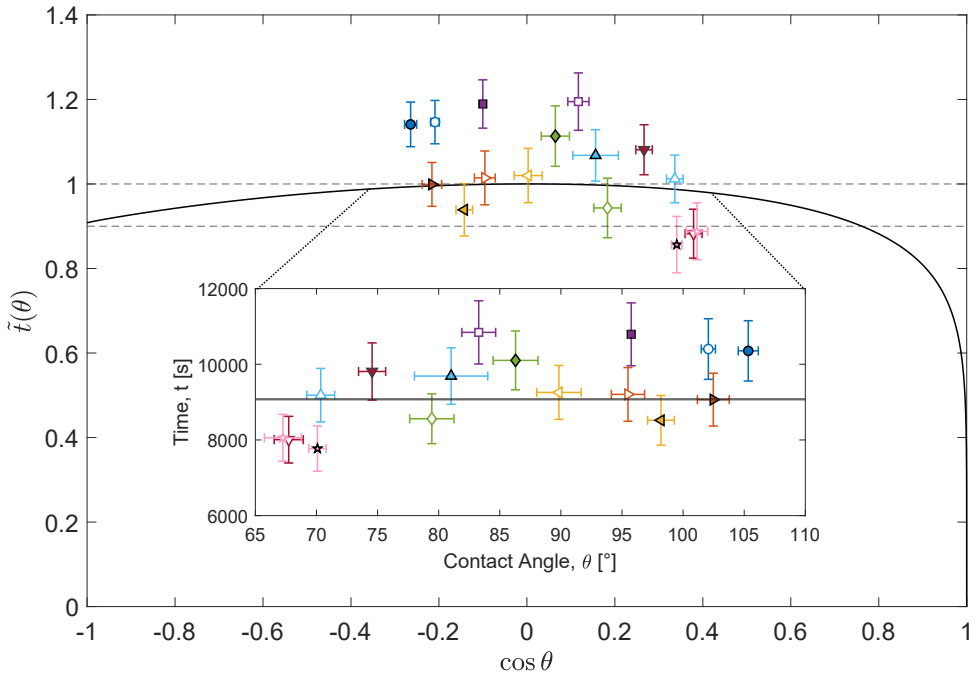

Figure 6.5: Drop lifetime contact angle dependence factor, $\tilde{t}(\theta)$ (Solid line theory, solid symbols are experimental data for SLIPS and empty symbols are experimental data for SOCAL surfaces). Inset: expanded view of the contact angle range $67°-105°$ (i.e. $\cos\theta = 0.39$ to -0.26) plotted with absolute time as the vertical axis (eq. (2.29)).

To analyse the contact angle dependence of the experimentally determined lifetimes, an assumed initial droplet volume of $8.0 \pm 0.1\,\mu\text{L}$ and temperature $22 \pm 2\,°\text{C}$ and evaporated in air with a relative humidity $70 \pm 1\,\%$ which gives a value of $\xi(\lambda)\Omega^{2/3} = 9070 \pm 990$. The values of droplet lifetime t_f from table 6 scaled down by this value are plotted in figure 6.5 for comparison to the theory with the absolute lifetimes shown in the inset; the average value for t_f from Table 6 is $9330 \pm 1000\,\text{s}$. The solid symbols show the data from the SLIPS and the empty symbols show the data from the SOCAL surface. This data covers a contact angle range from hydrophilic (lowest value$\theta_c = 67°$) to hydrophobic $106°$ (highest value) and shows a scatter around an average value without an obvious contact angle trend. The data appears to lie slightly above equation (6.5) suggesting a slight systematic error in the value of $\xi(\lambda)\Omega^{2/3}$ used in the analysis. From the

results, it is concluded that in the constant contact angle mode of evaporation and for constant contact angles above $40°$, drop lifetimes can be predicted within a 10% tolerance range without precise knowledge of the exact value of the contact angle by using equation (6.4) with $\tilde{t} \sim 1$. Improved estimates could also be made by calibrating experimentally over a specific contact angle range to use a value of $\tilde{t}$ slightly below unity. It should also be possible to decide a desired tolerance on the droplet lifetime and from that determine what range of contact angles needs to be achieved. In practical applications where drying is important, knowledge of initial droplet volume, the liquid density and the temperature and relative humidity (or diffusion coefficient and difference in saturation and ambient vapour concentration) should be sufficient to predict drying time providing the surface allows a mobile contact line without contact line pinning and the contact angle is above $\sim 40°$. These results also show that the initial droplet contact area on a slippery surface can be selected when the contact angle is above $\sim 40°$ without significantly changing the overall droplet evaporation time.

6.5 Conclusion

The results of this chapter show control of constant contact angle mode evaporation over a wide range of receding contact angles from hydrophilic to hydrophobic of droplets on pinning free SLIPS and SOCAL surfaces can be achieved using electrowetting. The results are consistent with the model of diffusion-controlled evaporation of sessile droplets and can be used to estimate the diffusion coefficient. The contact angle-voltage relationship is in excellent agreement with the Young-Lippmann equation for electrowetting of droplets on both types of slippery surfaces. It has been observed that over a range of contact angles above $67°$ on these surfaces, droplet evaporation times are relatively insensitive to the precise value of the contact angle. Thus, a desired tolerance on droplet lifetime can be used to determine what contact angle range and accuracy is required. This may have practical application in processes involving evaporation, such as inkjet printing, where consistent drying times would then depend mainly on the liquid density, control of droplet deposition volume and environmental factors, such as temperature and relative humidity.

Chapter 7

Summary & Future Works

This thesis has explored evaporation of sessile droplets on slippery surfaces. The experiments detailed in the results chapters have explored the optimisation and creation of reproducible SOCAL surfaces and shown they can evaporate in an ideal CCA mode of evaporation. Experimental techniques have been developed to allow the observation of voltage programmable contact angle on SOCAL surfaces for the first time. Electrowetting is employed as a tool to control the constant contact angle droplets on SLIPS and SOCAL evaporate at allowing control of the evaporation time of droplets using contact angle.

Optimisation of the experimental parameters used to create SOCAL have shown to reliably produce pinning-free, low hysteresis surfaces. The plasma treatment is found to be crucial to successful creation of surfaces. an envelope of low hysteresis is found at $5\,\mathrm{min}$ plasma time at $100\,\mathrm{W}$. Either increasing or decreasing the plasma time by a couple of minutes increases the hysteresis, and the reproducibility is unreliable with a large standard deviation in the contact-angle hysteresis ($\Delta\theta_{CAH} = 1.8 \pm 0.7°$). Changing the plasma power to $20\,\mathrm{W}$ opens this envelope to provide lower hysteresis and more repeatable results ($\Delta\theta_{CAH} = 0.4 \pm 0.2°$). Creating pinning-free low hysteresis SOCAL is an achievement which has not been widely replicated in research, with this work expanding upon the work of Wang & McCarthy enabling wider usage of SOCAL in research that requires improved droplet mobility [3].

The first experimental results chapter (Chapter 4: Evaporation on SOCAL surfaces) shows constant contact angle mode evaporation of sessile droplets of water for the first time on a smooth

flat solid surface. Experiments showed this result was valid for a broad range of relative humidities. This has allowed accurate calculations of the diffusion coefficient of water ($D_E = 2.44 \pm 0.48 \times 10^{-5}\,\mathrm{m^2\,s^{-1}}$) which is within 2% of the literature value. Because SOCAL surfaces are reported to be omniphobic and have low contact-angle hysteresis to a wide range of liquids, this work determining the diffusion coefficient of water suggests SOCAL could be used to determine the diffusion coefficient for a wide range of other liquids. An unexpected step-change increase in the constant contact angle observed when evaporating at relative humidities $\geq 40\%$. The step change was further verified by conducting additional experiments between 30-40% relative humidity. The step change is reminiscent of a type V adsorption isotherm, although, attempts to quantify this using DVS and QCM proved inconclusive. In future works, AFM could provide an opportunity to measure the adhesion forces of water molecules on the surface at different relative humidities to try and elucidate this effect. Evaporation is a widely studied field with many practical applications, specifically the evaporation of particle laden droplets and particle deposition, contact-line pinning is a widely documented challenge for such applications, one which SOCAL has the potential to address.

The second results chapter (Chapter 5: Electrowetting on SOCAL) shows successful manipulation of droplet contact angle using an applied voltage via electrowetting. Initial experiments showed PTFE to have a non-reversible electrowetting cycle due to contact-angle hysteresis. Hysteresis-free electrowetting cycles are then shown on SLIPS coated glass coverslips. These experiments inform electrowetting device design in conjunction with theory to select an appropriate dielectric thickness that will be thick enough to prevent dielectric breakdown while being thin enough to allow the contact angle to reduce to the electrowetting limit of contact angle saturation at $< 600\,\mathrm{V}$. SOCAL coated glass coverslips behaved unexpectedly compared to theory. There was a decrease in the contact angle after the first cycle, this decrease is larger than the receding angle expected in contact-angle hysteresis experiments on SOCAL. The salt type and concentration was varied to observe the effect on hysteresis. $0.01\,\mathrm{mol}\ \mathrm{CaCl_2}$ was found to have the lowest hysteresis, although, none of the tested concentrations or salt types effected the hysteresis as much as was being observed after the initial electrowetting cycle. The AC frequency was varied to see the effect on hysteresis, $10\,\mathrm{kHz}$ appeared to give the electrowetting curve with the least visible pinning, however the initial decrease in contact angle was still present. The rate of change in voltage was

studied to see if the contact-angle was simply not left enough time to recover to the original angle. While the rate prevented the contact angle to follow the same path during decreasing voltage as it took during increasing voltage, the contact angle was still lower than expected after the voltage was removed. The conclusion is that the parameters used in these experiments were still to fast to observe the quasi-static contact-angle/ voltage relationship expected from theory. These results help inform good experimental design for pinning-free electrowetting on SOCAL coated coverslips. It also seems clear that whilst SOCAL is virtually pinning-free (low to vanishing static friction) droplets moves slowly suggesting higher dynamic friction. This is unusual and contrasts with SLIPS, Further work could be done to investigate this.

The third and final results chapter (Chapter 6: Tunable Evaporaion on Slippery Surfaces) shows consant contact angle mode evaporation on SLIPS and SOCAL with tunable evaporation across a broad reange of contact angles $105°-65°$. This is the first report of CCA mode evaporation of sessile droplets of water at hydrophillic contact angles $\theta < 90°$. SOCAL and SLIPS coated devices are made from $100\,\mu\mathrm{m}$ glass dielectric coverslips, with an aluminium coating as a bottom contact. $8\,\mu\mathrm{L}$ $0.01\,\mathrm{mol}$ $\mathrm{CaCl_2}$ DI water droplets are placed on the device with a thin probe placed in the top of the droplet. The evaporation of the droplet is observed, measuring the base radius and contact angle while applying a fixed voltage $0 - 450\,\mathrm{V}$. Analysis of the evaporation sequences allows calculation of the diffusion coefficient for water to be recovered for both SLIPS and SOCAL using the standard sessile droplet diffusion model. This shows the effect of the electric field and the oil layer on the SLIPS sample are negligible. The he implied inhibition by the electric field of cloaking of a water droplet by silicone oil is also an interesting future topic. When comparing the average constant contact value obtained for a given voltage and the expected value from the Young-Lippmann equation for the given experimental parameters, both values are in good agreement. In experiments from the previous chapter, this result was not obtained for SOCAL, this result shows that the contact-angle will follow the expected value at long times. From the sessile droplet evaporation theory, it is possible to isolate the effect of the contact angle on the total evaporation time. This shows that for all contact angles below $\cos\theta < 0.75$ the contact angle has $< 10\%$ effect on the total evaporation time. The effect of the contact angle on the evaporation is at a minimum around $90°$ which can be achieved using electrowetting on slippery surfaces, this could prove a useful tool in applications where the total drying time is important such as inkjet printing.

The results of this thesis are important and directly applicable for applications which utilise sessile droplet evaporation, from heat transfer, to inkjet printing and DNA florescence in spotted micro arrays. Removing contact-line pinning is also a challenge in other other applications where the ability to easily move droplets on a surface is desired. This can include micro-fluidics, Surface Acoustic Wave (SAW) devices and self cleaning surfaces. At the time of writing, few labs have reported successful creation of low hysteresis SOCAL surfaces, hopefully this thesis provides an insight into how to optimise SOCAL creation and allow more widespread adoption in applications which will benefit from the removal of contact-line pinning. While the thesis focuses on the removal of pinning in sessile droplet evaporation and the control of the contact angle during evaporation, this work provides the foundations of further studies into evaporation on SOCAL, such as particle laden droplets and evaporation of other liquids and binary mixtures.

References

[1] T. Young, "An essay on the cohesion of fluids," *Philosophical Transactions of the Royal Society of London*, vol. 95, pp. 65–87, 1805.

[2] P.-G. de Gennes, F. Brochard-Wyart, and D. Quéré, *Capillarity and Wetting Phenomena*. New York, NY: Springer New York, 2004.

[3] L. Wang and T. J. McCarthy, "Covalently attached liquids: Instant omniphobic surfaces with unprecedented repellency," *Angewandte Chemie - International Edition*, vol. 55, no. 1, pp. 244–248, 2016.

[4] D. Bonn, J. Eggers, J. Indekeu, and J. Meunier, "Wetting and spreading," *Reviews of Modern Physics*, vol. 81, no. 2, pp. 739–805, 2009.

[5] E. Bertrand, D. Bonn, D. Broseta, H. Dobbs, J. O. Indekeu, J. Meunier, K. Ragil, and N. Shahidzadeh, "Wetting of alkanes on water," *Journal of Petroleum Science and Engineering*, vol. 33, no. 1-3, pp. 217–222, 2002.

[6] H. Y. Erbil, "Evaporation of pure liquid sessile and spherical suspended drops: A review," jan 2012.

[7] T. Lim, S. Han, J. Chung, J. T. Chung, S. Ko, and C. P. Grigoropoulos, "Experimental study on spreading and evaporation of inkjet printed pico-liter droplet on a heated substrate," *International Journal of Heat and Mass Transfer*, vol. 52, no. 1-2, pp. 431–441, 2009.

[8] M. C. Yuen and L. W. Chen, "Heat-transfer measurements of evaporating liquid droplets," *International Journal of Heat and Mass Transfer*, vol. 21, pp. 537–542, may 1978.

[9] M. S. Sadullah, G. Launay, J. Parle, R. Ledesma-Aguilar, Y. Gizaw, G. McHale, G. Wells, and H. Kusumaatmaja, "Bidirectional motion of droplets on gradient liquid infused surfaces," 2020.

[10] L. P. D, "Crc handbook of chemistry and physics," *Journal of Molecular Structure*, vol. 268, no. 1-3, p. 320, 1992.

[11] N. J. Shirtcliffe, G. McHale, S. Atherton, and M. I. Newton, "An introduction to superhydrophobicity," *Advances in Colloid and Interface Science*, vol. 161, no. 1-2, pp. 124–138, 2010.

[12] G. W. C. Kaye and T. H. Laby, *Kaye & Laby Tables of physical & chemical constants.* [Middlessex England]: National Physical Laboratory, web editio ed., 2005.

[13] H. Tavana, N. Petong, A. Hennig, K. Grundke, and A. W. Neumann, "Contact angles and coating film thickness," *Journal of Adhesion*, vol. 81, pp. 29–39, jan 2005.

[14] D. Quéré, "Wetting and roughness," *Annual Review of Materials Research*, vol. 38, no. 1, pp. 71–99, 2008.

[15] N. J. Shirtcliffe, G. McHale, and M. I. Newton, "The superhydrophobicity of polymer surfaces: Recent developments," *Journal of Polymer Science, Part B: Polymer Physics*, vol. 49, no. 17, pp. 1203–1217, 2011.

[16] P. Roach, N. J. Shirtcliffe, and M. I. Newton, "Progess in superhydrophobic surface development," *Soft Matter*, vol. 4, no. 2, pp. 224–240, 2008.

[17] A. B. D. Cassie and S. Baxter, "Wettability of porous surfaces," *Transactions of the Faraday Society*, vol. 40, p. 546, jan 1944.

[18] R. N. Wenzel, "Resistance of solid surfaces to wetting by water," *Industrial and Engineering Chemistry*, vol. 28, no. 8, pp. 988–994, 1936.

[19] G. McHale, "Wetting properties of surfaces and drag reduction," *Non-wettable Surfaces: Theory, Preparation, and Applications*, no. 5, pp. 253–284, 2017.

[20] P. G. De Gennes, "Wetting: Statics and dynamics," *Reviews of Modern Physics*, vol. 57, pp. 827–863, jul 1985.

[21] M. Singh, H. M. Haverinen, P. Dhagat, and G. E. Jabbour, "Inkjet printing-process and its applications," *Advanced Materials*, vol. 22, pp. 673–685, feb 2010.

[22] R. D. Deegan, O. Bakajin, T. F. Dupont, G. Huber, S. R. Nagel, and T. A. Witten, "Capillary flow as the cause of ring stains from dried liquid drops," *Nature*, vol. 389, pp. 827–829, oct 1997.

[23] P. J. Yunker, T. Still, M. A. Lohr, and A. G. Yodh, "Suppression of the coffee-ring effect by shape-dependent capillary interactions," *Nature*, vol. 476, pp. 308–311, aug 2011.

[24] C. N. Baroud, F. Gallaire, and R. Dangla, "Dynamics of microfluidic droplets," aug 2010.

[25] D. C. Leslie, A. Waterhouse, J. B. Berthet, T. M. Valentin, A. L. Watters, A. Jain, P. Kim, B. D. Hatton, A. Nedder, K. Donovan, E. H. Super, C. Howell, C. P. Johnson, T. L. Vu, D. E. Bolgen, S. Rifai, A. R. Hansen, M. Aizenberg, M. Super, J. Aizenberg, and D. E. Ingber, "A bioinspired omniphobic surface coating on medical devices prevents thrombosis and biofouling," *Nature Biotechnology*, vol. 32, pp. 1134–1140, oct 2014.

[26] S. Ling, Y. Luo, L. Luan, Z. Wang, and T. Wu, "Inkjet printing of patterned ultra-slippery surfaces for planar droplet manipulation," *Sensors and Actuators, B: Chemical*, vol. 235, pp. 732–738, nov 2016.

[27] H. B. Eral, D. J. C. M. 't Mannetje, and J. M. Oh, "Contact angle hysteresis: a review of fundamentals and applications," *Colloid and Polymer Science*, vol. 291, no. 2, pp. 247–260, 2013.

[28] C. Extrand and Y. Kumagai, "An experimental study of contact angle hysteresis," *Journal of Colloid and Interface Science*, vol. 191, pp. 378–383, jul 1997.

[29] L. Gao and T. J. McCarthy, "Contact angle hysteresis explained," *Langmuir*, vol. 22, no. 14, pp. 6234–6237, 2006.

[30] N. Gao, F. Geyer, D. W. Pilat, S. Wooh, D. Vollmer, H.-J. J. Butt, and R. Berger, "How drops start sliding over solid surfaces," *Nature Physics*, vol. 14, pp. 191–196, nov 2018.

[31] D. Daniel, J. V. Timonen, R. Li, S. J. Velling, M. J. Kreder, A. Tetreault, and J. Aizenberg, "Origins of extreme liquid repellency on structured, flat, and lubricated hydrophobic surfaces," *Physical Review Letters*, vol. 120, no. 24, p. 244503, 2018.

[32] O. V. Voinov, "Hydrodynamics of wetting," *Fluid Dynamics*, vol. 11, pp. 714–721, sep 1976.

[33] R. G. Cox, "The dynamics of the spreading of liquids on a solid surface. part 2. surfactants," *Journal of Fluid Mechanics*, vol. 168, pp. 195–220, 1986.

[34] R. A. Hayes and J. Ralston, "The molecular-kinetic theory of wetting," jan 1994.

[35] R. J. Plunkett, "Tetrafluoroethylene polymers," *U.S. Patent No. 2,230,654, issued 4 February 1941*, pp. 2–3, feb 1941.

[36] W. Barthlott and C. Neinhuis, "Purity of the sacred lotus, or escape from contamination in biological surfaces," *Planta*, vol. 202, pp. 1–8, apr 1997.

[37] C. Neinhuis and W. Barthlott, "Characterization and distribution of water-repellent, self-cleaning plant surfaces," *Annals of Botany*, vol. 79, no. 6, pp. 667–677, 1997.

[38] T. Onda, S. Shibuichi, N. Satoh, and K. Tsujii, "Super-water-repellent fractal surfaces," *Langmuir*, vol. 12, pp. 2125–2127, may 1996.

[39] J. Bico, C. Marzolin, and D. Quéré, "Pearl drops," *Europhysics Letters*, vol. 47, no. 2, pp. 220–226, 1999.

[40] D. Öner and T. J. McCarthy, "Ultrahydrophobic surfaces. effects of topography length scales on wettability," *Langmuir*, vol. 16, pp. 7777–7782, oct 2000.

[41] N. J. Shirtcliffe, G. McHale, M. I. Newton, G. Chabrol, and C. C. Perry, "Dual-scale roughness produces unusually water-repellent surfaces," *Advanced Materials*, vol. 16, no. 21, pp. 1929–1932, 2004.

[42] H. Y. Erbil, A. L. Demirel, Y. Avci, and O. Mert, "Transformation of a simple plastic into a superhydrophobic surface," *Science*, vol. 299, pp. 1377–1380, feb 2003.

[43] N. Geraldi, R. Morris, G. McHale, and M. Newton, "Snail deterrent properties of a soot based flexible superhydrophobic surface," in *1st International Electronic Conference on Materials*, p. a001, 2014.

[44] J. T. Luo, N. R. Geraldi, J. H. Guan, G. McHale, G. G. Wells, and Y. Q. Fu, "Slippery liquid-infused porous surfaces and droplet transportation by surface acoustic waves," *Physical Review Applied*, vol. 7, p. 014017, jan 2017.

[45] D. Wang, Q. Sun, M. J. Hokkanen, C. Zhang, F. Y. Lin, Q. Liu, S. P. Zhu, T. Zhou, Q. Chang, B. He, Q. Zhou, L. Chen, Z. Wang, R. H. Ras, and X. Deng, "Design of robust superhydrophobic surfaces," *Nature*, vol. 582, pp. 55–59, jun 2020.

[46] U. Bauer and W. Federle, "The insect-trapping rim of nepenthes pitchers: surface structure and function.," *Plant signaling & behavior*, vol. 4, pp. 1019–23, nov 2009.

[47] T.-S. Wong, S. H. Kang, S. K. Y. Tang, E. J. Smythe, B. D. Hatton, A. Grinthal, and J. Aizenberg, "Bioinspired self-repairing slippery surfaces with pressure-stable omniphobicity," *Nature*, vol. 477, no. 7365, pp. 443–447, 2011.

[48] J. D. Smith, R. Dhiman, S. Anand, E. Reza-Garduno, R. E. Cohen, G. H. McKinley, and K. K. Varanasi, "Droplet mobility on lubricant-impregnated surfaces," *Soft Matter*, vol. 9, no. 6, pp. 1772–1780, 2013.

[49] C. E. Stauffer, "The measurement of surface tension by the pendant drop technique," *Journal of Physical Chemistry*, vol. 69, no. 6, pp. 1933–1938, 1965.

[50] I. Pászli, I. Mohammed-Ziegler, and Z. Hórvögyi, "Obtaining surface tension from contact angle data by the individual representation approach," *Colloid and Polymer Science*, vol. 285, pp. 1009–1018, jun 2007.

[51] R. J. Good, "Contact angle, wetting, and adhesion: A critical review," *Journal of Adhesion Science and Technology*, vol. 6, no. 12, pp. 1269–1302, 1992.

[52] P. Lecomte Du Noüy, "An interfacial tensiometer for universal use," *Journal of General Physiology*, vol. 7, pp. 625–632, may 1925.

[53] C. Semprebon, G. McHale, and H. Kusumaatmaja, "Apparent contact angle and contact angle hysteresis on liquid infused surfaces," *Soft Matter*, vol. 13, no. 1, pp. 101–110, 2016.

[54] I. Langmuir, "Oil lenses on water and the nature of monomolecular expanded films," *The Journal of Chemical Physics*, vol. 1, pp. 756–776, nov 1933.

[55] R. Reeves, "Molecular theory of capillarity," *Journal of Electroanalytical Chemistry and Interfacial Electrochemistry*, vol. 167, no. 1-2, p. 325, 1984.

[56] Y. Jin, L. Zhang, and P. Wang, "Atmospheric water harvesting: Role of surface wettability and edge effect," *Global Challenges*, vol. 1, no. 4, p. 1700019, 2017.

[57] S. D. N. Lourenço, Y. Saulick, S. Zheng, H. Kang, D. Liu, H. Lin, and T. Yao, "Soil wettability in ground engineering: fundamentals, methods, and applications," *Acta Geotechnica*, vol. 13, pp. 1–14, feb 2018.

[58] T. Mizutani, U. Satake, and T. Enomoto, "Surgical diamond wheels for minimally invasive surgery in bone resection under small quantity of coolant supply," *Precision Engineering*, vol. 77, pp. 243–246, jan 2018.

[59] X. Wang, Z. Wang, L. Heng, and L. Jiang, "Stable omniphobic anisotropic covalently grafted slippery surfaces for directional transportation of drops and bubbles," *Advanced Functional Materials*, vol. 30, p. 1902686, jan 2020.

[60] H. Zhao, C. A. Deshpande, L. Li, X. Yan, M. J. Hoque, G. Kuntumalla, M. C Rajagopal, H. C. Chang, Y. Meng, S. Sundar, P. M. Ferreira, C. Shao, S. Salapaka, S. Sinha, and N. Miljkovic, "Extreme anti-scaling performance of slippery omniphobic covalently attached liquids," *ACS Applied Materials & Interfaces*, p. acsami.9b22145, feb 2020.

[61] T. Frommelt, M. Kostur, M. Wenzel-Schäfer, P. Talkner, P. Hänggi, and A. Wixforth, "Microfluidic mixing via acoustically driven chaotic advection," *Physical Review Letters*, vol. 100, no. 3, pp. 1–4, 2008.

[62] H. B. Eral, D. M. Augustine, M. H. Duits, and F. Mugele, "Suppressing the coffee stain effect: How to control colloidal self-assembly in evaporating drops using electrowetting," *Soft Matter*, vol. 7, pp. 4954–4958, may 2011.

[63] G. McHale, "Surface free energy and microarray deposition technology," 2007.

[64] A. Wixforth, C. Strobl, C. Gauer, A. Toegl, J. Scriba, and Z. V. Guttenberg, "Acoustic manipulation of small droplets," *Analytical and Bioanalytical Chemistry*, vol. 379, pp. 982–991, aug 2004.

[65] A.-M. Cazabat and G. Guéna, "Evaporation of macroscopic sessile droplets," *Soft Matter*, vol. 6, p. 2591, jun 2010.

[66] R. G. Larson, "Transport and deposition patterns in drying sessile droplets," *AIChE Journal*, vol. 60, pp. 1538–1571, may 2014.

[67] R. G. Picknett and R. Bexon, "The evaporation of sessile or pendant drops in still air," *Journal of Colloid And Interface Science*, vol. 61, no. 2, pp. 336–350, 1977.

[68] H. Y. Erbil, G. McHale, and M. M. I. Newton, "Drop evaporation on solid surfaces: Constant contact angle mode," *Langmuir*, vol. 18, pp. 2636–2641, apr 2002.

[69] J. M. Stauber, S. K. Wilson, B. R. Duffy, and K. Sefiane, "On the lifetimes of evaporating droplets with related initial and receding contact angles," *Physics of Fluids*, vol. 27, no. 12, p. 124102, 2015.

[70] G. McHale, S. Aqil, N. J. Shirtcliffe, M. I. Newton, and H. Y. Erbil, "Analysis of droplet evaporation on a superhydrophobic surface," *Langmuir*, vol. 21, pp. 11053–11060, nov 2005.

[71] X. Zhang, S. Tan, N. Zhao, X. Guo, X. Zhang, Y. Zhang, and J. Xu, "Evaporation of sessile water droplets on superhydrophobic natural lotus and biomimetic polymer surfaces," *ChemPhysChem*, vol. 7, pp. 2067–2070, oct 2006.

[72] M. L. McLauchlin, D. Yang, P. Aella, A. A. Garcia, S. T. Picraux, and M. A. Hayes, "Evaporative properties and pinning strength of laser-ablated, hydrophilic sites on lotus-leaf-like, nanostructured surfaces," *Langmuir*, vol. 23, no. 9, pp. 4871–4877, 2007.

[73] S.-x. Tan, X.-y. Zhang, N. Zhao, and J. Xu, "Simulation of sessile water-droplet evaporation on superhydrophobic polymer surfaces," *Chinese Journal of Chemical Physics*, vol. 20, pp. 140–144, apr 2007.

[74] Y. C. Jung and B. Bhushan, "Wetting behaviour during evaporation and condensation of water microdroplets on superhydrophobic patterned surfaces," *Journal of Microscopy*, vol. 229, pp. 127–140, jan 2008.

[75] S. Kulinich and M. Farzaneh, "Effect of contact angle hysteresis on water droplet evaporation from super-hydrophobic surfaces," *Applied Surface Science*, vol. 255, pp. 4056–4060, jan 2009.

[76] H. Gelderblom, Á. G. Marín, H. Nair, A. Van Houselt, L. Lefferts, J. H. Snoeijer, and D. Lohse, "How water droplets evaporate on a superhydrophobic substrate," *Physical Review E - Statistical, Nonlinear, and Soft Matter Physics*, vol. 83, p. 026306, feb 2011.

[77] J. H. Guan, G. G. Wells, B. Xu, G. McHale, D. Wood, J. Martin, and S. Stuart-Cole, "Evaporation of sessile droplets on slippery liquid-infused porous surfaces (slips)," *Langmuir*, vol. 31, pp. 11781–11789, nov 2015.

[78] M. Vallet, M. Vallade, and B. Berge, "Limiting phenomena for the spreading of water on polymer films by electrowetting," *European Physical Journal B*, vol. 591, pp. 583–591, 1999.

[79] F. Mugele and J.-C. Baret, "Electrowetting: from basics to applications," *Journal of Physics: Condensed Matter*, vol. 17, no. 28, pp. R705–R774, 2005.

[80] M. G. Pollack, R. B. Fair, and A. D. Shenderov, "Electrowetting-based actuation of liquid droplets for microfluidic applications," *Applied Physics Letters*, vol. 77, pp. 1725–1726, sep 2000.

[81] P. Paik, V. K. Pamula, M. G. Pollack, and R. B. Fair, "Electrowetting-based droplet mixers for microfluidic systems," *Lab on a Chip*, vol. 3, pp. 28–33, feb 2003.

[82] K. Xie, Y. Lai, X. Guo, and R. J. Campbell, "A three-phased circular electrode array for electro-osmotic microfluidic pumping," *Microsystem Technologies*, vol. 17, pp. 367–372, mar 2011.

[83] B. Berge and J. Peseux, "Variable focal lens controlled by an external voltage: An application of electrowetting," *European Physical Journal E*, vol. 3, no. 2, pp. 159–163, 2000.

[84] G. McHale, C. V. Brown, M. I. Newton, G. G. Wells, and N. Sampara, "Developing interface localized liquid dielectrophoresis for optical applications," in *Optical Design and Testing V* (Y. Wang, C. Du, H. Hua, K. Tatsuno, and H. P. Urbach, eds.), vol. 8557, p. 855703, SPIE, nov 2012.

[85] C. Hao, Y. Liu, X. Chen, Y. He, Q. Li, K. Y. Li, and Z. Wang, "Electrowetting on liquid-infused film (ewolf): Complete reversibility and controlled droplet oscillation suppression for fast optical imaging," *Scientific Reports*, vol. 4, no. 6846, 2014.

[86] E. Bormashenko, R. Pogreb, Y. Bormashenko, R. Grynyov, and O. Gendelman, "Low voltage reversible electrowetting exploiting lubricated polymer honeycomb substrates," *Applied Physics Letters*, vol. 104, p. 171601, apr 2014.

[87] F. Mugele and J. Heikenfeld, *Electrowetting: Fundamental Principles and Practical Applications*. Wiley VCH, 2019.

[88] X. Li, H. Tian, J. Shao, Y. Ding, X. Chen, L. Wang, and B. Lu, "Decreasing the saturated contact angle in electrowetting-on-dielectrics by controlling the charge trapping at liquid-solid interfaces," *Advanced Functional Materials*, vol. 26, pp. 2994–3002, may 2016.

[89] J. S. Hong, S. H. Ko, K. H. Kang, and I. S. Kang, "A numerical investigation on ac electrowetting of a droplet," *Microfluidics and Nanofluidics*, vol. 5, pp. 263–271, aug 2008.

[90] H. Lee, S. Yun, S. H. Ko, and K. H. Kang, "An electrohydrodynamic flow in ac electrowetting," *Biomicrofluidics*, vol. 3, no. 4, 2009.

[91] P. García-Sánchez, A. Ramos, and F. Mugele, "Electrothermally driven flows in ac electrowetting," *Physical Review E - Statistical, Nonlinear, and Soft Matter Physics*, vol. 81, jan 2010.

[92] T. B. Jones, K. L. Wang, and D. J. Yao, "Frequency-dependent electromechanics of aqueous liquids: Electrowetting and dielectrophoresis," *Langmuir*, vol. 20, pp. 2813–2818, mar 2004.

[93] Y. J. Li and B. P. Cahill, "Frequency dependence of low-voltage electrowetting investigated by impedance spectroscopy," *Langmuir*, vol. 33, pp. 13139–13147, nov 2017.

[94] G. McHale, C. V. Brown, M. I. Newton, G. G. Wells, and N. Sampara, "Dielectrowetting driven spreading of droplets," *Physical Review Letters*, vol. 107, p. 186101, oct 2011.

[95] Z. Brabcova, G. McHale, G. G. Wells, C. V. Brown, M. I. Newton, and A. M. J. Edwards, "Near axisymmetric partial wetting using interface-localized liquid dielectrophoresis," *Langmuir*, vol. 32, pp. 10844–10850, oct 2016.

[96] A. M. J. Edwards, R. Ledesma-Aguilar, M. I. Newton, C. V. Brown, and G. McHale, "Not spreading in reverse: The dewetting of a liquid film into a single drop.," *Science advances*, vol. 2, p. e1600183, sep 2016.

[97] A. Edwards, C. Brown, M. Newton, and G. McHale, "Dielectrowetting: The past, present and future," *Current Opinion in Colloid & Interface Science*, vol. 36, pp. 28–36, 2018.

[98] Z. Brabcova, G. McHale, G. G. Wells, C. V. Brown, and M. I. Newton, "Electric field induced reversible spreading of droplets into films on lubricant impregnated surfaces," *Applied Physics Letters*, vol. 110, no. 12, p. 121603, 2017.

[99] G. Sauerbrey, "Verwendung von schwingquarzen zur wägung dünner schichten und zur mikrowägung," *Zeitschrift für Physik*, vol. 155, no. 2, pp. 206–222, 1959.

[100] K. Keiji Kanazawa and J. G. Gordon, "The oscillation frequency of a quartz resonator in contact with liquid," *Analytica Chimica Acta*, vol. 175, pp. 99–105, jan 1985.

[101] C. Furmidge, "The sliding of liquid drops on solid surfaces and a theory for spray retention," *Journal of Colloid Science*, vol. 4, no. 17, pp. 309–324, 1962.

[102] D. Quéré, M. J. Azzopardi, and L. Delattre, "Drops at rest on a tilted plane," *Langmuir*, vol. 14, pp. 2213–2216, apr 1998.

[103] B. Liu, K. Zhang, C. Tao, Y. Zhao, X. Li, K. Zhu, and X. Yuan, "Strategies for anti-icing: Low surface energy or liquid-infused?," jul 2016.

[104] M. J. Kreder, D. Daniel, A. Tetreault, Z. Cao, B. Lemaire, J. V. Timonen, and J. Aizenberg, "Film dynamics and lubricant depletion by droplets moving on lubricated surfaces," *Physical Review X*, vol. 8, no. 3, 2018.

[105] V. Kumar and N. N. Sharma, "Synthesis of hydrophilic to superhydrophobic su8 surfaces," *Journal of Applied Polymer Science*, vol. 132, may 2015.

[106] L. Ejenstam, A. Swerin, and P. M. Claesson, "Toward superhydrophobic polydimethylsiloxane-silica particle coatings," *Journal of Dispersion Science and Technology*, vol. 37, pp. 1375–1383, sep 2016.

[107] G. McHale, B. V. Orme, G. G. Wells, and R. Ledesma-Aguilar, "Apparent contact angles on lubricant-impregnated surfaces/slips: From superhydrophobicity to electrowetting," *Langmuir*, vol. 35, pp. 4197–4204, mar 2019.

[108] B. V. Orme, G. McHale, R. Ledesma-Aguilar, and G. G. Wells, "Droplet retention and shedding on slippery substrates," *Langmuir*, vol. 35, no. 28, pp. 9146–9151, 2019.

[109] N. R. Geraldi, J. H. Guan, L. E. Dodd, P. Maiello, B. B. Xu, D. Wood, M. I. Newton, G. G. Wells, and G. McHale, "Double-sided slippery liquid-infused porous materials using conformable mesh," *Scientific Reports*, vol. 9, p. 13280, dec 2019.

[110] S. J. Goodband, S. Armstrong, H. Kusumaatmaja, and K. Voitchovsky, "Effect of ageing on the structure and properties of model liquid-infused surfaces," *Langmuir : the ACS journal of surfaces and colloids*, vol. 36, pp. 3461–3470, apr 2020.

[111] A. Keiser, L. Keiser, C. Clanet, and D. Quéré, "Drop friction on liquid-infused materials," *Soft Matter*, vol. 13, no. 39, pp. 6981–6987, 2017.

[112] L. Landau and B. Levich, "Dragging of a liquid by a moving plate," in *Dynamics of Curved Fronts*, pp. 141–153, Elsevier, jan 1988.

[113] B. Derjaguin, "On the thickness of the liquid film adhering to the walls of a vessel after emptying," *Progress in Surface Science*, vol. 43, pp. 134–137, may 1993.

[114] J. Seiwert, C. Clanet, and D. Quéré, "Coating of a textured solid," *Journal of Fluid Mechanics*, vol. 669, pp. 55–63, 2011.

[115] R. Blossey, "Self-cleaning surfaces - virtual realities," *Nature Materials*, vol. 2, pp. 301–306, may 2003.

[116] Y. H. Yeong, C. Wang, K. J. Wynne, and M. C. Gupta, "Oil-infused superhydrophobic silicone material for low ice adhesion with long-term infusion stability," *ACS Applied Materials and Interfaces*, vol. 8, pp. 32050–32059, nov 2016.

[117] A. K. Epstein, T. S. Wong, R. A. Belisle, E. M. Boggs, and J. Aizenberg, "Liquid-infused structured surfaces with exceptional anti-biofouling performance," *Proceedings of the National Academy of Sciences of the United States of America*, vol. 109, pp. 13182–13187, aug 2012.

[118] J. S. Wexler, I. Jacobi, and H. A. Stone, "Shear-driven failure of liquid-infused surfaces," *Physical Review Letters*, vol. 114, p. 168301, apr 2015.

[119] Y. Liu, J. S. Wexler, C. Schönecker, and H. A. Stone, "Effect of viscosity ratio on the shear-driven failure of liquid-infused surfaces," *Physical Review Fluids*, vol. 1, nov 2016.

[120] J. S. Wexler, A. Grosskopf, M. Chow, Y. Fan, I. Jacobi, and H. A. Stone, "Robust liquid-infused surfaces through patterned wettability," *Soft Matter*, vol. 11, no. 25, pp. 5023–5029, 2015.

[121] Z. Qiu, R. Qiu, Y. Xiao, J. Zheng, and C. Lin, "Slippery liquid-infused porous surface fabricated on cuzn: A barrier to abiotic seawater corrosion and microbiologically induced corrosion," *Applied Surface Science*, vol. 457, pp. 468–476, nov 2018.

[122] T. Xiang, M. Zhang, H. R. Sadig, Z. Li, M. Zhang, C. Dong, L. Yang, W. Chan, and C. Li, "Slippery liquid-infused porous surface for corrosion protection with self-healing property," *Chemical Engineering Journal*, vol. 345, pp. 147–155, aug 2018.

[123] V. Singh, Y. J. Sheng, and H. K. Tsao, "Self-healing atypical liquid-infused surfaces: Superhydrophobicity and superoleophobicity in submerged conditions," *Journal of the Taiwan Institute of Chemical Engineers*, vol. 97, pp. 96–104, apr 2019.

[124] P. Kim, T. S. Wong, J. Alvarenga, M. J. Kreder, W. E. Adorno-Martinez, and J. Aizenberg, "Liquid-infused nanostructured surfaces with extreme anti-ice and anti-frost performance," *ACS Nano*, vol. 6, pp. 6569–6577, aug 2012.

[125] C. S. Ware, T. Smith-Palmer, S. Peppou-Chapman, L. R. Scarratt, E. M. Humphries, D. Balzer, and C. Neto, "Marine antifouling behavior of lubricant-infused nanowrinkled polymeric surfaces," *ACS Applied Materials and Interfaces*, vol. 10, pp. 4173–4182, jan 2018.

[126] J. Li, E. Ueda, D. Paulssen, and P. A. Levkin, "Slippery lubricant-infused surfaces: Properties and emerging applications," *Advanced Functional Materials*, vol. 29, jan 2019.

[127] Y. Zhang, L. Zhang, Z. Xiao, S. Wang, and X. Yu, "Fabrication of robust and repairable superhydrophobic coatings by an immersion method," *Chemical Engineering Journal*, vol. 369, pp. 1–7, aug 2019.

[128] G. Launay, "pyDSA," *https://framagit.org/gabylaunay/pyDSA_gui*, jun 2019.

[129] K. Scientific, "Drop shape analyzer-dsa25," *https://www.kruss-scientific.com/en/products-services/products/dsa25s*, dec 2020.

[130] Sigma-Aldrich, "Syringe needle gauge chart," *https://www.sigmaaldrich.com/chemistry/stockroom-reagents/learning-center/technical-library/needle-gauge-chart.html*, 2015.

[131] M. Vuckovac, M. Latikka, K. Liu, T. Huhtamäki, and R. H. Ras, "Uncertainties in contact angle goniometry," *Soft Matter*, vol. 15, no. 35, pp. 7089–7096, 2019.

[132] J. Canny, "A computational approach to edge detection," *IEEE Transactions on Pattern Analysis and Machine Intelligence*, vol. PAMI-8, no. 6, pp. 679–698, 1986.

[133] A. Bateni, S. S. Susnar, A. Amirfazli, and A. W. Neumann, "A high-accuracy polynomial fitting approach to determine contact angles," *Colloids and Surfaces A: Physicochemical and Engineering Aspects*, vol. 219, pp. 215–231, jun 2003.

[134] E. Atefi, J. A. Mann, and H. Tavana, "A robust polynomial fitting approach for contact angle measurements," *Langmuir*, vol. 29, pp. 5677–5688, may 2013.

[135] M. A. Quetzeri-Santiago, J. R. Castrejón-Pita, and A. A. Castrejón-Pita, "On the analysis of the contact angle for impacting droplets using a polynomial fitting approach," *Experiments in Fluids*, vol. 61, p. 143, jun 2020.

[136] G. McHale, S. M. Rowan, M. I. Newton, and M. K. Banerjee, "Evaporation and the wetting of a low-energy solid surface," *The Journal of Physical Chemistry B*, vol. 102, no. 11, pp. 1964–1967, 1998.

[137] H. Y. Erbil and M. Dogan, "Determination of diffusion coefficient-vapor pressure product of some liquids from hanging drop evaporation," *Langmuir*, vol. 16, no. 24, pp. 9267–9273, 2000.

[138] S. David, K. Sefiane, and L. Tadrist, "Experimental investigation of the effect of thermal properties of the substrate in the wetting and evaporation of sessile drops," *Colloids and Surfaces A: Physicochemical and Engineering Aspects*, vol. 298, no. 1-2, pp. 108–114, 2007.

[139] K. S. W. Sing, "Reporting physisorption data for gas/solid systems with special reference to the determination of surface area and porosity (provisional)," *Pure and Applied Chemistry*, vol. 57, pp. 603–619, jan 1982.

[140] J. L. Pérez-Díaz, M. A. Álvarez-Valenzuela, and J. C. García-Prada, "The effect of the partial pressure of water vapor on the surface tension of the liquid water-air interface," *Journal of Colloid and Interface Science*, vol. 381, no. 1, pp. 180–182, 2012.

[141] E. Portuguez, A. Alzina, P. Michaud, M. Oudjedi, and A. Smith, "Evolution of a water pendant droplet: Effect of temperature and relative humidity," *Natural Science*, vol. 09, no. 01, pp. 1–20, 2017.

[142] C. T. Burkhart, K. L. Maki, and M. J. Schertzer, "Coplanar electrowetting-induced droplet detachment from radially symmetric electrodes," 2020.

[143] S. Armstrong, G. McHale, R. A. Ledesma-Aguilar, and G. G. Wells, "Pinning-free evaporation of sessile droplets of water from solid surfaces," *Langmuir*, vol. 35, pp. 2989–2996, feb 2019.

[144] A. G. Banpurkar, K. P. Nichols, and F. Mugele, "Electrowetting-based microdrop tensiometer," *Langmuir*, vol. 24, pp. 10549–10551, oct 2008.

[145] J. M. Stauber, S. K. Wilson, B. R. Duffy, and K. Sefiane, "On the lifetimes of evaporating droplets," *Journal of Fluid Mechanics*, vol. 744, p. R2, apr 2014.

Published Works

1. S. Armstrong, G. McHale, R. A. Ledesma-Aguilar, and G. G. Wells, "Pinning-Free Evaporation of Sessile Droplets of Water from Solid Surfaces," Langmuir, vol. 35, no. 8, pp. 2989–2996, Feb. 2019, doi: 10.1021/acs.langmuir.8b03849.

2. S. J. Goodband, S. Armstrong, H. Kusumaatmaja, and K. Voitchovsky, "Effect of Ageing on the Structure and Properties of Model Liquid-Infused Surfaces," Langmuir, Apr. 2020, doi: 10.1021/acs.langmuir.0c00059.

3. S. Armstrong, G. McHale, R. A. Ledesma-Aguilar, and G. G. Wells, "Evaporation and Electrowetting of Sessile Droplets on Slippery Liquid-like Surfaces and Slippery Liquid-Infused Porous Surfaces (SLIPS)," Langmuir, Sep. 2020, doi: 10.1021/acs.langmuir.0c02020

4. R. McCerery, J. Woodward, G. McHale, K. Winter, S. Armstrong, B. V. Orme "Slippery Liquid-Infused Porous Surfaces: The Effect of Oil on the Water Repellency of Hydrophobic and Superhydrophobic Soils" European Journal of Soil Science, Sep. 2020, doi: 10.1111/ejss.13053

LANGMUIR Article
Cite This: Langmuir 2019, 35, 2989−2996
pubs.acs.org/Langmuir

Pinning-Free Evaporation of Sessile Droplets of Water from Solid Surfaces

Steven Armstrong, Glen McHale,* Rodrigo Ledesma-Aguilar, and Gary G. Wells

Smart Materials & Surfaces Laboratory, Faculty of Engineering & Environment, Northumbria University, Newcastle upon Tyne NE1 8ST, U.K.

ABSTRACT: Contact-line pinning is a fundamental limitation to the motion of contact lines of liquids on solid surfaces. When a sessile droplet evaporates, contact-line pinning typically results in either a stick−slip evaporation mode, where the contact line pins and depins from the surface in an uncontrolled manner, or a constant contact-area mode with a pinned contact line. Pinning prevents the observation of the quasi-equilibrium constant contact-angle mode of evaporation, which has never been observed for sessile droplets of water directly resting on a smooth, nontextured, solid surface. Here, we report the evaporation of a sessile droplet from a flat glass substrate treated with a smooth, slippery, omniphobic covalently attached liquid-like coating. Our characterization of the surfaces shows high contact line mobility with an extremely low contact-angle hysteresis of ∼1° and reveals a step change in the value of the contact angle from 101° to 105° between a relative humidity (RH) of 30 and 40%, in a manner reminiscent of the transition observed in a type V adsorption isotherm. We observe the evaporation of small sessile droplets in a chamber held at a constant temperature, $T = (25.0 \pm 0.1)$ °C and at constant RH across the range RH = 10−70%. In all cases, a constant contact-angle mode of evaporation is observed for most of the evaporation time. Furthermore, we analyze the evaporation sequences using the Picknett and Bexon ideal constant contact-angle mode for diffusion-limited evaporation. The resulting estimate for the diffusion coefficient, D_E, of water vapor in air of $D_E = (2.44 \pm 0.48) \times 10^{-5}$ m^2 s^{-1} is accurate to within 2% of the value reported in the literature, thus validating the constant contact-angle mode of the diffusion-limited evaporation model.

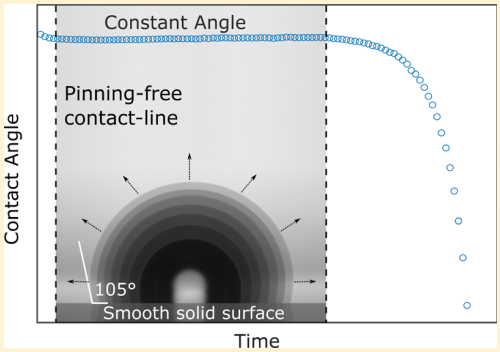

1. INTRODUCTION

Evaporation of liquids occurs when the atmosphere surrounding the liquid is not saturated with the vapor of the liquid.[1] It is a widely observed natural phenomenon and is important for many applications, including inkjet printing,[2] fuel delivery,[3] and heat exchange.[4] In these applications, droplets rest on a solid surface and this introduces two fundamental differences as to how evaporation occurs compared to spherical droplets in free space far from any surface. First, the spherical symmetry for diffusion of vapor into the space around the droplet is broken by the presence of the surface. Second, droplet contact with a surface introduces contact-line pinning, which can be problematic, for example, causing nonuniform deposition of colloidal particles as in the well-known formation of coffee-ring stains.[5] Nonuniform particle deposition causes problems in a diverse range of applications, from nonuniform delivery of the active components in aerosols used in pesticides to nonuniform fluorescence in spotted microarrays.[1,5−8] While, the effect on diffusion of a surface can be modeled, contact-line pinning is usually an unavoidable consequence of the contact between a droplet and the surface to which it is attached.

When a droplet is in contact with a solid surface, and at thermodynamic equilibrium, the contact angle that the droplet makes with the surface, θ_e, in principle, is determined by the interfacial tension of the three interfaces as described by Young's law[9]

$$\cos\theta_e = \frac{\gamma_{SV} - \gamma_{SL}}{\gamma_{LV}} \quad (1)$$

where γ_{SV} is the solid−vapor interfacial tension, γ_{SL} is the solid−liquid interfacial tension, and γ_{LV} is the liquid−vapor interfacial tension. When a droplet is small compared to its capillary length $\kappa^{-1} = (\gamma_{LV}/\rho g)^{1/2}$, where ρ is the density of the liquid and $g = 9.81$ m s^{-2}, it adopts an axisymmetric spherical cap shape when the surface is flat and smooth with no contact-line pinning. However, in practice, contact-line pinning has always been observed to some extent. Picknett and Bexon provided an analytical model describing the ideal case of diffusion-limited evaporation of a sessile droplet in the absence of gravity.[10] Their analysis includes two ideal modes of evaporation.[10] The first corresponds to a constant contact radius (CCR) mode, where the apparent contact angle decreases during evaporation. Because the CCR mode of evaporation requires complete pinning of the contact line, it

Received: November 15, 2018
Revised: January 28, 2019
Published: January 31, 2019

DOI: 10.1021/acs.langmuir.8b03849
Langmuir 2019, 35, 2989−2996

can be achieved experimentally and has been widely studied.[1] The second mode is a constant contact angle (CCA) mode evaporation, where the contact angle is expected to retain a constant value approximating the contact angle predicted by Young's law, while the square of the base radius of the droplet decreases linearly in time.

The observation of the CCA mode evaporation on a smooth (nontextured) flat solid surface remains elusive because it requires complete mobility of the contact line, and the roughness of ordinary flat solid surfaces always results in some contact-line pinning. Contact-line pinning is quantified experimentally by the so-called contact-angle hysteresis: the difference between the advancing and receding contact angles of the droplet. Instead, many experimental studies have reported a stick−slip mode of evaporation, whereby the droplet's contact line is repeatedly pinned until the force from the out-of-equilibrium contact angle increases sufficiently and a depinning event and rapid contact-line motion occurs. Stauber et al. have also detailed another mode of evaporation known as the stick−slide mode of evaporation, where the contact line and contact angle decrease at the same time. They provide a model to predict the lifetime of evaporating drops in stick−slide mode evaporation.[11] Recent comprehensive reviews of sessile drop evaporation are given by Erbil,[1] Cazabat and Guéna,[12] and Larson.[13]

Attempts to experimentally observe the CCA mode of evaporation have included the use of superhydrophobic surfaces and slippery liquid-infused porous surfaces (SLIPS), sometimes referred to as liquid-infused surfaces.[14,15] Superhydrophobic surfaces take advantage of surface texture to suspend droplets in a Cassie−Baxter state[16] on a small solid surface fraction, thereby reducing the droplet−solid contact area, increasing its contact angle and reducing contact-angle hysteresis.[17−19] McHale et al.[20] reported the first experiments of this type using SU-8 textured surfaces with water droplets initially evaporating in CCR mode evaporation, before retreating in a step-wise fashion as the droplet jumps between micropillars and ultimately converting into a Wenzel state, where the droplet is impaled in the texture with a completely pinned contact line.[21] Since then, many works studying evaporation on super hydrophobic surfaces and the effect of contact angle hysteresis has been reported.[22−27] In all of these studies, the surface is no longer smooth but is textured or rough and hydrophobic, with a contact angle far from the value given by Young's law for a smooth nontextured solid surface.

A second approach to observing a CCA mode of evaporation was introduced by Guan et al. who used a SLIPS approach, with a lubricant oil impregnated into a hydrophobic SU-8 textured surface.[28] The lubricant oil completely coats the solid and is immiscible to water, therefore, is not displaced by it. SLIPS enable droplets to slide at tilt angles of less than 1°. However, the high mobility of droplets on SLIPS arises by the replacement of the droplet−solid interface by a droplet−lubricant interface and the removal of all direct contact between the droplet and the solid. On SLIPS, contact angles and contact radii have to be interpreted as apparent contact angles and apparent contact radii from the change in slope of the droplet close to the surface. Guan et al. were able to observe the pinning-free evaporation of water droplets on SLIPS and interpret their evaporation using the Picknett and Bexon diffusion-limited model, modified for the presence of a wetting ridge of the impregnated oil, which surrounds the droplet's base.[28] Ultimately, neither of these two approaches have provided observation of the evaporation of sessile droplets on flat smooth (nontextured) solid surfaces without contact-line pinning. A key challenge remains the ability to remove contact-line pinning during evaporation of sessile droplets from nontextured solid surfaces.

Recently, Wang and McCarthy have reported a method to create slippery omniphobic covalently attached liquid-like (SOCAL) surfaces with contact-angle hysteresis less than 1°.[29] SOCAL surfaces use polydimethylsiloxane (PDMS) chains grafted to the substrate. The chains are flexible and have the ability to move independently of each other. This flexibility results in a completely mobile contact line on the solid that enables droplets to move across a surface with virtually no pinning. Importantly, SOCAL is a covalently attached layer, rather than a liquid coating retained by a surface texture as occurs in SLIPS. It also provides a coating that is on the nanometric scale as opposed to the micrometric scale of SLIPS, allowing for a clearly defined contact angle for a sessile droplet on the coated flat smooth solid surface. The report by Wang and McCarthy of smooth low-hysteresis surfaces via a liquid-like coating with advancing and receding water contact angles of θ_A = 104.6° and θ_R = 103.6° and tilt angles for motion of 4.7° and 1.3° for droplet volumes of 3 and 20 μL, respectively,[29] has been noted by a range of researchers, but few have implemented the method. Jin et al. reported SOCAL contact angles of θ_A = 103.0° and θ_R = 98.2° on silicon substrates[30] and Mizutani et al. have reported grafting SOCAL to surgical diamond wheels for minimally invasive bone surgery, and they also grafted SOCAL to a nickel substrate with a static contact angle θ_s = 94.1° and a sliding angle of 40°.[31] Daniel et al. also reported dissipative force acting on a droplet moving on several types of low-hysteresis surfaces, including a SOCAL surface (prepared following the Wang and McCarthy method) with a minimum critical tilt angle between 5° and 15° to move a 10 μL water droplet but with no values reported for their advancing or receding contact angles.[32]

Here, we report experiments of the evaporation of sessile droplets of water on SOCAL-coated glass surfaces with contact-angle hysteresis of less than 1° over a wide range of relative humidity (RH, from 10 to 70%). In Section 2.1, we describe preparation of SOCAL coatings with highly reproducible contact angles ∼101°−105° and low contact-angle hysteresis $\Delta\theta_{CAH} \approx 1°$. In Section 3, we report data showing the CCA mode evaporation for small sessile water droplets; we consistently measure contact angles close to the static values, and within the bounds expected from the measured and extremely low contact-angle hysteresis. In Section 4, we discuss the entire evaporation sequence including a step change in the observed value of the CCA that occurs at RH between 30 and 40%. Finally, we use the Picknett and Bexon model to analyze the evaporation of individual droplets and provide a set of estimates of the diffusion coefficient. By comparing the evaporation rate to the RH across all experiments, we obtain a second estimate of the diffusion coefficient. Both types of estimate are within 2% of the literature value and show how SOCAL surfaces, which are omniphobic, provide a simple but accurate methodology to determine the diffusion coefficient of volatile liquids.

2. EXPERIMENTAL METHOD

2.1. SOCAL Preparation. SOCAL surfaces were created on 25 × 75 mm glass slides, using the method detailed by Wang and McCarthy, adapted to our specific equipment and with process

DOI: 10.1021/acs.langmuir.8b03849
Langmuir 2019, 35, 2989−2996

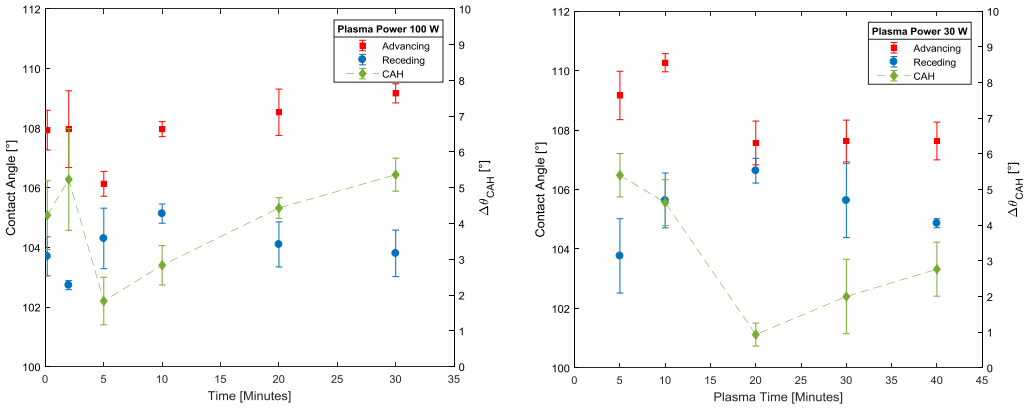

Figure 1. Contact-angle hysteresis ($\Delta\theta_{CAH}$) as a function of plasma time. (Left) shows $\Delta\theta_{CAH}$ as a function of time for 100 W plasma power. (Right) shows $\Delta\theta_{CAH}$ as a function of time for 30 W. The green dashed line is a guide to the eye.

parameters iteratively developed until a reproducible and low contact-angle hysteresis method was achieved.[29] Our optimized method used clean glass slides placed into a Henniker plasma cleaner (HPT-100) at 30% power for 20 min. This step adds OH bonds to the surface. The slide was then dipped into a reactive solution of isopropanol, dimethyldimethoxysilane, and sulphuric acid (90, 9, and 1% wt) for 5 s, and then slowly withdrawn. The slides were then placed in a bespoke humidity-controlled environment at 60% RH and 25 °C for 20 min. During this step, an acid-catalyzed graft polycondensation of dimethyldimethoxysilane creates a homogeneous layer of PDMS grafted to the surface. Unreacted material was then rinsed away with deionized (DI) water, isopropanol, and toluene.

We found that to reliably produce SOCAL surfaces with low contact-angle hysteresis, the following parameters need to be carefully controlled and optimized: plasma exposure time; the RH at which the reaction takes place and the reaction time. With the plasma cleaner set to 100 W power and varying the treatment duration from 30 s to 30 min, we found a minimum in the contact-angle hysteresis occurs at 5 min plasma time ($\Delta\theta_{CAH}$ = 1.8 ± 0.7°). Although very low, this contact-angle hysteresis is larger than previously reported by Wang and McCarthy.[29] By reducing the plasma power to 30 W, we were able to reduce the time sensitivity and achieve $\Delta\theta_{CAH}$ = (0.9 ± 0.3°) with 20 min plasma cleaning time (Figure 1). To assess the reproducibility and the uniformity of results across a surface, the contact-angle hysteresis for each change in the process parameter was assessed using advancing and receding contact-angle measurements taken at three different locations on the surface; the average of the results across all the three locations is reported with its standard deviation.

2.2. Contact-Angle Measurements. Contact-angle measurements of droplets of water on the SOCAL surfaces were carried out using a Krüss drop shape analyzer (DSA 30) and Krüss DSA4 software. A 4 μL droplet of DI water was dispensed onto the surface at room temperature (20−25 °C). A video sequence at 5 frames per s captured the inflation and deflation of the droplet to determine advancing and receding contact angles. The droplet was inflated by 2 μL at 20 μL/min, left to stabilize for 5 s, and then, 2 μL was withdrawn at 1 μL/min. A slow withdrawal speed was used for contact-angle hysteresis measurements to limit the risk that the measured angles were dynamic angles. In all reported measurements, the advancing angle, θ_A, is the angle immediately before the droplet radius begins to increase. Similarly, the receding angle, θ_R, is the angle immediately before the droplet radius begins to decrease. Each reported contact-angle hysteresis value, $\Delta\theta_{CAH} = (\theta_A - \theta_R)$, is the average of contact-angle hysteresis values measured at three different locations on the SOCAL-treated glass slide.

2.3. Evaporation Experimental Procedure. Small (4.0 ± 0.3 μL) droplets of room-temperature DI water (type III, purified in an Elga PURELAB Option-Q lab water purification system) were deposited on a SOCAL-treated glass slide, in a commercial humidity and temperature-controlled chamber (TC30) that had been equilibrated at (25 ± 0.1) °C, attached to a Krüss (DSA 25). The evaporation of the droplets was observed for a range of RH from 10 to 70% (±0.5%) in intervals of 10%. A further sequence of evaporation experiments refined the RH range between 30 and 40% in steps of 2%. The evolution of the contact angle and the contact radius as a function of time were recorded using a Krüss drop shape analyzer (DSA 25), with time-lapse image capture at 10 s intervals (Figure 2). The data and images for each evaporation sequence were analyzed individually to verify the absence of contact-line pinning.

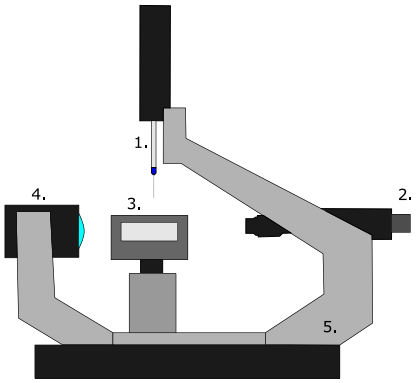

Figure 2. Diagram of experimental setup for evaporation. (1) Automatic syringe dosing unit. (2) Camera with macro lens and barrel. (3) Humidity and temperature-controlled chamber (TC30). (4) Light-emitting diode backlight. (5) Krüss DSA 25.

The contact radius was calculated by identifying the contact base line using the eye; the Krüss Advance software package then tracks the drop radius throughout the evaporation. The contact angle was evaluated using an elliptical fit in the Krüss Advance software, which uses the tangent of the ellipse intersecting the contact base line. This gives a mean contact angle from the average of the left and right contact angle. Because SOCAL is a transparent coating, we were also able to confirm that droplets on the surfaces retained an axisymmetric shape during evaporation by conducting control experiments using the simultaneous side profile and bottom up views.

Data presented in this paper show typical curves for each RH obtained from the average of three repeated evaporations. The data for each RH was averaged into 100 equally spaced bins for each measured quantity (elapsed time, contact angle, contact radius). All of the experiments were carried out on five separately made SOCAL-treated glass slides at various locations on the slides. The different humidity experiments were carried out nonsequentially to ensure that no aging effects were observed.

DOI: 10.1021/acs.langmuir.8b03849
Langmuir 2019, 35, 2989−2996

3. EXPERIMENTAL RESULTS

3.1. Typical Evaporation Sequence. Figure 3 shows the contact angle θ, and contact area, πr^2, as a function of time during a typical

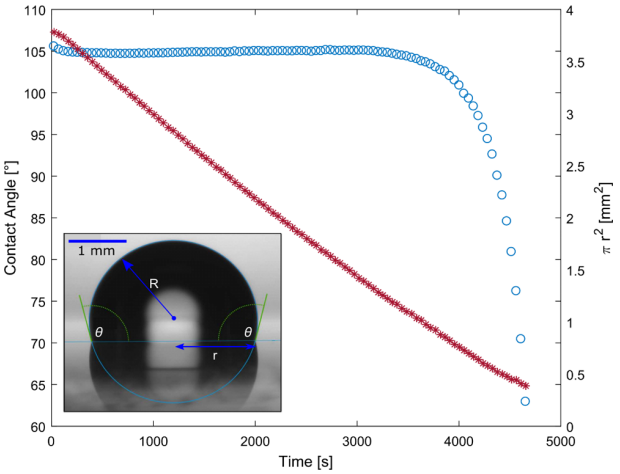

Figure 3. Typical evaporation showing the contact angle (ooo) and contact area (***) as a function of time. The conditions of this typical evaporation are a 4 μL droplet of DI water, 25 °C, and 70% RH. The inset shows the ellipse fitting of the droplet to measure the contact angle (θ), contact radius (r), and spherical radius (R).

sessile droplet evaporation sequence. After short initial relaxation, when a droplet is deposited, a CCA is observed for the majority of the evaporation time. During the CCA period, the contact area reduces linearly with time. The short initial relaxation is likely to be due to the droplet equilibrating to the surface, temperature, and RH (e.g., see McHale et al.[33]). The final stage of evaporation appears to be correlated to the observation of mineral deposit formation when the droplet radius reduced to ~0.5 mm, which is the radius at which the contact angle first begins to decrease.

3.2. Influence of RH. The CCA mode of evaporation occurs across a broad range of RH (10−70%). Figure 4 illustrates a typical evaporation at the lowest and highest values of RH. Even though these extremes in RH result in significantly different total evaporation times of 23 min and 2 h 15 min, the droplet evaporation sequences demonstrate the same behavior. The presence of the syringe (seen at the top of each image in Figure 4) illustrates that an evaporating droplet remains centered, close its initial deposition location, from the start to end of their evaporation. This provides confidence that the droplet contact line is completely mobile and free from pinning at all locations around the droplet.

Figure 5 shows a full set of sessile droplet evaporation sequences across the range of RH from 10 to 70% in steps of 10% and using the volume as the horizontal axis to collapse all the data onto a single plot. The central inset in Figure 5 reveals that the CCA during evaporation has two distinct values. The contact angle in the range of the RH of 10−30% is 101° while in the range of the RH of 30−40%, there is a

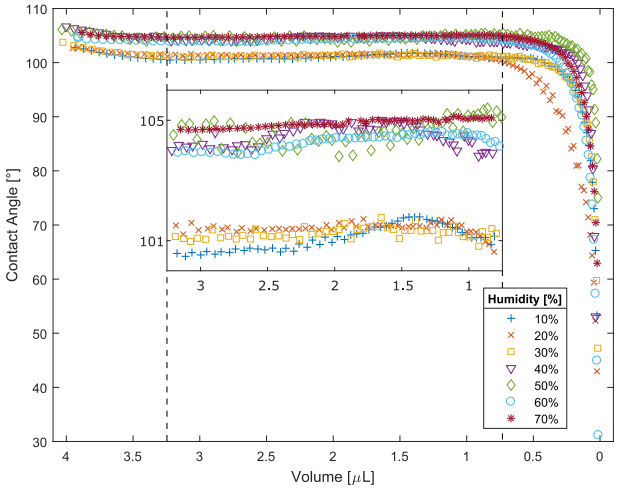

Figure 5. Contact angle as a function of volume. The dashed lines indicate the CCA mode of evaporation. The central inset is a magnification of the CCA mode evaporation, showing the two contact angles for low (10−30%) and high (40−70%) RH.

sharp rise in the CCA to 104.5°, which remains the value observed for the range from 40 to 70%. The step nature of this transition is further detailed in Figure 6, which presents data for the RH range 30−40%

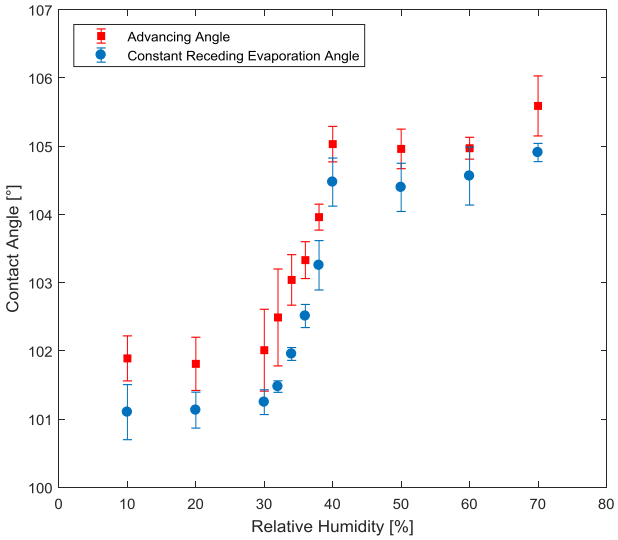

Figure 6. Step change in the value of the CCA for evaporation at different RH values.

using steps in the RH of 2%. Advancing angle measurements were carried out at each RH value to confirm the surface retained low

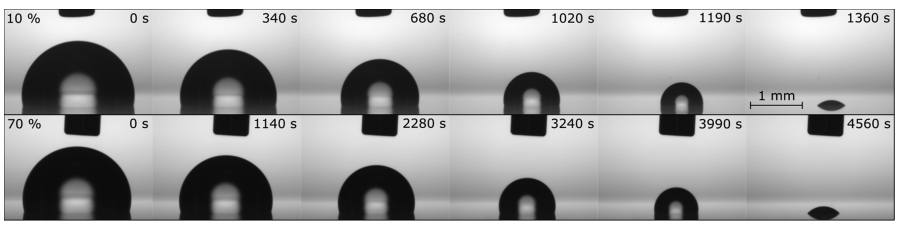

Figure 4. Evaporation time lapse at 10 and 70% RH. The syringe needle is kept in the image to show the droplets evaporate, moving radially inward in all directions.

DOI: 10.1021/acs.langmuir.8b03849
Langmuir 2019, 35, 2989−2996

contact-angle hysteresis despite this step change in the contact angle. Evaporation causes the contact line to retreat slower than a needle withdrawing liquid; therefore, the receding angle at a given RH is the angle observed during evaporation of liquid at that RH. Contact-angle hysteresis estimated using the constant receding angle during evaporation and the measured advancing contact angle prior to evaporation was largest at RH = 34% with $\Delta\theta_{CAH} = (1.09 \pm 0.27)^\circ$ and lowest at RH = 60% with $\Delta\theta_{CAH} = (0.41 \pm 0.16^\circ)$. Figure 6 shows $\Delta\theta_{CAH}$ remains low for both contact angle regimes with $\Delta\theta_{CAH} < 2^\circ$.

4. ANALYSIS AND DISCUSSION

We first focus on the qualitative features of typical evaporation sequences. After a droplet is deposited, there is an immediate and short duration initial relaxation of the contact angle. The decrease in the contact angle could be due to changes in temperature as evaporation establishes itself and evaporative cooling of the droplet and substrate occurs. For isolated evaporating spherical drops, the cooling is determined by the evaporation rate,[34] and this will also occur for sessile droplets with the evaporative cooling correlated to the RH, which controls the rate of evaporation. In addition, thermal properties of the substrate will influence how effectively thermal energy can be supplied to maintain the temperature of the substrate surface. For example, Sefiane et al. show a link between the cooling effect on a droplet and the thermal properties of the substrate.[35] A further possibility is that evaporation creates a local RH which, given the contact angle is over 90°, may be important for the precise value of the contact angle because of the confined wedge space defined by the droplet and the substrate near the contact line. The simplest interpretation is that, although the contact-angle hysteresis is very small, an evaporating droplet is simply adopting a receding contact angle, which is slightly lower (1−2°) than its initial value on deposition.

The initial relaxation is then followed by a CCA period that dominates the overall evaporation time. An unexpected feature in our data is the apparent separation into two distinct values of the CCA of 101° and 104.5° for this CCA evaporation mode. This step change for RH between 30 and 40% is shown in Figure 6 and is reminiscent of the shape of a type V adsorption isotherm.[36] These two contact angle values can be compared to the 0.6° increase in contact-angle hysteresis at the lower RH values quantified using measurements via addition and withdrawal of liquid to a droplet. We excluded the step change being a consequence of a dynamic contact angle, defined by the speed of retreat of the contact line, by conducting receding contact-angle measurement by withdrawal of liquid at different rates. We can also consider possible origins of the step change using Young's law (eq 1), for which there are two interfacial tensions, γ_{LV} and γ_{SV}, that depend on the vapor. The first of these, the surface tension γ_{LV}, is known from pendant drop measurements to have a smooth change with temperature and RH over the range used in our experiments (72.2−75.5 mN m^{-1}).[37,38] However, the second of these, the solid−vapor interfacial tension γ_{SV}, is a candidate for the origin of a step change in the observed contact angle. This might occur if a film of vapor condensed on the solid over the narrow 30−40% range of RH, thereby replacing the solid−vapor interface by solid−liquid and liquid−vapor interfaces. To consider this possibility, we attempted to measure mass change on a SOCAL-coated glass surface using a dynamic vapor sorption (DVS) method, but unfortunately, it was not possible to obtain reliable results because of the small relative changes in mass. We also visually observed changes in reflectivity with RH changes using a glass surface which had half of its area treated with the SOCAL coating but did not observe any change indicating condensation had occurred. Another possibility is that the solid−vapor interfacial tension changes because of the adsorption of a monolayer of vapor. This could cause an increase in the contact angle as the RH increases, as observed experimentally, because of increased cohesion of the water molecules and, hence, a decrease in the solid−vapor interfacial tension γ_{SV}. A further possibility is that adsorption of a monolayer of water vapor could cause a step change in the mobility of the PDMS chains in the SOCAL coating for RH above and below the 30−40% range. From these possibilities, vapor adsorption appears to be the most likely reason for the step change in the contact angle with increasing RH.

In the very final stages of evaporation, the contact angle reduces rapidly and after the droplet had completely evaporated, we observed deposits were present over an area corresponding to that at which the contact angle first began to reduce. We therefore verified that the water we used did not contain solid particles. Energy-dispersive X-ray spectroscopy and scanning electron microscopy analysis of these deposits showed them to be composed of NaCl, AlCl, MgCl, and KCl. This suggests trace amounts of salts precipitated out of water at a volume of 0.6 ± 0.1 μL, and their deposition on the SOCAL-coated glass surface then created a self-pinning effect.

We now focus on a quantitative analysis of the evaporation sequences. Consider a sphere of liquid suspended in air far from any surface for which the rate of change in its volume due to diffusion-limited evaporation is given by

$$\frac{dV}{dt} = \frac{4\pi RD\Delta c}{\rho} \tag{2}$$

where V is volume, R is the spherical radius of the droplet, D is the diffusion coefficient of water vapor in air, Δc is the difference between the vapor concentration close to the droplet and far away ($\Delta c = c_0 - c_\infty$), and ρ is the density of the liquid. Here, the rate of change of volume arises from the net flux at the liquid−vapor interface integrated over the free surface of the droplet as discussed in the review by Cazabat and Guéna.[12] The same droplet resting on a solid surface will adopt a spherical cap shape, provided it is smaller than the capillary length, which for water is κ^{-1} = 2.73 mm, and its contact area is not prevented by contact-line pinning from adopting a circular shape. Geometrically, this shape is defined by its contact angle, θ, with the surface and a contact radius r, as illustrated in the inset to Figure 3. Knowing these two parameters enables the volume of a spherical cap to be calculated using

$$V = \frac{\pi}{3}\frac{(\cos\theta - 1)^2(2 + \cos\theta)r^3}{\sin^3\theta} \tag{3}$$

Other geometrical parameters, such as the spherical radius, R, can also be calculated

$$R = \left(\frac{3V}{\pi(2 - 3\cos\theta + \cos^3\theta)}\right)^{1/3} \tag{4}$$

In addition to the change in the droplet geometry from spherical to spherical cap, diffusion-limited evaporation is also influenced by the change in space into which vapor can diffuse. Thus, a completely spherical droplet with a contact angle of

DOI: 10.1021/acs.langmuir.8b03849
Langmuir 2019, 35, 2989−2996

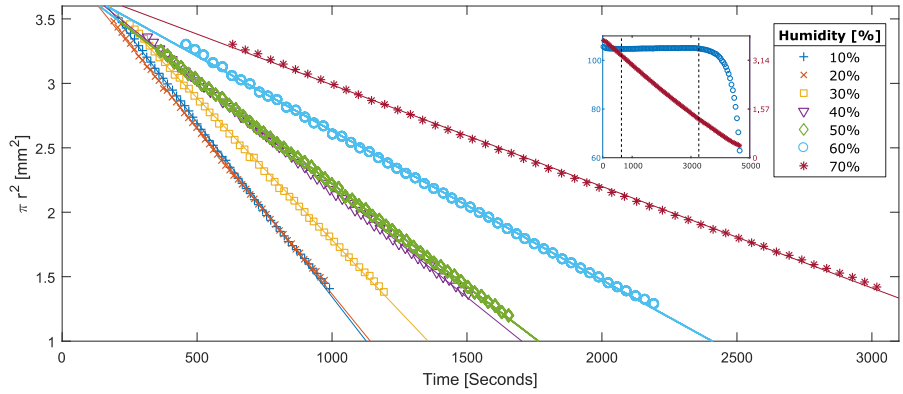

Figure 7. Contact area πr^2 as a function of time for evaporations at RH 10−70%. The line through each data set represents the linear fit used to calculate D_{RH}. The inset shows the representative contact angle and contact area as a function of time, where the data between the dashed lines show the section of the evaporation that is the CCA mode.

180° just touching in the flat solid surface does not evaporate as fast as a spherical droplet far from the surface. Picknett and Bexon considered sessile droplet evaporation and provided an exact closed-form solution for its diffusion-limited evaporation, which has a similar form to eq 2 but with an additional factor, $f(\theta)$, which is a function of the contact angle

$$\frac{dV}{dt} = \frac{4\pi RD\Delta c}{\rho} f(\theta) \tag{5}$$

To aid numerical calculations, they provided polynomial fits to $f(\theta)$, covering the full contact-angle range. For our experiments, the appropriate polynomial fit is for angles between $10° < \theta < 180°$ and is

$$f_{PB}(\theta) = \frac{1}{2}(0.00008957 + 0.6333\theta + 0.116\theta^2 - 0.8878\theta^3 + 0.01033\theta^4) \tag{6}$$

where θ is in radians. Because the droplets in our experiments conform to spherical caps, and unlike the work of Guan et al. on SLIPS[28] there is no wetting ridge present, these equations can be used directly to analyze our data. For the CCA mode with side profile observations providing both contact angle and contact radius, the most appropriate equation arises by substituting eq 3 into eq 5 to give

$$\frac{d(\pi r^2)}{dt} = \frac{8\pi D\Delta c \sin^2\theta f_{PB}(\theta)}{\rho(\cos\theta - 1)^2(2 + \cos\theta)} \tag{7}$$

As the right-hand side of eq 7 does not depend on time for the CCA mode of evaporation, the contact area should reduce linearly with time.

Figure 7 shows representative data for sessile droplet evaporation on our SOCAL surfaces for each value of RH (10−70%) and each can be seen to provide excellent agreement with a linear fit; the inset in Figure 7 illustrates the time range used to define the CCA range. From the slopes in Figure 7, the diffusion coefficient for each RH, D_{RH}, has been calculated using eq 6 and is shown in Table 1. These values of D_{RH} range from 2.31×10^{-5} to 2.87×10^{-5} m^2 s^{-1} with an average of $(2.58 \pm 0.20) \times 10^{-5}$ m^2 s^{-1}, which compares well to the literature value of 2.48×10^{-5} m^2 s^{-1}.[39]

Figure 7 provides confidence that we have observed CCA mode evaporation, which is diffusion-limited, and Table 1 confirms that the extracted diffusion coefficients from each RH

Table 1. Calculated Diffusion Coefficient for Each RH Compared to the Literature Value

RH [%]	$d\pi r^2/dt$ [mm^2 s^{-1}]	D_{RH} [$\times 10^{-5}$ m^2 s^{-1}]	D literature [$\times 10^{-5}$ m^2 s^{-1}]
10	−0.002699	2.47	2.48
20	−0.002513	2.58	2.48
30	−0.002202	2.58	2.48
40	−0.001678	2.44	2.48
50	−0.001640	2.87	2.48
60	−0.001297	2.82	2.48
70	−0.000754	2.31	2.48
	average	**2.58 ± 0.20**	**2.48**

are consistent with the literature values. However, because the diffusion coefficient should not depend on the RH, rearranging eq 7 and relating the RH to vapor concentration by $\Delta c = c_0((RH/100) - 1)$, allows a single estimated diffusion coefficient, D_E, to be calculated using all experiments across the range of RH 10−70%

$$\frac{\rho(\cos\theta - 1)^2(2 + \cos\theta)}{8\pi\Delta c \sin^2\theta f_{PB}(\theta)} \frac{d(\pi r^2)}{dt} = D_E\left(\frac{RH}{100} - 1\right) \tag{8}$$

Figure 8 shows data from Figure 7 plotted using eq 8, and the gradient from this gives an estimate of the diffusion coefficient of $D_E = (2.44 \pm 0.48) \times 10^{-5}$ m^2 s^{-1}, which is an improved estimate compared to the single RH estimates and which is within 2% of the literature value.

Finally, because Wang and McCarthy have reported that SOCAL surfaces are omniphobic and have low contact-angle hysteresis to a wide range of liquids, including diiodomethane, toluene, hexadecane, cyclohexane, decane, and hexane,[29] the accuracy of our evaporation method of determining the diffusion coefficient for water suggests that a SOCAL-coated glass surface could be used to determine the diffusion coefficients for a wide range of other liquids.

5. CONCLUSIONS

In this work, we have shown it is possible to observe the CCA evaporation mode on a flat smooth (nontextured) solid surface by creating SOCAL-coated surfaces with extremely low contact-angle hysteresis. This differs from previous attempts to observe the CCA mode, which have relied on the use of

DOI: 10.1021/acs.langmuir.8b03849
Langmuir 2019, 35, 2989−2996

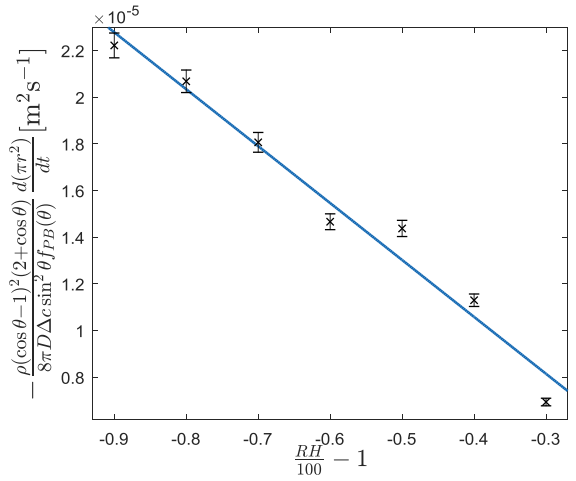

Figure 8. $d\pi r^2/dt$ as a function of RH. The gradient of the plot gives the calculated diffusion coefficient D_E.

textured solid surfaces, or a lubricant oil that removes all contacts with a solid surface. We have also observed a step change in the CCA value occurring in a narrow range of RH (30−40%), which is indicative of the adsorption of water vapor on the surface and reminiscent of a type V isotherm. The value of the CCA during evaporation has been shown to be consistent with the ideal contact angle from Young's law estimated by using independent measurements of the advancing and receding contact angle. Quantitative analysis of the sessile droplet evaporation sequences provides accurate measurements of the diffusion constant of the evaporating liquid. Hence, this methodology can provide a simple and reliable way to characterize the volatility of a wide range of other liquids.

AUTHOR INFORMATION

Corresponding Author

*E-mail: glen.mchale@northumbria.ac.uk.

ORCID

Steven Armstrong: 0000-0002-0520-8498

Glen McHale: 0000-0002-8519-7986

Rodrigo Ledesma-Aguilar: 0000-0001-8714-0556

Notes

The authors declare no competing financial interest.

ACKNOWLEDGMENTS

The authors gratefully acknowledge Professor Chris Hardacre and Huan Xiang from the School of Chemical Engineering & Analytical Science, University of Manchester, for assistance with DVS measurements and discussion of the results and Professor Doris Vollmer (Max Planck Institute for Polymer Research, Mainz) for discussion on the SOCAL method. R.L.-A. acknowledges support from EPSRC (grant no. EP/P024408/1). S.A. would also like to acknowledge Dr. G. Launay, Dr. E. Ruiz-Gutierrez, Dr. P. Agrawal and H. Barrio-Zhang for valuable advice and technicals support. S.A. would also like to acknowledge Northumbria University at Newcastle for financial support.

REFERENCES

(1) Erbil, H. Y. Evaporation of Pure Liquid Sessile and Spherical Suspended Drops: A Review. *Adv. Colloid Interface Sci.* **2012**, *170*, 67−86.

(2) Lim, T.; Han, S.; Chung, J.; Chung, J. T.; Ko, S.; Grigoropoulos, C. P. Experimental Study on Spreading and Evaporation of Inkjet Printed Pico-Liter Droplet on a Heated Substrate. *Int. J. Heat Mass Transf.* **2009**, *52*, 431−441.

(3) Li, T.; Xu, M.; Hung, D.; Wu, S.; Cheng, S. Understanding the Effects of Fuel Type and Injection Conditions on Spray Evaporation Using Optical Diagnostics. *2015 SAE World Congress and Exhibition*; SAE Technical Paper Series, 2015 April (March).

(4) Yuen, M. C.; Chen, L. W. Heat-Transfer Measurements of Evaporating Liquid Droplets. *Int. J. Heat Mass Transf.* **1978**, *21*, 537−542.

(5) Deegan, R. D.; Bakajin, O.; Dupont, T. F.; Huber, G.; Nagel, S. R.; Witten, T. A. Capillary Flow as the Cause of Ring Stains from Dried Liquid Drops. *Nature* **1997**, *389*, 827−829.

(6) McHale, G. Surface Free Energy and Microarray Deposition Technology. *Analyst* **2007**, *132*, 192−195.

(7) Frommelt, T.; Kostur, M.; Wenzel-Schäfer, M.; Talkner, P.; Hänggi, P.; Wixforth, A. Microfluidic Mixing via Acoustically Driven Chaotic Advection. *Phys. Rev. Lett.* **2008**, *100*, 034502.

(8) Eral, H. B.; Augustine, D. M.; Duits, M. H. G.; Mugele, F. Suppressing the Coffee Stain Effect: How to Control Colloidal Self-Assembly in Evaporating Drops Using Electrowetting. *Soft Matter* **2011**, *7*, 4954−4958.

(9) Young, T. III. An Essay on the Cohesion of Fluids. *Philos. Trans. R. Soc. London* **1805**, *95*, 65−87.

(10) Picknett, R. G.; Bexon, R. The Evaporation of Sessile or Pendant Drops in Still Air. *J. Colloid Interface Sci.* **1977**, *61*, 336−350.

(11) Stauber, J. M.; Wilson, S. K.; Duffy, B. R.; Sefiane, K. On the Lifetimes of Evaporating Droplets with Related Initial and Receding Contact Angles. *Phys. Fluids* **2015**, *27*, 122101.

(12) Cazabat, A.-M.; Guéna, G. Evaporation of Macroscopic Sessile Droplets. *Soft Matter* **2010**, *6*, 2591.

(13) Larson, R. G. Transport and Deposition Patterns in Drying Sessile Droplets. *AIChE J.* **2014**, *60*, 1538−1571.

(14) Wong, T.-S.; Kang, S. H.; Tang, S. K. Y.; Smythe, E. J.; Hatton, B. D.; Grinthal, A.; Aizenberg, J. Bioinspired Self-Repairing Slippery Surfaces with Pressure-Stable Omniphobicity. *Nature* **2011**, *477*, 443−447.

(15) Smith, J. D.; Dhiman, R.; Anand, S.; Reza-Garduno, E.; Cohen, R. E.; McKinley, G. H.; Varanasi, K. K. Droplet Mobility on Lubricant-Impregnated Surfaces. *Soft Matter* **2013**, *9*, 1772−1780.

(16) Cassie, A. B. D.; Baxter, S. Wettability of Porous Surfaces. *Trans. Faraday Soc.* **1944**, *40*, 546.

(17) Onda, T.; Shibuichi, S.; Satoh, N.; Tsujii, K. Super-Water-Repellent Fractal Surfaces. *Langmuir* **1996**, *12*, 2125−2127.

(18) Barthlott, W.; Neinhuis, C. Purity of the Sacred Lotus, or Escape from Contamination in Biological Surfaces. *Planta* **1997**, *202*, 1−8.

(19) Shirtcliffe, N. J.; McHale, G.; Atherton, S.; Newton, M. I. An Introduction to Superhydrophobicity. *Adv. Colloid Interface Sci.* **2010**, *161*, 124−138.

(20) McHale, G.; Aqil, S.; Shirtcliffe, N. J.; Newton, M. I.; Erbil, H. Y. Analysis of Droplet Evaporation on a Superhydrophobic Surface. *Langmuir* **2005**, *21*, 11053−11060.

(21) Wenzel, R. N. Resistance of Solid Surfaces to Wetting by Water. *Ind. Eng. Chem.* **1936**, *28*, 988−994.

(22) Zhang, X.; Tan, S.; Zhao, N.; Guo, X.; Zhang, X.; Zhang, Y.; Xu, J. Evaporation of Sessile Water Droplets on Superhydrophobic Natural Lotus and Biomimetic Polymer Surfaces. *ChemPhysChem* **2006**, *7*, 2067−2070.

(23) McLauchlin, M. L.; Yang, D.; Aella, P.; Garcia, A. A.; Picraux, S. T.; Hayes, M. A. Evaporative Properties and Pinning Strength of Laser-Ablated, Hydrophilic Sites on Lotus-Leaf-Like, Nanostructured Surfaces. *Langmuir* **2007**, *23*, 4871−4877.

DOI: 10.1021/acs.langmuir.8b03849
Langmuir 2019, 35, 2989−2996

(24) Tan, S.-x.; Zhang, X.-y.; Zhao, N.; Xu, J. Simulation of Sessile Water-Droplet Evaporation on Superhydrophobic Polymer Surfaces. *Chin. J. Chem. Phys.* **2007**, *20*, 140−144.
(25) Jung, Y. C.; Bhushan, B. Wetting Behaviour during Evaporation and Condensation of Water Microdroplets on Superhydrophobic Patterned Surfaces. *J. Microsc.* **2008**, *229*, 127−140.
(26) Kulinich, S. A.; Farzaneh, M. Effect of Contact Angle Hysteresis on Water Droplet Evaporation from Super-Hydrophobic Surfaces. *Appl. Surf. Sci.* **2009**, *255*, 4056−4060.
(27) Gelderblom, H.; Marín, Á. G.; Nair, H.; van Houselt, A.; Lefferts, L.; Snoeijer, J. H.; Lohse, D. How Water Droplets Evaporate on a Superhydrophobic Substrate. *Phys. Rev. E: Stat., Nonlinear, Soft Matter Phys.* **2011**, *83*, 026306.
(28) Guan, J. H.; Wells, G. G.; Xu, B.; McHale, G.; Wood, D.; Martin, J.; Stuart-Cole, S. Evaporation of Sessile Droplets on Slippery Liquid-Infused Porous Surfaces (SLIPS). *Langmuir* **2015**, *31*, 11781−11789.
(29) Wang, L.; McCarthy, T. J. Covalently Attached Liquids: Instant Omniphobic Surfaces with Unprecedented Repellency. *Angew. Chem., Int. Ed.* **2015**, *55*, 244−248.
(30) Jin, Y.; Zhang, L.; Wang, P. Atmospheric Water Harvesting: Role of Surface Wettability and Edge Effect. *Glob. Challenges* **2017**, *1*, 1700019.
(31) Mizutani, T.; Enomoto, T.; Satake, U. Surgical diamond wheels for minimally invasive surgery in bone resection under saline supply. *Precis. Eng.* **2018**, *77*, 243−246.
(32) Daniel, D.; Timonen, J. V. I.; Li, R.; Velling, S. J.; Kreder, M. J.; Tetreault, A.; Aizenberg, J. Origins of Extreme Liquid Repellency on Structured, Flat, and Lubricated Hydrophobic Surfaces. *Phys. Rev. Lett.* **2018**, *120*, 244503.
(33) McHale, G.; Rowan, S. M.; Newton, M. I.; Banerjee, M. K. Evaporation and the Wetting of a Low-Energy Solid Surface. *J. Phys. Chem. B* **1998**, *102*, 1964−1967.
(34) Erbil, H. Y.; Dogan, M. Determination of Diffusion Coefficient−Vapor Pressure Product of Some Liquids from Hanging Drop Evaporation. *Langmuir* **2000**, *16*, 9267−9273.
(35) David, S.; Sefiane, K.; Tadrist, L. Experimental Investigation of the Effect of Thermal Properties of the Substrate in the Wetting and Evaporation of Sessile Drops. *Colloids Surf., A* **2007**, *298*, 108−114.
(36) Sing, K. S. W. Reporting Physisorption Data for Gas/solid Systems with Special Reference to the Determination of Surface Area and Porosity (Recommendations 1984). *Pure Appl. Chem.* **1985**, *57*, 603−619.
(37) Pérez-Díaz, J. L.; Álvarez-Valenzuela, M. A.; García-Prada, J. C. The Effect of the Partial Pressure of Water Vapor on the Surface Tension of the Liquid Water-Air Interface. *J. Colloid Interface Sci.* **2012**, *381*, 180−182.
(38) Portuguez, E.; Alzina, A.; Michaud, P.; Oudjedi, M.; Smith, A. Evolution of a Water Pendant Droplet: Effect of Temperature and Relative Humidity. *Nat. Sci.* **2017**, *09*, 1−20.
(39) Lide, D. R. *CRC Handbook of Chemistry and Physics: A Ready Reference Book of Chemical and Physical Data*, 1992; Vol. *268*.

DOI: 10.1021/acs.langmuir.8b03849
Langmuir 2019, 35, 2989−2996

LANGMUIR

pubs.acs.org/Langmuir Article

Effect of Ageing on the Structure and Properties of Model Liquid-Infused Surfaces

Sarah J. Goodband, Steven Armstrong, Halim Kusumaatmaja,* and Kislon Voïtchovsky*

Cite This: *Langmuir* 2020, 36, 3461−3470 Read Online

ACCESS | Metrics & More | Article Recommendations | Supporting Information

ABSTRACT: Liquid-infused surfaces (LISs) exhibit unique properties that make them ideal candidates for a wide range of applications, from antifouling and anti-icing coatings to self-healing surfaces and controlled wetting. However, when exposed to realistic environmental conditions, LISs tend to age and progressively lose their desirable properties, potentially compromising their application. The associated ageing mechanisms are still poorly understood, and results reflecting real-life applications are scarce. Here, we track the ageing of a model LIS composed of glass surfaces functionalized with hydrophobic nanoparticles and infused with silicone oil. The LISs are fully submerged in aqueous solutions and exposed to acoustic pressure waves for set time intervals. The ageing is monitored by periodic measurements of the LIS's wetting properties. We also track the changes to the LIS's nanoscale structure. We find that the LISs rapidly lose their slippery properties because of a combination of oil loss, smoothing of the nanoporous functional layer, and substrate degradation when directly exposed to the solution. The oil loss is consistent with water microdroplets entering the oil layer and displacing oil away from the surface. These mechanisms are general and could play a role in the ageing of most LISs.

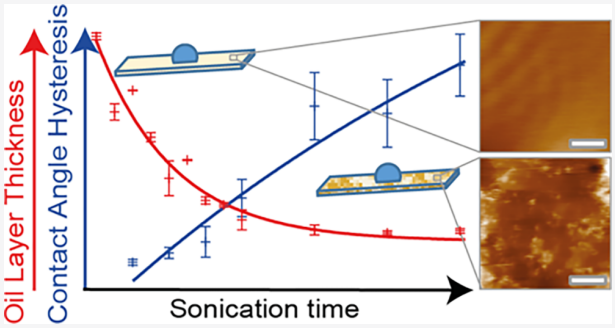

INTRODUCTION

Liquid-infused surfaces (LISs) represent a family of functional surfaces inspired by the Nepenthes pitcher plant whose porous outer surface is imbibed with a lubricating liquid. This effectively replaces the plant's exposed outer surface with a fluid layer that creates a slippery surface able to shed liquid droplets and trap insects.[1] LISs are of considerable economical interest because they provide a nontoxic method for preventing the fouling and corrosion of surfaces by blocking the attachment of organisms or blocking direct interaction between the solid support and the outside environment.[2,3] Potential applications range from reducing the natural fouling of buildings, windows, transport vehicles, and underwater structures (e.g., rigs, turbines, water treatment systems, and power plants) to preventing biofilm formation on the surface of medical devices and implants.[4−7] Moreover, LISs have been shown to be anti-icing[8−10] and self-healing,[2,11] exhibit low roll-off angles[12] and drag reduction,[13] present a high optical transparency,[2,9] and may be used for fog-harvesting applications.[14]

Regardless of the intended application, all designs of LISs have to meet three main criteria: (1) the chemical affinity between the lubricating fluid and the solid should be higher than that between the ambient fluid and the solid, (2) the solid should preferably be roughened so as to increase the surface area for the adhesion of the lubricating fluid and its immobilization, and (3) the lubricating fluid and the ambient fluid must be largely immiscible.[2,3] Since the initial development of LISs,[2,15−17] many different geometries and materials have been proposed for the porous substructure and lubricating fluid. These include the development of flexible surfaces from self-assembling polymers[18] or using novel ferrofluids to infuse surfaces.[19] Experimental advances have further been complemented by theoretical studies to examine ideal geometries and the interplay of the infused liquid with supported liquid droplets moving across the LIS.[20−22]

While there is abundant research investigating the design of LISs, their ageing and wear is often overlooked despite it being considered one of the biggest problem facing self-cleaning surfaces.[23] When available, studies typically examine LIS ageing during static storage in air or in solution at room temperature,[10] or under steady external perturbations on a freshly made LIS.[3,24−26] Durability is assessed in terms of substrate recovery after damage incidents (such as incision or impact in the infused layer),[4,5,27] oil loss, and the ageing of surfaces under soaking conditions. Generally, LISs retain their

Received: January 8, 2020
Revised: March 12, 2020
Published: March 13, 2020

https://dx.doi.org/10.1021/acs.langmuir.0c00059
Langmuir 2020, 36, 3461−3470

slippery properties[8,28,29] provided the oil layer is not depleted, and periodic reimmersion in oil has been shown to allow most LISs to regain their self-healing properties and high droplet mobility.[30] Indeed, in nature, the nepenthes pitcher plant exhibits a unique system of continuous liquid transport, which is used to allow the surface to retains its slippery properties.[31] Synthetic mimics have also been designed to replicate this spreading behavior.[32−34]

This suggests the integrity of the infused oil layer to be the single most important factor; upon oil depletion, LISs progressively lose their antifouling properties and biomaterial is able to attach.[28] Several mechanisms may be responsible for the oil loss, including exposure to shear flows,[24−26] failure under gravity,[26] and aqueous droplet cloaking by the oil resulting in the LIS material being carried away.[35]

In this study, we investigate the ageing of a model LIS exposed to an environment that aims to mimic real-life applications such as waves in the sea, rain falling, or localized impacts. This is achieved by immersing our model LIS in aqueous solutions and exposing them to ultrasonic pressure waves. The use of well-defined ultrasonic waves ensures a reproducible but accelerated LIS ageing compared to ambient laboratory conditions. This strategy enables us to identify some of the mechanisms responsible for the oil loss and degradation of the porous layer, including the impact of dissolved salt ions in the aqueous solution that are in contact with the LIS. Significantly, we track the functional evolution of the ageing LIS and link it to nanoscale changes that occur within the different LIS components. We do this by combining macroscopic contact angle (CA) and CA hysteresis (CAH) measurements with atomic force microscopy (AFM) of the porous and liquid-infused surface. This approach allows for a systematic study into the effects of ageing across different length scales.

EXPERIMENTAL METHODS

Preparation of LIS Substrates. Glass slides were prepared following a literature protocol as described elsewhere.[36] Briefly, glass substrates were cleaned using Decon 90 (Sigma-Aldrich-Merck, Gillingham, UK), followed by alternating steps of rinsing and sonication (30 min bursts) in ultrapure water (18.2 MΩ, Merck-Millipore, Hertfordshire, UK). The slides were then left to dry in air. Subsequent rinsing of the slides was carried out consecutively in acetone (purity 99% (Emplura), Sigma-Aldrich-Merck, Gillingham, UK) and isopropanol (purity 99.8%, Fisher Scientific, Loughborough, UK) and dried under a stream of nitrogen. After 30 min in air, a layer of hydrophobized nanoparticles (NPs) was sprayed evenly across the slide surface (GLACO spray, SOFT 99 Corp. Japan) and left to dry for 60 min. Additional layers were applied every hour until a total of five coats was achieved unless otherwise specified. A drop (0.5 mL) of silicone oil (20 cSt @ 25 °C, Sigma-Aldrich-Merck, Gillingham, UK) was then placed at the center of the slides and immediately spin-coated (1000 rpm 1 min, then 500 rpm 1 min). Slides were used fresh, and any storage (outside ageing) was done with the slides placed in Petri-dishes with closed lids at ambient temperatures.

Preparation of the Dichlorodimethylsilane Hydrophobized Glass Substrate. Glass slides were hydrophobized with dichlorodimethylsilane (DMS) to serve in control experiments. The preparation followed established protocol.[37] Slides were soaked sequentially in acetone and isopropanol, each for a minimum of 30 min. They were then dried using a stream of nitrogen, plasma-cleaned for 15 min (>30 W, VacuLAB-X, Tantec, UK), and subsequently dehydrated in an oven at 100 °C for 60 min. The slides were then immediately placed inside a desiccator next to 1 mL of DMS placed in an open dish. The desiccator was then placed under vacuum overnight to allow for DMS vapor deposition on the slides. After functionalization, the slides were rinsed with acetone and ultrapure water and dried overnight at 40 °C.

Ageing Using Static Soaking. Freshly prepared NP-functionalized slides and the LIS were placed in a sealed beaker containing either ultrapure water or a 600 mM NaCl solution. The samples were removed periodically to make CA measurements or for nanoscale imaging with AFM.

Accelerated Ageing Using Sonication. Samples were placed in a beaker containing either ultrapure water or a 600 mM NaCl solution and sonicated in bursts of 1 min, using a VWR, USC-TH bath sonicator (VWR, Lutterworth, UK). The ultrasonic bath operates at 45 kHz and has an average output power of 180 W. Using a bespoke liquid displacement sensor built from piezo-ceramic bi-morph (RS PRO Vibration Sensor, model 285-784, RS Components, Northants, NN17 9RS, UK), it was possible to estimate the average ultrasonication power at the location of the sample, yielding a value of 800 ± 400 Wm^{-2}. The associated oscillatory displacement velocity of the aqueous solution at the sample's surface is in the order of 8 ms^{-1}. Details about the setup geometry and the deduction of the above estimations are presented in the Supporting Information (Section S1 and Figure S1). Similar to static ageing, samples were removed periodically to make CA measurements or for nanoscale imaging with AFM.

High-resolution AFM imaging. In order to fit into the AFM chamber, glass slides were cut into small (<10 mm) pieces and epoxy-glued to steel disks (12 mm, SPI Supplies, West Chester, USA) before undergoing the ageing procedures described above (either sonication or soaking). AFM imaging was carried out in amplitude modulation using a commercial Cypher ES equipped with photothermal excitation of the cantilever (Asylum Research, Oxford Instruments, Santa Barbara, CA, USA). Imaging was carried out in air or in the aqueous solutions using Arrow-UFHAuD-10 cantilevers (nominal stiffness of 1 N/m, Nanoworld, Neuchatel, Switzerland). Image optimization was achieved following established protocol.[38]

CA and CAH Measurements. All CA images were captured using a portable digital microscope (Dino-lite Edge) and analyzed using the ImageJ freeware, in particular FIJI plugins Dropsnake[39,40] (100 μL drops) or CA[41] (10-20 μL drops). Static CA measurements were conducted with 100 μL droplets. For CAH measurements, a 10 μL droplet was first deposited on the surface. A second 10 μL droplet was then added to measure the advancing angle and subsequently removed by gently tilting the surface to obtain the receding angle while video-recording the experiment. Stills of the videos were then analyzed to infer the advancing and receding angles.

Characterization of the Infused Oil Layer Thickness. The NP-coated slides were weighed before and after spin coating with silicone oil. Knowing the oil density and the area of the slide, a thickness for the oil film could be derived. This approach is convenient to track oil losses and rapidly estimate changes in the infused layer thickness. However, it rests on the assumption of a uniform, homogenous oil film and neglects any of the oil contained within the rough porous NP layer. These assumptions are justified considering the order of magnitude in thickness difference between the oil and porous layers, at least for the fresh samples. Values obtained are in the range of 6−8 μm. Alternatively, an estimation of the oil film thickness can be derived from the equation for the thin film thickness after spin coating. This determines the oil film thickness to be around 5 μm, in good agreement with the weight measurements (see Section S2 of the Supporting Information).

RESULTS AND DISCUSSION

In order to objectively and systematically investigate the ageing of the model LISs, we have organized the study in three consecutive parts. First, we establish the ideal LIS model to be used in the ageing study and characterize its surface properties at the nano and macroscopic scale. The stability of the resulting LIS is also examined (standard ageing under nominal laboratory conditions and with no external perturbations). Second, we investigate the impact of ultrasonication and

https://dx.doi.org/10.1021/acs.langmuir.0c00059
Langmuir 2020, 36, 3461−3470

soaking on the LISs and their NP-based retention substrates, both from structural and functional perspectives. Finally, the different experiments are brought together, revealing a dynamical ageing mechanism able to remove the infused LIS liquid and degrade the underlying nanoporous NP substrate.

Determination of an Ideal LIS Model. To maximize the practical relevance of our findings, we use a model LIS made with a commercially available spray of hydrophobized silica NPs (GLACO, see the Experimental Methods section), which creates a porous nanolayer that can be readily infused with silicone oil.[42] GLACO-based LISs are often used to create inexpensive and facile LIS model systems,[36,43,44] making them an ideal research platform for this study. There is, however, no set protocol to create an optimal porous layer of hydrophobized NPs. We therefore started by testing a variety of NP-functionalized supports with a varying number of NP layers for oil infusion. We characterized these supports and tested the resulting LIS (Figure 1).

AFM images of a sample taken in ultrapure water, immediately after coating with a single layer of NPs (Figure 1a,b) reveal a full layer composed of NPs 20−50 nm in size, and creating a surface with an average root-mean-square (rms) roughness of 60 ± 5 nm. Interestingly, the associated phase image (Figure 1b) shows additional contrast over single NPs with the cores appearing darker than the hydrophobic shell (inset with arrows). The phase image is sensitive to the local viscoelastic properties of the surface,[38,45,46] and able to distinguish between the stiffer silica cores and the softer perfluoroalkyltrichlorosilane shell when operated with a sufficiently large imaging amplitude.[47] Consistently, the cores appear well-defined, but the shells induce a fuzzy outer ring. The NPs are often clustered, which can lead to the solid centers appearing to overlap in some areas, with a range of particle sizes. This can also be seen in the EM image taken on a glass substrate (Figure 1c). The layer is uniform and around 1.6 μm thick. The NPs layers were extensively characterized by AFM in air and water, demonstrating them to be consistent, stable, and well-attached (Supporting Information Figure S2). Increasing the number of layers tends to decrease the surface roughness of the coating (Figure 1e, see also Figure S2). This is expected, as additional layers allow for newly added particles to settle in more stable positions by filling up grooves in the previous coating layer. After 5 coats, the rms roughness is comparable to the size of single NPs (~40 nm), suggesting 5 layers to be close to the optimal limit for a smooth, regular coating (45 ± 5 nm). In order to create control surfaces, we used glass slides coated with a single monolayer of DMS directly evaporated onto the surface, resulting in a significantly lower roughness of 9 ± 1 nm when imaged under identical conditions (Figure 1e). The DMS-functionalized surfaces can be considered flat and hydrophobic, and hence serve as a reference to single out the effect of porosity on oil retention when compared to a NP-functionalized surface.

To create a full LIS, the NP- and DMS-functionalized glass slides were infused with silicone oil (see the Experimental Methods section). AFM imaging of the oil−water interface atop an infused 5-layer NPs sample reveals a smooth regular surface with occasional ripples, presumably due to the AFM tip probing the oil−water interface and causing small disturbances (Figure 1d). Estimates of the average oil layer thickness based on the weight of the samples after infusion yields values between 6 and 8 μm. These values are typical, but can vary,

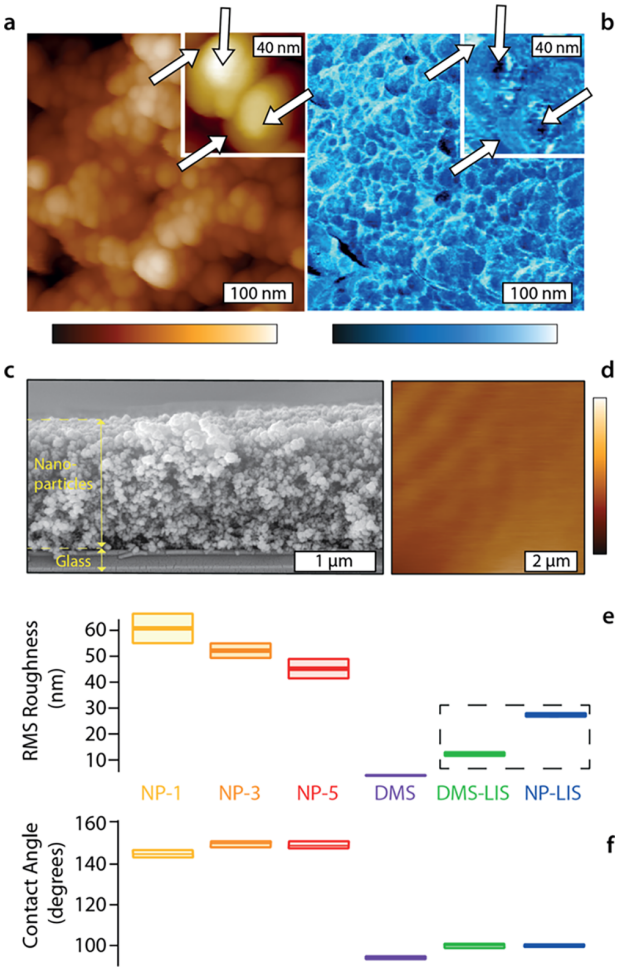

Figure 1. Characterization of the different surface functionalizations used to create the model LIS. AFM images of the NP-functionalized glass surface taken in ultrapure water (a,b) reveal a cohesive but rough NP layer with multiple NP clusters (a, topography). The associated phase information (b) exhibits some contrast between the harder silica core (darker) and the softer perfluoroalkyltrichlorosilane corona, which appear lighter and less well-defined (inset with arrows indicating the center and edge of two NPs). An scanning electron microscopy image of the section of the NP-functionalized glass taken after 5 NP layers were applied shows a homogeneous ~1.6 μm thick NP coating (c). After infusion with silicone oil, AFM imaging of the oil−water interface shows a smooth surface with occasional tip-induced ripples (d). The surface roughness of the NP-functionalized glass tends to decrease with the number of NP layers sprayed but remains significantly larger than the glass substrate directly coated with a single evaporated layer of DMS (e). The rms roughness of each sample was systematically quantified by analyzing 3 distinct regions of 2 μm × 2 μm in each case. All the measurements were taken in air except for the LIS, yielding an overall rms roughness ranging between 20 and 50 nm. Roughness measurements conducted on the LISs are unreliable because of the probing technique inducing ripples in the oil layer. The corresponding roughness values should be considered as indicative only (dashed box). Static CA measurements conducted over all samples (f) yield a value of ~150° for all the NP-functionalized surfaces (within experimental error), changing to 101 ± 1° after infusion with silicone oil. On DMS-functionalized surfaces, the CA changes from 95 ± 1 to 101 ± 1° upon infusion with silicone oil. The plotted CA values represent 20 or more independent measurements on a minimum of 2 samples for each set of surfaces. The error boxes (e,f) represent the standard error on the

https://dx.doi.org/10.1021/acs.langmuir.0c00059
Langmuir 2020, 36, 3461−3470

Figure 1. continued

measurements. Samples were stored horizontally and measurements taken over the entire slide length. The color scale bar represents a height variation of 140 nm (a), 60 nm (inset a), 500 nm (d) and phase variation of 30 (b) and 10° (inset b).

depending on the oil temperature during spin coating, and the environmental conditions in the laboratory.

Static CA measurements, taken across the different surfaces, show the biggest difference between the infused and the noninfused surfaces for any type of functionalization (Figure 1f). For NP-functionalized surfaces, infusion with silicone oil reduces the CA from ∼150 to ∼101°. Within the experimental error, no differences can be observed between NP-functionalized surfaces with different numbers of layers, which remain stable over days (Figure S3). This is not surprising, given that we expect the oil to fully cover the surface corrugations. For DMS-functionalized surfaces, the CA changes from ∼95 to ∼101° upon silicone oil infusion, with an initial measured oil layer thickness comparable to that of the NP-functionalized surfaces (Figure S4). Overall, the CA values are identical for all fresh LISs within the experimental error, reflecting the fact that the CA is then entirely determined by the oil−water interfaces, with no direct effect on the functionalization. The measured values are also in agreement with the predictions based on a liquid-equivalent of Young's CA equation[21]

$$\theta = \cos^{-1}\left(\frac{\sigma_{og} - \sigma_{ol}}{\sigma_{lg}^{eff}}\right) = 104 \pm 2^{\circ} \quad (1)$$

where σ_{og} and σ_{ol} represent the interfacial energies between oil and air, and oil and water, respectively, and σ_{lg}^{eff} represents the effective interfacial energy between water and air. For simplicity, here, we have used $\sigma_{lg}^{eff} = \sigma_{og} + \sigma_{ol}$ because the water droplet is expected to be cloaked by the silicone oil. We note that CA values can exhibit changes of several degrees when measured multiple times over days because of the changes in the ambient laboratory relative humidity and temperature (Figure 2). The error associated with the above derivation takes into account such changes, which will be discussed later in detail.

Next, to ensure the basic stability of our model LIS, we examined the effect of surface porosity on oil retention as the sample aged unperturbed in air. This was done by comparing the ability of a 5-layer NP−LIS and the control DMS−LIS to retain the infused silicone oil, evaluated by periodic weighing and CA measurements. The results are shown in Figure 2.

Static CA measurements on the freshly oil-infused LIS give a similar CA consistent with Figure 1a. As the LIS ages, oil is lost from both the porous and nonporous surface, but the oil loss occurs more rapidly from the nonporous surface, with the initial oil layer thickness halving over ∼4 days. This rapid loss correlates to a change in CA for the DMS−LIS, a behavior not observed for the NP-functionalized LIS, even after partial oil loss. For the NP−LIS, the CA remains constant at ∼104°. The apparent insensitivity of the CA on the oil layer thickness for the NP-based LIS has been demonstrated in previous computer simulation studies. These predict a negligible change in the CA for relatively large water droplets (>2−3 mm as used here) on thin oil films upon changes in the film thickness.[21] This is because the typical size ratio between the oil film and the droplet is very small (less than 0.01). We note that this is not true for smaller aqueous droplets whose oil ridge becomes comparable to the droplet size, resulting in an apparent CA that noticeably depends on the oil layer thickness.[48]

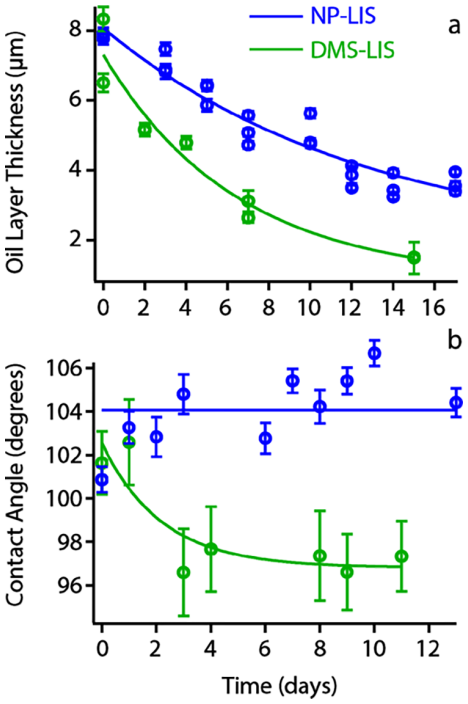

Figure 2. Oil retention ability of the DMS- and 5-layer NP−LIS in air under ambient laboratory conditions compared to the static CA. The thickness of the silicone oil layer decreases in time because of the losses to the environment (a). The loss is significantly more pronounced for the DMS-functionalized LIS, which depletes to below an oil layer thickness of 2 μm within 15 days. Static CA measurements (b) show no evolution over the NP-functionalized LIS, but a progressive return to oil-free values for the DMS-functionalized LIS. This is consistent with the almost complete oil depletion measured in (a). The two data sets are independent and were taken on different samples but placed together for comparison. Each point represents an average of 3 measurements with its standard error. The solid lines in (a,b) serve as eye guides.

The main source of error in the experimental measurements of the CA comes from fluctuations in the laboratory's temperature T (16 °C < T < 25 °C) and relative humidity RH (50% < RH < 90%), both of which are not controlled throughout the experiments. The associated variations in the CA over the same sample are ∼2% because of T variations and ∼2% because of RH variations (See Section S4 of the Supporting Information). These uncertainties are in agreement with previous reports indicating CA variations of up to 15%.[49] Changes in RH would, in principle, also affect the droplet evaporation rate, but given the short experimental timescales and the relatively large droplets this can be neglected here. Oil loss over the course of hours can be considered negligible, as can be the impact of gravity due to vertical storage of the LIS (see Supporting Information Figures S4 and S5, respectively). Overall, the results presented in Figures 1 and 2 confirm the suitability of the 5-layer NP−LIS as a model system to investigate the ageing of the LIS under external perturbations. The 5-layer NP−LIS will hence be used systematically hereafter unless otherwise specified.

https://dx.doi.org/10.1021/acs.langmuir.0c00059
Langmuir 2020, 36, 3461−3470

Accelerated LIS Ageing. To assess the impact of ageing in more realistic conditions, the 5-layer NP−LIS samples were immersed in aqueous solutions containing either ultrapure water or a 600 mM NaCl (saline) solution and exposed to pressure waves by ultrasonication. The choice of the saline solution is to mimic conditions in a number of LIS applications, such as for medical devices, transport vehicles, and underwater structures. The ageing process used here is harsher than most natural conditions (Table 1) and can be seen as accelerated ageing.

Table 1. Comparison of the Mechanical Energy Experienced by Surfaces in Various Natural and Experimental Situations[a]

process	energy [Wm^{-2}]
ultrasonic waves (bath sonicator)	400−1200
ocean wave	100−6000[50,51]
rain fall (vertically, per drop)	0.6−12[52]
rain fall (on a windscreen@100 km/h, per drop)	120−620

[a]The typical power per surface area associated with natural processes such as the impact of an ocean wave or a raindrop. The values are compared with that calculated for the ultrasonic bath used for accelerated ageing of the LIS in this study. Detailed calculations for the different estimates can be found in Sections S1 and S5 of the Supporting Information.

In both the pure water and the saline solution, the static CA remains on average constant over time (Box plot in Figure 3a,b) with no observable trend within error (standard deviation of the measurements). This is despite an exponential decay in the oil layer's thickness (Figure 3c). Both solutions exhibit a large spread of measured CA values with a rapid increase past 8 min of sonication. This transition approximately coincides with the point where the oil layer thickness starts to plateau after an initial rapid decrease (Figure 3c). This behavior suggests the appearance of defects in the oil layer, with possible localized exposure of the NP-functionalized surface underneath. This exposure is localized enough not to affect the CA value on average, but sufficient to induce droplet pinning and a higher CA variability. To better quantify this effect and confirm its origins, we conducted CAH measurements on a new set of ageing samples, simultaneously tracking the oil layer thickness (Figure 4). While the strategy allows for less measurement points than in Figure 3, it provides a more complete picture of the ageing process.

The CAH values in both solutions are initially low, starting with ∼2° and increasing to ∼6° with a wider spread after 4 min of sonication (Figure 4a,d). The hysteresis spread rapidly increases up to values exceeding 30° for times exceeding 12 min. This variability can be quantified by an increase in the CAH standard deviation (Figure 4b, e) and directly visualized by comparing representative images of the aqueous droplets sitting on the LIS during ageing (Figure 4c,f): little variation is seen in early droplets, whereas the droplets on the aged LIS exhibit pinning and significant variations between droplets, consistent with the apparition of multiple localized defects in the oil layer. The details of these local surface changes are not trivial. Simple oil depletion would be consistent with the increased CA variability and CAH values, but directly exposing hydrophobic NPs should increase the CA upon ageing. This is clearly not the case (Figure 3) pointing to localized structural and chemical changes to the porous NPs structure.

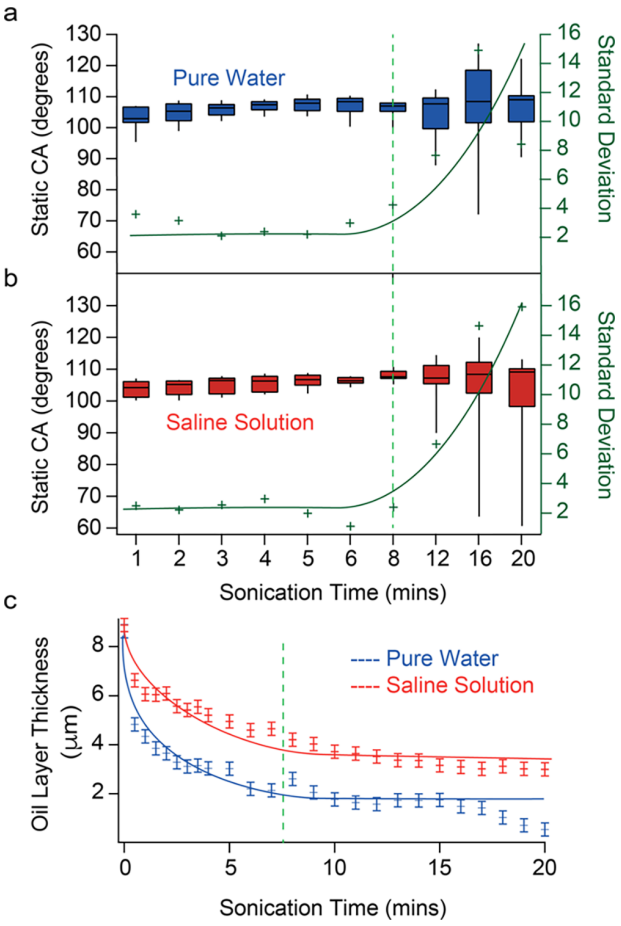

Figure 3. Accelerated ageing of the model LIS under ultrasonication in ultrapure water and in a 600 mM NaCl (saline) solution. For both ultrapure water (a) and saline solution (b), the evolution of the CAH is presented in box and whisker plots (black) showing the median value and the upper and lower quartiles. The standard deviation (green) is shown as a function of sonication time with a fitted curve serving as an eye guide. In both liquids, the average CA remains unchanged within error as the infused oil layer thickness decreases (c), but the spread of the CA values increases rapidly past ∼8 min of sonication (green dashed line). This indicates significant fluctuations arising with time, presumably due to pinning effects as the oil layer progressively becomes patchy. The oil layer thickness (c) was deduced from weight measurements taken every 30 s (<5 min) or every 60 s (>5 min). Separate samples were used for the CAH data (a,b) and the weight measurements in (c) to avoid the extended time periods necessary to take CAH hysteresis measurements between weight measurements. The data represents 20 CA measurements taken over 5 different locations for each sample and at each time step for the box plots (a,b).

Ageing Mechanisms. Examining the nanoscale details of the ageing porous NPs structure indicate that several related processes are simultaneously operating during the depletion of the initially thick oil layer (Figure 5). First, the oil removal partly exposes the NPs structures underneath enabling them to become visible by AFM (Figure 5a,b). Second, the exposed NP-functionalized regions degrade in time, as will be shown later in Figure 6. (It is worth noting that these exposed features in general have distinct wetting properties compared to surface regions that are never infused). Third, water microdroplets get trapped in the oil layer (Figure 5c,d), locally changing the

https://dx.doi.org/10.1021/acs.langmuir.0c00059
Langmuir 2020, 36, 3461−3470

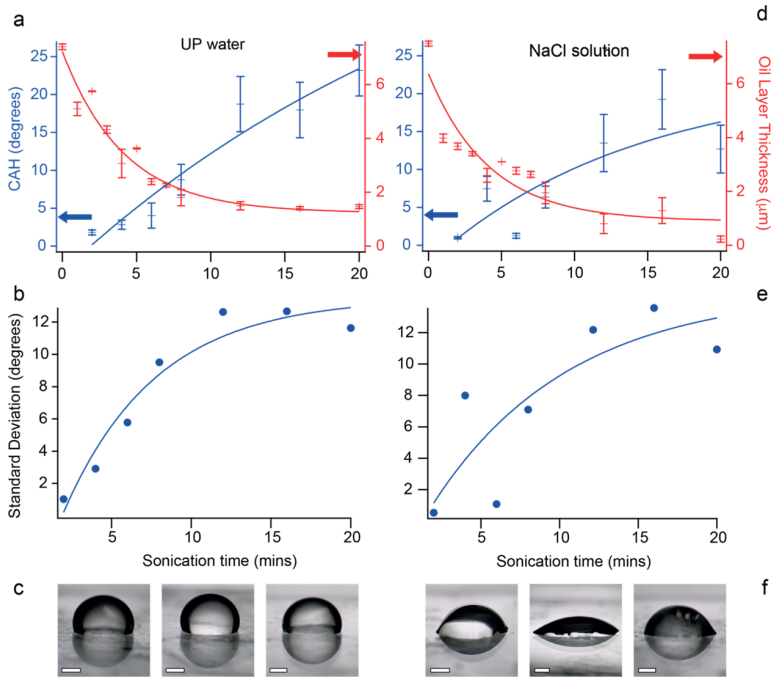

Figure 4. Changes in CAH upon accelerated ageing of the LIS in ultrapure water and a 600 mM NaCl solution. The evolution of the CAH is shown in both solutions (a,d) with an exponential fit (blue line) and the errors bars representing the data standard error. The infused oil layer thickness is superimposed (red curve, exponential fit) for comparison. The standard deviation of the CAH (b,e) can be seen to increase with the sonication time, supporting the hypothesis of localized defects forming in the infused layer. Images (c,f) show representative droplets at early and late sonication times in both media (left to right). Each CAH data point in (a,d) represents 12 measurements taken over 4 samples for each solution. Arrows indicate the direction of the reference axis label. The scale bars in images (e,f) represent 1 mm.

layer's wetting properties, and paving the way for degradation of the NP-functionalized surface. This entrapment of the aqueous solution can be directly visualized at the nanoscale by AFM imaging, with aqueous microdroplets appearing as circular depressions in the oil−water interface (arrows in Figure 5c,d), leading to macroscopic consequences for the LIS's wetting properties (Figure 5e,f). The entrapment results in oil droplets being pinched off the surface, and previously submerged microdroplets leaving the oil layer cloaked. As a result, it is impossible to remove the sonicated LIS from its aqueous bath without losing some of the infused oil layer.

This effect could be confirmed by assessing the stability of pure water and saline emulsion formed in silicone oil by sonication (Figure S6). Over a timescale of hours, the microdroplets can been seen, on average, to increase in size with the saline solution exhibiting a slightly higher stability. This is likely to be due to the fact that saline droplets have a higher colloidal stability than their pure water counterpart where only hydroxyl ions are able to stabilize the droplet.[53] When NaCl is added at high molarity, the co-ions preferentially sit at the oil−water interface next to the hydroxyl ions, effectively creating an ionic surfactant layer, which renders the droplet positively charged and more stable against coalescence.[54]

The porous NP-layer substrate used for the LIS ages too as a result of sonication. This occurs not only as a direct, mechanical result of the sonication waves, but also by increased exposure to the aqueous solution,[29] an effect exacerbated in the presence of more stable saline droplets. Controlled sonication experiments carried out on NP-functionalized surfaces without any oil present show that direct mechanical effects mainly decrease the porous layer's roughness from ∼60 to 35−40 nm (Figure S7). This is likely due the removal of loose or protruding particles, leaving a more uniform surface. As can be expected, the wetting properties of the surface change with the roughness[55,56] (Figure 6a; NP-5 in water). Superhydrophobic surfaces have poor underwater stability due to the difficulty in retaining air pockets.[29,57] Here, sonication could force water against the surface, displacing any residual air pockets. However, the surface itself remains fully and uniformly covered with the NPs well attached (Figure S7). This suggests a limited impact of the pressure waves on the integrity of the nanoporous surface. Instead, damage to the nanoporous layer mainly results from prolonged exposure to the saline solution, which can cause the NPs to detach or become loose.

Upon soaking in a saline solution, the uncoated nanoporous NPs layer exhibits a progressive decrease of static CA values (Figure 6a; NP-5 in saline), suggesting a transition between two wetting states, similar to a Cassie to Wenzel transition. This interpretation is supported by the presence of some degradation of the surface with localized irregularities and NPs clustering, revealed by AFM (Figure 6c). The surface is also fragile with NPs easily removed during AFM imaging after only two days of soaking. The CA measurement (5-layer NP−LIS in saline, Figure 6a) does not show any significant change. This result indicates that without any external perturbation the oil layer provides a protective coating, preventing the solution from interacting with the NPs and degrading the surface (Figure 6d). If the solution comes into contact with the NPs, it can destabilize and modify the surface, likely due to metal ions facilitating the removal of the hydrophobic ligands from the surface of the silica NPs. Because the ligand is tethered to the

https://dx.doi.org/10.1021/acs.langmuir.0c00059
Langmuir 2020, 36, 3461−3470

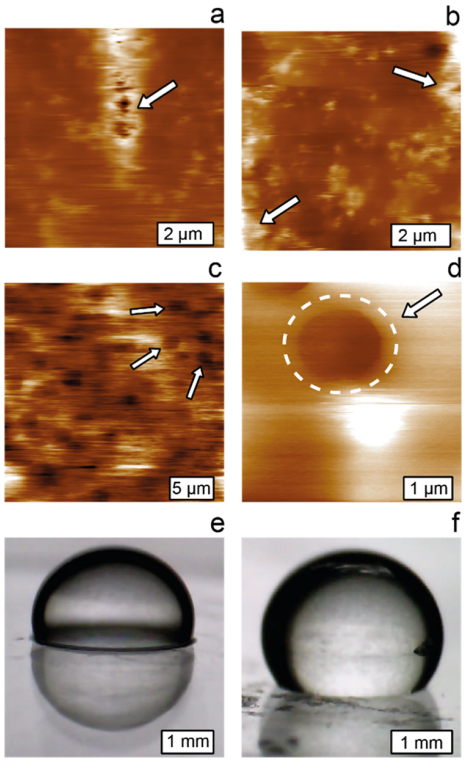

Figure 5. Images of the oil–aqueous solution interface during accelerated ageing. AFM images reveal a progressive depletion of the infused oil-layer, exposing some surface features of the NPs nanoporous layer (a). More features are visible at longer sonication time (b), consistent with the oil layer shedding to reveal the surface underneath with small nano-ridges emerging from the depleted oil layer (arrows in a,b). The main mechanism for oil removal (c) is the replacement of oil microdroplet by aqueous droplets, inducing characteristic circular depleted regions in the oil layer (arrows). A magnified view of one such circular depletion is highlighted by a white dashed circle and arrow (d). The horizontal streaks in (c,d) confirm that the AFM tip is still scanning a fluid and mobile layer. Optical images of droplets on fresh (e) samples show an oil ridge at the drop edge. When the layer is sufficiently depleted (f), the oil ridge is no longer visible. The color scale is as for Figure 1, with a maximum height variation of 124 (a), 242 (b), 129 (c), and 90 nm (d).

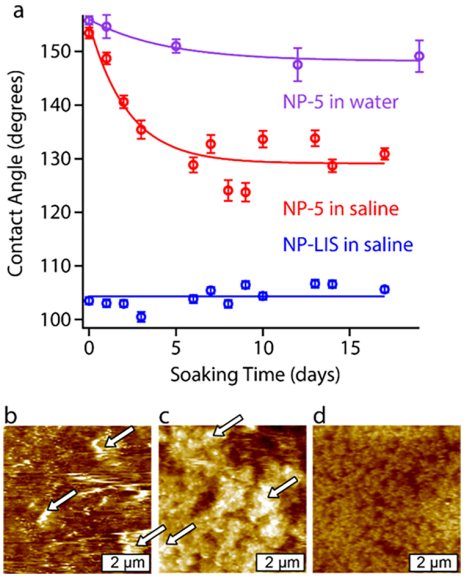

Figure 6. Impact of NP-5 soaking in an aqueous solution on the integrity and properties of the NPs layer. Over 20 days, the static CA decreases significantly on the nanoporous NP-5 surfaces in saline solution while no evolution is seen for the LIS (a). AFM images taken on the NP-5 surface at day 5 in pure water (b), the NP-5 surface at day 2 in saline solution (c), and the LIS at day 14 in the saline solution (d), reveal some key differences in ageing. Permanent surface degradation is evident for the non-infused surfaces (b,c) where large clusters are present (arrows) and more pronounced in the saline solution. Increased roughness is also visible on the LIS but much less pronounced, and the characteristic scanning streaks confirms the presence of a mobile oil layer. The color scale in all AFM images represents a height variation of 400 nm (as for Figure 1).

silica core by silane chemistry, they can be displaced under appropriate conditions.[58] This would result in hydrophobic ligand clusters aggregating on the surface, consistent with the AFM images of the degraded surface (Figure 6b,c).

General Discussion. LISs have the potential to revolutionize antifouling coating, offering a more efficient and environmentally friendly alternative to existing solutions. However, any real-life application requires a clear understanding of the LIS ageing over time so as to enable the targeted development of better, more flexible surfaces that can withstand the demands of their intended application. Here, we track the ageing of the model LIS prepared according to standard protocols. Using a dual micro- and macroscale experimental strategy, we link functional changes in the LIS's performance with specific oil loss mechanisms and nanoscale effects in the porous layer. We find that the initial oil layer is usually not at equilibrium, leading to significant oil loss, even when stored under ambient conditions and without any external perturbation. When immersed in aqueous solutions and exposed to high intensity ultrasonic pressure waves, the oil loss significantly accelerates, inducing changes in the CA and CAH. The pressure waves create aqueous micro-droplets in the oil layer, progressively pinching out the oil from the LIS, as cloaked droplets move out of the oil phase back into the bulk aqueous solution. The rapidity of the depletion process is weakly dependent on the colloidal stability of the micro-droplets. This mechanism, to the best of our knowledge has not been previously reported, appears central to the ageing of the LIS exposed to the impact of waves. In our simple model LIS, this "pinching" mechanism induces an important side-effect: the irreversible degradation of the hydrophobic NP coating used to retain the LIS' liquid. The NP coating plays an important role in the LIS performance, which is maintained more than ten times longer for the nanoporous NP-coated supports compared to the smooth flat supports. However, the current findings highlight inherent weaknesses in the use of facile nano-structured NP coating exposure of the LIS support to the aqueous solution causing both chemical and structural degradations.

Taken together, the present results provide clues to design robust LISs, for example, aimed at real-life applications that entail the impact of water drops or waves. First, using a retention support that does not require chemical functionalization, unlike the hydrophobized particles used here, would offer an obvious strategy to remedy LIS degradation, potentially increasing the lifetime of both the support and the resulting LIS. This is especially true for substrates exposed to saline solutions, where the contaminate degrades the substrate more

https://dx.doi.org/10.1021/acs.langmuir.0c00059
Langmuir 2020, 36, 3461−3470

quickly. If the LIS is designed for being reinfused periodically, chemical resistance to the environment (other than the infusing liquid) is necessary to avoid degradation over short timescales. Second, mechanical restructuring of the porous layer may also need to be considered depending on the application.

CONCLUSIONS

Overall, this work shows that the ageing effect on LISs can be significant when exposed to nonideal environmental conditions. Practical and application-oriented developments of LISs are likely to become a key aspect to LIS adoption in technology and industry, beyond the many fundamental developments currently driving the field.[3,9,10,59,60] The ageing mechanisms depend on the specific details of the system considered and should be tailored for the applications of interest.[4−7,28] The present work could act as a reference point for future work involving the testing of new LIS applications, particularly the development of a standardized, accelerated ageing strategy, to determine the robustness and durability of novel products.

ASSOCIATED CONTENT

Supporting Information

The Supporting Information is available free of charge at https://pubs.acs.org/doi/10.1021/acs.langmuir.0c00059.

Estimation of the ultrasonic bath characteristics, calculation of the spin-coated oil layer thickness, supplementary results, effect of humidity and temperature on CA measurements, estimation of the energy associated with real-life phenomena, and supplementary references (PDF)

AUTHOR INFORMATION

Corresponding Authors

Halim Kusumaatmaja − *Department of Physics, Durham University, Durham DH1 3LE, U.K.*; orcid.org/0000-0002-3392-9479; Email: halim.kusumaatmaja@durham.ac.uk

Kislon Voïtchovsky − *Department of Physics, Durham University, Durham DH1 3LE, U.K.*; orcid.org/0000-0001-7760-4732; Email: kislon.voitchovsky@durham.ac.uk

Authors

Sarah J. Goodband − *Department of Physics, Durham University, Durham DH1 3LE, U.K.*

Steven Armstrong − *Smart Materials & Surfaces Laboratory, Faculty of Engineering & Environment, Northumbria University, Newcastle Upon Tyne NE18ST, U.K.*; orcid.org/0000-0002-0520-8498

Complete contact information is available at: https://pubs.acs.org/10.1021/acs.langmuir.0c00059

Author Contributions

S.J.G., H.K., and K.V. designed the experiments. S.J.G. performed all the measurements with help from S.A. S.J.G. analyzed the results with help from H.K. and K.V. S.J.G., H.K., and K.V. wrote the paper.

Funding

EPSRC for funding through the SOFI (Soft Matter and Functional Interfaces) center for doctoral training (grant EP/L015536/1).

Notes

The authors declare no competing financial interest.

ACKNOWLEDGMENTS

The authors would like to thank Lisong Yang and Colin Bain for help with DMS sample preparation (silanization protocol and use), Bethany V. Orme, Gary Wells, and Glen McHale for their help with the preparation of the LIS samples and SEM image, and Clodomiro Cafolla for his help with AFM. S.J.G. is grateful to the EPSRC for funding through the Soft Matter and Functional Interfaces (SOFI) doctoral training school.

REFERENCES

(1) Scholz, I.; Buckins, M.; Dolge, L.; Erlinghagen, T.; Weth, A.; Hischen, F.; Mayer, J.; Hoffmann, S.; Riederer, M.; Riedel, M.; Baumgartner, W. Slippery Surfaces of Pitcher Plants: Nepenthes Wax Crystals Minimize Insect Attachment via Microscopic Surface Roughness. *J. Exp. Biol.* **2010**, *213*, 1115−1125.

(2) Wong, T.-S.; Kang, S. H.; Tang, S. K. Y.; Smythe, E. J.; Hatton, B. D.; Grinthal, A.; Aizenberg, J. Bioinspired Self-Repairing Slippery Surfaces with Pressure-Stable Omniphobicity. *Nature* **2011**, *477*, 443−447.

(3) Epstein, A. K.; Wong, T.-S.; Belisle, R. A.; Boggs, E. M.; Aizenberg, J. Liquid-Infused Structured Surfaces with Exceptional Anti-Biofouling Performance. *Proc. Natl. Acad. Sci. U.S.A.* **2012**, *109*, 13182−13187.

(4) Qiu, Z.; Qiu, R.; Xiao, Y.; Zheng, J.; Lin, C. Slippery Liquid-Infused Porous Surface Fabricated on CuZn: A Barrier to Abiotic Seawater Corrosion and Microbiologically Induced Corrosion. *Appl. Surf. Sci.* **2018**, *457*, 468−476.

(5) Xiang, T.; Zhang, M.; Sadig, H. R.; Li, Z.; Zhang, M.; Dong, C.; Yang, L.; Chan, W.; Li, C. Slippery Liquid-Infused Porous Surface for Corrosion Protection with Self-Healing Property. *Chem. Eng. J.* **2018**, *345*, 147−155.

(6) Song, Z.; Borgwardt, L.; Høiby, N.; Wu, H.; Sørensen, T. S.; Borgwardt, A. Prosthesis Infections after Orthopedic Joint Replacement: The Possible Role of Bacterial Biofilms. *Orthop. Rev.* **2013**, *5*, 65−71.

(7) Besinis, A.; Hadi, S. D.; Le, H. R.; Tredwin, C.; Handy, R. D. Antibacterial Activity and Biofilm Inhibition by Surface Modified Titanium Alloy Medical Implants Following Application of Silver, Titanium Dioxide and Hydroxyapatite Nanocoatings. *Nanotoxicology* **2017**, *11*, 327−338.

(8) Kim, P.; Wong, T.-S.; Alvarenga, J.; Kreder, M. J.; Adorno-martinez, W. E.; Aizenberg, J. Liquid-Infused Nanostructured Surfaces with Extreme Anti-Ice and Anti-Frost Performance. *ACS Nano* **2012**, *6*, 6569−6577.

(9) Yamazaki, T.; Tenjimbayashi, M.; Manabe, K.; Moriya, T.; Nakamura, H.; Nakamura, T.; Matsubayashi, T.; Tsuge, Y.; Shiratori, S. Antifreeze Liquid-Infused Surface with High Transparency, Low Ice Adhesion Strength, and Antifrosting Properties Fabricated through a Spray Layer-by-Layer Method. *Ind. Eng. Chem. Res.* **2019**, *58*, 2225−2234.

(10) Yeong, Y. H.; Wang, C.; Wynne, K. J.; Gupta, M. C. Oil-Infused Superhydrophobic Silicone Material for Low Ice Adhesion with Long-Term Infusion Stability. *ACS Appl. Mater. Interfaces* **2016**, *8*, 32050−32059.

(11) Zhang, M.; Liu, Q.; Liu, J.; Yu, J.; Wang, J. Self-Healing Liquid-Infused Surfaces with High Transparency for Optical Devices. *MRS Commun.* **2019**, *9*, 92−98.

(12) Schellenberger, F.; Xie, J.; Encinas, N.; Hardy, A.; Klapper, M.; Papadopoulos, P.; Butt, H.-J.; Vollmer, D. Direct Observation of Drops on Slippery Lubricant-Infused Surfaces. *Soft Matter* **2015**, *11*, 7617−7626.

(13) Fu, M. K.; Arenas, I.; Leonardi, S.; Hultmark, M. Liquid-Infused Surfaces as a Passive Method of Turbulent Drag Reduction. *J. Fluid Mech.* **2017**, *824*, 688−700.

(14) Dai, X.; Sun, N.; Nielsen, S. O.; Stogin, B. B.; Wang, J.; Yang, S.; Wong, T. S. Hydrophilic Directional Slippery Rough Surfaces for Water Harvesting. *Sci. Adv.* **2018**, *4*, No. eaaq0919.
(15) Yao, X.; Hu, Y.; Grinthal, A.; Wong, T.-S.; Mahadevan, L.; Aizenberg, J. Adaptive Fluid-Infused Porous Films with Tunable Transparency and Wettability. *Nat. Mater.* **2013**, *12*, 529−534.
(16) Bico, J.; Tordeux, C.; Quéré, D. Rough Wetting. *Europhys. Lett.* **2001**, *55*, 214−220.
(17) Anand, S.; Rykaczewski, K.; Subramanyam, S. B.; Beysens, D.; Varanasi, K. K. How Droplets Nucleate and Grow on Liquids and Liquid Impregnated Surfaces. *Soft Matter* **2015**, *11*, 69−80.
(18) Zhou, X.; Lee, Y.-Y.; Chong, K. S. L.; He, C. Superhydrophobic and Slippery Liquid-Infused Porous Surfaces Formed by the Self-Assembly of a Hybrid ABC Triblock Copolymer and Their Antifouling Performance. *J. Mater. Chem. B* **2018**, *6*, 440−448.
(19) Wang, W.; Timonen, J. V. I.; Carlson, A.; Drotlef, D.-M.; Zhang, C. T.; Kolle, S.; Grinthal, A.; Wong, T.-S.; Hatton, B.; Kang, S. H.; Kennedy, S.; Chi, J.; Blough, R. T.; Sitti, M.; Mahadevan, L.; Aizenberg, J. Multifunctional Ferrofluid-Infused Surfaces with Reconfigurable Multiscale Topography. *Nature* **2018**, *559*, 77−82.
(20) Wu, D.; Zhang, D.; Ye, Y.; Ma, L.; Minhas, B.; Liu, B.; Terryn, H. A.; Mol, J. M. C.; Li, X. Durable Lubricant-Infused Anodic Aluminum Oxide Surfaces with High-Aspect-Ratio Nanochannels. *Chem. Eng. J.* **2019**, *368*, 138−147.
(21) Semprebon, C.; McHale, G.; Kusumaatmaja, H. Apparent Contact Angle and Contact Angle Hysteresis on Liquid Infused Surfaces. *Soft Matter* **2017**, *13*, 101−110.
(22) Sadullah, M. S.; Semprebon, C.; Kusumaatmaja, H. Drop Dynamics on Liquid-Infused Surfaces: The Role of the Lubricant Ridge. *Langmuir* **2018**, *34*, 8112−8118.
(23) Blossey, R. Self-Cleaning Surfaces — Virtual Realities. *Nat. Mater.* **2003**, *2*, 301−306.
(24) Wexler, J. S.; Jacobi, I.; Stone, H. A. Shear-Driven Failure of Liquid-Infused Surfaces. *Phys. Rev. Lett.* **2015**, *114*, 168301.
(25) Liu, Y.; Wexler, J. S.; Schönecker, C.; Stone, H. A. Effect of Viscosity Ratio on the Shear-Driven Failure of Liquid-Infused Surfaces. *Phys. Rev. Fluids* **2016**, *1*, 074003.
(26) Wexler, J. S.; Grosskopf, A.; Chow, M.; Fan, Y.; Jacobi, I.; Stone, H. A. Robust Liquid-Infused Surfaces through Patterned Wettability. *Soft Matter* **2015**, *11*, 5023−5029.
(27) Singh, V.; Sheng, Y.-J.; Tsao, H.-K. Self-Healing Atypical Liquid-Infused Surfaces: Superhydrophobicity and Superoleophobicity in Submerged Conditions. *J. Taiwan Inst. Chem. Eng.* **2019**, *97*, 96−104.
(28) Ware, C. S.; Smith-Palmer, T.; Peppou-Chapman, S.; Scarratt, L. R. J.; Humphries, E. M.; Balzer, D.; Neto, C. Marine Antifouling Behavior of Lubricant-Infused Nanowrinkled Polymeric Surfaces. *ACS Appl. Mater. Interfaces* **2018**, *10*, 4173−4182.
(29) Li, J.; Ueda, E.; Paulssen, D.; Levkin, P. A. Slippery Lubricant-Infused Surfaces: Properties and Emerging Applications. *Adv. Funct. Mater.* **2019**, *29*, 1802317.
(30) Zhang, Y.; Zhang, L.; Xiao, Z.; Wang, S.; Yu, X. Fabrication of Robust and Repairable Superhydrophobic Coatings by an Immersion Method. *Chem. Eng. J.* **2019**, *369*, 1−7.
(31) Chen, H.; Zhang, P.; Zhang, L.; Liu, H.; Jiang, Y.; Zhang, D.; Han, Z.; Jiang, L. Continuous Directional Water Transport on the Peristome Surface of Nepenthes Alata. *Nature* **2016**, *532*, 85−89.
(32) Zhang, P.; Zhang, L.; Chen, H.; Dong, Z.; Zhang, D. Surfaces Inspired by the Nepenthes Peristome for Unidirectional Liquid Transport. *Adv. Mater.* **2017**, *29*, 1702995.
(33) Zhang, P.; Chen, H.; Li, L.; Liu, H.; Liu, G.; Zhang, L.; Zhang, D.; Jiang, L. Bioinspired Smart Peristome Surface for Temperature-Controlled Unidirectional Water Spreading. *ACS Appl. Mater. Interfaces* **2017**, *9*, 5645−5652.
(34) Zhou, S.; Yu, C.; Li, C.; Dong, Z.; Jiang, L. Programmable Unidirectional Liquid Transport on Peristome-Mimetic Surfaces under Liquid Environments. *J. Mater. Chem. A* **2019**, *7*, 18244−18248.
(35) Howell, C.; Vu, T. L.; Johnson, C. P.; Hou, X.; Ahanotu, O.; Alvarenga, J.; Leslie, D. C.; Uzun, O.; Waterhouse, A.; Kim, P.; Super, M.; Aizenberg, M.; Ingber, D. E.; Aizenberg, J. Stability of Surface-Immobilized Lubricant Interfaces under Flow. *Chem. Mater.* **2015**, *27*, 1792−1800.
(36) Orme, B. V.; McHale, G.; Ledesma-Aguilar, R.; Wells, G. G. Droplet Retention and Shedding on Slippery Substrates. *Langmuir* **2019**, *35*, 9146−9151.
(37) Deng, R.; Yang, L.; Bain, C. D. Combining Inkjet Printing with Emulsion Solvent Evaporation to Pattern Polymeric Particles. *ACS Appl. Mater. Interfaces* **2018**, *10*, 12317−12322.
(38) Miller, E. J.; Trewby, W.; Farokh Payam, A.; Piantanida, L.; Cafolla, C.; Voïtchovsky, K. Sub-Nanometer Resolution Imaging with Amplitude-Modulation Atomic Force Microscopy in Liquid. *J. Visualized Exp.* **2016**, *118*, 1−10.
(39) Stalder, A. F.; Kulik, G.; Sage, D.; Barbieri, L.; Hoffmann, P. A Snake-Based Approach to Accurate Determination of Both Contact Points and Contact Angles. *Coll. Surf. A* **2006**, *286*, 92−103.
(40) Stalder, A. F.; Melchior, T.; Müller, M.; Sage, D.; Blu, T.; Unser, M. Low-Bond Axisymmetric Drop Shape Analysis for Surface Tension and Contact Angle Measurements of Sessile Drops. *Coll. Surf. A* **2010**, *364*, 72−81.
(41) Buahom, P. *Contact Angle Plugin*; University of Trento: Trento, Italy, 2006.
(42) Kato, M.; Tanaka, A.; Sasagawa, M.; Adachi, H. Durable Automotive Windshield Coating and the Use Thereof. U.S. Patent 8,043,421 B2, March 12, 2008.
(43) Brabcova, Z.; McHale, G.; Wells, G. G.; Brown, C. V.; Newton, M. I. Electric Field Induced Reversible Spreading of Droplets into Films on Lubricant Impregnated Surfaces. *Appl. Phys. Lett.* **2017**, *110*, 121603.
(44) Keiser, A.; Keiser, L.; Clanet, C.; Quéré, D. Drop Friction on Liquid-Infused Materials. *Soft Matter* **2017**, *13*, 6981−6987.
(45) Ricci, M.; Quinlan, R. A.; Voïtchovsky, K. Sub-Nanometre Mapping of the Aquaporin-Water Interface Using Multifrequency Atomic Force Microscopy. *Soft Matter* **2017**, *13*, 187−195.
(46) Xu, X.; Melcher, J.; Basak, S.; Reifenberger, R.; Raman, A. Compositional Contrast of Biological Materials in Liquids Using the Momentary Excitation of Higher Eigenmodes in Dynamic Atomic Force Microscopy. *Phys. Rev. Lett.* **2009**, *102*, 13−16.
(47) Voïtchovsky, K. Anharmonicity, Solvation Forces, and Resolution in Atomic Force Microscopy at the Solid-Liquid Interface. *Phys. Rev. E* **2013**, *88*, 022407.
(48) McHale, G.; Orme, B. V.; Wells, G. G.; Ledesma-Aguilar, R. Apparent Contact Angles on Lubricant-Impregnated Surfaces/SLIPS: From Superhydrophobicity to Electrowetting. *Langmuir* **2019**, *35*, 4197−4204.
(49) Perez-Diaz, J. L.; Alvarez-Valenzuela, M. A.; Valiente-Blanco, I.; Jimenez-Lopez, S.; Palacios-Cuesta, M.; García, O.; Diez-Jimenez, E.; Sanchez-García-Casarrubios, J.; Cristache, C. On the Influence of Relative Humidity on the Contact Angle of a Water Droplet on a Silicon Wafer. *Proceedings ASME*, 2013, IMECE2013-63781.
(50) Holfhuisen, L. H. *Waves in Oceanic and Coastal Waters*, 1st ed; Cambridge University Press: Cambridge, U.K., 2007.
(51) Muetze, A.; Vining, J. G. Ocean Wave Energy Conversion - A Survey. *IAS Annual Meeting IEEE Industry Application Society*, 2006; Vol. 3, pp 1410−1417.
(52) Guigon, R.; Chaillout, J. J.; Jager, T.; Despesse, G. Harvesting Raindrop Energy: Theory. *Smart Mater. Struct.* **2008**, *17*, 015038.
(53) Wang, J.-H.; Lien, S.-Y.; Ho, J.-R.; Shih, T.-K.; Chen, C.-F.; Chen, C.-C.; Whang, W.-T. Optical Diffusers Based on Silicone Emulsions. *Opt. Mater.* **2009**, *32*, 374−377.
(54) Sainath, K.; Ghosh, P. Stabilization of Silicone Oil-in-Water Emulsions by Ionic Surfactant and Electrolytes: The Role of Adsorption and Electric Charge at the Interface. *Ind. Eng. Chem. Res.* **2013**, *52*, 15808−15816.
(55) Cassie, A. B. D.; Baxter, S. Wettability of Porous Surfaces. *Trans. Faraday Soc.* **1944**, *40*, 546−551.

https://dx.doi.org/10.1021/acs.langmuir.0c00059
Langmuir 2020, 36, 3461−3470

(56) Wenzel, R. N. Resistance of Solid Surfaces to Wetting by Water. *Ind. Eng. Chem.* **1936**, *28*, 988−994.
(57) Bobji, M. S.; Kumar, S. V.; Asthana, A.; Govardhan, R. N. Underwater Sustainability of the "Cassie" State of Wetting. *Langmuir* **2009**, *25*, 12120−12126.
(58) Wei, M.; Bowman, R. S.; Wilson, J. L.; Morrow, N. R. Wetting Properties and Stability of Silane-Treated Glass Exposed to Water, Air, and Oil. *J. Colloid Interface Sci.* **1993**, *157*, 154−159.
(59) Wang, D.; Guo, Z.; Liu, W. Bioinspired Edible Lubricant-Infused Surface with Liquid Residue Reduction Properties. *Research* **2019**, *2019*, 1−12.
(60) Ganesh, V. A.; Raut, H. K.; Nair, A. S.; Ramakrishna, S. A Review on Self-Cleaning Coatings. *J. Mater. Chem.* **2011**, *21*, 16304−16322.

https://dx.doi.org/10.1021/acs.langmuir.0c00059
Langmuir 2020, 36, 3461−3470

LANGMUIR

pubs.acs.org/Langmuir Article

Evaporation and Electrowetting of Sessile Droplets on Slippery Liquid-Like Surfaces and Slippery Liquid-Infused Porous Surfaces (SLIPS)

S. Armstrong, G. McHale,* R. Ledesma-Aguilar, and G. G. Wells

Cite This: https://dx.doi.org/10.1021/acs.langmuir.0c02020 Read Online

ACCESS | Metrics & More | Article Recommendations

ABSTRACT: Sessile droplet evaporation underpins a wide range of applications from inkjet printing to coating. However, drying times can be variable and contact-line pinning often leads to undesirable effects, such as ring stain formation. Here, we show voltage programmable control of contact angles during evaporation on two pinning-free surfaces. We use an electrowetting-on-dielectric approach and Slippery Liquid-Infused Porous (SLIP) and Slippery Omniphobic Covalently Attached Liquid-Like (SOCAL) surfaces to achieve a constant contact angle mode of evaporation. We report evaporation sequences and droplet lifetimes across a broad range of contact angles from 105°−67°. The values of the contact angles during evaporation are consistent with expectations from electrowetting and the Young-Lippman equation. The droplet contact areas reduce linearly in time, and this provides estimates of diffusion coefficients close to the expected literature value. We further find that the total time of evaporation over the broad contact angle range studied is only weakly dependent on the value of the contact angle. We conclude that on these types of slippery surfaces, droplet lifetimes can be predicted and controlled by the droplet's volume and physical properties (density, diffusion coefficient, and vapor concentration difference to the vapor phase) largely independent of the precise value of contact angle. These results are relevant to applications, such as printing, spraying, coating, and other processes, where controlling droplet evaporation and drying is important.

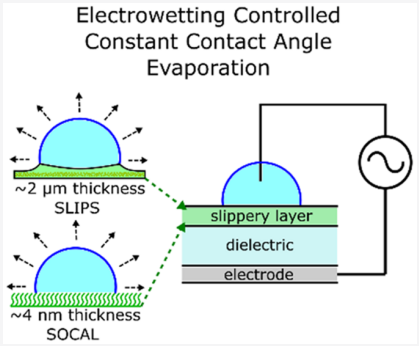

INTRODUCTION

The evaporation of sessile droplets of liquids from solids occurs in many applications including heat exchange,[1] particle deposition,[2] and inkjet printing.[3] Due to its importance to a wide range of physical processes, the literature is extensive (see, e.g., Erbil,[4] Cazabat and Guéna,[5] and Larson[6]). For a sessile droplet, the presence of the solid surface results in an evaporation rate, and hence drop drying time, which depends on the droplet's contact angle. Inhomogeneities in practical surfaces also mean there is contact line pinning which has consequences for predicting and controlling evaporation. It can prevent the contact area between the liquid and solid with it being circular thus giving irregular drying spots and drying times. If the evaporating droplet is a suspension, it can cause nonuniform particle deposition, similar to the coffee-ring stain effect.[6] This can cause problems in a broad range of applications from nonuniform delivery of the active components in aerosols used in pesticides to nonuniform fluorescence in spotted microarrays.[2,7−9] One way to prevent ring-stain patterns is to remove contact line pinning so that the contact line is completely mobile during evaporation, but this is the exception on solid surfaces unless active means, such surface acoustic wave[10] or electrowetting-induced agitation of the liquid, are used.[11] It is therefore desirable to investigate contact angle dependence of evaporation of droplets on surfaces which do not have contact line pinning to understand control of the evaporation sequence and droplet lifetimes.

One possible approach to removing contact line pinning is to use superhydrophobic surfaces with contact angles above ca. 150°,[12−14] and the first example of using such a surface for evaporation was provided by McHale et al.[15] In their case, the texture of their micropost surface led to quantization of the receding contact line into stepwise jumps from pillar to pillar before a collapse into the structure and complete pinning. In other cases, evaporation of sessile droplets from nanoparticle-based superhydrophobic surfaces has shown droplets evaporate for a relatively constant contact angle ca. 150°.[16] However, these surfaces have high contact angles toward 180° with small contact areas to create a Cassie−Baxter state and so use texture or roughness for which there remains the risk of impalement of the drop into the texture through, for example, pressure-

Received: July 9, 2020
Revised: September 3, 2020
Published: September 3, 2020

https://dx.doi.org/10.1021/acs.langmuir.0c02020
Langmuir XXXX, XXX, XXX−XXX

induced or condensation of vapor-induced transitions, to the Wenzel state. An alternative approach to removing contact line-pinning, which avoids the risk of an impalement transition, is the use of a Slippery Liquid-Infused Porous Surface (SLIPS),[17] and this has been shown to support a constant contact angle type mode of evaporation.[18] However, while SLIPS provide a smooth surface, the droplet is never in direct contact with the underlying solid but rests on the layer of lubricant used to infuse the porous (or textured) solid surface structure. Thus, the observed contact angle is an apparent contact angle and is not determined by interaction with the underlying solid surface, and the lubricant may alter the evaporation rate. This apparent contact angle on SLIPS can be theoretically described,[19] and for thin layers of lubricant, the contact angle can be predicted using a liquid/lubricant form of Young's law, which also provides an upper bound for thicker layers of lubricant.[19,20] Most recently, Wang and McCarthy introduced a new type of slippery surface which they named Slippery Omniphobic Covalently Attached Liquid (SOCAL) surfaces obtained through acid-catalyzed graft polycondensation of dimethyldimethoxysilane.[21] This has allowed the observation of pinning-free constant contact angle mode evaporation on smooth slippery liquid-like, but solid, surfaces.[22] In the case of SLIPS, created using silicone oil as a lubricant, and for SOCAL, the contact angle for droplets of water are ca. 108° and 104° and so can be regarded as hydrophobic surfaces. At present, there are no examples of pinning-free evaporations of sessile water droplets from hydrophilic surfaces.

An outstanding challenge for studies of pinning-free evaporation of sessile droplets is control of the range of contact angles on smooth slippery surfaces. Here, our primary objective is to address this challenge by introducing electrowetting-on-dielectric (EWOD)[23,24] as a technique to control the contact angle during evaporation. Electrowetting is an important tool that can manipulate and control droplets, e.g., in microfluidics,[25−27] liquid lenses,[28] and optofluidics,[29] and can be used with SLIP surfaces (see e.g., ref 30−32). In this type of electrowetting, the solid−liquid contact area of a sessile droplet acts as one electrode in a capacitive structure allowing the contact angle to be reduced by the application of a voltage. Electrowetting does not alter the spherical cap shape of small sessile droplets provided the voltage is below the saturation voltage,[33] and since charges are stored at the solid−liquid interface, we anticipate it will not significantly influence the evaporation of sessile droplets. In the remainder of this paper, we describe the theory for the constant contact angle mode of evaporation and the creation of two types of slippery surfaces (SOCAL and SLIPS) in an electrowetting configuration. We then report data for the constant contact angle evaporation mode over a range of contact angles from 105° to 67° including a comparison to expected values from the Young-Lippmann equation to show consistency with theory and provide confidence in the technique. We report estimates for the diffusion coefficient of water vapor and for droplet lifetimes and show that droplet lifetime is largely insensitive to the precise value of the contact angle over the range studied.

THEORY OF CONSTANT CONTACT ANGLE MODE EVAPORATION

Picknett and Bexon provided the first solution for the diffusion-controlled evaporation of a spherical cap shaped sessile droplet on a smooth and homogeneous surface and identified two ideal modes.[34] In the first mode, the contact line is completely pinned, and the evaporation occurs with a constant contact radius, so that the contact angle decreases throughout the entire evaporation. This mode of evaporation has been achieved experimentally and is widely studied.[4,35] In the second mode the contact line is mobile, and the contact angle remains constant, resulting in a linear decrease in the contact area with time. Constant contact angle mode evaporation on surfaces has been experimentally difficult to observe because surfaces tend to exhibit contact angle hysteresis and contact line pinning. In practice, most droplets evaporate in a stick−slip mode of evaporation, where the contact line is repeatedly pinned on the surface, depinning when the contact angle is sufficiently out of equilibrium to exceed the force necessary to move the contact line. A number of authors have also observed another mode of evaporation known as stick-slide mode evaporation, where the contact area and contact angle decrease at the same time, e.g., ref 34. In particular, Stauber et al. have provided a model to predict the lifetime of droplets in stick-slide, constant contact radius, and constant contact angle mode evaporation.[36,37]

In the ideal case without contact line pinning and when a droplet is in thermodynamic equilibrium, the contact angle, θ_e, a sessile droplet makes with a smooth solid surface is determined by three interfacial tensions as described by Young's law

$$\cos\theta_e = \frac{(\gamma_{SV} - \gamma_{SL})}{\gamma_{LV}} \tag{1}$$

where γ_{SV} is the solid−vapor interfacial tension, γ_{SL} is the solid−liquid interfacial tension, and γ_{LV} is the liquid−vapor interfacial tension.[38] This applies to droplets in equilibrium with contact angles from 0°, where a droplet just forms a film between the solid surface and the surrounding vapor phase, to 180° where a droplet completely balls up on the surface.

For a small sessile droplet with a size below the capillary length $l_c = (\gamma_{LV}/\rho g)^{1/2}$ where ρ is the density of the liquid and g = 9.81 ms^{-2} is the acceleration due to gravity, the droplet adopts an axially symmetric spherical cap shape with well-defined geometric parameters that can be measured from side profile images. These include the spherical cap radius R, contact radius r, contact angle θ, and the apex height h, above the contact surface. Geometrically, the volume, Ω, is defined as

$$\Omega = \frac{\pi\beta(\theta)R^3}{3} \tag{2}$$

where

$$\beta(\theta) = (1 - \cos\theta)^2(2 + \cos\theta) \tag{3}$$

and the contact radius is related to the spherical radius by $r = R\sin\theta$. In general, the rate for diffusion-limited loss of a liquid volume by evaporation through a liquid−vapor interface using a surface integral of the concentration gradient is

$$\frac{d\Omega}{dt} = -\frac{D}{\rho}\int \nabla C.\, \underline{dS} \tag{4}$$

where D is the diffusion coefficient of the vapor.[5] Combining the geometrical assumptions with eq 4 and a concentration gradient model gives

$$\frac{d\Omega}{dt} = -2\lambda R f(\theta) \tag{5}$$

https://dx.doi.org/10.1021/acs.langmuir.0c02020
Langmuir XXXX, XXX, XXX−XXX

where

$$\lambda = \frac{2D(c_s - c_\infty)}{\rho} \tag{6}$$

Here, $(c_s - c_\infty)$ is the difference in the vapor concentration at the liquid−vapor interface of the droplet c_s, which is assumed to be its saturation value and that far removed from the droplet surface c_∞, which is assumed to be its ambient value. For analyzing data, an exact solution for eq 5 was derived by Picknett and Bexon[34] and they gave a numerically accurate polynomial interpolation, $f_{PB}(\theta)$, for the exact solution $f(\theta)$ covering the entire contact angle range

$$f_{PB}(\theta) = \begin{cases} \frac{1}{2}(0.6366\theta + 0.09591\theta^2 - 0.06144\theta^3) & 0° < \theta < 10° \\ \frac{1}{2}(0.00008957 + 0.6333\theta + 0.116\theta^2 - 0.08878\theta^3 + 0.01033\theta^4) & 10° < \theta < 180° \end{cases} \tag{7}$$

where θ in the series is in radians. For the constant contact angle evaporation mode, the rate of change of the contact area is

$$\frac{d(\pi r^2)}{dt} = -\frac{4\lambda \sin^2 \theta_c f(\theta_c)}{\beta(\theta_c)} \tag{8}$$

where θ_c is the constant value for the contact angle. Thus, the contact area has a linear change with time from its initial value determined by the initial contact radius, r_i, at $t = 0$, i.e.,

$$\pi r(t)^2 = \pi r_i^2 - \frac{4\lambda \sin \theta_c f(\theta_c) t}{\beta(\theta_c)} \tag{9}$$

Similarly, the rate of change in volume can be expressed in terms of the instantaneous volume and the constant contact angle

$$\frac{d\Omega}{dt} = -2\lambda \left(\frac{3\Omega}{\pi\beta(\theta_c)}\right)^{1/3} f(\theta_c) \tag{10}$$

and this integrates to give a 2/3 power law for the volume

$$\Omega(t)^{2/3} = \Omega_i^{2/3} - \frac{4\lambda}{3}\left(\frac{3\Omega}{\pi\beta(\theta_c)}\right)^{1/3} f(\theta_c) t \tag{11}$$

where Ω_i is the initial droplet volume at $t = 0$. The droplet lifetime, t_f, is then defined by the time at which the droplet contact area (eq 9), or equivalently the droplet volume (eq 11), vanishes, i.e.,

$$t_f(\theta_c, r_i, \lambda) = \frac{\pi r_i^2 \beta(\theta_c)}{4\lambda \sin^2 \theta_c f(\theta_c)} \tag{12}$$

which can also be written as

$$t_f(\theta_c, \Omega_i, \lambda) = \frac{3}{4\lambda f(\theta_c)}\left(\frac{\pi\beta(\theta_c)\Omega_i^2}{3}\right)^{1/3} \tag{13}$$

Thus, the total droplet lifetime during constant contact angle evaporation of a spherical cap shaped sessile droplet depends on the value of the contact angle and the initial contact radius (or volume) and a parameter, λ, combining the diffusion coefficient, density of liquid, and the vapor concentration difference.

EXPERIMENTAL METHODS AND MATERIALS

Our experiments required surfaces that were both free of contact line pinning and had contact angles that could be adjusted to different constant values. To do this, we used two types of surfaces, SOCAL and SLIPS, as slippery layers on a glass substrate (as the dielectric) in an electrowetting configuration as described below (Figure 1). The

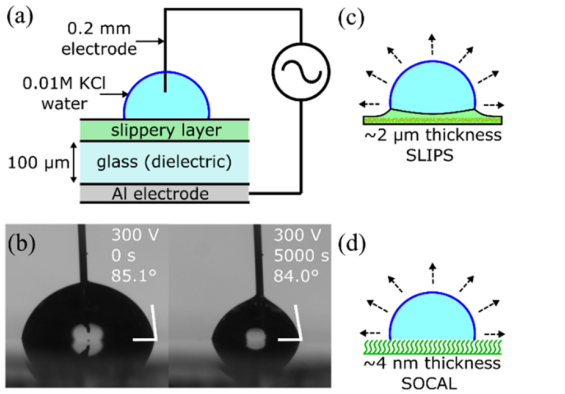

Figure 1. Electrowetting and evaporation on slippery surfaces: (a) Schematic of droplet in an electrowetting setup with a glass dielectric substrate and a slippery top layer. (b) Example images of droplets evaporating under fixed rms voltage (300 V) at constant angle on SOCAL. Sketches of the two types of slippery top-layers (c) Droplet on hydrophobic nanoparticle SLIPS, and (d) droplet on SOCAL.

electrowetting configuration allows the initial contact angle determined by the droplet-solid, droplet-lubricant, and other interfacial tensions to be reduced in a programmable manner by application of a voltage.

The electrowetting configuration to investigate evaporation at different constant contact angles on these surfaces is shown in Figure 1a with example evaporation images in Figure 1b and the schematics showing the two types of slippery surfaces in Figure 1c,d. An alternating current (AC) system was generated using a signal generator (TTi Instruments TGA1244) to generate a 10 kHz sinusoidal wave which was then amplified (Trek PZD700A) as a programmable root-mean-square (rms) voltage, V, within the range 0 to 450 V. The amplified signal was then applied to an aluminum-coated glass slide (100 μm, vapor deposited) as one electrode and a thin metal, 0.2 mm diameter, in the center of the droplet, as the second electrode. The cross sectional area of the needle is ~0.13 mm^2, compared to the surface area of a 8 μL droplet with 105° contact angle which is ~15.6 mm^2 (less than 1% of the total surface area); the needle is therefore not expected to have a significant effect on the spherical cap shape during the evaporation. The 100 μm thick glass coverslip on which the slippery coating (SOCAL or SLIPS) was attached acts as a dielectric that enables storage of capacitive energy and allows the contact area, and hence contact angle, to be adjusted by altering the balance between capacitive and interfacial energies. The droplets of deionized water used in the experiments had a volume of 8 μL, and 0.01 M KCl was added to ensure the electrical conductivity required for electrowetting. The thin metal electrode was lowered into the center of the droplet after deposition, and evaporation experiments were conducted at room temperature (22 ± 2 °C) at a controlled relative humidity of 70% within a transparent chamber to regulate the conditions local to the droplet. The chamber also shields the droplet from the presence of air drafts which might otherwise entrain the lubricant from a SLIP surface over an evaporating droplet.[39] Droplet evaporation sequences were recorded

https://dx.doi.org/10.1021/acs.langmuir.0c02020
Langmuir XXXX, XXX, XXX−XXX

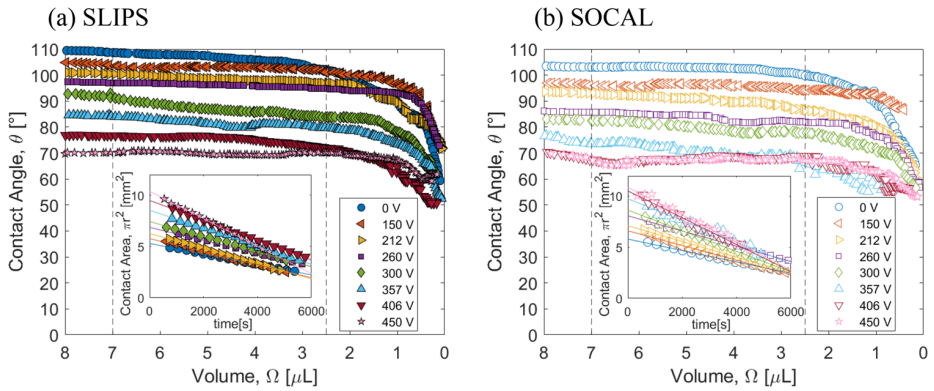

Figure 2. Contact angle as a function of reducing volume for 0.01 M KCl deionized water droplets evaporating at fixed electrowetting voltages on: (a) SLIPS and (b) SOCAL surface. Inset shows contact area as a function of time for the constant contact angle regime indicated by dashed lines.

using a camera at 0.05 frames per second, and contact radius r and contact angle θ measurements were determined using open-source pyDSA software.[40] Experimentally, profiles of the droplet were accurately described by a spherical cap to within a slight distortion around the electrode needle. The volume of the droplet during evaporation was calculated using the contact radius and contact angle. The data set presented in the Results and Discussion is a representative sample of wider body of experiments, and each evaporation at a fixed voltage for each surface is the average of three evaporation sequences.

The first type of slippery surface used SLIPS samples prepared by taking new glass coverslips (Thorlabs, CG00K1) of thickness (100 ± 5) μm, coating them with 5 layers of Glaco Mirror Coat (Nippon Shine) to create a nanoparticle-based superhydrophobic porous structure, and then infusing a layer of lubricant by withdrawal from a bath of 20 cSt silicone oil (Sigma-Aldrich, 378348) at 0.1 mm s^{-1}. Excess oil was rinsed off to ensure only a thin conformal oil layer remained on the surface so that there was no visible wetting ridge of oil on subsequent sessile droplets. The water contact angle hysteresis $\Delta\theta$ was determined by measuring advancing contact angle θ_A and receding contact angle θ_R through the average of three droplet inflation/deflation experiments in different locations on the substrate ($\Delta\theta$ = 0.4 ± 0.3°, θ_A/θ_R = 109.6°/109.2°). Sliding angles α were also measured by placing a 20 μL droplet of deionized water on the surface and tilting the substrate until the droplet begins to slide, and the average of three measurements gives $\alpha_{20\mu L}$ = 0.2 ± 0.2°. The measured contact angle is consistent with theoretical expectations of ca. 108° based on a liquid-form of Young's law (eq 4 in reference[20]) using an effective droplet-vapor interfacial tension as sum of the droplet-oil and oil-vapor interfacial tensions and indicates silicone oil should cloak the droplet-vapor interface despite the absence of a visible wetting ridge at the contact line.[19,20]

The second type of slippery surface used smooth liquid-like SOCAL surfaces prepared on glass samples (see refs 21 and 22). New glass coverslips of thickness of (100 ± 5) μm were exposed to air plasma in a (Henniker HPT-100) at 30W for 20 min. The coverslips were then dipped in a reactive solution of 91.45 mL isopropyl alcohol (≥99.7%, Sigma-Aldrich, 292907), 8.16 mL dimethyldimethoxysilane (95%, Sigma-Aldrich, 104906), and 0.39 mL sulfuric acid (95.0−98.0%, Sigma-Aldrich, 258105) for 5−10 s and then slowly removed. These coated glass slides were subsequently placed in a bespoke humidity chamber for 20 min at 60% ± 2% relative humidity to allow the acid-catalyzed polycondensation to take place. After this time, the surface was rinsed with isopropyl alcohol, toluene (≥99.5%, Sigma-Aldrich, 179418), and deionized water (type III, purified in an Elga PURELAB Option-Q lab water purification system) to remove any remaining reactive solution. This creates flexible polydimethylsiloxane chains approximately 4 nm in length that allow mobility of the droplet contact-line thereby minimizing contact line pinning.[21] For the confirmation of successful and homogeneous coating, contact angle hysteresis and sliding angles were measured in the same manner as that for the first surface and were determined to be $\Delta\theta$ = 1.0 ± 0.5°, θ_A/θ_R = 105.7°/104.7°, and $\alpha_{20\mu L}$ = 5.6 ± 0.4°. These values are in good agreement with Wang and McCarthy who reported $\Delta\theta$ = 1.0°, θ_A/θ_R = 104.6°/103.6°, and $\alpha_{20\mu L}$ = 4° for droplets of water. Using the same interfacial tensions as those for the silicone oil in the SLIPS but assuming the PDMS chains on a SOCAL surface cannot cloak the droplet-vapor interface, the liquid-form of Young's law suggests the water droplet should have a contact angle on SOCAL of ca. 104°, and this is consistent with the measured value.

RESULTS AND DISCUSSION

Constant Contact Angle Evaporation and the Diffusion Coefficient. We first discuss the qualitative features of the droplet evaporation. We observed that after a brief initial period (corresponding to a volume reduction from 8 to 7 μL), the contact angle remained approximately constant during the evaporation for most of the evaporation period on both types of slippery surfaces (Figure 2). In the last stage of the evaporation (corresponding to a volume reduction from 2.5 to 0 μL), we observe a decrease in the contact angle for both SLIPS and SOCAL surfaces. We rule out an effect from electric field causing the decrease in contact angle when the droplet is small, as the decrease also occurs for the 0 V evaporation. In our previous study on sessile water droplets evaporating on SOCAL surfaces, we suggest the decrease in contact angle could be due self-pinning after the precipitation of the trace salt in the droplet,[22] and it is plausible such an effect is occurring in our current study. We now look in detail at the constant contact angle region of the evaporation. Focusing on SLIP surfaces, the droplet evaporation sequences were consistent with prior literature.[18] However, because the samples here use thin conformal SLIP layers based on a hydrophobic nanoparticle coating, rather than lithographically produced micropillar textures with thicker layers of lubricant, there were no visible wetting ridges around the contact line. This is an improvement for evaporation studies since the oil in a wetting ridge removes some of the droplet-vapor surface area for evaporation. The application of a constant amplitude electrowetting voltage reduced the initial contact angle in a reproducible manner over many voltage cycles on the SLIP surfaces consistent with our previous report.[32] Figure 2a provides the first reports of droplet evaporation sequences with voltage selectable constant contact angle (ca. 70° to 105°) on SLIPS and covers the voltage range up to the saturation region well-known for electrowetting (see, e.g., ref 41).

https://dx.doi.org/10.1021/acs.langmuir.0c02020
Langmuir XXXX, XXX, XXX−XXX

Table 1. Experimentally Determined Diffusion Coefficients

slippery layer	rms voltage [V]	constant contact angle, θ_c [°]	$d(\pi r^2)/dt$ [$\times 10^{-4}$ mm^{2}s^{-1}]	$d\Omega^{2/3}/dt$ [$\times 10^{-3}\mu$L s^{-1}]	total evap time, t_f [s]	D_{Exp} [$\times 10^{-5}$m^{2}s^{-1}]
SLIPS	0	105.3 ± 1.6	−5.18 ± 0.03	−4.49 ± 0.03	8034 ± 960	1.84 ± 0.06
	150	102.5 ± 2.6	−6.60 ± 0.09	−4.43 ± 0.05	7877 ± 940	2.17 ± 0.07
	212	98.2 ± 2.2	−7.31 ± 0.05	−4.97 ± 0.04	9416 ± 1100	2.28 ± 0.08
	260	95.8 ± 0.4	−6.42 ± 0.02	−3.98 ± 0.02	8698 ± 1040	1.89 ± 0.05
	300	86.3 ± 3.6	−7.15 ± 0.06	−4.25 ± 0.04	10876 ± 1300	1.76 ± 0.09
	357	81.0 ± 6.0	−8.70 ± 0.09	−4.35 ± 0.02	9255 ± 1100	1.95 ± 0.16
	406	74.6 ± 2.2	−9.83 ± 0.05	−4.46 ± 0.02	9004 ± 1070	2.03 ± 0.09
	450	70.1 ± 1.4	−13.27 ± 0.12	−5.12 ± 0.05	10151 ± 1210	2.54 ± 0.11
SOCAL	0	102.1 ± 1.2	−5.76 ± 0.06	−4.10 ± 0.02	7806 ± 930	2.06 ± 0.06
	150	95.5 ± 2.8	−7.41 ± 0.10	−4.09 ± 0.04	9692 ± 1160	2.17 ± 0.09
	212	89.8 ± 3.6	−7.68 ± 0.08	−4.34 ± 0.03	9779 ± 1170	2.06 ± 0.10
	260	83.3 ± 2.8	−7.43 ± 0.06	−3.89 ± 0.03	10323 ± 1230	1.78 ± 0.07
	300	79.4 ± 3.6	−9.88 ± 0.08	−4.27 ± 0.04	10712 ± 1280	2.23 ± 0.11
	357	70.3 ± 2.2	−10.29 ± 0.30	−4.83 ± 0.07	8560 ± 1020	2.00 ± 0.10
	406	67.7 ± 2.4	−13.43 ± 0.26	−5.72 ± 0.04	8810 ± 1050	2.44 ± 0.12
	450	67.2 ± 3.0	−13.57 ± 0.29	−4.54 ± 0.08	10252 ± 1220	2.35 ± 0.13

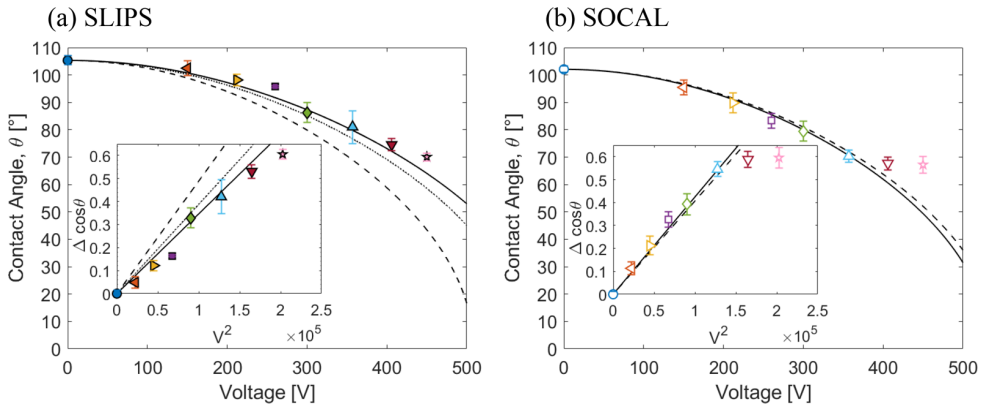

Figure 3. Cosine of average contact angle during evaporation (constant contact angle regime) as a function of voltage: (a) SLIPS and (b) SOCAL. Inset shows $\Delta\cos\theta$ as a function of V^2_{rms} fit (solid line) before saturation (voltage rms < 400 V). The dashed and dotted lines for SLIPS are predictions from theory assuming the droplet is cloaked and not cloaked in oil, respectively. The dashed lines for SOCAL are predictions from theory.

Focusing now on SOCAL surfaces, we observed the evaporation sequences to be consistent with that on the SLIPS surfaces and at zero applied voltage consistent with a prior report of evaporation on SOCAL.[41] We were also able to reduce the contact angle by the application of the electrowetting voltage and observe, for the first time, evaporation sequences with voltage selectable constant contact angle (ca. 67° to 102°) on SOCAL (Figure 2b). When repeatedly cycling the electrowetting voltage the contact angle hysteresis increased to ca. 3.6 ± 0.4°, which nonetheless remains low compared to other hydrophobic coatings. In such experiments, the contact angle measured during the constant contact angle period of evaporation at zero voltage after the first cycle was reduced from (102.1 ± 1.2°) to (94.9 ± 1.5°). However, it was possible to apply a constant electrowetting voltage to a freshly deposited droplet on different areas of a SOCAL surface and observe smoothly receding contact lines as the droplets evaporated. Figure 2b shows such data with each data point of an average of three droplets on a sample and shows constant contact angles of 102.1 ± 1.2° to 67.2 ± 3.0° for voltages with rms values between 0 and 450 V. The corresponding contact areas of droplets decrease linearly in time during the constant contact angle period of the evaporation (Figure 2a inset).

We now consider the quantitative analysis of the constant contact angle regime for both types of slippery surfaces to confirm the absolute slopes from the data in Figure 2 are physically reasonable. Rearranging eq 9, the diffusion coefficient can be determined from the evaporation of a droplet using the average rate of change in contact area (slope in the insets to Figure 2), i.e.,

$$D = -\frac{\rho\beta(\theta)}{8\pi(c_s - c_\infty)\sin^2\theta f_{PB}(\theta)}\frac{d(\pi r^2)}{dt} \quad (14)$$

where $f(\theta)$ is evaluated using the Picknett and Bexon interpolation formula (eq 7). Table 1 shows these calculated diffusion coefficients across the electrowetting voltage range (prior to contact angle saturation) are in good agreement with the literature diffusion coefficient. On the SLIP surfaces, the average diffusion coefficient measured experimentally is $D_{Exp} = (2.06 \pm 0.26) \times 10^{-5}$ m^{2}s^{-1} compared to the literature value of $D_{lit} = (2.41 \pm 0.05) \times 10^{-5}$ m^{2}s^{-1}.[42] On the SOCAL surfaces, the experimental average was found to be $D_{Exp} = (2.14 \pm 0.21) \times 10^{-5}$ m^{2}s^{-1}, and using data for droplets on both types of

https://dx.doi.org/10.1021/acs.langmuir.0c02020
Langmuir XXXX, XXX, XXX−XXX

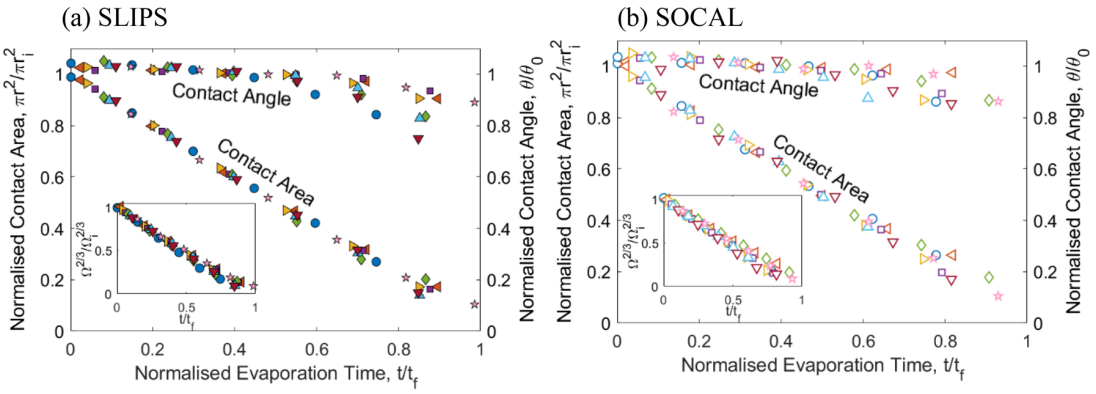

Figure 4. Scaling of evaporation measurements with droplet lifetime. Normalized contact area, $\pi r^2/\pi r_i^2$ as a function of normalized time, t/t_f and normalized contact angle, θ/θ_c as a function of normalized time t/t_f. Insets: normalized volume $\Omega^{2/3}/\Omega_i^{2/3}$ as a function of normalized time, t/t_f. Data presented is every 50th data point for clarity of presentation.

surfaces, the experimental average was $D_{Exp} = (2.10 \pm 0.24) \times 10^{-5}$ m^{2}s^{-1}. We also verified that the 2/3 power law for the drop volume (i.e., eq 11) was obeyed, and the slopes from that analysis are also given in Table 1 along with the value determined for the constant contact angle and the droplet lifetime (see analysis and discussion in the section Dependence of Initial Contact Angle on the Voltage). These results also support the assumption that electrowetting does not significantly alter the evaporation of sessile droplets from these surfaces.

Dependence of Initial Contact Angle on the Voltage. We now consider the consistency of the observed voltage-selected contact angles with expectations from the theory of electrowetting. In the absence of contact line pinning, the initial contact angle without an applied voltage is assumed to be given by Young's law. The effect of applying a voltage and charging a dielectric using the contact area of a droplet as one electrode is to introduce a capacitive energy in addition to interfacial energies. This causes a voltage dependent contact angle, $\theta(V)$, described by the Young-Lippmann equation

$$\cos\theta(V) = \cos\theta_o + \frac{\varepsilon_0\varepsilon_d}{2\gamma_{LV}d}V^2 \tag{15}$$

where $\theta_0 = \theta(V = 0)$ is the initial contact angle prior to the application of a voltage, ε_0 is the permittivity of free space, ε_d is the relative permittivity of the dielectric, and d is the dielectric thickness. We therefore expect a quadratic power law dependence of cos θ on the voltage, and this is confirmed for both the SLIP and SOCAL surfaces by Figure 3. The insets in Figure 3 show a linear plot of the $\Delta\cos\theta$ with V^2, and the saturation effect of wetting is clearly visible for the SOCAL surface.

To compare quantitively to the theoretical expectations from eq 15, we first consider the slippery SOCAL layer. This has a sufficiently small thickness (ca. 4 nm) to be a negligible correction to the dielectric thickness due to the 100 μm thick glass substrate, and the covalently attached PDMS chains mean there is no cloaking of the droplet-vapor interface. The glass has a manufacturer-stated relative permittivity $\varepsilon_{glass} = 6.7$; therefore, using a surface tension for water of $\gamma_{LV} = 72.8$ mN m^{-1} gives $\varepsilon_o\varepsilon_d/2\gamma_{LV}d = 4.07 \times 10^{-6}$ V^{-2}. This can be compared to the slope $\Delta\cos\theta/V^2$ in the inset in Figure 3b for the experimental data for SOCAL. The experimental result of $(4.20 \pm 0.10) \times 10^{-6}$ V^{-2} using data below the contact angle saturation voltage of 400 V is in excellent agreement with the theoretical value.

We now consider the consistency theory between the theory and the experimental results for droplets on SLIPS. In this case, we regard the glass substrate and the SLIPS layer as a series capacitive combination of the glass with the SLIPS layer so that the relative dielectric thickness is $(d/\varepsilon_r)_{total} = (d/\varepsilon_r)_{glass} + (d/\varepsilon_r)_{SLIPS}$. The major contribution to the capacitance is therefore from the glass substrate and this gives an order of magnitude estimate consistent with the experimental data. To estimate the small correction due to the SLIPS, we use the thickness of the porous Glaco layer, ~2 μm, infused with silicone oil with excess oil removed through rinsing, as the thickness of the SLIPS later. Moreover, since the relative permittivity of the silica nanoparticles ($\varepsilon_r = 2.5-3.5$) and oil ($\varepsilon_r = 2.68$) in the SLIPS layer are similar and the layer is a small correction, we can approximate it to a uniform dielectric layer with $\varepsilon_r \sim 2.68$. This provides an estimate of $(d/\varepsilon_r)_{SLIPS} = 6.38 \times 10^4$ m. In addition to these dielectric considerations, we also expect the droplet-vapor interface to be cloaked so that an effective interfacial tension should be used in eq 15 replacing γ_{LV} by $\gamma_{Eff} = \gamma_{WO} + \gamma_{OA}$, where γ_{WO} and γ_{OA} are the water-oil and oil-air interfacial tensions, respectively. Using the interfacial tension data from Banpurkar et al.,[43] the oil–water interfacial is estimated at $\gamma_{OW} = 38$ mN m^{-1}, and from the data of McHale et al.,[20] the oil-air interfacial tension is $\gamma_{OA} = 19.8$ mN m^{-1} giving an effective interfacial tension of $\gamma_{Eff} = 57.8$ mN m^{-1}. Including this cloaking effect gives $\varepsilon_o\varepsilon_d/2\gamma_{Eff}d = 4.89 \times 10^{-6}$ V^{-2} and thus overestimates the contact angle changes compared to the experimental data (dashed line compared to symbols in Figure 3a). However, assuming that oil does not cloak the droplet-air interface gives $\varepsilon_o\varepsilon_d/2\gamma_{LV}d = 3.88 \times 10^{-6}$ V^{-2}, where $\gamma_{LV} = 72.8$ mN m^{-1}, and this is closer to the fit to the data which is $\varepsilon_o\varepsilon_d/2\gamma_{LV}d = (3.47 \pm 0.11) \times 10^{-6}$ V^{-2} (dotted lines compared to solid lines in Figure 3a). This is contrary to expectations on the state expected from the analysis by Smith et al. (i.e., their A3-W3 state) and therefore suggests an additional effect from the electric field.[44] To fit the curve using eq 15 and an oil-cloaked droplet-air, we would require a significantly smaller value of the relative permittivity (~75%) than the manufacturer-provided value and/or a significantly thicker (~40%) glass substrate.

Droplet Lifetime Dependence on Contact Angle. We now consider the extent to which the lifetime of an evaporating

https://dx.doi.org/10.1021/acs.langmuir.0c02020
Langmuir XXXX, XXX, XXX−XXX

droplet, t_f, depends on its initial contact angle. From the fits to the contact area for each evaporating droplet sequence, the lifetime was determined (Figure 2 inset), and these values are given in Table 1 for each surface. For scaling dependence, Figure 4 shows the contact area normalized by the initial contact area (using the intercepts in the insets in Figure 2) as a function of time normalized by total evaporation time for droplets on each surface. The secondary y-axis in each figure shows the contact angle normalized by the constant contact angle. A similar collapse of data onto a single scaling curve can be observed for the 2/3 power law for the drop volume, and this illustrates the good agreement with the power law on these slippery surfaces (insets in Figure 4).

Equation 13 shows that the lifetime is a separable product of three functions involving the constant contact angle, θ_c, the initial droplet volume, Ω_i, and the parameter λ which incorporates the density, ρ, difference in vapor concentration, Δc, and diffusion coefficient, D, i.e.,

$$t_f(\theta_c, \lambda, \Omega_i) = \tilde{t}(\theta_c)\xi(\lambda)\Omega_i^{2/3} \tag{16}$$

where the contact angle dependent factor is

$$\tilde{t}(\theta_c) = \frac{\beta^{1/3}(\theta_c)}{2^{4/3}f(\theta_c)} \tag{17}$$

and various other dependencies have been grouped together as

$$\xi(\lambda) = \frac{4(18\pi)^{1/3}}{\lambda} = \frac{2(18\pi^2)^{1/3}\rho}{D(c_s - c_\infty)} \tag{18}$$

According to Stauber et al., the droplet lifetime in the constant contact angle mode of evaporation has a maximum at $\theta = 90°$.[36] This is illustrated by the solid curve in Figure 5

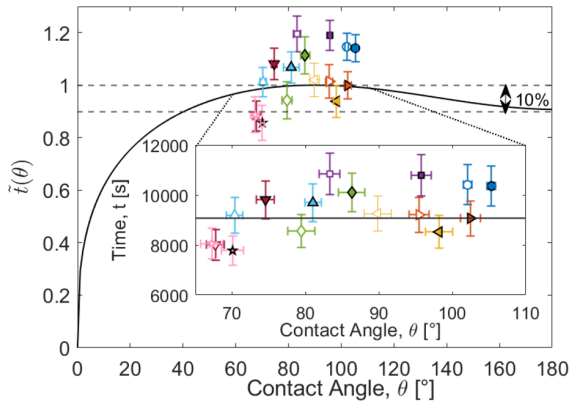

Figure 5. Drop lifetime contact angle dependence factor, $\tilde{t}(\theta)$ (Solid line theory, solid symbols are experimental data for SLIPS and empty symbols are experimental data for SOCAL surfaces). Inset: expanded view of the contact angle range 67°−105° (i.e., cos θ = 0.39 to −0.26) plotted with absolute time as the vertical axis (eq 16).

showing a plot of eq 17 over the full contact angle range, from a film with $\theta = 0°$, to a spherical sessile droplet with $\theta = 180°$ using the Picknett and Bexon polynomial interpolation (eq 7) for $f(\theta)$ in eq 17. To understand the contact angle dependence of the total evaporation time for surfaces with contact angles close to the maximum (i.e., $\theta = 90°$), we approximate eq 17 to quadratic order around $\theta = 90°$ using Stauber et al.'s formula for $f(\theta)$. This gives a quadratic expansion approximation around the maximum of

$$\tilde{t}(\theta) \approx 1 - \frac{(9\pi - 32)(\theta - \pi/2)^2}{6} \tag{19}$$

where θ is in radians. One can obtain the same result by numerically fitting a second order polynomial to eq 17 using the explicit expression $f_{PB}(\theta)$ provided by Picknett and Bexon. From the full plot in Figure 5, we note the contact angle dependence is predicted to be relatively insensitive to the precise value of θ and remains within 10% of the maximum value over the contact angle range from 40° to 180°. In experiments using smooth surfaces, i.e., not superhydrophobic, the maximum achievable contact angles with surface chemistry is ∼115° rather than the parameter maximum of 180° in the theory. We have therefore provided an inset in Figure 5 showing the more limited range bounded by the lower limit due to contact angle saturation in electrowetting (∼67°) and the maximum achievable contact angle (105°) on our smooth surfaces; this covers a wide range of cos θ from 0.39 to −0.26.

To analyze the contact angle dependence of the experimentally determined lifetimes, we assume a droplet had an initial volume of (8.0 ± 0.1) μL and a temperature of (22 ± 2 °C) and was evaporated in air with a relative humidity of (70 ± 1%) which gives a value of $\xi(\lambda)\Omega_i^{2/3}$ = 9070 ± 990. The values of droplet lifetime from Table 1 scaled down by this value are plotted in Figure 5 for comparison to the theory with the absolute lifetimes shown in the inset; the average value for t_f from Table 1 is (9330 ± 1000) s. The solid symbols show the data from the SLIP surface and the empty symbols show the data from the SOCAL surface. This data covers a contact angle range from hydrophilic (lowest value θ_c = 67°) to hydrophobic 106° (highest value) and shows a scatter around an average value without an obvious contact angle trend. The data appears to lie slightly above eq 17 suggesting a slight systematic error in the value of $\xi(\lambda)\Omega_i^{2/3}$ used in the analysis.

From our results, we conclude that in the constant contact angle mode of evaporation and for constant contact angles above 40°, drop lifetimes can be predicted within a 10% tolerance range without precise knowledge of the exact value of the contact angle by using eq 16 with $\tilde{t} \sim 1$, i.e., drop lifetimes have a weak dependence on the contact angle for a broad range of constant contact angles above 40°. Improved estimates could also be made by calibrating experimentally over a specific contact angle range to use a value of $\tilde{t}$ slightly below unity, i.e.,

$$t_f(\lambda, \Omega_i) = \langle\tilde{t}\rangle\xi(\lambda)\Omega_i^{2/3} \tag{20}$$

where $\langle\tilde{t}\rangle$ is an experimentally determined calibration constant (with a value close to unity) over the relevant contact angle range, which should be above 40°. It should also be possible to decide a desired tolerance on the droplet lifetime and from that determine what range of contact angles needs to be achieved. In practical applications where drying is important, knowledge of initial droplet volume, the liquid density, the temperature, and relative humidity (or diffusion coefficient and difference in saturation and ambient vapor concentration) should be sufficient to predict drying time providing the surface allows a mobile contact line without contact line pinning and the contact angle is above ∼40°. These results also show that the initial droplet contact area on a slippery surface can be selected when the contact angle is above ∼40° without significantly changing the overall droplet evaporation time.

https://dx.doi.org/10.1021/acs.langmuir.0c02020
Langmuir XXXX, XXX, XXX−XXX

CONCLUSION

Our results show that control of constant contact angle mode evaporation over a wide range of receding contact angles, from hydrophilic to hydrophobic, of droplets on pinning free SOCAL and SLIP surfaces can be achieved by using electrowetting. The results are consistent with the model of diffusion-controlled evaporation of sessile droplets and can be used to estimate the diffusion coefficient. The contact angle-voltage relationship is in excellent agreement with the Young-Lippmann equation for electrowetting of droplets on both types of slippery surfaces. We have also observed that over a range of contact angles above 67° on these surfaces, droplet evaporation times are relatively insensitive to the precise value of the contact angle. Thus, a desired tolerance on droplet lifetime can be used to determine what contact angle range and accuracy is required. This may have practical application in processes involving evaporation, such as inkjet printing, where consistent drying times would then depend mainly on the liquid density, control of droplet deposition volume, and environmental factors, such as temperature and relative humidity.

AUTHOR INFORMATION

Corresponding Author

G. McHale − *Smart Materials & Surfaces Laboratory, Faculty of Engineering & Environment, Northumbria University, Newcastle upon Tyne NE1 8ST, U.K.; School of Engineering, University of Edinburgh, Edinburgh EH9 3FB, U.K.;* orcid.org/0000-0002-8519-7986; Email: glen.mchale@ed.ac.uk

Authors

S. Armstrong − *Smart Materials & Surfaces Laboratory, Faculty of Engineering & Environment, Northumbria University, Newcastle upon Tyne NE1 8ST, U.K.; School of Engineering, University of Edinburgh, Edinburgh EH9 3FB, U.K.;* orcid.org/0000-0002-0520-8498

R. Ledesma-Aguilar − *Smart Materials & Surfaces Laboratory, Faculty of Engineering & Environment, Northumbria University, Newcastle upon Tyne NE1 8ST, U.K.; School of Engineering, University of Edinburgh, Edinburgh EH9 3FB, U.K.;* orcid.org/0000-0001-8714-0556

G. G. Wells − *Smart Materials & Surfaces Laboratory, Faculty of Engineering & Environment, Northumbria University, Newcastle upon Tyne NE1 8ST, U.K.; School of Engineering, University of Edinburgh, Edinburgh EH9 3FB, U.K.;* orcid.org/0000-0002-8448-537X

Complete contact information is available at: https://pubs.acs.org/10.1021/acs.langmuir.0c02020

Notes

The authors declare no competing financial interest.

ACKNOWLEDGMENTS

S.A. would like to thank Dr. Andrew M.J. Edwards at Nottingham Trent University for discussions and advice on electrowetting. S.A. would like to acknowledge the University of Northumbria at Newcastle for financial support.

REFERENCES

(1) Yuen, M. C.; Chen, L. W. Heat-Transfer Measurements of Evaporating Liquid Droplets. *Int. J. Heat Mass Transfer* **1978**, *21* (5), 537−542.

(2) McHale, G. Surface Free Energy and Microarray Deposition Technology. *Analyst* **2007**, *132*, 192−195.

(3) Lim, T.; Han, S.; Chung, J.; Chung, J. T.; Ko, S.; Grigoropoulos, C. P. Experimental Study on Spreading and Evaporation of Inkjet Printed Pico-Liter Droplet on a Heated Substrate. *Int. J. Heat Mass Transfer* **2009**, *52* (1−2), 431−441.

(4) Erbil, H. Y. Evaporation of Pure Liquid Sessile and Spherical Suspended Drops: A Review. *Adv. Colloid Interface Sci.*. Elsevier B.V: January 2012; pp 67−86. DOI: 10.1016/j.cis.2011.12.006.

(5) Cazabat, A.-M.; Guéna, G. Evaporation of Macroscopic Sessile Droplets. *Soft Matter* **2010**, *6* (12), 2591.

(6) Larson, R. G. Transport and Deposition Patterns in Drying Sessile Droplets. *AIChE J.* **2014**, *60* (5), 1538−1571.

(7) Frommelt, T.; Kostur, M.; Wenzel-Schäfer, M.; Talkner, P.; Hänggi, P.; Wixforth, A. Microfluidic Mixing via Acoustically Driven Chaotic Advection. *Phys. Rev. Lett.* **2008**, *100* (3), 1−4.

(8) Eral, H. B.; Augustine, D. M.; Duits, M. H. G.; Mugele, F. Suppressing the Coffee Stain Effect: How to Control Colloidal Self-Assembly in Evaporating Drops Using Electrowetting. *Soft Matter* **2011**, *7* (10), 4954−4958.

(9) Deegan, R. D.; Bakajin, O.; Dupont, T. F.; Huber, G.; Nagel, S. R.; Witten, T. A. Capillary Flow as the Cause of Ring Stains from Dried Liquid Drops. *Nature* **1997**, *389* (6653), 827−829.

(10) Wixforth, A.; Strobl, C.; Gauer, C.; Toegl, A.; Scriba, J.; Guttenberg, Z. V. Acoustic Manipulation of Small Droplets. *Anal. Bioanal. Chem.* **2004**, *379* (7−8), 982−991.

(11) Eral, H. B.; Augustine, D. M.; Duits, M. H. G.; Mugele, F. Suppressing the Coffee Stain Effect: How to Control Colloidal Self-Assembly in Evaporating Drops Using Electrowetting. *Soft Matter* **2011**, *7* (10), 4954−4958.

(12) Onda, T.; Shibuichi, S.; Satoh, N.; Tsujii, K. Super-Water-Repellent Fractal Surfaces. *Langmuir* **1996**, *12* (9), 2125−2127.

(13) Neinhuis, C.; Barthlott, W. Characterization and Distribution of Water-Repellent, Self-Cleaning Plant Surfaces. *Ann. Bot.* **1997**, *79* (6), 667−677.

(14) Shirtcliffe, N. J.; McHale, G.; Atherton, S.; Newton, M. I. An Introduction to Superhydrophobicity. *Adv. Colloid Interface Sci.* **2010**, *161* (1−2), 124−138.

(15) McHale, G.; Aqil, S.; Shirtcliffe, N. J.; Newton, M. I.; Erbil, H. Y. Analysis of Droplet Evaporation on a Superhydrophobic Surface. *Langmuir* **2005**, *21* (24), 11053−11060.

(16) Gibbons, M. J.; Di Marco, P.; Robinson, A. J. Local Heat Transfer to an Evaporating Superhydrophobic Droplet. *Int. J. Heat Mass Transfer* **2018**, *121*, 641−652.

(17) Wong, T.-S.; Kang, S. H.; Tang, S. K. Y.; Smythe, E. J.; Hatton, B. D.; Grinthal, A.; Aizenberg, J. Bioinspired Self-Repairing Slippery Surfaces with Pressure-Stable Omniphobicity. *Nature* **2011**, *477* (7365), 443−447.

(18) Guan, J. H.; Wells, G. G.; Xu, B.; McHale, G.; Wood, D.; Martin, J.; Stuart-Cole, S. Evaporation of Sessile Droplets on Slippery Liquid-Infused Porous Surfaces (SLIPS). *Langmuir* **2015**, *31* (43), 11781−11789.

(19) Semprebon, C.; McHale, G.; Kusumaatmaja, H. Apparent Contact Angle and Contact Angle Hysteresis on Liquid Infused Surfaces. *Soft Matter* **2017**, *13* (1), 101−110.

(20) McHale, G.; Orme, B. V.; Wells, G. G.; Ledesma-Aguilar, R. Apparent Contact Angles on Lubricant-Impregnated Surfaces/SLIPS: From Superhydrophobicity to Electrowetting. *Langmuir* **2019**, *35* (11), 4197−4204.

(21) Wang, L.; McCarthy, T. J. Covalently Attached Liquids: Instant Omniphobic Surfaces with Unprecedented Repellency. *Angew. Chem., Int. Ed.* **2016**, *55* (1), 244−248.

(22) Armstrong, S.; McHale, G.; Ledesma-Aguilar, R. A.; Wells, G. G. Pinning-Free Evaporation of Sessile Droplets of Water from Solid Surfaces. *Langmuir* **2019**, *35* (8), 2989−2996.

(23) Vallet, M.; Vallade, M.; Berge, B. Limiting Phenomena for the Spreading of Water on Polymer Films by Electrowetting. *Eur. Phys. J. B* **1999**, *591*, 583−591.
(24) Mugele, F.; Baret, J.-C. Electrowetting: From Basics to Applications. *J. Phys.: Condens. Matter* **2005**, *17* (28), R705−R774.
(25) Pollack, M. G.; Fair, R. B.; Shenderov, A. D. Electrowetting-Based Actuation of Liquid Droplets for Microfluidic Applications. *Appl. Phys. Lett.* **2000**, *77* (11), 1725−1726.
(26) Paik, P.; Pamula, V. K.; Pollack, M. G.; Fair, R. B. Electrowetting-Based Droplet Mixers for Microfluidic Systems. *Lab Chip* **2003**, *3* (1), 28−33.
(27) Xie, K.; Lai, Y.; Guo, X.; Campbell, R. J. A Three-Phased Circular Electrode Array for Electro-Osmotic Microfluidic Pumping. *Microsyst. Technol.* **2011**, *17* (3), 367−372.
(28) Berge, B.; Peseux, J. Variable Focal Lens Controlled by an External Voltage: An Application of Electrowetting. *Eur. Phys. J. E: Soft Matter Biol. Phys.* **2000**, *3* (2), 159−163.
(29) McHale, G.; Brown, C. V.; Newton, M. I.; Wells, G. G.; Sampara, N. *Proc. SPIE* **2012**, *8557*, 855703.
(30) Hao, C.; Liu, Y.; Chen, X.; He, Y.; Li, Q.; Li, K. Y.; Wang, Z. Electrowetting on Liquid-Infused Film (EWOLF): Complete Reversibility and Controlled Droplet Oscillation Suppression for Fast Optical Imaging. *Sci. Rep.* 2014, *4* (6846). DOI: 10.1038/srep06846.
(31) Bormashenko, E.; Pogreb, R.; Bormashenko, Y.; Grynyov, R.; Gendelman, O. Low Voltage Reversible Electrowetting Exploiting Lubricated Polymer Honeycomb Substrates. *Appl. Phys. Lett.* **2014**, *104* (17), 171601.
(32) Brabcova, Z.; McHale, G.; Wells, G. G.; Brown, C. V.; Newton, M. I. Electric Field Induced Reversible Spreading of Droplets into Films on Lubricant Impregnated Surfaces. *Appl. Phys. Lett.* **2017**, *110* (12), 121603.
(33) Ruiz-Gutiérrez, É.; Ledesma-Aguilar, R. Lattice-Boltzmann Simulations of Electrowetting Phenomena. *Langmuir* **2019**, *35* (14), 4849−4859.
(34) Picknett, R. G.; Bexon, R. The Evaporation of Sessile or Pendant Drops in Still Air. *J. Colloid Interface Sci.* **1977**, *61* (2), 336−350.
(35) Erbil, H. Y.; McHale, G.; Newton, M. I. M. I. Drop Evaporation on Solid Surfaces: Constant Contact Angle Mode. *Langmuir* **2002**, *18* (7), 2636−2641.
(36) Stauber, J. M.; Wilson, S. K.; Duffy, B. R.; Sefiane, K. On the Lifetimes of Evaporating Droplets. *J. Fluid Mech.* **2014**, *744*, R2.
(37) Stauber, J. M.; Wilson, S. K.; Duffy, B. R.; Sefiane, K. On the Lifetimes of Evaporating Droplets with Related Initial and Receding Contact Angles. *Phys. Fluids* **2015**, *27* (12), 124102.
(38) Young, T. An Essay on the Cohesion of Fluids. *Philos. Trans. R. Soc. London* **1805**, *95*, 65−87.
(39) Kreder, M. J.; Daniel, D.; Tetreault, A.; Cao, Z.; Lemaire, B.; Timonen, J. V. I.; Aizenberg, J. Film Dynamics and Lubricant Depletion by Droplets Moving on Lubricated Surfaces. *Phys. Rev. X* 2018, *8* (3). DOI: 10.1103/PhysRevX.8.031053.
(40) Launay, G. PyDSA: Drop Shape Analysis in Python https://framagit.org/gabylaunay/pyDSA_gui (accessed Feb 10, 2019).
(41) Mugele, F.; Heikenfeld, J. *Electrowetting: Fundamental Principles and Practical Applications*; Wiley VCH: 2019.
(42) Lide, D. R. *CRC Handbook of Chemistry and Physics: A Ready Reference Book of Chemical and Physical Data*; 1992; Vol. *268*. DOI: 10.1016/0022-2860(92)85083-S.
(43) Banpurkar, A. G.; Nichols, K. P.; Mugele, F. Electrowetting-Based Microdrop Tensiometer. *Langmuir* **2008**, *24* (19), 10549−10551.
(44) Smith, J. D.; Dhiman, R.; Anand, S.; Reza-Garduno, E.; Cohen, R. E.; McKinley, G. H.; Varanasi, K. K. Droplet Mobility on Lubricant-Impregnated Surfaces. *Soft Matter* **2013**, *9* (6), 1772−1780.

https://dx.doi.org/10.1021/acs.langmuir.0c02020
Langmuir XXXX, XXX, XXX−XXX

Received: 5 May 2020 | Revised: 18 September 2020 | Accepted: 20 September 2020

DOI: 10.1111/ejss.13053

ORIGINAL ARTICLE

European Journal of Soil Science WILEY

Slippery liquid-infused porous surfaces: The effect of oil on the water repellence of hydrophobic and superhydrophobic soils

Rebecca McCerery[1] | **John Woodward**[1] | **Glen McHale**[2,3] | **Kate Winter**[1] | **Steven Armstrong**[2,3] | **Bethany V. Orme**[2]

[1]Department of Geography and Environmental Sciences, Faculty of Engineering and Environment, Northumbria University, Newcastle-Upon-Tyne, UK

[2]Smart Materials and Surfaces Laboratory, Faculty of Engineering and Environment, Northumbria University, Newcastle-Upon-Tyne, UK

[3]Institute for Multiscale Thermofluids, School of Engineering, University of Edinburgh, Edinburgh, UK

Correspondence
Rebecca McCerery, Department of Geography and Environmental Sciences, Faculty of Engineering and Environment, Northumbria University, Newcastle-upon-Tyne, NE1 8ST, UK.
Email: rebecca.mccerery@northumbria.ac.uk

Abstract

Soil wettability is important for understanding a wide range of earth system processes, from agricultural productivity to debris flows and sediment fan formation. However, there is limited research considering how soil–water interactions, where the soil grains are naturally hydrophobic, might change in the presence of oil from natural hydrocarbon leakage or oil spills. Here we show how slippery liquid-infused porous surfaces (SLIPS) apply to hydrophobic soils, by physical modelling of surfaces of different grain sizes and examining their interactions with water before and after impregnation with silicone oil. Using contact and sliding angle measurements and laser scanning fluorescence confocal microscopy, we demonstrate that soil SLIPS can be created with thick oil layers and thin conformal oil layers on median grain sizes of 231 μm and 32 μm, respectively. Until now, SLIPS have only been observed in human-made materials and biological surfaces. The mechanisms reported here demonstrate that SLIPS can occur in natural granular materials, providing a new mechanism for water-shedding in soil and sediment systems. Furthermore, the water-shedding properties may be long lasting as conformal oil layers are stabilized by capillary forces. These results have important implications for understanding soil physics and mechanics where oil is present in a soil, and for agricultural hydrophobicity on shallow slopes.

Highlights

- We model oil contamination on a hydrophobic model soil as a mechanism for creating SLIPS.
- Soil SLIPS have implications for water-shedding, oil spill remediation and earth processes.
- Our model soils exhibit extreme water-shedding, illustrated by low water droplet sliding angles.

- This is the first physical modelling observation of SLIPS arising from hydrophobic soil.

KEYWORDS

earth processes, hydrophobicity, oil contamination, sediments, slippery liquid-infused porous surfaces, soil systems, soil water repellence, superhydrophobicity

1 | INTRODUCTION

Wettability is a measure of a soil's affinity for water. Water-repellent, or hydrophobic, soil has a low affinity for water and low rates of infiltration, with hydrological and geomorphological consequences (Jordán, Zavala, Mataix-Solera, & Doerr, 2013). Water-repellent soils are prevalent across the world in different climates and environments, from the sub-tropics to the Arctic (Dekker & Ritsema, 1994; Jordán et al., 2013). The negative consequences of water repellence are widely reported; one of the most observed is a reduction in soil productivity. This is widespread in southern and western Australia, which contains the world's largest area of water-repellent soils, with over 5 million hectares of agricultural land being affected (Blackwell, 2000). Water repellence leads to poor agricultural productivity due to the formation of preferential flow paths and finger flow, which affects the transport of water and solutes (Shakesby, Doerr, & Walsh, 2000; van Ommen, Dekker, Dijksma, Hulshof, & van der Molen, 1988; Wang et al., 2018). In some circumstances, this can also lead to groundwater contamination through leaching of pesticides and other substances (Blackwell, 2000; Van Dam et al., 1990). Water repellence also influences surface processes as soils become more susceptible to both water and wind erosion (Cannon, Bigio, & Mine, 2001; Cannon, Gartner, Wilson, Bowers, & Laber, 2008; Parise & Cannon, 2012). High water repellence can increase the occurrence of debris flow events, considered to be one of the most destructive consequences of soil water repellence with a known risk to human life (DiBiase & Lamb, 2020). However, a reduction in water infiltration can also have beneficial consequences, by improving the structural and aggregate stability of affected soils (Bachmann et al., 2008; Hallett, Baumgartl, & Young, 2001). For hydrophobic soil, this stability can also lead to reduced evaporation of water from deep within the soil profile (Hallett, 2007); a similar process also increases carbon sequestration, through reduced biodegradation of organic matter or increased aggregate stability (Bachmann et al., 2008; Piccolo, Spaccini, Haberhauer, & Gerzabek, 1999; Spaccini, Piccolo, Conte, Haberhauer, & Gerzabek, 2002).

There are at least five pathways by which water repellence can be induced in soil environments. First, it can be created beneath particular types of plants (DeBano, 2000; Doerr et al., 2006; Doerr, Ritsema, Dekker, Scott, & Carter, 2007; Doerr, Shakesby, & Walsh, 2000). This occurs where hydrophobic waxes and other organic substances create a coating on the soil grains through degradation of plant litter (Doerr, Shakesby, & Walsh, 1996). This is common in eucalyptus forests, where water repellence can develop rapidly after eucalyptus is planted on previously hydrophilic soil (Doerr, Shakesby, & Walsh, 1998). Second, the presence of hydrophobins (small amino acids found in filamentous fungi such as mycelia) (Wessels, 1996) can induce water repellence due to the inherent hydrophobicity of the hydrophobin proteins on the fungi surface (Chau, Goh, Vujanovic, & Si, 2012; Linder, 2009). A similar process caused by bacteria extracellular polymeric substances has also been linked to soil water repellence, with the creation of hydrophobic bacterial biofilms by certain species (Doerr et al., 2007; Schaumann et al., 2007). Third, wildfire events burning organic materials can cause volatilization of waxes in the surface litter, creating a hydrophobic coating on affected soil grains (DeBano, 2000; Doerr et al., 2000, 2006; McHale, Shirtcliffe, Newton, Pyatt, & Doerr, 2007). This process is commonly seen in the western USA and can result in increased runoff and erosion (Woods, Birkas, & Ahl, 2007). The fourth mechanism is the disposal of wastewater into the environment. This occurs through irrigation of soils using greywater, containing oil, grease and other hydrophobic compounds, a practice that is increasing in regions of the world that experience water scarcity (Hamlett et al., 2011; Maimon, Gross, & Arye, 2017; Mataix-Solera et al., 2011). Finally, oil contamination either through direct oil spills or hydrocarbon seepage from sedimentary basins can induce water repellence (Ellis & Adams, 1961; McHale, Shirtcliffe, Newton, Pyatt, & Doerr, 2007; Roy & McGill, 1998). Oil contamination is particularly difficult to remediate, with water repellence persisting for decades after contamination (Roy, McGill, & Rawluk, 1999). For example, crude oil spill sites in Alberta, Canada, have been unable to naturally rectify themselves after oil spills in Devon in 1947 and Bruderheim in 1982 (Roy & McGill, 1998). These soils continue to be non-wettable and unable to support plant growth (Roy et al., 1999; Roy & McGill, 1998, 2000).

Several structural and environmental properties influence the expression of water repellence in soils. Smaller, sand-sized grains tend to display the highest degree of water repellence, attributed to the existence of gaps between grains and a higher organic matter content (de Jonge, Jacobsen, & Moldrup, 1999; Doerr et al., 1996, 2007; McHale, Shirtcliffe, Newton, & Pyatt, 2007). Studies have also attempted to correlate changes in soil water content (e.g. de Jonge, Moldrup, & Jacobsen, 2007; Dekker, Doerr, Oostindie, Ziogas, & Ritsema, 2001; Leelamanie & Karube, 2007; Regalado & Ritter, 2006) and soil temperature (e.g., de Jonge et al., 1999; Doerr et al., 2007; Doerr, Dekker, Ritsema, Shakesby, & Bryant, 2002; Jordán et al., 2013; van Ommen et al., 1988) with different degrees of hydrophobicity, but contradictory results suggest these processes are not fully understood.

2 | CONCEPTS OF WATER REPELLENCE

Soil water repellence can be measured in the field and the laboratory using a range of water-droplet methods. When a droplet rests on a surface, it will adopt a shape based on its volume and liquid surface tension (γ_{LV}), and the surface properties, influenced by the extent of their water repellence. For small droplets, of a size less than the capillary length (l_c):

$$l_c = (\gamma_{LV}/\rho g)^{1/2}, \quad (1)$$

where ρ is the liquid density and $g = 9.81\ \mathrm{ms}^{-2}$ is the acceleration due to gravity; capillary forces dominate over gravity, creating a spherical cap shape. When the surface is granular, like soils, evaporation and infiltration of water into the pore structure may occur over time, with their relative importance determined by the wettability (Letey, Osborn, & Pelishek, 1962). If infiltration is more prevalent than evaporation, water drop penetration time (WDPT) measurements can be employed (Robichaud, Lewis, & Ashmun, 2008; Tessler, Wittenberg, Malkinson, & Greenbaum, 2008). If droplets do not infiltrate rapidly, a contact angle (θ) may be measured from the side profile of a droplet. This method was adapted by Bachmann, Ellies, and Hartge (2000) for use in characterizing the wettability of soils, whereby monolayers of soil particles were fixed to a surface to capture the wetting properties through contact angle measurements on the interfacial layer.

For an ideal simple solid with a flat surface, the interfacial tensions, γ_{IJ}, of the solid–liquid, solid–vapour and liquid–vapour interfaces determine the ideal contact angle, θ_e, described by Young's Law (Equation (2)) (Figure 1a) (Young, 1832):

$$\cos\theta_e = \frac{\gamma_{SV} - \gamma_{SL}}{\gamma_{LV}}. \quad (2)$$

The hydrophobic coatings on soil grains have different surface energies than the grains without a hydrophobic coating, influencing the action of the three-phase contact line shown in Figure 1. Grains with a lower surface energy coating than water will lead to a degree of water repellence (Roy & McGill, 2002). Young's Law, however, is only applicable to ideal solid flat surfaces (Leelamanie & Karube, 2012). Where the surface is rough, structured or granular/porous, such as that created by soil grains, a droplet will interact with (or wet) the structure in several different ways. The droplet may sit in a pure Cassie-Baxter state (Cassie & Baxter, 1944), suspended on the tops of the solid protrusions, bridging air pockets that are unfavourable for water penetration

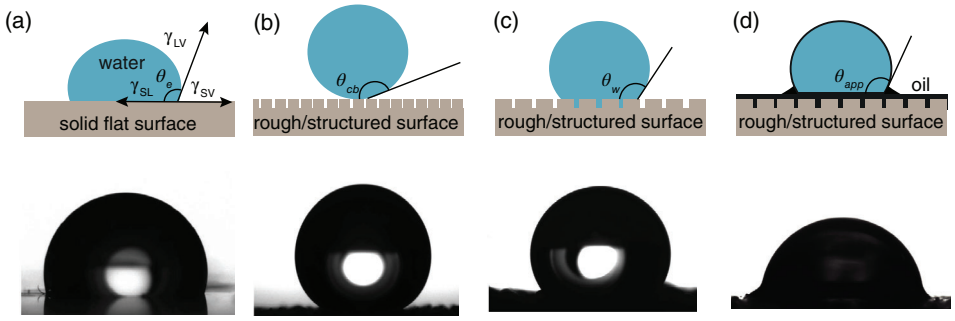

FIGURE 1 Four models of water interaction with different surfaces and corresponding droplet images (10 μL). Panels (a) to (d) show: a water droplet on (a) a smooth flat surface with contact angle (θ_e) controlled by the solid–liquid (γ_{SL}), solid-vapor (γ_{SV}) and liquid–vapor (γ_{LV}) interfaces; (b) a rough/structured surface with air in the gaps representing a Cassie-Baxter state and contact angle (θ_{cb}); (c) a rough/structured surface with water penetration representing a Wenzel state and contact angle (θ_w); and (d) a slippery liquid-infused porous surface (SLIPS) state and apparent contact angle (θ_{app}). The surface roughness/structure in the lower panels of (b) to (d) is caused by the granular nature of the hydrophobic surface [Color figure can be viewed at wileyonlinelibrary.com]

because of the interfacial forces (Figure 1b). In this case, the contact angle increases beyond that created by the surface chemistry alone. The decreased contact of the droplet with the solid makes the droplet highly mobile, and this is known as a "slippy" surface (Bachmann et al., 2006; Cassie & Baxter, 1944; Quére, Lafuma, & Bico, 2003). Where the droplet fully penetrates the surface structure, maintaining complete contact of water with the solid, a Wenzel state is entered (Wenzel, 1936). This results in a pinned and immobile droplet, and the solid is deemed a "sticky" surface (Figure 1c) (Dai, Stogin, Yang, & Wong, 2015; Quére et al., 2003; Wenzel, 1936). These effects can occur on biological surfaces (i.e., sacred lotus leaves) (Barthlott & Neinhuis, 1997; Neinhuis, 1997) and can be synthetically created through chemical alterations and the creation of micro- and nanostructures (Roach, Shirtcliffe, & Newton, 2008). They have also been observed in granular materials such as soils and sediments, where studies have shown that changing grain size has some influence over the degree of water repellence, with smaller grains displaying more water repellence (Bachmann, Horton, van der Ploeg, & Woche, 2000; de Jonge et al., 1999). Surfaces that are observed to have extremely high static contact angles (above 150°) (Erbil, Demirel, Avci, & Mert, 2003), where static refers to the contact angle observed in a side profile directly after droplet deposition, and which move easily at low angles of surface tilt are referred to here as superhydrophobic. In these concepts, a key assumption for a surface formed by grains is that the droplet does not lift the grains and coat itself due to capillary forces (i.e., a liquid marble effect does not occur) (Aussillous & Quéré, 2001).

As shown by the Wenzel state (Figure 1c), a high contact angle surface is not necessarily a slippery surface with good water-shedding properties, where water-shedding refers to the ease with which a droplet moves on a surface (via rolling or slipping) with minimal force (Quére et al., 2003). Excellent water-shedding abilities can be achieved through low contact angle hysteresis irrespective of the absolute value of the static contact angle (see Tao et al., 2020) and is typically seen when a droplet interacts with a surface in a Cassie-Baxter state where there is less solid–liquid contact (McHale, Newton, & Shirtcliffe, 2005). However, water-shedding surfaces can also be created by exposing structured, rough or granular/porous hydrophobic surfaces to oil, to create bio-inspired slippery liquid-infusedporous surfaces (Wong et al., 2011) and lubricant-impregnated surfaces (LIS) (Lafuma & Quéré, 2011; Smith et al., 2013). SLIPS/LIS technology aims to replicate the excellent slippery surfaces of the *Nepenthes* pitcher plant by taking inspiration from its nanostructures, lubricative surface chemistry and hygroscopic nectar and applying it to synthetic materials, for purposes such as anti-biofouling and ice repellence (Bauer & Federle, 2009; Nosonovsky, 2011; Wang, Zhang, & Lu, 2015; Wilson et al., 2013). In SLIPS an infused oil preferentially (compared to water) and completely wets the solid due to its surface chemistry, thus providing a continuous oil surface on which the water droplet rests (McHale, Orme, Wells, & Ledesma-Aguilar, 2019; Wong et al., 2011). It remains possible to observe an (apparent) static contact angle, θ_{app}, which for vanishingly thin layers of oil can be predicted from a liquid form of Young's law, but the value of which decreases as the thickness of the oil increases (McHale et al., 2019; Semprebon, Mchale, & Kusumaatmaja, 2017). Because the water only ever contacts the immiscible oil (and not the solid), there is a lubricating effect reducing surface friction, creating excellent water-shedding abilities demonstrated by very small water droplet sliding angles, typically $\leq 5°$ for a droplet ≥ 2 μL. (Figure 1d) (Wang et al., 2015; Wong et al., 2011). These sliding angles, and the observed contact angle hysteresis (albeit small), are then dependent on the thickness of the oil layer (Semprebon et al., 2017). A significant characteristic of these surfaces is their ability to lock-in and retain a thin oil layer (due to capillary forces from the surface chemistry), which cannot be displaced by water, resulting in stable and long-term water-shedding properties (Bauer & Federle, 2009; Nosonovsky, 2011; Wang et al., 2015; Wilson et al., 2013).

Until now, the creation of SLIPS has never been proposed for soils or demonstrated in model hydrophobic soils. We hypothesize that exposing hydrophobic soils to oil can cause them to acquire enhanced water-shedding properties without the need for the high contact angles required for a hydrophobic soil. This mechanism is analogous to that used by the *Nepenthes* pitcher plant to create a super-slippery surface, which has been mimicked in materials science with slippery liquid-infused porous surfaces (SLIPS). We aim to identify a mechanism by which soils and other granular materials such as sediments can form SLIPS and how this will affect their water repellence and water-shedding properties. We achieve this by replicating oil contamination on model hydrophobic soils and characterizing these surfaces using water droplet contact angles and sliding angles.

3 | EXPERIMENTAL METHODS

3.1 | Preparation of model soils

To create model soils we used monolayers of grains attached to a glass slide as outlined by the Bachmann, Ellies, and Hartge (2000) method for performing the

TABLE 1 Grain sizes used in this study, with the corresponding grain size classification of Wentworth and the spin speed used for polydimethylsiloxane (PDMS) coating, PDMS thickness for each grain size and the % void space for the final surface

Grain size range (μm)	Median grain size (μm)	Median phi size (ϕ)	Wentworth conversion	Spin speed (rpm) for 5 min	PDMS thickness (μm)	% void space
4–25	15	6.47	Clay aggregates	6,000	5	14
9–54	32	5.50	Medium silt	6,000	5	15
32–63	58	4.47	Coarse silt	6,000	5	19
63–90	77	3.73	Very fine sand	6,000	5	19
90–125	108	3.24	Very fine sand	5,000	6	17
125–180	153	2.74	Fine sand	5,000	6	21
180–212	196	2.35	Fine sand	5,000	6	14
212–250	231	2.12	Fine sand	5,000	6	16
250–300	275	1.87	Medium sand	4,000	7	17
300–355	328	1.61	Medium sand	4,000	7	27
355–712	533	0.99	Coarse sand	4,000	7	27

sessile drop method on soils. Silver-grade general purpose silica sand (sourced from Fisher Scientific, Loughborough, UK), silica silt (sourced from Fantasy Quartz Sand Supply, Kowloon, Hong Kong) and kaolin clay (sourced from American Elements, Los Angeles, California) were sieved into grain-size fractions (shown in Table 1). Sand, silt and clay of different grain sizes were used to recreate the natural roughness, shape and size of a soil surface as per Bachmann et al. (2000) and Bachmann, Goebel, and Woche (2013) for our model soils. This method was chosen over using glass spheres, another method of modelling hydrophobic soils. Previous works have used uniform glass spheres to model soils without any chemical or mechanical alterations to the surface; this tends to limit the contact angles of model soils as they remove the soil surface texture and high aspect ratio, which are critical in creating extreme water repellence (McHale, Shirtcliffe, Newton, & Pyatt, 2007; Shirtcliffe et al., 2004). To combat this, some studies have applied chemical or mechanical action to the uniform glass spheres, creating a degree of surface roughness (Ibekwe, Tanino, & Pokrajac, 2019; Utermann, Aurin, Benderoth, Fischer, & Schröter, 2011). However, for this study, we preferred to use a natural material with surface roughness more reflective of the natural environment, rather than an artificially created synthetic analogue.

Grains were cleaned as per Hamlett et al. (2013); they were first immersed in (3% v/v in water) HCl for 24 hr and rinsed with deionised water, then re-immersed in (3% v/v in water) HCl for 3 hr. The concentration of HCl was gradually increased to 30% and the grains left for 1 hr before being rinsed with deionised water, 5 M KOH solution, and again with deionised water at 1:1 grains:solution three times or until the solution ran clear. The grains were then re-immersed in (3% v/v in water) HCl for a further 16 hr before being rinsed with deionised water at a ratio of 1:2 grains:water a minimum of five times or until the solution ran clear, and dried at 100°C for 24 hr. The dried grains were hydrophobized by immersion in a bath of Grangers Footwear Repel (a non-pore-clogging siloxane-based hydrophobizing agent) as per Atherton et al. (2016), Hamlett et al. (2013) and McHale, Shirtcliffe, Newton, Pyatt, and Doerr (2007) for 24 hr and dried at 70°C for 6 hr. This ensured the surface chemistry of all types of grains was uniform, by creating a nanometric coating of the siloxane-based hydrophobizing agent on each grain (independent of mineralogy), and that our model soils satisfied two of the key conditions for SLIP surfaces: (a) the lubricating oil must wick into, wet and stably adhere within the substrate and (b) preferential wetting by oil compared to water. Thus, the oil forms a completely wetting film on the model soil when in air and, in the presence of a droplet of water, this wetting film of oil is maintained between the model soil and the droplet. To allow for tilting experiments and to prevent the creation of liquid marbles, the grains were fixed using a glass microscope slide coated with polydimethylsiloxane (PDMS) at a thickness of 5–7 μm, measured by a stylus profilometer (Bruker DektakXT) (Figure 2). The PDMS mixture (10:1 elastomer to curing agent ratio) was degassed for 45 min and then spun to the correct thickness for each grain size (Table 1) using a spin coater within 30 min of degassing at 5000–6000 rpm for 5 min. Loose sand grains were sprinkled onto the PDMS surface and agitated by hand for 10 s to prevent clumping of grains, then placed in the oven at 120 °C for 5 hr to cure. Excess sand was shaken off and the surface was rinsed with deionised water to prevent the formation of liquid marbles.

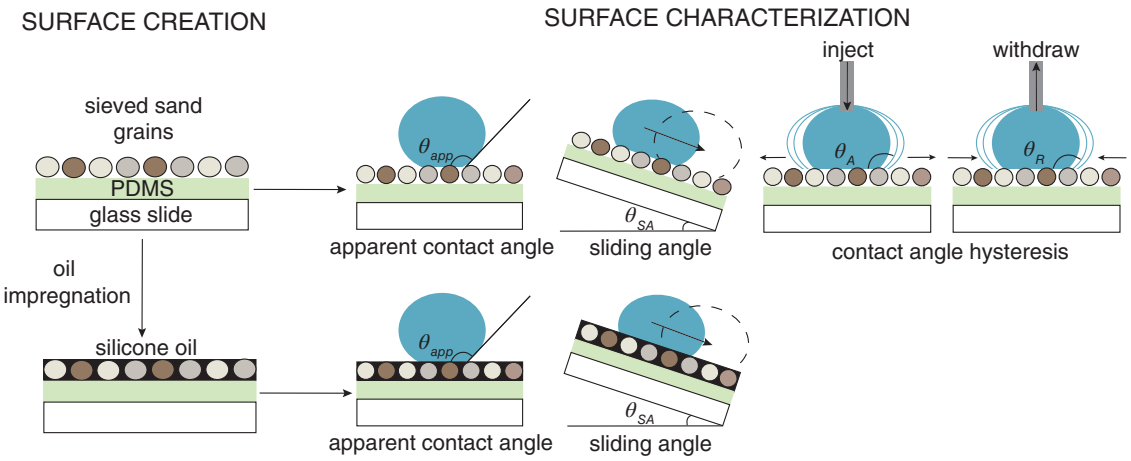

FIGURE 2 Schematic illustrating surface creation and characterization techniques. Surfaces were created using sieved sand, silt and clay grains that were hydrophobized using a commercial hydrophobizing agent and attached to a glass microscope slide using polydimethylsiloxane (PDMS). The hydrophobic oil-free surfaces were characterized by measuring the apparent contact angles (θ_{app}), sliding angles (θ_{SA}) and advancing (θ_A) and receding (θ_R) angles to determine the contact angle hysteresis. Surfaces were then impregnated with silicone oil using three different withdrawal speeds. Oil-impregnated samples were characterized by measuring the apparent contact angles (θ_{app}) and sliding angles (θ_{SA}) [Color figure can be viewed at wileyonlinelibrary.com]

The void fraction of the surface was measured by using microscope images of each surface and inputting these images into a MATLAB code. The code is designed to find the void fraction of the image by creating a binary image before calculating the ratio of particles versus pore space as the ratio of black to white space. The percentage void space for each of our surfaces is stated in Table 1.

3.2 | Oil impregnation

Oil contamination was replicated by impregnating all hydrophobic samples with 20cSt silicone oil (Figure 2), made fluorescent for detection with the laser scanning fluorescence confocal microscope (LSFCM) by dosing with a solution of Nile Red at a 0.01% by weight ratio. Three scenarios of oil impregnation were modelled to represent different environmental conditions. Thick oil layers were used to simulate environments where excess oil has contaminated soil and filled all the pore spaces between the individual grains. Thin oil layers were used to simulate an environment where oil still penetrates all of the spaces between the grains but leaves only a thin coating on the top of the surface. The thinnest oil layers simulate an environment where all excess oil has drained away, leaving a conformal oil layer across each grain, stabilized by capillary forces formed by the hydrophobic chemistry but with the limited filling of excess oil in the pore spaces. The dip coating was performed using a dip-coating machine (Fisnar F4200N) with adjustable and controlled withdrawal speeds, with an accuracy of ± 0.02 mm s^{-1}. The surfaces were fully immersed in the bath of silicone oil for 10 s before being vertically withdrawn at a set constant speed according to the desired oil thickness as per Geraldi et al. (2019). The silicone oil preferentially coated the grains due to the hydrophobic chemistry and by controlling the withdrawal speed of the surface from the oil bath it was possible to control the oil thickness, with a faster withdrawal speed producing a thicker layer of oil (Landau & Levich, 1988; Seiwert, Clanet, & Quéré, 2011). The thick oil layer was created by withdrawing the samples at 0.5 mm s^{-1}, the thin oil layer was created by withdrawing the sample at 0.1 mm s^{-1}, and the thinnest (or conformal) oil layer was created by withdrawing the samples at 0.1 mm s^{-1} and suspending them for 24 hr to remove excess oil, leaving only the thinnest possible thermodynamically stable oil layer. To measure the changes in oil thickness with increasing grain size as well as withdrawal speed, a Nikon A1 SHS laser scanning fluorescence confocal microscope was used to measure the oil thickness (thick, thin and thinnest) on the four surfaces we created, with median grain sizes of 15 μm (phi 6.47), 77 μm (phi 3.73), 231 μm (phi 2.12) and 533 μm (phi 0.99).

3.3 | Water droplet contact angle measurements

The apparent (static) water droplet contact angle, θ_{app}, was measured using a Krüss Droplet Shape Analyser (DSA30) at ambient room temperature (20–25°C). Using the sessile drop method, a 10 μL droplet of deionised water was placed on the horizontally mounted surface

and a side-view image of the two-dimensional profile of the droplet was taken (Figure 2). This was repeated 10 times per surface at different locations across the surface. The open source program PyDSA was used to analyse the images taken on the Krüss DSA30 to determine the θ_{app}. The PyDSA OpenCV Canny edge detection function was used to detect the edges of the droplet and a fixed straight baseline was used to measure the triple-phase point where the droplet makes contact with the surface (Launay, 2018). This multistage algorithm detected the edge between two threshold values while filtering noise to give a single smooth edge (Canny, 1986). This returned an array of coordinates showing where the edge was detected. The programme then performs an elliptical fit using the fitEllipse function in the OpenCV library, which uses the Fitzgibbon direct least square fitting method to obtain these values, taking the contact angle from the tangent of the fitted ellipse and the baseline (Fitzgibbon, Pilu, & Fisher, 1999; Launay, 2018).

3.4 | Water droplet contact angle hysteresis measurements

Contact angle hysteresis (CAH) was measured using the advancing (θ_A) and receding (θ_R) contact angles of water droplets, which shows the range of contact angles a droplet can take on a surface whilst the contact line remains stationary. A superhydrophobic surface will exhibit low hysteresis as the droplet easily de-pins from the surface. We measured the CAH on the hydrophobic surfaces before oil impregnation by increasing and decreasing the volume of water in the droplet until the contact line was observed to move (Figure 2). Measurements were recorded with the inbuilt video sequencing software on the Krüss DSA30 at five frames per second to capture the inflation and deflation of the water droplet. The advancing contact angle was measured by depositing a 6 μL droplet on the surface and adding 10 μL of water at 10 μL min^{-1} into the droplet. The droplet was left to stabilize for 10 s before the receding angle was measured by withdrawing 10 μL of water at 10 μL min^{-1}. This was repeated 10 times at different locations across the surface.

The videos were then analysed using Image J. The advancing and receding frames were extracted from the full video by importing the frames into ImageJ and stepping through the video one frame at a time. For the determination of the advancing frame, the "zoom tool" was used in ImageJ to focus on the contact point of the shadow graphed droplet. The frame at which the black pixel of the droplet advanced, or filled the white pixels of the background, was deemed to be the frame post θ_A. The frame prior is where θ_A was measured as the droplet will have assumed the largest angle possible on that surface before the inflation forced the droplet to grow in terms of droplet footprint. To measure θ_A the "angle tool" in ImageJ was used. The baseline was placed at the bottom of the droplet (on the sample) and the angle fitted as a tangent to the side of the droplet where the black pixels turn to white pixels near the contact point. The same process was followed for θ_R, where the receding frame was determined by the retraction of the contact line, or where the black pixels of the droplet turn into white background. The CAH for the surface can then be calculated using Equation (3):

$$\Delta\theta_{CAH} = \theta_A - \theta_R. \quad (3)$$

Due to the pinning of water droplets onto asperities of individual grains, some advancing and receding angles could not be measured (the number of data points excluded due to pinning for each grain size can be found in the Supporting Information). Furthermore, CAH on SLIPS, with their highly mobile contact line with minimal pinning points, are small (within contact angle measurement error) (Guan et al., 2015; Wong et al., 2011). For this reason, the SLIPS literature focuses on sliding angle measurements for a defined droplet volume to characterize droplet mobility.

3.5 | Water droplet sliding angle measurements

Water droplet sliding angles (θ_{SA}) were used to determine the water-shedding ability of the hydrophobized surfaces before and after impregnation with silicone oil using the Krüss DSA30 tilt table. The θ_{SA} was measured as the substrate angle (where the surface is tilted from the horizontal) at which the water droplet unpinned from its position and began to move on the inclined surface (Cui et al., 2019) (Figure 2). The platform was levelled using a spirit level before tilting each surface. A droplet of 20 μL was then deposited on the surface and slowly inclined at 0.2° per second until the droplet began to move. The sliding angle was measured on both the hydrophobic samples with no oil impregnation and each silicone oil impregnation scenario. Ten sliding angles were measured for each surface. The Krüss DSA30 proprietary software (DSA4) was used to determine the θ_{SA} within an error of ±0.2°.

4 | RESULTS

Figure 3a shows apparent, advancing and receding contact angles, and hence CAH, as a function of grain size.

The CAH is the difference between the advancing (triangle) and receding (diamond) contact angles and the independently measured apparent contact angle is shown as a dashed line in Figure 3a. The apparent contact angle of around 150° and a CAH of less than 10° shows that at median grain sizes of 15 μm (phi 6.47), droplets are clearly in a superhydrophobic state. The overall trend shows apparent decreasing of the contact angle and CAH increasing with increasing grain size.

Sliding angles were also measured for these surfaces before oil impregnation (shown in Figure 3b). Small sliding angles were observed at the lowest grain size, with sliding angles increasing as grain size increased. This trend shows that droplets at low grain sizes are highly mobile, which is consistent with the low CAH and high apparent contact angles at low grain sizes in Figure 3a. The inset images in Figure 3b show the maximum recorded angle before water droplets slide on our model hydrophobic soils. The low sliding angle at the smallest grain size and the retention of the droplet on the near-vertical surface at the highest grain size dramatically illustrate the concepts of "slippy" and "sticky" surfaces we introduced in the *Concepts of Water Repellence* section. Figure 3b also shows a plateau in sliding angle on median grain sizes 58-275 μm (phi 4.47–1.87), where the droplets are in neither a pure Cassie-Baxter nor a Wenzel state.

Figure 4a shows apparent contact angles of water on our model hydrophobic soils, after impregnation with oil and then allowing the oil to drain to the thinnest possible layer as a function of grain size. The inset images show droplets of water with similar contact angles of between 86° and 98° across the full range of grain sizes. These images can be contrasted with the clear decrease in apparent contact angle with increasing grain size (inset images in Figure 3a) for the model hydrophobic soils before oil impregnation.

Sliding angles were also measured for the oil-impregnated hydrophobic model soils, shown in Figure 4b. At the lowest median grain size of 15 μm (phi 6.47), the sliding angle of between 1° and 3° is lower than the superhydrophobic state for the model hydrophobic soil shown in Figure 3b. As the grain size increases the sliding angle also slowly increases, but it remains lower than the sliding angles in the intermediate state for the model hydrophobic soils (shown in Figure 3b). The inset droplet images in Figure 4b show the maximum sliding angle on the model hydrophobic soils with the thinnest oil layer. The contrast in the maximum sliding

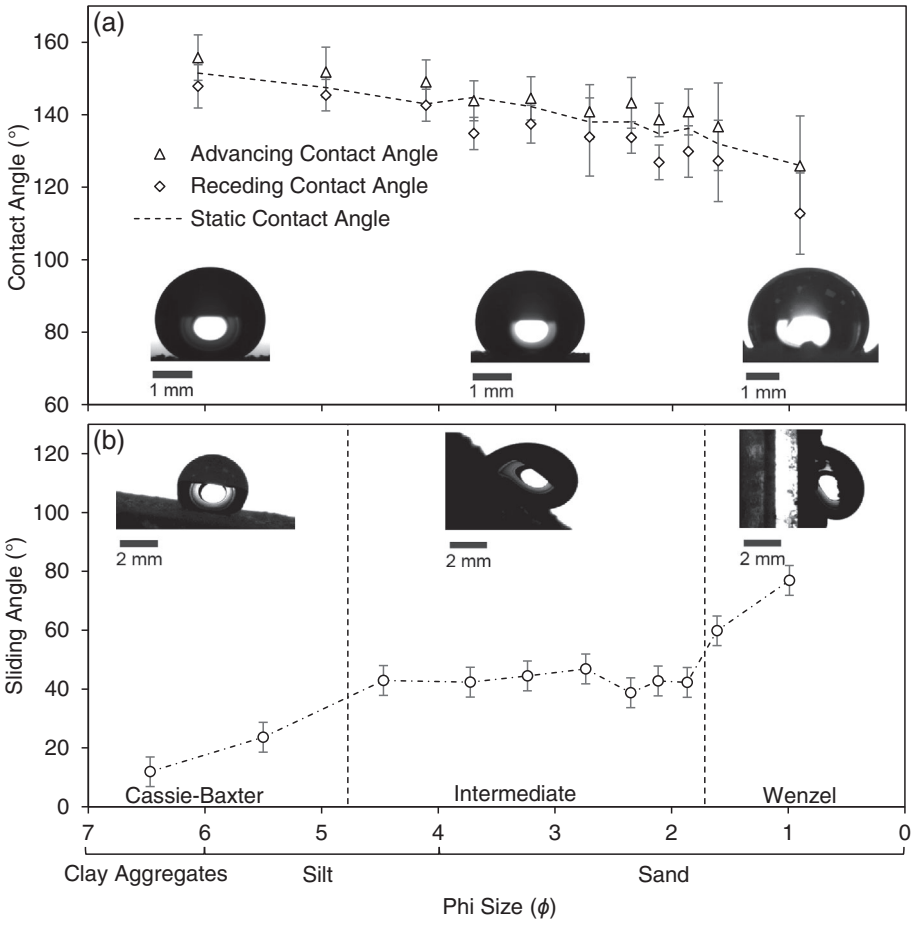

FIGURE 3 (a) Median advancing, receding and apparent contact angles on model hydrophobic soil (with standard deviation error bars, produced from 10 measurements per surface using a 10 μL droplet). The inset images are a droplet on (from left to right) clay aggregates, fine sand and coarse sand. (b) Median sliding angles on model hydrophobic soil without oil impregnation (with standard deviation error bars, produced from 10 measurements per surface using a 20 μL droplet). The inset images are a droplet on an inclined surface at the point of depinning on (from left to right) clay aggregates, fine sand and coarse sand

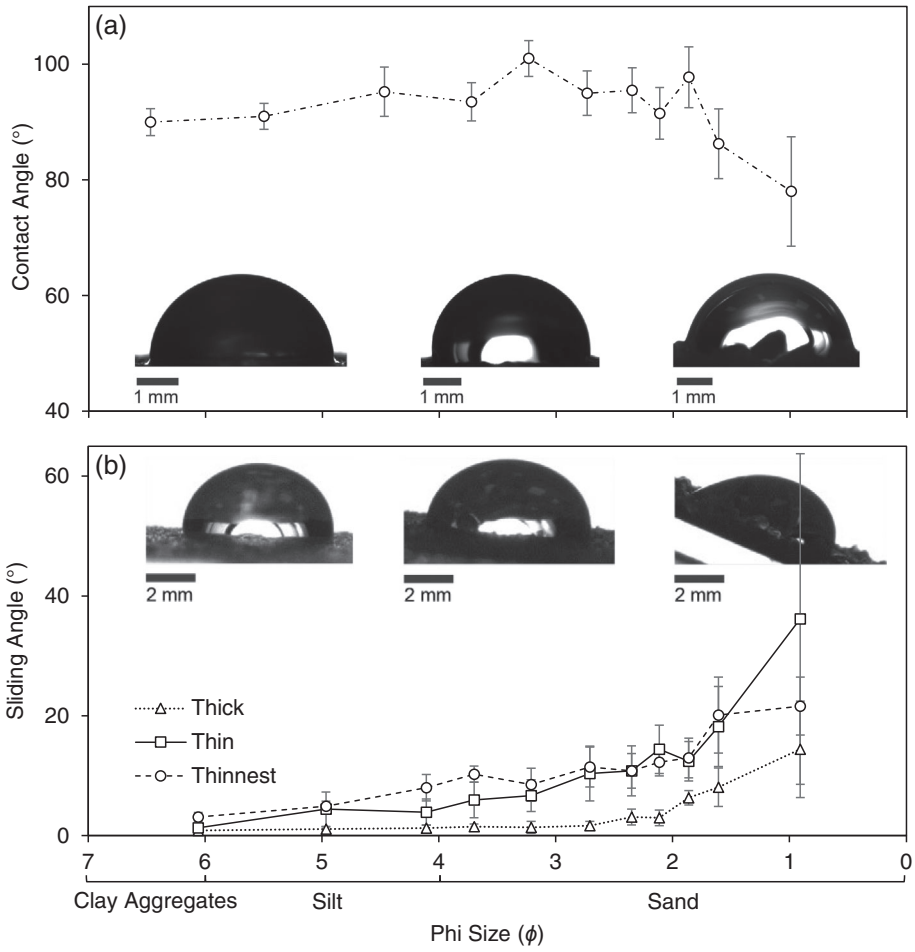

FIGURE 4 (a) Median apparent contact angles on the thinnest oil layer (with standard deviation error bars, produced from 10 measurements per surface using a 10 μL droplet). Inset images show a droplet on a conformal oil layer on (from left to right) clay aggregates, fine sand and coarse sand. (b) Median sliding angles of water droplets on oil impregnated surfaces (with standard deviation error bars, produced from 10 measurements per surface using 20 μL droplets). Inset images show a droplet on a conformal oil layer at the point of depinning on (from left to right) clay aggregates, fine sand and coarse sand

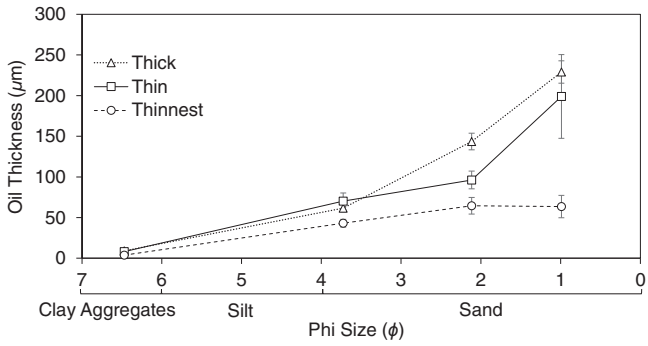

FIGURE 5 Oil thickness measurements taken on the laser scanning fluorescence confocal microscope for the thinnest, thin and thickest oil layer scenarios, for median grain sizes 15 μm (phi 6.47), 77 μm (phi 3.73), 231 μm (phi 2.12) and 533 μm (phi 0.99)

angle between the inset images in Figures 3b and 4b illustrates the significant increase in water-shedding ability of the oil-impregnated hydrophobic model soils, particularly at the higher grain sizes. The trends in Figure 4b are the same regardless of whether we consider the thinnest coating of oil or the thicker layers of oil. The water-shedding ability of oil-impregnated hydrophobic model soils remains strong even with the thinnest coating of oil.

Because we used three different oil impregnation techniques on a wide range of grain sizes, our oil impregnation will result in different thicknesses of oil. We can envisage two possible extreme states, with the first being a conformal coating of individual grains, leaving gaps between the coated grains, and the second being a thick layer completely coating grains and filling the pores between them. However, there is also an intermediate state, with the possibility of a conformal coating of grains, but a partial filling of the pores between the grains. To investigate these possibilities, we performed LSFCM analysis on median grain sizes of 15 μm (phi 6.47), 77 μm (phi 3.73), 231 μm (phi 2.12) and 533 μm (phi 0.99), using the three oil impregnation techniques. We measured the average thickness of the oil between the grains on nine single points on all 12 oil-impregnated hydrophobic model soils.

Figure 5 shows the results of these measurements. For grain size 15 μm (phi 6.47), the measured oil thicknesses were 0.85 μm, 1.3 μm and 3.1 μm, which are all substantially smaller than the grain size itself. The thick and thin oil coating scenarios show an increase in oil

thickness with increasing grain size, approaching around 40% of the grain size. The thinnest oil coating reaches a maximum thickness of ~64 μm between 231 μm (phi 2.12) and 533 μm (phi 0.99) median grain sizes, representing 15–30% of the grain size. Figure 6a–c illustrates these changes for the 77 μm (phi 3.73) median grain size. This corresponds to Figure 4b, which shows an increase in sliding angle from 1.5° to 10.25° as the oil coating thickness decreases. The red haze from the Nile red dye shows that in all cases the grains have a thin coating of oil across the entirety of their upper surface. This is consistent with the relatively low sliding angles recorded in all three cases. Figure 6d–f shows equivalent images for median grain sizes of 15 μm (phi 6.47), 231 μm (phi 2.12) and 533 μm (phi 0.99), for the thinnest (conformal) coating of oil. The naturally rough/structured form of the surface (before the oil coating) is maintained, but each grain has a conformal coating of oil. Comparisons to Figure 4b show that the sliding angle remains below 10° up to the largest median grain size of 533 μm (phi 0.99), for which the sliding angle increases to 14.4°.

5 | DISCUSSION

5.1 | Superhydrophobic soils

Our results show that before oil contamination soils composed of clay aggregates can exhibit superhydrophobicity, characterized by an apparent contact angle above 150° (Figure 3a). This supports the earlier works of McHale, Shirtcliffe, Newton, and Pyatt (2007), who showed that a

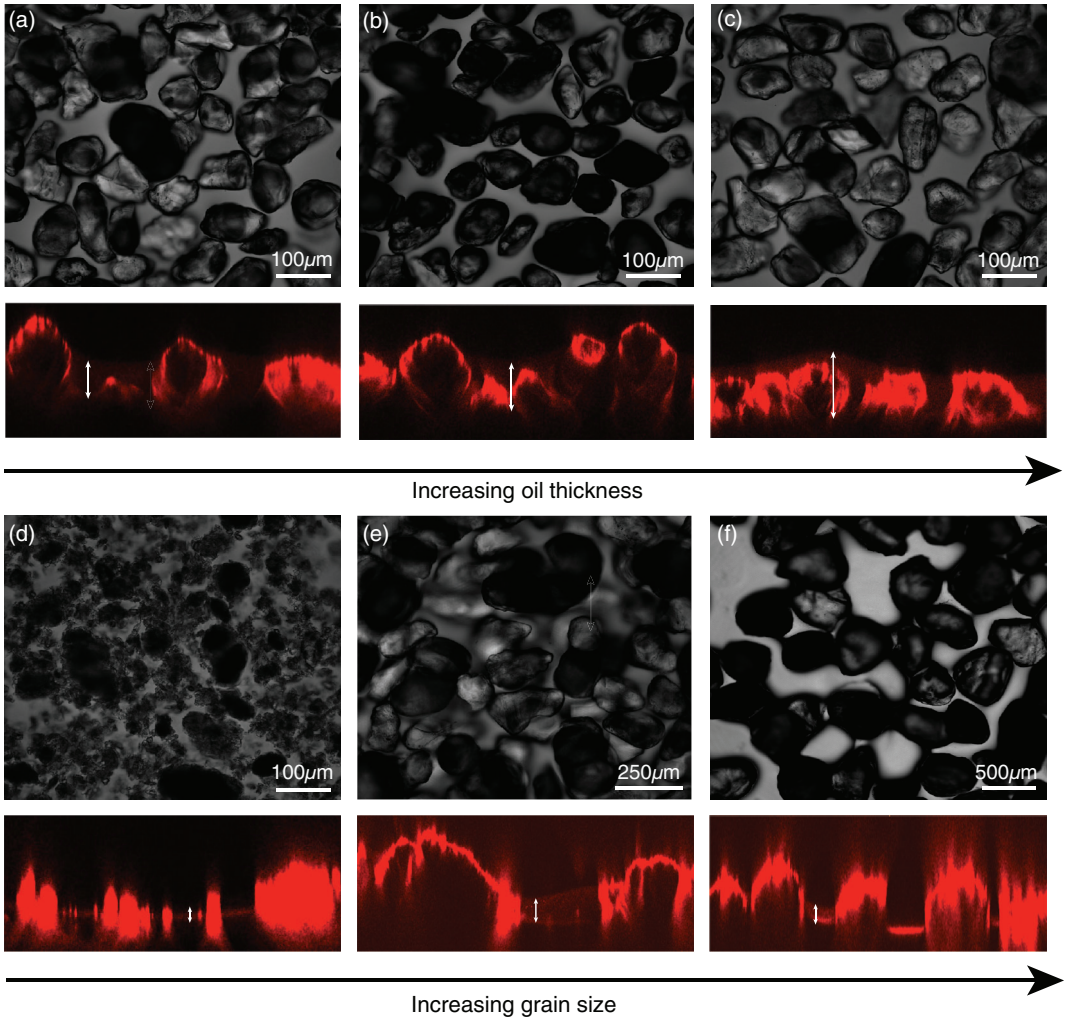

FIGURE 6 Oil impregnated samples imaged on the laser scanning fluorescence confocal microscope from top-down (black and white image) and side profiles (black and red image). In the side profiles the bright red outline shows the shape of the individual grains, with the red haze showing the oil coating. White arrows indicate the thickness of the oil. Panels (a) to (c) show median grain size 77 μm (phi 3.73) soils impregnated with (a) a thick oil coating (b) a thin oil coating and (c) a conformal oil coating. The lower panels show a conformal oil coating on median grain size (d) 15 μm (6.47), (e) 231 μm (2.12) and (f) 533 μm (0.99) [Color figure can be viewed at wileyonlinelibrary.com]

Cassie-Baxter wetting regime could exist in water-repellent soils, and where this is extreme, has the potential to create superhydrophobicity. For soils where studies have used either real soils consisting of a mixture of different grain sizes (Bachmann et al., 2006; Leelamanie, Karube, & Yoshida, 2008) or where grain fractions as small as clay or clay aggregates were not isolated in grain size-dependent contact angle studies (Saulick, Lourenço, and Baudet (2016), typical values of contact angles are reported in the range of 100–130°. Higher contact angles have been recorded in model soils; for example, Bachmann et al. (2013) measured contact angles of 140° using a small-scale contact angle measurement technique, and Ng and Lourenço (2016) report angles up to 143° for silane-treated soils. Contact angles of ≥150° have also been observed on structured surfaces composed of silica particles up to 10 μm (e.g., Cao, Jones, Sikka, Wu, & Gao, 2009; Tsai, Yang, & Lee, 2006) and on particle assembled surfaces where particle sizes range from the nanometric to hundreds of microns (e.g. McHale et al., 2005; Roach et al., 2008). We therefore consider the high contact angle values recorded in this study, particularly for the smaller grain sizes, as arising from the topography of the sieved grains and their attachment to the substrate providing a high aspect ratio, which amplified the intrinsic hydrophobicity of the surface chemistry.

We also observed a shift in wetting regime on the hydrophobic surfaces, with apparent contact angles decreasing and CAH increasing with increasing grain size (Figure 3a), illustrating the shift between a "slippy" Cassie-Baxter and "sticky" Wenzel state. At lower grain sizes the droplet sits in a Cassie-Baxter state, with high droplet mobility because of the increase in the fraction of the water–air interface below the droplet. For larger grain sizes, the droplet begins to penetrate the surface structure, resulting in lower droplet mobility, due to more solid surface contact. This is consistent with observations of other soils (de Jonge et al., 1999; Doerr et al., 1996; Saulick et al., 2016) and synthetically created textured hydrophobic surfaces (Erbil et al., 2003; McHale et al., 2005; Öner & McCarthy, 2000; Yeh, Chen, & Chang, 2008).

Although we rule out an effect of the mineralogy on the hydrophobicity of the grains due to the homogeneous surface chemistry created by the siloxane-based hydrophobizing agent, because the topography of natural surfaces such as soils and sediments, which are much more complex and heterogeneous than the synthetic surfaces created in material physics, it is more likely that the droplet will be in neither a pure Cassie-Baxter nor a pure Wenzel state (Shirtcliffe, McHale, Atherton, & Newton, 2010). This is illustrated by the plateau in sliding angle between 58 and 275 μm (phi 4.47–1.87) in Figure 3b, which we believe is caused by the droplet being in a partially penetrating wetting regime (Chang, Hong, Sheng, & Tsao, 2009).

5.2 | Soils-based SLIPS

Silicone oil can be expected to completely wet hydrophobic grains and will preferentially wet them compared to water (McHale et al., 2019; Smith et al., 2013). Therefore, we expect that droplets of water will always rest on the oil on our oil-impregnated hydrophobic model soils and would not displace the oil layer. This also prevents the water droplet from interacting with the underlying grains to an extent dependent on the oil thickness, as illustrated by the varying sliding angles on the three oil thickness scenarios (Figure 4b). With this, we were able to create soils-based SLIPS with all three thicknesses of oil characterized by sliding angles of less than 5°, up to a median grain size of 231 μm (phi 2.12). Despite the most efficient water-shedding properties being observed on the thick and thin coatings of oil, sliding angles on the thinnest layer of oil are also extremely low in comparison to the hydrophobic soil. This extreme water-shedding ability on thin conformal oil layers is highlighted by the creation of SLIPS on median grain sizes up to 32 μm (phi 5.50). Therefore, we conclude the significant improvement in water-shedding ability of the hydrophobic oil-impregnated soils seen in Figure 4b compared to that observed for the hydrophobic soils in Figure 3b, arises from the thin coating of oil on the grains stabilized by capillary forces from the surface hydrophobic chemistry. Until now, this phenomenon has only been observed in human-made materials and biological surfaces (Wong et al., 2011). Figure 4b further shows that increasing grain size results in an increase in sliding angle and we can therefore assume more force is required to move the droplet across the surface. Roughness and porosity are important factors for creating SLIPS; where the pores are sufficiently small, the lubricant (in this case silicone oil) can bridge the pores between the grains and provide a smooth slippery surface, whereby water droplets cannot penetrate the structure (Niemelä-Anttonen et al., 2018). The increase in sliding angle with increasing grain size suggests that the oil is not thick enough to smooth the macroscale roughness of the model soils, leading to partial penetration of the droplet to the structure (Tonelli, Peppou-Chapman, Ridi, & Neto, 2019). This is further supported by the LSFCM analysis (Figure 5 and Figure 6), which shows that oil thickness on the largest grain size does not exceed 40% of the grain size even for the thick layer of oil scenario.

Current research on SLIPS focuses on their use in material science and engineering by harnessing their

water-shedding and icephobic properties for purposes such as anti-icing in aviation (Tas, Memon, Xu, Ahmed, & Hou, 2020), anti-wetting in biomedical devices (Wong et al., 2011) and anti-biofouling in marine engineering (Keller et al., 2019; Xiao et al., 2013). These impacts, however, have not yet been investigated in an environment where SLIPS could occur in soils or sediment and prevent water infiltration to a greater extent than hydrophobicity. The extreme water-shedding abilities of SLIPS are achieved without the need for high contact angles whilst also resisting adhesion of other substances such as ice and microbes. The impact of these properties will have important implications for soil science and wider earth processes. For example, due to the stability of the thin oil layers, it is unlikely that repeated wetting cycles will remediate the water repellence and water-shedding properties, as is sometimes seen in other hydrophobic soils (Quyum, Achari, & Goodman, 2002). Furthermore, the stability of these surfaces, demonstrated by the creation of very thin conformal oil layers that are not removed by gravity or an immiscible liquid, highlights how little oil contamination is needed for these extreme water-shedding properties to exist. This provides a possible mechanism for long-lasting water repellence in areas of oil contamination, such as that seen at old oil spill sites in Alberta, Canada (Roy et al., 1999; Roy & McGill, 2000). Furthermore, our study shows that soil SLIPS could have important water-shedding properties with micron-thick oil coatings, which might go undetected in field studies. Such properties have the potential to impact other soil and sediment processes, such as debris flow events, to which hydrophobic soils and sediments are susceptible, and potentially, wider sediment transport processes such as sediment fan formation.

6 | CONCLUSION

By creating a thermodynamically stable oil layer on model hydrophobic soils, we show a potential mechanism for a surface to acquire water-shedding properties. On these surfaces, the apparent contact angle does not need to take on the extreme values that must occur on extreme water-repellent oil-free soils to have effective water-shedding properties. Such oil coatings can occur through human activity (e.g., oil spills) or natural processes (e.g., hydrocarbon seepage from sedimentary basins). Because the oil preferentially wets the hydrophobic soil and is maintained by capillary forces, depletion of excess oil by water erosion may not remove even the thinnest coating of oil and may therefore maintain its water-shedding properties. It is also the case that oil-coated grains may combine with a larger-scale roughness/structure to create Cassie-Baxter states (water droplets are suspended on the structure) and Wenzel states (water droplets penetrate the structure) (McHale et al., 2019). These results have important implications for our understanding of soil mechanics where a soil may become contaminated with an oil. We also believe the processes reported here, inspired by *Nepenthes* pitcher plants and their synthetic material analogues (SLIPS/LIS), may provide new mechanisms for hydrophobic and water-shedding properties in shallow slope earth systems, including soil environments and other sedimentary and slope processes, such as debris flows and sediment fan formation.

ACKNOWLEDGEMENTS

We would like to acknowledge Dr G.G. Wells and Dr P. Agrawal for their advice, technical support and guidance. We also thank the two anonymous reviewers who provided helpful comments. R. McCerery would like to acknowledge Northumbria University at Newcastle for financial support.

CONFLICT OF INTEREST

No conflict of interest to declare.

DATA AVAILABILITY STATEMENT

Data available in the Supplementary Material.

ORCID

Rebecca McCerery https://orcid.org/0000-0001-6520-3667

REFERENCES

Atherton, S., Polak, D., Hamlett, C. A. E., Shirtcliffe, N. J., McHale, G., Ahn, S., ... Newton, M. I. (2016). Drop impact behaviour on alternately hydrophobic and hydrophilic layered bead packs. *Chemical Engineering Research and Design*, *110*, 200–208.

Aussillous, P., & Quéré, D. (2001). Liquid marbles. *Nature*, *411*, 924–927. https://doi.org/10.1038/35082026

Bachmann, J., Arye, G., Deurer, M., Woche, S. K., Horton, R., Hartge, K.-H., & Chen, Y. (2006). Universality of a surface tension—Contact-angle relation for hydrophobic soils of different texture. *Journal of Plant Nutrition and Soil Science*, *169*, 745–753. https://doi.org/10.1002/jpln.200622022

Bachmann, J., Ellies, A., & Hartge, K. H. (2000). Development and application of a new sessile drop contact angle method to assess soil water repellency. *Journal of Hydrology*, *231*, 66–75.

Bachmann, J., Goebel, M.-O., & Woche, S. K. (2013). Small-scale contact angle mapping on undisturbed soil surfaces. *Journal of Hydrology and Hydromechanics*, *61*, 3–8.

Bachmann, J., Guggenberger, G., Baumgartl, T., Ellerbrock, R. H., Urbanek, E., Goebel, M.-O., ... Fischer, W. R. (2008). Physical carbon-sequestration mechanisms under special consideration

of soil wettability. *Journal of Plant Nutrition and Soil Science*, *171*, 14–26. https://doi.org/10.1002/jpln.200700054

Bachmann, J., Horton, R., van der Ploeg, R. R., & Woche, S. (2000). Modified sessile drop method for assessing initial soil–water contact angle of sandy soil. *Soil Science Society of America Journal*, *64*, 564–567. https://doi.org/10.2136/sssaj2000.642564x

Barthlott, W., & Neinhuis, C. (1997). Purity of the sacred lotus, or escape from contamination in biological surfaces. *Planta*, *202*, 1–8. https://doi.org/10.1007/s004250050096

Bauer, U., & Federle, W. (2009). The insect-trapping rim of Nepenthes pitchers. *Plant Signaling & Behavior*, *4*, 1019–1023. https://doi.org/10.4161/psb.4.11.9664

Blackwell, P. (2000). Management of water repellency in Australia, and risks associated with preferential flow, pesticide concentration and leaching. *Journal of Hydrology*, *231–232*, 384–395. https://doi.org/10.1016/S0022-1694(00)00210-9

Cannon, S. H., Bigio, E. R., & Mine, E. (2001). A process for fire-related debris flow initiation, Cerro Grande fire, New Mexico. *Hydrological Processes*, *15*, 3011–3023. https://doi.org/10.1002/hyp.388

Cannon, S. H., Gartner, J. E., Wilson, R. C., Bowers, J. C., & Laber, J. L. (2008). Storm rainfall conditions for floods and debris flows from recently burned areas in southwestern Colorado and southern California. *Geomorphology*, *96*, 250–269. https://doi.org/10.1016/j.geomorph.2007.03.019

Canny, J. (1986). A computational approach to edge detection. *IEEE Transactions on Pattern Analysis and Machine Intelligence*, *PAMI, 8*, 679–698.

Cao, L., Jones, A. K., Sikka, V. K., Wu, J., & Gao, D. (2009). Anti-icing superhydrophobic coatings. *Langmuir*, *25*, 12444–12448. https://doi.org/10.1021/la902882b

Cassie, A. B. D., & Baxter, S. (1944). Wettability of porous surfaces. *Transactions of the Faraday Society*, *40*, 546. https://doi.org/10.1039/tf9444000546

Chang, F.-M., Hong, S.-J., Sheng, Y.-J., & Tsao, H.-K. (2009). High contact angle hysteresis of superhydrophobic surfaces: Hydrophobic defects. *Applied Physics Letters*, *95*, 064102. https://doi.org/10.1063/1.3204006

Chau, H. W., Goh, Y. K., Vujanovic, V., & Si, B. C. (2012). Wetting properties of fungi mycelium alter soil infiltration and soil water repellency in a γ-sterilized wettable and repellent soil. *Fungal Biology*, *116*, 1212–1218. https://doi.org/10.1016/j.funbio.2012.10.004

Cui, J., Zhu, H., Tu, Z., Niu, D., Liu, G., Bei, Y., & Zhu, Q. (2019). Effect of the texture geometry on the slippery behavior of liquid-infused nanoporous surfaces. *Journal of Materials Science*, *54*, 2729–2739. https://doi.org/10.1007/s10853-018-2972-2

Dai, X., Stogin, B. B., Yang, S., & Wong, T.-S. (2015). Slippery wenzel state. *ACS Nano*, *9*, 9260–9267. https://doi.org/10.1021/acsnano.5b04151

de Jonge, L. W., Jacobsen, O. H., & Moldrup, P. (1999). Soil water repellency: Effects of water content, temperature, and particle size. *Soil Science Society of America Journal*, *63*, 437–442. https://doi.org/10.2136/sssaj1999.03615995006300030003x

de Jonge, L. W., Moldrup, P., & Jacobsen, O. H. (2007). Soil-water content dependency of water repellency in soils: Effect of crop type, soil management, and physical-chemical parameters. *Soil Science*, *172*, 577–588. https://doi.org/10.1097/Ss.06013e318065c090

DeBano, L. F. (2000). The role of fire and soil heating on water repellency in wildland environments: A review. *Journal of Hydrology*, *231–232*, 195–206. https://doi.org/10.1016/S0022-1694(00)00194-3

Dekker, L. W., Doerr, S. H., Oostindie, K., Ziogas, A. K., & Ritsema, C. J. (2001). Water repellency and critical soil water content in a dune sand. *Soil Science Society of America Journal*, *65*, 1667–1674. https://doi.org/10.2136/sssaj2001.1667

Dekker, L. W., & Ritsema, C. J. (1994). How water moves in a water repellent sandy soil: 1. Potential and actual water repellency. *Water Resources Research*, *30*, 2507–2517. https://doi.org/10.1029/94WR00749

DiBiase, R. A., & Lamb, M. P. (2020). Dry sediment loading of headwater channels fuels post-wildfire debris flows in bedrock landscapes. *Geology*, *48*, 189–193. https://doi.org/10.1130/G46847.1

Doerr, S. H., Dekker, L. W., Ritsema, C. J., Shakesby, R. A., & Bryant, R. (2002). Water repellency of soils. *Soil Science Society of America Journal*, *66*, 401–405. https://doi.org/10.2136/sssaj2002.4010

Doerr, S. H., Ritsema, C. J., Dekker, L. W., Scott, D. F., & Carter, D. (2007). Water repellence of soils: New insights and emerging research needs. *Hydrological Processes*, *21*, 2223–2228. https://doi.org/10.1002/hyp.6762

Doerr, S. H., Shakesby, R. A., Blake, W. H., Chafer, C. J., Humphreys, G. S., & Wallbrink, P. J. (2006). Effects of differing wildfire severities on soil wettability and implications for hydrological response. *Journal of Hydrology*, *319*, 295–311. https://doi.org/10.1016/j.jhydrol.2005.06.038

Doerr, S. H., Shakesby, R. A., & Walsh, R. P. D. (1996). Soil hydrophobicity variations with depth and particle size fraction in burned and unburned Eucalyptus globulus and *Pinus pinaster* forest terrain in the Águeda Basin, Portugal. *Catena*, *27*, 25–47. https://doi.org/10.1016/0341-8162(96)00007-0

Doerr, S. H., Shakesby, R. A., & Walsh, R. P. D. (1998). Spatial variability of soil hydrophobicity in fire-prone eucalyptus and pine forests, Portugal. *Soil Science*, *163*, 313–324. https://doi.org/10.1097/00010694-199804000-00006

Doerr, S. H., Shakesby, R. A., & Walsh, R. P. D. (2000). Soil water repellency: Its causes, characteristics and hydro-geomorphological significance. *Earth-Science Reviews*, *51*, 33–65. https://doi.org/10.1016/S0012-8252(00)00011-8

Ellis, R., & Adams, R. S. (1961). Contamination of soils by petroleum hydrocarbons. In A. G. Norman (Ed), *Advances in agronomy* (pp. 197–216). Cambridge, Massachusetts: Academic Press.

Erbil, H., Demirel, A. L., Avci, Y., & Mert, O. (2003). Transformation of a simple plastic into a superhydrophobic surface. *Science*, *299*, 1377–1380. https://doi.org/10.1126/science.1078365

Fitzgibbon, A., Pilu, M., & Fisher, R. B. (1999). Direct least square fitting of ellipses. *IEEE Transactions on pattern analysis and machine intelligence*, *21*(5), 476–480.

Geraldi, N. R., Guan, J. H., Dodd, L. E., Maiello, P., Xu, B. B., Wood, D., … McHale, G. (2019). Double-sided slippery liquid-infused porous materials using conformable mesh. *Scientific Reports*, *9*, 13280. https://doi.org/10.1038/s41598-019-49887-3

Guan, J. H., Wells, G. G., Xu, B., McHale, G., Wood, D., Martin, J., & Stuart-Cole, S. (2015). Evaporation of sessile droplets on slippery liquid-infused porous surfaces (SLIPS). *Langmuir*, *31*, 11781–11789. https://doi.org/10.1021/acs.langmuir.5b03240

Hallett, P.D. 2007. An introduction to soil water repellency. In R.E. Gaskin (Ed.), *Proceedings of the 8th International Symposium on Adjuvants for Agrochemicals* (pp. 6–9). Columbus, OH: International Society for Agrochemical Adjuvants.

Hallett, P. D., Baumgartl, T., & Young, I. M. (2001). Subcritical water repellency of aggregates from a range of soil management practices. *Soil Science Society of America Journal*, *65*, 184–190. https://doi.org/10.2136/sssaj2001.651184x

Hamlett, C. A. E., Atherton, S., Shirtcliffe, N. J., McHale, G., Ahn, S., Doerr, S. H., ... Newton, M. I. (2013). Transitions of water-drop impact behaviour on hydrophobic and hydrophilic particles. *European Journal of Soil Science*, *64*, 324–333. https://doi.org/10.1111/ejss.12003

Hamlett, C. A. E., Shirtcliffe, N. J., McHale, G., Ahn, S., Bryant, R., Doerr, S. H., & Newton, M. I. (2011). Effect of particle size on droplet infiltration into hydrophobic porous media as a model of water repellent soil. *Environmental Science & Technology*, *45*, 9666–9670. https://doi.org/10.1021/es202319a

Ibekwe, A., Tanino, Y., & Pokrajac, D. (2019). A low-cost, non-hazardous protocol for surface texturing of glass particles. *Tribology Letters*, *67*, 115. https://doi.org/10.1007/s11249-019-1230-3

Jordán, A., Zavala, L. M., Mataix-Solera, J., & Doerr, S. H. (2013). Soil water repellency: Origin, assessment and geomorphological consequences. *Catena*, *108*, 1–5. https://doi.org/10.1016/j.catena.2013.05.005

Keller, N., Bruchmann, J., Sollich, T., Richter, C., Thelen, R., Kotz, F., ... Rapp, B. E. (2019). Study of biofilm growth on slippery liquid-infused porous surfaces made from fluoropor. *ACS Applied Materials & Interfaces*, *11*, 4480–4487. https://doi.org/10.1021/acsami.8b12542

Lafuma, A., & Quéré, D. (2011). Slippery pre-suffused surfaces. *EPL (Europhysics Letters)*, *96*, 56001. https://doi.org/10.1209/0295-5075/96/56001

Landau, L., & Levich, B. (1988). Dragging of a liquid by a moving plate. In P. Pelce & A. Libchaber (Eds), *Dynamics of curved fronts* (pp. 141–153). San Diego: Academic Press.

Launay, G. (2018). PyDSA_core: drop shape analysis in python. https://framagit.org/gabylaunay/pyDSA_core. [Online; accessed: 12th Nov 2019].

Leelamanie, D. A. L., & Karube, J. (2007). Effects of organic compounds, water content and clay on the water repellency of a model sandy soil. *Soil Science and Plant Nutrition*, *53*, 711–719. https://doi.org/10.1111/j.1747-0765.2007.00199.x

Leelamanie, D. A. L., & Karube, J. (2012). Drop size dependence of soil-water contact angle in relation to the droplet geometry and line tension. *Soil Science and Plant Nutrition*, *58*, 675–683. https://doi.org/10.1080/00380768.2012.745798

Leelamanie, D. A. L., Karube, J., & Yoshida, A. (2008). Characterizing water repellency indices: Contact angle and water drop penetration time of hydrophobized sand. *Soil Science and Plant Nutrition*, *54*, 179–187. https://doi.org/10.1111/j.1747-0765.2007.00232.x

Letey, J., Osborn, J., & Pelishek, R. E. (1962). The influence of the water-solid contact angle on water movement in soil. *Hydrological Sciences Journal*, *7*, 75–81. https://doi.org/10.1080/02626666209493272

Linder, M. B. (2009). Hydrophobins: Proteins that self assemble at interfaces. *Current Opinion in Colloid & Interface Science*, *14*, 356–363. https://doi.org/10.1016/j.cocis.2009.04.001

Maimon, A., Gross, A., & Arye, G. (2017). Greywater-induced soil hydrophobicity. *Chemosphere*, *184*, 1012–1019. https://doi.org/10.1016/j.chemosphere.2017.06.080

Mataix-Solera, J., García-Irles, L., Morugán, A., Doerr, S. H., Garcia-Orenes, F., Arcenegui, V., & Atanassova, I. (2011). Longevity of soil water repellency in a former wastewater disposal tree stand and potential amelioration. *Geoderma*, *165*, 78–83. https://doi.org/10.1016/j.geoderma.2011.07.006

McHale, G., Newton, M. I., & Shirtcliffe, N. J. (2005). Water-repellent soil and its relationship to granularity, surface roughness and hydrophobicity: A materials science view. *European Journal of Soil Science*, *56*, 445–452. https://doi.org/10.1111/j.1365-2389.2004.00683.x

McHale, G., Orme, B. V., Wells, G. G., & Ledesma-Aguilar, R. A. (2019). Apparent contact angles on lubricant impregnated surfaces/SLIPS: From superhydrophobicity to electrowetting. *Langmuir*, *35*, 4197–4204. https://doi.org/10.1021/acs.langmuir.8b04136

McHale, G., Shirtcliffe, N. J., Newton, M. I., & Pyatt, F. B. (2007). Implications of ideas on super-hydrophobicity for water repellent soil. *Hydrological Processes*, *21*, 2229–2238. https://doi.org/10.1002/hyp.6765

McHale, G., Shirtcliffe, N. J., Newton, M. I., Pyatt, F. B., & Doerr, S. H. (2007). Self-organization of hydrophobic soil and granular surfaces. *Applied Physics Letters*, *90*, 054110. https://doi.org/10.1063/1.2435594

Neinhuis, C. (1997). Characterization and distribution of water-repellent, self-cleaning plant surfaces. *Annals of Botany*, *79*, 667–677. https://doi.org/10.1006/anbo.1997.0400

Ng, S. H. Y., & Lourenço, S. D. N. (2016). Conditions to induce water repellency in soils with dimethyldichlorosilane. *Geotechnique*, *66*, 441–444. https://doi.org/10.1680/jgeot.15.T.025

Niemelä-Anttonen, H., Koivuluoto, H., Tuominen, M., Teisala, H., Juuti, P., Haapanen, J., ... Vuoristo, P. (2018). Icephobicity of slippery liquid infused porous surfaces under multiple freeze-thaw and ice accretion-detachment cycles. *Advanced Materials Interfaces*, *5*, 1800828. https://doi.org/10.1002/admi.201800828

Nosonovsky, M. (2011). Slippery when wetted. *Nature*, *477*, 412–413. https://doi.org/10.1038/477412a

Öner, D., & McCarthy, T. J. (2000). Ultrahydrophobic surfaces. Effects of topography length scales on wettability. *Langmuir*, *16*, 7777–7782. https://doi.org/10.1021/la000598o

Parise, M., & Cannon, S. H. (2012). Wildfire impacts on the processes that generate debris flows in burned watersheds. *Natural Hazards*, *61*, 217–227. https://doi.org/10.1007/s11069-011-9769-9

Piccolo, A., Spaccini, R., Haberhauer, G., & Gerzabek, M. H. (1999). Increased sequestration of organic carbon in soil by hydrophobic protection. *Naturwissenschaften*, *86*, 496–499. https://doi.org/10.1007/s001140050662

Quére, D., Lafuma, A., & Bico, J. (2003). Slippy and sticky microtextured solids. *Nanotechnology*, *14*, 1109–1112. https://doi.org/10.1088/0957-4484/14/10/307

Quyum, A., Achari, G., & Goodman, R. H. (2002). Effect of wetting and drying and dilution on moisture migration through oil contaminated hydrophobic soils. *Science of the Total Environment*, *296*, 77–87. https://doi.org/10.1016/S0048-9697(02)00046-3

Regalado, C. M., & Ritter, A. (2006). Geostatistical tools for characterizing the spatial variability of soil water repellency

parameters in a Laurel forest watershed. *Soil Science Society of America Journal*, *70*, 1071–1081. https://doi.org/10.2136/sssaj2005.0177

Roach, P., Shirtcliffe, N. J., & Newton, M. I. (2008). Progess in superhydrophobic surface development. *Soft Matter*, *4*, 224–240. https://doi.org/10.1039/B712575P

Robichaud, P. R., Lewis, S. A., & Ashmun, L. E. (2008). *New procedure for sampling infiltration to assess post-fire soil water repellency* (Res. Note. RMRS-RN-33). Fort Collins, CO: U.S. Department of Agriculture, Forest Service, Rocky Mountain Research Station.

Roy, J. L., & McGill, W. B. (1998). Characterization of disaggregated nonwettable surface soils found at old crude oil spill sites. *Canadian Journal of Soil Science*, *78*, 331–344. https://doi.org/10.4141/S97-039

Roy, J. L., & McGill, W. B. (2000). Investigation into mechanisms leading to the development, spread and persistence of soil water repellency following contamination by crude oil. *Canadian Journal of Soil Science*, *80*, 595–606. https://doi.org/10.4141/S99-091

Roy, J. L., & McGill, W. B. (2002). Assessing soil water repellency using the molarity of ethanol droplet (MED) test. *Soil Science*, *167*, 83–97. https://doi.org/10.1097/00010694-200202000-00001

Roy, J. L., McGill, W. B., & Rawluk, M. D. (1999). Petroleum residues as water-repellent substances in weathered nonwettable oil-contaminated soils. *Canadian Journal of Soil Science*, *79*, 367–380. https://doi.org/10.4141/S97-040

Saulick, Y., Lourenço, S. & Baudet, B. 2016. Effect of particle size on the measurement of the apparent contact angle in sand of varying wettability under air-dried conditions. P. Delage, Y.-J. Cui, S. Ghabezloo, J.-M. Pereira and A.-M. Tang In E3S Web of Conferences, Vol. 9.

Schaumann, G. E., Braun, B., Kirchner, D., Rotard, W., Szewzyk, U., & Grohmann, E. (2007). Influence of biofilms on the water repellency of urban soil samples. *Hydrological Processes*, *21*, 2276–2284. https://doi.org/10.1002/hyp.6746

Seiwert, J., Clanet, C., & Quéré, D. (2011). Coating of a textured solid. *Journal of Fluid Mechanics*, *669*, 55–63.

Semprebon, C., Mchale, G., & Kusumaatmaja, H. (2017). Apparent contact angle and contact angle hysteresis on liquid infused surfaces. *Soft Matter*, *13*, 101–110.

Shakesby, R. A., Doerr, S. H., & Walsh, R. P. D. (2000). The erosional impact of soil hydrophobicity: Current problems and future research directions. *Journal of Hydrology*, *231–232*, 178–191. https://doi.org/10.1016/S0022-1694(00)00193-1

Shirtcliffe, N. J., Aqil, S., Evans, C., McHale, G., Newton, M. I., Perry, C. C., & Roach, P. (2004). The use of high aspect ratio photoresist (SU-8) for super-hydrophobic pattern prototyping. *Journal of Micromechanics and Microengineering*, *14*, 1384–1389. https://doi.org/10.1088/0960-1317/14/10/013

Shirtcliffe, N. J., McHale, G., Atherton, S., & Newton, M. I. (2010). An introduction to superhydrophobicity. *Advances in Colloid and Interface Science*, *161*, 124–138. https://doi.org/10.1016/j.cis.2009.11.001

Smith, J. D., Dhiman, R., Anand, S., Reza-Garduno, E., Cohen, R. E., McKinley, G. H., & Varanasi, K. K. (2013). Droplet mobility on lubricant-impregnated surfaces. *Soft Matter*, *9*, 1772–1780. https://doi.org/10.1039/C2SM27032C

Spaccini, R., Piccolo, A., Conte, P., Haberhauer, G., & Gerzabek, M. H. (2002). Increased soil organic carbon sequestration through hydrophobic protection by humic substances. *Soil Biology and Biochemistry*, *34*, 1839–1851. https://doi.org/10.1016/S0038-0717(02)00197-9

Tao, R., Mchale, G., Reboud, J., Cooper, J. M., Torun, H., Luo, J. T., … Fu, Y. (2020). Hierarchical nanotexturing enables acoustofluidics on slippery yet sticky, flexible surfaces. *Nano Letters*, *20*, 3263–3270. https://doi.org/10.1021/acs.nanolett.0c00005

Tas, M., Memon, H., Xu, F., Ahmed, I., & Hou, X. (2020). Electrospun nanofibre membrane based transparent slippery liquid-infused porous surfaces with icephobic properties. *Colloids and Surfaces A: Physicochemical and Engineering Aspects*, *585*, 124177. https://doi.org/10.1016/j.colsurfa.2019.124177

Tessler, N., Wittenberg, L., Malkinson, D., & Greenbaum, N. (2008). Fire effects and short-term changes in soil water repellency – Mt. Carmel, Israel. *Catena*, *74*, 185–191. https://doi.org/10.1016/j.catena.2008.03.002

Tonelli, M., Peppou-Chapman, S., Ridi, F., & Neto, C. (2019). Effect of pore size, lubricant viscosity, and distribution on the slippery properties of infused cement surfaces. *Journal of Physical Chemistry C*, *123*, 2987–2995.

Tsai, P. S., Yang, Y. M., & Lee, Y. L. (2006). Fabrication of hydrophobic surfaces by coupling of Langmuir-Blodgett deposition and a self-assembled monolayer. *Langmuir*, *22*, 5660–5665. https://doi.org/10.1021/la053152m

Utermann, S., Aurin, P., Benderoth, M., Fischer, C., & Schröter, M. (2011). Tailoring the frictional properties of granular media. *Physical Review E*, *84*, 031306. https://doi.org/10.1103/PhysRevE.84.031306

Van Dam, J. C., Hendrickx, J. M. H., Van Ommen, H. C., Bannink, M. H., Van Genuchten, M. T., & Dekker, L. W. (1990). Water and solute movement in a coarse-textured water-repellent field soil. *Journal of Hydrology*, *120*, 359–379. https://doi.org/10.1016/0022-1694(90)90159-U

van Ommen, H. C., Dekker, L. W., Dijksma, R., Hulshof, J., & van der Molen, W. H. (1988). A new technique for evaluating the presence of preferential flow paths in nonstructured soils. *Soil Science Society of America Journal*, *52*, 1192–1193. https://doi.org/10.2136/sssaj1988.03615995005200040056x

Wang, P., Zhang, D., & Lu, Z. (2015). Slippery liquid-infused porous surface bio-inspired by pitcher plant for marine anti-biofouling application. *Colloids and Surfaces B: Biointerfaces*, *136*, 240–247. https://doi.org/10.1016/j.colsurfb.2015.09.019

Wang, Y., Wang, X., Chau, H. W., Si, B., Yao, N., & Li, Y. (2018). Water movement and finger flow characterization in homogeneous water-repellent soils. *Vadose Zone Journal*, *17*, 1–12. https://doi.org/10.2136/vzj2018.01.0021

Wenzel, R. N. (1936). Resistance of solid surfaces to wetting by water. *Industrial & Engineering Chemistry*, *28*, 988–994. https://doi.org/10.1021/ie50320a024

Wessels, J. G. H. (1996). Fungal hydrophobins: Proteins that function at an interface. *Trends in Plant Science*, *1*, 9–15. https://doi.org/10.1016/S1360-1385(96)80017-3

Wilson, P. W., Lu, W., Xu, H., Kim, P., Kreder, M. J., Alvarenga, J., & Aizenberg, J. (2013). Inhibition of ice nucleation by slippery liquid-infused porous surfaces (SLIPS). *Physical Chemistry Chemical Physics*, *15*, 581–585. https://doi.org/10.1039/C2CP43586A

Wong, T.-S., Kang, S. H., Tang, S. K. Y., Smythe, E. J., Hatton, B. D., Grinthal, A., & Aizenberg, J. (2011). Bioinspired self-repairing

slippery surfaces with pressure-stable omniphobicity. *Nature*, *477*, 443–447. https://doi.org/10.1038/nature10447

Woods, S. W., Birkas, A., & Ahl, R. (2007). Spatial variability of soil hydrophobicity after wildfires in Montana and Colorado. *Geomorphology*, *86*, 465–479. https://doi.org/10.1016/j.geomorph.2006.09.015

Xiao, L., Li, J., Mieszkin, S., Di Fino, A., Clare, A. S., Callow, M. E., ... Levkin, P. A. (2013). Slippery liquid-infused porous surfaces showing marine antibiofouling properties. *ACS Applied Materials and Interfaces*, *5*, 10074–10080. https://doi.org/10.1021/am402635p

Yeh, K.-Y., Chen, L.-J., & Chang, J.-Y. (2008). Contact angle hysteresis on regular pillar-like hydrophobic surfaces. *Langmuir*, *24*, 245–251. https://doi.org/10.1021/la7020337

Young, T. I. (1832). An essay on the cohesion of fluids. *Abstracts of the Papers Printed in the Philosophical Transactions of the Royal Society of London*, *1*, 171–172. https://doi.org/10.1098/rspl.1800.0095

SUPPORTING INFORMATION

Additional supporting information may be found online in the Supporting Information section at the end of this article.

How to cite this article: McCerery R, Woodward J, McHale G, Winter K, Armstrong S, Orme BV. Slippery liquid-infused porous surfaces: The effect of oil on the water repellence of hydrophobic and superhydrophobic soils. *Eur J Soil Sci*. 2020;1–16. https://doi.org/10.1111/ejss.13053